Probing the large-scale structure of the universe with future galaxy redshift surveys

Hatton, Stephen John

Probing the large-scale structure of the Universe with future galaxy redshift surveys

Stephen John Hatton

A thesis submitted to the University of Durham
in accordance with the regulations for
admittance to the Degree of Doctor of Philosophy.

Department of Physics
University of Durham
February 25, 1999

Probing the large-scale structure of the Universe with future galaxy redshift surveys

Stephen John Hatton

February 25, 1999

Abstract

Several projects are currently underway to obtain large galaxy redshift surveys over the course of the next decade. The aim of this thesis is to study how well the resultant three-dimensional maps of the galaxy distribution will be able to constrain the various parameters of the standard Big Bang cosmology.

The work is driven by the need to deal with data of far better quality than has previously been available. Systematic biases in the treatment of existing datasets have been dwarfed by random errors due to the small size of the sample, but this will not be the case with the wealth of data that will shortly become available.

We employ a set of high-resolution *N*-body simulations spanning a range of cosmologies and galaxy biasing schemes. We use the power spectrum of the galaxy density field, measured using the fast Fourier transform process, to develop models and statistics for extracting cosmological information. In particular, we examine the distortion of the power spectrum by galaxy peculiar velocities when measurements are made in redshift space.

Mock galaxy catalogues are drawn from these simulations, mimicking the geometries and selection functions of the large surveys we wish to model. Applying the same models to the mock catalogues is not a trivial task, as geometrical effects distort the power spectrum, and measurement errors are determined by the survey volume. We develop methods for assessing these effects and present an in-depth analysis of the likely confidence intervals we will obtain from the surveys on the parameters that determine the power spectrum.

Real galaxy catalogues are prone to additional biases that must be assessed and removed. One of these is the effect of extinction by dust in the Milky Way, which imprints its own angular clustering signal on the measured power spectrum. We investigate the strength of this effect for the SDSS survey.

Contents

Declaration

The work described in this thesis was undertaken between 1995 and 1998 whilst the author was a research student under the supervision of Dr S M Cole and Prof C S Frenk in the Department of Physics at the University of Durham. This work has not been submitted for any other degree at the University of Durham or at any other University.

Portions of this work have appeared in the papers:

- Hatton S., Cole S., 1998, MNRAS, 296, 10 (Chapter 6).
- Cole S., Hatton S., Weinberg D. H., Frenk C. S., 1998, MNRAS, 300, 945 (Chapter 4)

Chapter 1

Galaxy redshift surveys

THE ARGUMENT. In this chapter we summarize our understanding of galaxy redshift in the context of an expanding Universe. We briefly outline the history of redshift observations through the twentieth century, particularly with reference to attempts to compile large catalogues of galaxies to examine their three-dimensional clustering properties. We describe the current large datasets like the PSCz and Las Campanas redshift survey, and give details of several even more ambitious surveys that are currently in progress or planned. We explain the need for a study of the sort presented in this thesis.

1.1 Introduction

The first galaxy spectra were measured by Vesto Slipher at Lowell Observatory in the early 1910's. The existence of the Doppler effect in sound and light waves had been confirmed in the laboratory seventy years previously, and it was a short time before the wavelength shifts of these spectra were interpreted within this framework. The light was being emitted by objects which were moving with significant speeds relative to the observer, greater than the velocities of stars in the Milky Way. Continuing observations by Slipher, and later Edwin Hubble and Milton Humason at Mount Wilson, of the preponderance of redshifted over blueshifted galaxies lent credence to the work of de Sitter and others, whose cosmologies called for an expanding spacetime, ie. one in which all galaxies would be getting further away from each other.

During this century, our understanding of redshift within the context of the standard cosmology has remained broadly unaltered, but redshift observations have constantly provided support for this paradigm. Observational capabilities have grown fast enough to sustain an exponential growth in both the number of known redshifts, and the redshift of

the furthest galaxy observed. This rapid growth of data has given astronomers the ability to construct three-dimensional maps of the density distribution in the nearby Universe, as well as allowing accurate measurement of the statistics of the galaxy density field over large volumes of space, which can be tied to theoretical predictions in order to measure the key cosmological parameters.

In this introductory chapter, we first outline (section 1.2) what is meant by redshift, specifically galaxy redshift. We go on to present a brief history of galaxy redshift surveys to date in section 1.3, and in section 1.4 detail several surveys currently in progress, and what we may hope to learn from them. Section 1.5 presents the case for this work.

1.2 What is redshift?

Redshift is the observed change in the frequency or wavelength of signals emitted from a source which is moving with respect to the observer. The extent of the frequency shift depends on the radial velocity of this relative motion, so, if the signal has known spectral characteristics, the speed can be deduced by measuring the redshift.

For a source which emits radiation at a wavelength $\lambda_{\rm lab}$, which is measured by an observer at wavelength $\lambda_{\rm obs}$, the redshift is defined as:

$$z = \frac{\lambda_{\rm obs} - \lambda_{\rm lab}}{\lambda_{\rm lab}}. \tag{1.1}$$

1.2.1 The Doppler effect

Discovered by Christian Doppler (1805-1853), the Doppler effect refers to the change in frequency of a wave depending on the observer's motion relative to the source. The effect occurs for all waves, whether light, sound, or water. This effect is readily apparent in the change in pitch of a police siren as it approaches and (hopefully) passes the observer.

We can see the Doppler effect as the application of a Galilean transformation to a plane wave. The equation describing a plane wave is:

$$\Psi(\mathbf{r}, t) = Ae^{i(\mathbf{k}.\mathbf{r}-\omega t)}. \tag{1.2}$$

Under the Galilean transformation between two frames with relative velocity v,

$$x' = x + vt$$

$$t' = t. \tag{1.3}$$

The phase of the wave must be invariant, so

$$\begin{aligned} kx - \omega t &= k'x' - \omega' t' \\ &= k'(x + vt) - \omega' t. \end{aligned} \tag{1.4}$$

We equate coefficients of x and t,

$$\begin{aligned} k &= k' \text{ from } x, \text{ and} \\ \omega &= -k'v + \omega' \text{ from } t. \end{aligned} \tag{1.5}$$

Thus

$$\omega' = \omega(1 - v/c). \tag{1.6}$$

Under the Galilean transform, measuring rods do not change length, so the observed wavelength is unchanged, but peaks and troughs in the incoming wave will seem to arrive at a faster rate if the source is approaching the object or vice versa, so the frequency, and hence the sound speed, are shifted. In this regime, the fractional change in frequency is given by

$$z = \frac{\omega' - \omega}{\omega} = -\frac{v}{c}. \tag{1.7}$$

For moving objects emitting light, there is no "medium" for the wave to travel in; instead of the Galilean transformation, we must use the Lorentz transformation of special relativity to tackle the problem. In this case, we have

$$\begin{aligned} x' &= \gamma(x + vt), \\ t' &= \gamma(t + vx/c^2). \end{aligned} \tag{1.8}$$

where $\gamma = (1 - v/c)^{-1/2}$. The phase of a plane wave is again an invariant quantity, so

$$\begin{aligned} kx - \omega t &= k'x' - \omega' t' \\ &= k'\gamma(x + vt) - \omega'\gamma(t + vx/c^2). \end{aligned} \tag{1.9}$$

Given that the speed of light is invariant, ie. $\omega/k = \omega'/k'$, we obtain

$$\gamma\omega'(1 + v/c) = \omega. \tag{1.10}$$

So,

$$\omega' - \omega = \omega'[\gamma(v/c + 1) - 1], \tag{1.11}$$

and the expression for redshift under the Lorentz transformation is:

$$z = \sqrt{\frac{1 + v/c}{1 - v/c}} - 1 \approx \frac{v}{c}. \tag{1.12}$$

The final approximation in equation 1.12 is valid in the limit of $v \ll c$. We see, by comparison with equation 1.7, that for recession much slower than the speed of light, the redshift is equivalent to a Doppler shift. We can thus define a "symbolic" velocity for any object with a measured redshift, $v_s = cz$, which equates to the physical velocity of the object's recession in the low-z limit. Within our galaxy, Doppler shifts in the spectra of stars, whose atmospheres absorb light at discrete frequencies, are used to calculate their velocities, giving us important information about the dynamics of the Milky Way. Observations of binary stars show each star alternating between red and blue shift, as is expected if they are orbiting around each other, and measurements of these shifts enables the dynamics of such systems to be calculated.

1.2.2 Gravitational redshift

It takes work to climb out of a hole; under general relativity, this principle is extended to photons in a gravitational field. Thus a photon which reaches us having been emitted from a particularly deep potential will suffer a loss of energy, and hence a frequency shift towards the red. The effect itself has been measured in the laboratory, originally by Pound & Rebka (1959), who used γ-rays from ^{57}Fe travelling up and down a $22\mathrm{m}$ mine shaft and found the speeds needed to re-establish resonance via the Mossbauer effect. The effect has also been observed for photons from the Sun and from white dwarfs within our Galaxy. Gravitational redshift can also be viewed as a time-dilation effect; clocks run slow in the presence of a gravitational field, including the internal clocks that determine the period of electrons in an atom, and hence the energy levels of atomic transitions are lowered.

1.2.3 Cosmological redshift

In 1917, Slipher presented radial velocities from spectra of twenty-five galaxies. Twenty-one of these had a redshift associated with them, rather than a blueshift. Speeds were often in excess of $2000\mathrm{km\,s^{-1}}$, showing that the objects were moving substantially faster than the stars of our own galaxy. Hubble expanded Slipher's work a decade later, increasing the size of the sample by a factor of two. He was thus able to confirm that the surplus of redshifts was a statistically significant effect; over 90% of the galaxies were receding from us.

Hubble's great contribution (Hubble 1929) was to combine the redshift data with independent measures of galaxy distances (from Cepheid variable stars and novae). He was able to do this initially for half his sample of forty-six redshifts, and using this data he compiled the first graph of redshift against distance. A simple, linear relationship between the two quantities proved a remarkably good fit the data. This relationship has subsequently become known as Hubble's law.

These observations paved the way for a cosmological interpretation of galaxy redshifts. Hubble himself speculated that his results might be the signature of the de Sitter expansion of the Universe. A few years earlier, unknown to Hubble, Georges Lemaitre had worked out a connection between Slipher's redshifts and Einstein's general theory of relativity, showing that redshifts were a prediction of an expanding Universe model.

In the picture of an expanding universe, the scale factor of the metric, R, increases with time. It is this increase which causes redshift, rather than the motions of galaxies in the three physical dimensions. In the class of models where the scale factor can be separated from the positional part of the metric, such as the Friedmann-Robertson-Walker models, the expression for the metric can be written:

$$d\tau^2 = dt^2 + R(t)^2[X(r)^2 dr^2 + r^2 d\Omega^2]. \tag{1.13}$$

For a photon the proper time, $d\tau$, is zero, as is $d\Omega$. Then the equation is separable in t and r, and the integral of the time-dependent part depends only on the proper distance between emission and observation. Considering a source which emits a signal at t_e, which is observed at t_0, and then emits another signal a short time δ_e later,

$$\int_{t_\mathrm{e}}^{t_0} \frac{dt}{R(t)} = \int_{t_\mathrm{e}+\delta_\mathrm{e}}^{t_0+\delta_0} \frac{dt}{R(t)}. \tag{1.14}$$

This then implies

$$\frac{\delta_{\rm e}}{R(t_{\rm e})} = \frac{\delta_0}{R(t_0)}. \tag{1.15}$$

Hence, the cosmological redshift is given by:

$$z = \frac{R(t_0)}{R(t_{\rm e})} - 1. \tag{1.16}$$

1.2.4 Alternative explanations of redshift

A number of alternative explanations for the observed redshift of galaxies have been put forward. None of these ideas have generally been considered as viable alternatives to the expanding Universe by the majority of astronomers, and some of them rely on new, as yet unobserved physics. Among these hypotheses are:

- **Dust absorption**. As will be discussed in Chapter 5, the presence of dust along lines of sight to celestial objects results in a reddening of their starlight. Could this effect be responsible for redshift? Not really. Whilst the continuum may affected in this way, there is no way that dust absorption could produce the change in the wavelengths of spectral features that is observed.

- **Tired light**. The tired light hypothesis was first put forward by Zwicky. The idea is that as light travels, it naturally reddens by losing energy. A good physical explanation is lacking, although the theory has received a boost from modern particle physics. However, the problem of spectral lines remains; if it is a stochastic process that exhausts the photons, the lines would be expected to be washed out if substantial reddening occurs.

- **Active galaxies**. In a number of papers, Halton Arp has outlined phenomenological evidence that questions the expansion-origin of redshift. Most recently, Arp 1999 describes the existence of a "string" of five quasars at moderate redshifts, aligned along the minor axis of a local Seyfert galaxy. Moreover, the QSOs are lined up in descending order of redshift. This suggests that the QSOs represent some sort of ejecta from the nearby galaxy, and that the redshift in this case is certainly non-cosmological. This is an interesting point, but it is not obvious whether or not this could be a freak occurrence or whether the treatment is statistically rigorous.

- **Increasing α.** The atoms and molecules we use to build photon detectors are all bound together by electromagnetic force. The strength of this force depends on the value of the fine structure constant, α. Were α to vary, the wavelength of light that each atomic transition produces would change as well. Light from distant galaxies appears to have a longer wavelength; but could it just be that on Earth our detectors have contracted since the emission epoch? The effect seems impossible to distinguish from an expansion redshift (Barrow & Magueijo 1999), and one is left to choose whether one prefers an expanding Universe or a contracting measuring rod.

- **Information Mechanics.** In the formalism of Information Mechanics (Kantor 1977), the mass of a particle is a reflection of the amount of information it can convey to the observer. Recently, this approach has been applied to photon redshift (Kantor 1999). The methodology is similar in style to that of quantum mechanics. An observed photon is considered as a carrier of information about the location of its source. The source itself cannot be completely at rest. Thus the source will have moved since the photon was emitted. The direction of this motion is not known, so a source that emitted a photon long ago will now have a position that is uncertain by a larger amount than a local emitter. The photon from the distant source thus contains less positional information, resulting in a loss of "mass", ie. an increasing wavelength.

These examples are just some of the many alternatives to an expanding Universe that have been suggested. Some seem to have predictions that are testable, others appear to be completely unfalsifiable.

One key test of Universal expansion is the Tolman surface brightness test. All redshift models seek to explain the observed linear dependence of redshift on distance. Surface brightness falls off more quickly with distance if the Universe is expanding because of the evolution in the volume element with look-back time. This picture is confused by possible evolution of objects in the high redshift samples, but recent work (Pahre, Djorgovski, & De Carvalho 1996) has shown that a non-expanding Universe can be ruled out to a significant degree. This does not discriminate against the varying-α model, which explains the change in surface brightness by the fact that the area of our detectors has physically shrunk since the detected photons were emitted.

1.3 Brief history of surveys

Slipher's original sample of twenty-five galaxies is probably the first galaxy redshift catalogue to appear in the literature. Ten years later (Hubble 1929), Hubble gave the redshifts and magnitudes of forty-six nebulae, with independent distance estimates for twenty-four of them. These nebulae all had $v < 1800\mathrm{km\,s^{-1}}$, ie. $z < 0.06$. The exponential rise in the number of known redshifts with time was swiftly started by Humason's paper (Humason 1931), who observed another forty-six nebulae with the 100 inch reflector on Mount Wilson. Observational advances enabled this survey to be slightly deeper than Hubble's sample. From these early surveys, certain results were already emerging that have underpinned cosmological thought for the rest of this century, and have backed up the cosmological interpretation of redshift:

- The correlation of z with other methods of estimating distance has withstood the test of time, although the normalization, through the value of the Hubble parameter, H_0, is still poorly constrained.
- The relation $L_{\mathrm{obs}} \propto z^{-2}$ for eg. the brightest galaxies in clusters confirms that $z \propto r$, with a scatter that appears to be totally due to the intrinsic scatter in magnitude of galaxies, since it has no z dependence.
- For close pairs of galaxies in the sky, and indeed for galaxy clusters, the mean redshift is, in general, much larger than the difference in redshift between the objects. This fact suggests that physically close objects have similar redshifts. See eg. Arp 1999 for a conflicting view.
- Redshift is also seen to be inversely proportional to the angular diameter distance.

Following these initial discoveries, the number of galaxy redshifts observed increased rapidly after the Second World War. The question of the validity of the homogeneous Friedmann Universe model was seen as the crucial question of cosmology, and the Hubble law as one of its chief tests.

Research concentrated along two lines:

- **Clusters**. Galaxy clusters contain many members, whose redshifts are generally scattered about the mean redshift of the cluster with a dispersion caused by the Doppler

effect of their peculiar velocities. Making multiple redshift measurements of cluster galaxies can thus enable very accurate determination of this mean redshift. The effect of non-linear peculiar velocities is washed out, so the cluster redshift is expected to be close to that expected from a pure Hubble expansion. We thus have a technique for constraining the local Hubble relation very accurately.

- **Radio galaxies**. The first use of radio telescopes in the late 1940's and early 50's led to the observation of so-called "radio galaxies", galaxies with strong emission at radio frequencies. The identification of optical counterparts to these sources, and the subsequent measurement of their redshifts, showed that these galaxies are generally at rather higher distances than optically selected galaxies, implying that they are highly luminous objects. Radio galaxies thus act as a useful probe of the distant Universe, testing the Hubble law at very large distances.

We see two contrasting approaches here, and these approaches still characterize the way cosmological research is performed. On the one hand, one can focus on nearby regions were data is plentiful, and use this abundance to measure local laws to a very high degree of accuracy. Alternatively, one can make observations at greater and greater distances, where they are potentially much more powerful at discriminating between different cosmological models, but where data is far scarcer and harder to obtain, and where possible evolutionary effects can contaminate the signal. These approaches are of course entirely complementary, but the choice of how to allocate finite resources between the two is a major preoccupation of modern-day observational work.

In the late 1970's, the first surveys started to appear that set out to measure the large-scale distribution of galaxies. Gregory & Thompson (1978) combined pencil beam surveys to clusters like Coma and Perseus and began to identify superclusters. Kirshner et al. (1981) used three pencil beams in the Boötes constellation to identify a large void common to each of the lines of sight. Wide angle surveys started with the Revised Shapley-Ames catalogue (Sandage & Tammann 1987). This work started the trend for conducting homogeneous, unbiased surveys rather than assembling redshifts from disparate programmes.

The first real herald of the way surveys would work for the rest of the century came with the CfA survey (Huchra et al. 1983). Voids and filaments were readily apparent in the slices of this work, and the striking "stick-man" was first seen. The CfA has subsequently

be extended in a variety of different ways, and a southern counterpart, the SSRS, has been constructed (da Costa et al. 1988). With the advent of the CfA and its successors, researchers were finally able to do statistical, rather than anecdotal, science with redshift surveys.

The *IRAS* satellite was launched in 1983 with the purpose of conducting an all-sky survey in the infrared. A number of redshift surveys have been compiled using the resultant catalogue as parent. These have gradually improved over the last ten years in terms of sampling and magnitude limit, culminating in the PSCz survey (Saunders et al. 1994), which is complete to $0.6\mathrm{Jy}$, and contains 15,500 galaxies.

The Las Campanas Redshift survey (LCRS, Shectman et al. 1996) is the largest completed redshift survey currently in existence. It consists of 25,000 galaxies, selected from CCD photometry. A wealth of detailed structure is evident from angular slices through the survey, far more than the hints of walls and filaments provided by smaller surveys like the CfA. The LCRS represents the current state of the art, and can be seen as the bridge between the older surveys and the surveys which have recently been embarked upon or are currently being considered.

The focus today is much more concentrated on surveys with extremely good statistics dedicated to answering specific scientific goals. To do this, there are three basic considerations; we must probe a large volume, in a homogeneous way, with a high galaxy density.

In table 1.1 we summarize the details of some of the key redshift surveys that exist in the literature. Figure 1.1 is a graphical representation of the number of known redshifts as a function of time over the last century. It can be seen clearly that the rise in the number or galaxy redshifts has been an exponential one. There is a steep break in the relationship at around the present day, as we move on to projected redshift numbers from surveys currently or soon to be underway. The rise in the exponent can be attributed to the massive advantage given to us by the ability of modern instruments to multiplex, ie. measure the redshifts of many galaxies in a single exposure time.

Table 1.1. A brief summary of the major existing redshift surveys of the last century.

Name	Completion Year	Number of redshifts Total	New	Reference
—	1917	25	25	Slipher 1917
—	1929	46	46	Hubble 1929
—	1931	46	46	Humason 1931
HMS	1956	920	920	Humason, Mayall, & Sandage 1956
1BG	1964	1000	1000	de Vaucouleurs 1964
3CR	1972	110	110	Kristian & Minkowski 1972
—	1975	150	150	Roberts 1975
2BG	1976	4000	3000	de Vaucouleurs et al 1976
KOS	1978	164	164	Kirshner, Oemler, & Schechter 1978
RSA	1981	1191	1191	Sandage & Tammann 1987
NBG	1981	1787	1787	Tully & Fisher 1987
AARS	1983	320	320	Bean et al. 1983
CfA	1983	2417	2417	Huchra et al. 1983
XNBG	1987	2367	600	Tully & Fisher 1987
IRAS	1988	324	324	Soifer et al. 1987
SSRS	1988	1727	1727	da Costa et al. 1988
P-P	1988	5000	5000	Giovanelli & Haynes 1991
1.936Jy	1989	2658	2334	Strauss et al. 1992
CfA2N	1989	6500	6500	Geller & Huchra 1989
QDOT	1990	2185	1500	Rowan-Robinson et al. 1990
S-APM	1992	1787	1787	Loveday et al. 1992
CfA2S	1992	4283	4283	Huchra 1992
1.2Jy	1992	5339	2683	Fisher 1992
SSRS2	1994	3600	1900	da Costa et al. 1994
PSCz	1994	15,500	9000	Saunders et al. 1994
ESP	1995	3342	3342	Zucca et al. 1996
ORS	1995	8266	8266	Santiago et al. 1995
CNOC	1996	2600	2600	Yee, Ellingson, & Carlberg 1996
LCRS	1996	24,000	24,000	Shectman et al. 1996
DUKST	1996	2500	2500	Ratcliffe et al. 1996
CNOC2	1998	5000	5000	Carlberg et al. 1998

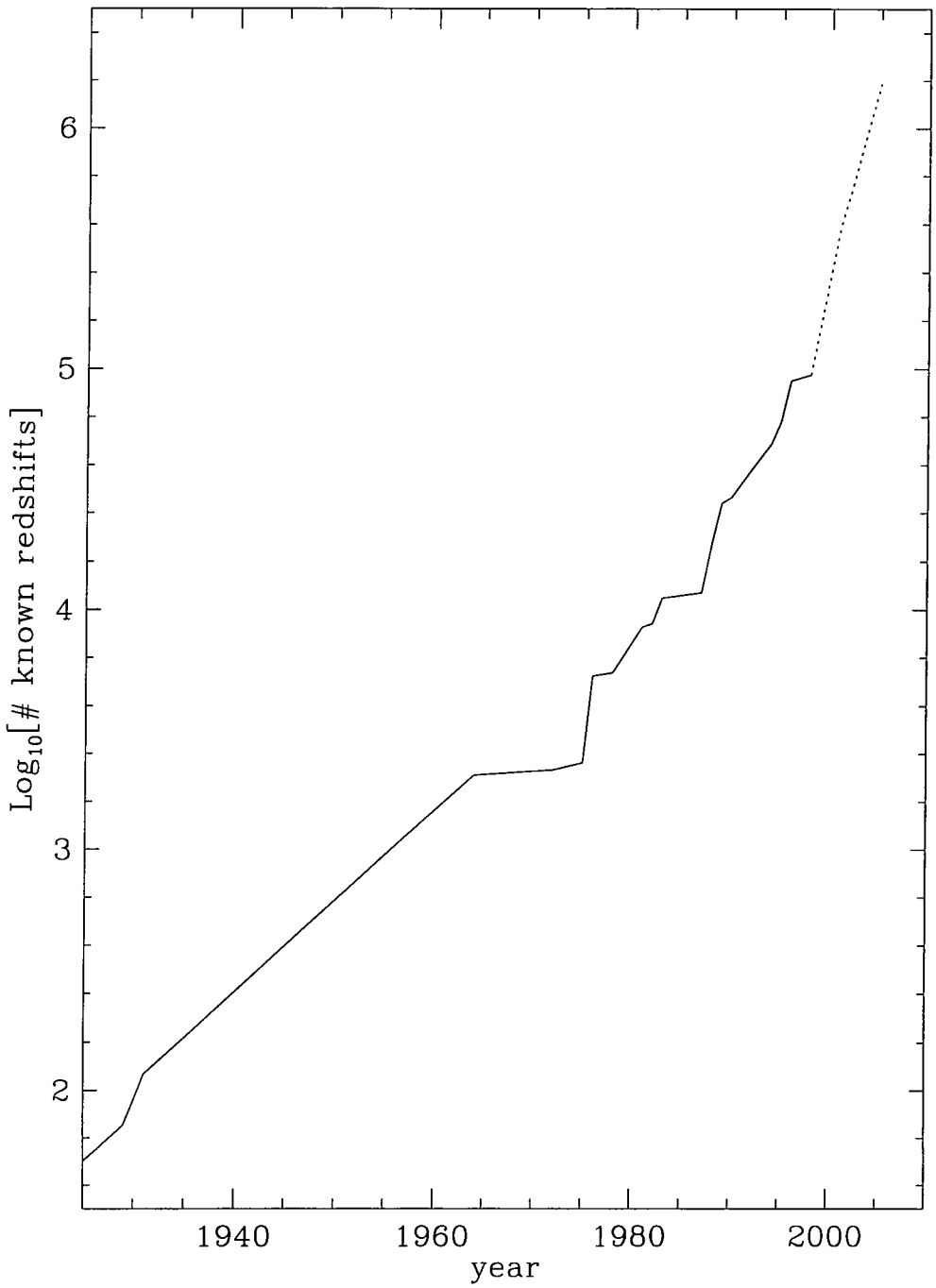

Figure 1.1: The number of known galaxy redshifts as a function of time. The dotted line represents the results expected from future surveys.

1.4 The future of redshift surveys

Recent times have seen further advances in observational capabilities. Primarily, the development of automated techniques for fibre positioning and redshift measurement has enabled observers to make much better use of telescope time. Efforts are directed towards obtaining statistically large samples of galaxies, with a high degree of homogeneity. Current surveys are much more reliable, with fewer selection problems, than their predecessors. Deep surveys also enable the study of evolution within the sample: both of galaxies themselves and of the way they cluster. Here we list and compare some of the large surveys currently being undertaken or planned.

- **2dF redshift survey**. The 2dF[1] galaxy redshift survey (Colless 1995) being carried out at the Anglo-Australian Telescope will measure a quarter of a million galaxies brighter than $b_{\rm J} = 19.5$, with a deeper extension to $R = 21$ making best use of good conditions. The brighter galaxies cover an area of 1700 square degrees selected from both the southern galactic cap APM survey and the north galactic cap equatorial region. In terms of clustering, the chief aim of the survey is to accurately measure the power spectrum for wavelengths greater than $30h^{-1}\,{\rm Mpc}$ allowing the first direct comparison with microwave background anisotropy constraints on the same scales.

  The survey's depth, particularly in its faint component, will provide measurements of the evolution of the galaxy luminosity function, clustering amplitude, and star formation rates out to redshifts of $z \sim 0.5$. The high density of observed galaxies will enable statistically useful sub-samples to be compiled, so the variations in their clustering properties as a function of luminosity, morphology and star formation history can all be studied. A study of clusters and groups of galaxies in the redshift survey will also be conducted. In particular this will examine infall in clusters and dynamical estimates of cluster masses at large radii.

  More information on the project can be found at the site
  `http://msowww.anu.edu.au/~colless/2dF/`

- **SDSS**. The Sloan Digital Sky Survey (Gunn & Weinberg 1995) will measure photometry for 10^8 galaxies in five filters. This catalogue will act as the parent for the simultaneous redshift survey, which aims to measure redshifts for nearly a million

[1] Two degree field, 2° being the size of the instrument field of view

galaxies complete to 18.0 magnitudes in the Sloan r'-band, centred on 6280Å. The particular advantages of this project are its sheer size and its highly homogeneous construction. The survey will look at an area covering one quarter of the sky in an ellipse centred on a region of very low extinction near the North Galactic Pole. This size will result in a very narrow window function in k-space, enabling power on extremely long wavelengths to be measured accurately. The survey is producing its own CCD-based photometry, making it immune from one of the chief criticisms of the 2dF and Stromlo-APM surveys, derived from the APM catalogue. The APM data was taken from photographic Schmidt-plates nearly ten years ago, and despite herculean efforts to eliminate errors resulting from the different calibration of the plates and so forth, small residuals could have a strong systematic effect on clustering statistics on large scales (Maddox, Efstathiou, & Sutherland 1996).

- **VLT-VIRMOS Deep Survey**. The VIRMOS project consists of two multi-object spectrometers: VMOS working in the visual range of the spectrum (0.37-1 μm), and NIRMOS which will cover the near infrared (1-1.8 μm). These instruments will be used on two of the four ESO/VLT 8m telescopes at Cerro Paranal in the Atacama Desert, northern Chile.

  The visual band can be used to study the redshifts of objects with $z < 1$ and $z > 3$, whilst the near infrared is useful for intermediate redshifts where the optical range has very little spectral information. The two instruments are thus highly complementary, and the VIRMOS survey has been designed to use this complementarity to produce a high-redshift galaxy catalogue with good statistics. The goal is to obtain a sample of 10^5 galaxies with $I < 22$, reaching to redshift of one. A further sample will contain half as many galaxies, going five times as faint ($I < 24$), thus probing out to redshifts of around $z = 4$.

  The survey strategy will be to take:

  - five strips of $16° \times 3°$ to $I = 22$.
  - three strips of $16° \times 1°$ to $I = 24$.
  - a small area $1' \times 1'$ to $I = 26$.

  The high redshift limit will effectively probe out to look-back times of 15% the current age of the universe or better. Currently, the only surveys that have looked at the

Universe to this sort of depth have been pencil beams, which contain very little volume, and are thus of limited statistical usefulness. The VIRMOS project will produce detailed data for the study of structure evolution and the epoch of formation. The volume probed by going to these depths will, despite the relatively small angular coverage, result in a survey of similar size to 2dF or SDSS, and in this respect it can be regarded as the high-redshift counterpart of these "local" surveys.

More details on the VIRMOS project can be found at the web-page
`http://lasm0b.astrsp-mrs.fr/www_root/projets/virmos/VIRMOS.HTML`

- **6dF Galaxy Survey**. The 6dF instrument is a proposed upgrade of the FLAIR II facility on the UK Schmidt telescope at the AAO. The proposed survey will measure the redshifts of 120,000 galaxies, NIR-selected from the DENIS sky survey (Epchtein et al. 1994) with $J < 13.7$, and optically selected with $J > 13.7$ and $B < 16.5$. The survey will cover the whole of the southern galactic sky with $|b| > 10°$, resulting in 18,000 square degrees. Although the survey is shallower than most of its planned contemporaries (its median redshift, $z = 0.03$, is similar to that of the PSCz), its wide coverage means that it probes a large volume of the local Universe, such that measurements will not be affected significantly by evolution in clustering or in the galaxy population, making it an ideal calibrator for looking at evolution in the deeper surveys. The other key advantage of this project is its use of selection in the near-infrared. This waveband picks up the luminosity of the old stellar population, rendering it a more direct probe of the stellar mass than the optical and far-infrared regions, which tend to be biased towards high current star formation rates. The NIR is also much less sensitive to dust extinction, so the survey can be used to look at galaxy centres that would otherwise be obscured, and to go to significantly lower galactic latitudes. At the moment no good cartography exists for $|b| < 20°$, and there is a lot of solid angle in the band between that and the $|b| > 10°$ that 6dF will be able to achieve. Interest in this strip of sky is especially keen since it is thought the Great Attractor lies in this obscured region, and much information about the local density field can therefore be obtained by looking at peculiar velocities of galaxies located here. 6dF will, then, be a useful, homogeneous sample of the local Universe. Further details are available at the web-site
`http://msowww.anu.edu.au/~colless/6dF/`

- **DEEP**. The DEEP project (standing for Deep Extragalactic Evolutionary Probe) will conduct a survey of around 25,000 distant, faint, field galaxies, using the twin $10\mathrm{m}$ Keck Telescopes and the Hubble Space Telescope (HST). The consortium of US institutions aim to use the DEIMOS spectrograph in conjunction with high resolution images from the WFPC-2 camera of HST to study evolution by looking at dynamic measures such as rotation curves and velocity widths. This should enable the study of objects containing similar mass over the range of look-back times covered by the survey. The observing strategy is to select galaxies with photometry implying a redshift of between 0.7 and 1.2. Four regions of the sky will be studied, each of $120' \times 15'$. Each strip then will represent a volume of approximately $500 \times 60 \times 8h^{-3}\,\mathrm{Mpc}^3$. Thus, DEEP is a powerful tool for studying galaxy formation and evolution and the origin of large-scale structure. A summary of DEEP's goals and strategies can be found in Davis & Faber 1998. The DEEP homepage address is

  `http://www.ucolick.org/~deep/home.html`

Survey	Solid Angle sr	z_{med}	Volume $h^{-3}\,\mathrm{Mpc}^3$	Number	Completion Year
2dF	0.52	0.14	1.0×10^7	2.5×10^5	2001
SDSS	3.1	0.11	2.3×10^7	1.0×10^6	2005
VIRMOS	0.015	1.00	2.7×10^7	5.0×10^4	2001
6dF	5.4	0.03	1.2×10^6	1.2×10^5	2002
DEEP	0.0008	1.00	1.0×10^6	2.5×10^4	2002

Table 1.2. Comparison of future large galaxy redshift surveys either planned or currently acquiring data.

Table 1.2 summarizes these details, and compares the volumes probed by the different surveys. We define the volume as one third the solid angle times the cube of the median depth.

1.5 The need for this work

In the next ten years we will have unbiased, high density, large volume probes of the local universe, the intermediate Universe where evolution begins to have an effect, and

the high-redshift universe where we can examine the origin of galaxies and large-scale structure.

Whilst most of these surveys purport to have similar goals (ie. measuring clustering, looking at evolution), the means of doing so is generally rather different. Once the data arrives, it is economically expedient to make sure that it is used in the best possible way. It is likely that the best use of the data will in fact depend very much on the details of the survey. Certain statistics will be better than others, for instance, at picking up evolutionary effects in particular samples. Certainly, we have never dealt with data of this quality or abundance before, and this proliferation will drive us to use new statistics that it has not been feasible to apply to current datasets of less quality. Knowing the details of the survey strategy in advance, though, enables us to develop new statistics and new models before the data itself becomes available, and this is the main concern of this work.

In this thesis, then, we study a variety of different effects on the data from large surveys. In Chapter 2 we outline the current status of cosmological thought, the so-called "Standard Model", and present constraints on the parameters that describe this model. We will frequently use the power spectrum as a measure of galaxy clustering; Chapter 3 presents the fast Fourier transform method for estimating this statistic from the galaxy distribution. Chapter 4 outlines a set of N-body simulations that are used to produce mock galaxy catalogues for the surveys we are interested in. These mocks have the same angular constraints and selection functions as the real surveys, and hence are an extremely useful testing ground for statistical analyses. One factor that can bias results is dust extinction in the Milky Way, and we examine this effect on the power spectrum from the SDSS in Chapter 5. In Chapter 6 we introduce redshift-space distortions to the power spectrum as a way of extracting information about cosmological parameters. Chapter 7 contains a detailed statistical treatment of the errors on measurements of the power spectrum, and shows how those errors propagate through to define confidence intervals on derived parameters. In Chapter 8 we compare the errors derived from this technique with those found from a sample of ten independent mock catalogues. We conclude in Chapter 9, presenting a brief summary and looking ahead to the work that still needs to be done.

References

Arp H., 1999, A&A, 341, L5

Barrow J. D., Magueijo J., 1999, Physics Letters B, in press, astro-ph/9811072

Bean A. J., Ellis R. S., Shanks T., Efstathiou G., Peterson B. A., 1983, MNRAS, 205, 605

Carlberg R. G. et al., 1998, in Large Scale Structure in the Universe, Royal Society Discussion Meeting, March 1998

Colless M., 1995, The 2df galaxy redshift survey, http://msowww.anu.edu.au/~heron/Colless/colless.html

da Costa L. N. et al., 1994, ApJ, 424, 1

da Costa L. N. et al., 1988, ApJ, 327, 544

Davis M., Faber S. M., 1998, astro-ph/9810489, Preprint

Epchtein N. et al., 1994, Ap&SS, 217, 3

Fisher K. B., 1992, Ph.D. thesis, AA (California Univ.)

Geller M. J., Huchra J. P., 1989, Science, 246, 897

Giovanelli R., Haynes M. P., 1991, ARA&A, 29, 499

Gregory S. A., Thompson L. A., 1978, ApJ, 222, 784

Gunn J. E., Weinberg D. H., 1995, in proceedings of the 35th Herstmonceux workshop. Cambridge University Press, Cambridge, astro-ph/9412080

Hubble E., 1929, Proc N.A.S., 15, 168

Huchra J. E. et al., 1992, in Center for Astrophysic Redshift catalog, 1992 version.

Huchra J. E., Davis M., Latham D., Tonry J., 1983, ApJS, 52, 89

Humason M. L., 1931, ApJ, 74, 35

Humason M. L., Mayall N. U., Sandage A. R., 1956, AJ, 61, 97

Kantor F. W., 1977, Information Mechanics. Wiley, New York

Kantor F. W., 1999, International Journal of Theoretical Physics, accepted, astro-ph/9812444

Kirshner R. P., Oemler J., A., Schechter P. L., 1978, AJ, 83, 1549

Kirshner R. P., Oemler J., A., Schechter P. L., Shectman S. A., 1981, ApJ Lett, 248, L57

Kristian J., Minkowski R., 1972, in Sandage A., Sandage M., Kristian J., ed, Galaxies in the Universe. University of Chicago press

Loveday J., Efstathiou G., Peterson B. A., Maddox S. J., 1992, ApJ Lett, 400, L43

Maddox S. J., Efstathiou G., Sutherland W. J., 1996, MNRAS, 283, 1227

Pahre M. A., Djorgovski S. G., De Carvalho R. R., 1996, ApJ Lett, 456, L79

Pound R. V., Rebka G. A., 1959, Phys. Rev. Lett., 3, 439

Ratcliffe A., Shanks T., Broadbent A., Parker Q. A., Watson F. G., Oates A. P., Fong R., Collins C. A., 1996, MNRAS, 281, L47

Rowan-Robinson M. et al., 1990, MNRAS, 247, 1

Sandage A., Tammann G., 1987, in Carnegie Institution of Washington Publication, Washington: Carnegie Institution, 1987, 2nd ed.

Santiago B. X., Strauss M. A., Lahav O., Davis M., Dressler A., Huchra J. P., 1995, ApJ, 446, 457

Saunders W. et al., 1994, in Proceedings of the 35th Herstmonceux workshop. Cambridge University Press, Cambridge

Shectman S. A., Landy S. D., Oemler A., Tucker D. L., Lin H., Kirshner R. P., Schechter P. L., 1996, ApJ, 470, 172

Soifer B. T., Sanders D. B., Madore B. F., Neugebauer G., Danielson G. E., Elias J. H., Lonsdale C. J., Rice W. L., 1987, ApJ, 320, 238

Strauss M. A., Huchra J. P., Davis M., Yahil A., Fisher K. B., Tonry J., 1992, ApJ Supp, 83, 29

Tully R. B., Fisher J. R., 1987, in Cambridge: University Press, 1987

Yee H. K. C., Ellingson E., Carlberg R. G., 1996, ApJS, 102, 269

Zucca E. et al., 1996, Astrophysics Letters and Communications, 33, 99

Chapter 2

Current status of cosmology

THE ARGUMENT. In order to provide the background for the rest of the work in this thesis, we present a brief summary of the history of cosmological study to date. We review the generally accepted cosmic paradigm from both a theoretical and an observational viewpoint, summarizing the evidence that currently exists to support it. We introduce the various physical properties that parameterize this model, and describe the various constraints that recent observations have placed on these parameters.

2.1 Introduction

This thesis is chiefly concerned with what we can hope to learn about cosmological parameters from future galaxy redshift surveys. We will develop tools, and test them on artificial galaxy samples, which we obtain through the use of N-body simulation. There are a great many parameters that have an impact on the observations, even within the context of a single broad class of models, represented by the "standard" cosmology.

In order to make our objective tractable, we must restrict our analysis to certain models, and within those models to certain ranges of parameter space. The adoption of this standard cosmology, then, as an effective limit on the variety of the models, reflects generally a theoretical prejudice: many other cosmologies can and have been constructed that also fit the available data, but they are generally felt to be even more *ad hoc* than the standard model we put forward. The standard model represents the simplest explanation of the state of the Universe, with the fewest parameters, and is hence preferred. In contrast, the adoption of a range of parameter space within our standard model represents observational prejudice: we consider only values of the cosmological parameters that are within the measured bounds.

In this chapter we first set out a brief history of our changing cosmological world view before the development of modern cosmology in the early part of the twentieth century. Following this we present a qualitative description of the standard model as it stands now. In section 2.4 we summarize the available data as it is interpreted within the framework of this model. We conclude by presenting some examples of cosmologies that fit these observations, which we will use later in our analysis.

2.2 Brief history of cosmology

Cosmology's role is to present us with a coherent World View that is in keeping with the data available to us. Advances in cosmology have generally occurred when better data have been available, ie. through advances in the field of instrumentation.

In the Greek world, it was generally believed that the Universe was centred on the Earth (geocentric). Plato (427-347 BC) observed that celestial objects only moved in circles, and the philosophers of the time drew a hard distinction between the static, unchanging Heavens and the turbulent activity on Earth. The postulates from the time of Aristotle (384-322 BC) survived for nearly twenty centuries with little opposition. The Greeks knew the Earth was spherical in shape, since observers at different latitudes saw different constellations. Hence it was natural to see the Universe as a succession of spheres. Aristotle's cosmos used fifty-six such spheres for the planets and stars, but this simple view couldn't explain the observations of retrograde motion of the planets that the Greeks had made.

Aristarchus, in 290 BC, came up with the first heliocentric paradigm, with the Sun at the centre and the Earth spinning and revolving around the Sun. Despite what now seems to be the appealing simplicity of this view over Aristotle's multitudinous concentric spheres, in a prevalently geocentric climate it was felt to be even less elegant, and the idea remained undeveloped until the mediaeval renaissance.

Ptolemy (AD 100-c.178) used Aristotle's physics of circular motions in a geocentric framework, but offset the centres of his circles to explain retrograde motions. Planetary positions could only be predicted to 5° accuracy, but the model lasted unchanged for well over a millennium until the Age of Enlightenment, when intellectual freedom from religious dogma enabled enquiring minds to address such fundamental questions. A change in

perspective took place toward a heliocentric viewpoint with the work of Copernicus (1473-1543). His model had the Sun at the centre of the cosmos, with the Earth rotating on its axis and revolving around the Sun. The planets closer to the Sun move faster, and the distance to the stars is much greater than to the Sun.

Johannes Kepler (1571-1630), a student of the Danish astronomer Tycho Brahe, used Tycho's extremely precise data on Mars' retrograde motion to develop a physical realization of the Copernican model. He showed that Mars has an elliptical, rather than circular, orbit around the Sun, and went on to formulate his three laws of planetary motion, later incorporated by Newton into his theories of forces and gravity.

With a working view of our own solar system, it became interesting to study the nature of the stars, known since Ptolemy's time to lie at much greater distances than the planets. In the late eighteenth century, William Herschel developed the idea of using star counts to determine the shape of the stellar distribution. Assuming that stellar luminosities do not evolve with their distance away from us, but the only effect of distance is to dim their apparent magnitudes according to the inverse square law, counting the number of stars in each direction down to a certain magnitude limit produces a map of the spatial distribution of the stars. Well into the beginning of our century, the special place of the Earth in the Universe was still an accepted view point, backed up by Kapetyn's confirmation of Herschel's result that the Earth was at the centre of an "Island Universe". As will be discussed in Chapter 5, this was a result of dust obscuration dimming the starlight in excess of the inverse square law, preventing the number count technique from probing significant scales, and making deduced stellar distances much larger than their true values. Figure 2.1 shows a comparison of Kapetyn's Universe with the picture we currently have of the Milky Way, drawn to the same scale.

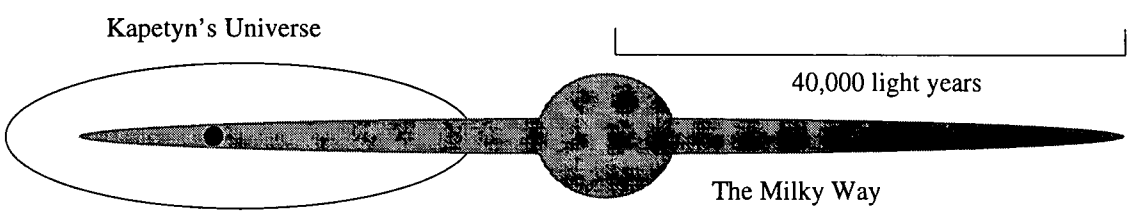

Figure 2.1: Kapetyn's view of the Galaxy, and our present understanding. Forty thousand light years is roughly 13kpc.

Some key factors in modern cosmology were foreseen by Immanuel Kant in his 1755 opus "A universal natural history and theory of the heavens". Kant suggested that the observed nebulae might be similar to our own Milky Way, but external to it. He was also the first to suggest that structures could grow via gravitational instability from tiny random perturbations in an initial density field. Despite Kant's prescience, modern cosmology would have to wait for more than a century until observational techniques enabled astronomers to break free of our own Galaxy. Pioneering work was done by Shapley in measuring the true shape of our Galaxy using Cepheid variable stars in globular clusters around the Milky Way as distance indicators. Shapley, however, was adamant that the spiral nebulae were small objects associated with our galaxy, and this stance provoked the Great Debate of the 1920's between Shapley and Curtis, who put forward Kant's hypothesis that they were distant copies of the Milky Way. The observation of high recession velocities resolved the debate in Curtis' favour. Modern observational cosmology thus began, with the final blow to the anthropocentric view that mans position in the Universe is somehow "special".

2.3 The standard cosmological model

The linchpin of modern cosmological thought is the the Copernican Principle, which states that our vantage point should not be at any preferred location in the Universe. Thus, all observers should measure a Universe that is the same in a statistical sense. The acceptance of this principle leads us to consider the concepts of *isotropy* and *homogeneity*. Isotropy is the invariance of the observed Universe when the observer undergoes a rotational transformation, and homogeneity is invariance under a translational transform. It is by no means obvious that the Universe should have such symmetries, and in no way does either symmetry, taken on its own, imply the other: an homogeneous universe could be anisotropic, if the anisotropy were in the same direction for all observers; and an isotropic universe could consist of concentric shells around the observer of varying density, hence being inhomogeneous.

An extension of the Copernican Principle is the Cosmological Principle, which states that the Universe must be homogeneous and isotropic. Isotropy can be measured using either number counts of distant galaxies or the cosmic microwave background. Homogeneity can be tested using the information from large redshift surveys to see

if the Universe looks the same to a distant observer as it does to us. If the CMB really is cosmological in origin, its high level of isotropy is a powerful argument for the Cosmological Principle. Direct evidence for homogeneity is, on the other hand, rather weak at the moment, although the forthcoming large redshift surveys should be able to probe the scales at which we expect to see the turnover to homogeneity in the galaxy distribution.

The observation that galaxies are moving away from each other provokes the highly pertinent question, what would we see if we reversed time's arrow and watched the Universe contract? Thanks to the finite speed of light, this is not an abstract question but is, up to a point where the density is such that the Universe is opaque to this light, eminently answerable. Going back further than this barrier, we are in the realms of speculation, but not *wild* speculation; if the laws of physics appear to apply all the way to the edge of the boundary, we are justified in extrapolating them back even further. This extrapolation must eventually break down; we have only tested our laws of physics in the laboratory up to certain finite extremes of temperature and density. Beyond these extremes we apply imagination, and a supposed feeling for "elegant solutions". But the onus isn't on the Universe to behave elegantly according to our concepts, as Aristotle would realize if he could see the state of the subject today. The onus is on us to push forward our understanding by experiment and observation.

2.3.1 Geometry of spacetime

In order to describe the topology of the expanding Universe, we employ the formalism of General Relativity. Unlike the Galilean or Special relativistic coordinate transforms employed in section 1.2, the transform of GR is curved, in the sense that it has a spatial dependence which is a function of the mass distribution. The transform is described by Einstein's field equations, and all cosmological models are solutions of these equations. Although the equations can be presented neatly using tensor calculus, in their general form the are difficult to solve, involving many dimensions. The adoption of the Cosmological Principle introduces several symmetries that make the equations far more tractable.

De Sitter solved Einstein's equations for the simplest case in 1917, but for this Universe to be static it can contain no matter – otherwise it will expand. It was this apparent paradox, before the expansion of the Universe was observed, that prompted Einstein

to introduce the cosmological constant into the equations, in order to counteract this expansion. The general case of the Einstein equations for an homogeneous Universe were solved by Friedmann in 1922. The Friedmann models assume that the space and time components are separable. The spatial geometry of the Universe is then fixed by the Robertson-Walker metric,

$$dr^2 = dt^2 - R^2(t)\left[\frac{dr^2}{1-kr^2} + r^2(d\theta^2 + \sin^2\theta d\phi^2)\right]. \tag{2.1}$$

The value of k is normalized to be 0, 1, or -1, reflecting a flat, positively curved (like a sphere), or negatively curved (like a saddle) geometry. Lemaitre independently solved the equations in 1927, and was the first to realize that an expanding Universe implied an initial creation point – big bang theory was born.

2.3.2 The big bang

Commencing in the realm of speculative physics at the beginning of the Universe, we are at an extreme of temperature and density completely beyond anything we could hope to re-create in the lab. Our picture of what goes on here is an extreme extrapolation of the laws of modern particle physics. Particle-antiparticle pairs can be created by the decay of the extremely energetic photons (and other bosons) that exist at this time. At early times, these gamma rays were energetic enough to produce hadrons, but as the Universe expanded it necessarily cooled, and the photons no longer had sufficient energy to decay in such a way. Without this replenishment, hadrons annihilated with their anti-matter partners, and the Universe was all but emptied of heavy particles.

Today, we see a local Universe in which the hadron component is made entirely of baryons, with very few anti-baryons. We are reasonably confident that none of the galaxies we see outside our locality could be made of anti-matter, as we do not observe the high-energy gamma-rays that would be expected to come from the interfaces of matter/anti-matter regions (Steigman 1976). This asymmetry, then, implies that either the baryon number (number of baryons minus number of anti-baryons) in the primordial Universe was non-zero, or some process has occurred which does not conserve baryon number. Despite the dominance of baryons today, the size of the asymmetry is tiny, since we witness only the baryons left after the majority have annihilated. When the temperature of the Universe was well above 1GeV, nucleons, anti-nucleons and photons

would have had approximately the same abundances. If we thus attribute one third the number of photons we see today to primordial abundance, and two-thirds to the reaction

$$b + \bar{b} \rightarrow \gamma + \gamma, \tag{2.2}$$

we see that the primordial excess of matter over antimatter is given by:

$$\frac{n_B}{n_{\bar{B}}} = \frac{n_B^0 + n_\gamma^0/3}{0 + n_\gamma^0/3} = 1 + 3n_B^0/n_\gamma^0, \tag{2.3}$$

where the superscript zero refers to current abundance. A measurement of the baryon-to-photon ratio comes from big bang nucleosynthesis theory, which will be discussed in section 2.4.6. Independent, but weaker, constraints come from comparing the baryonic component of galaxy clusters to the density of photons in the cosmic microwave background. The tiny value of η obtained from these techniques implies an original asymmetry of order one part in one billion.

The next phase of creation is the lepton era. Below the GeV level needed to produce hadrons, the photons can still produce electron-positron pairs. In this bath of leptons, the neutron and proton populations are kept in equilibrium since β-decay is balanced by the inverse process, positron capture by neutrons. This balance continues until the photon temperature drops below the MeV level needed for pair production, and neutrons can only decay. The neutron takes centre stage for its fifteen minutes of fame, for its mean life is just a quarter of an hour. Neutrons and protons can combine to produce the deuteron; these deuterons can then combine with another neutron to produce the third isotope of hydrogen, tritium. The final capture of another proton promotes our particles to Helium nuclei. Lithium and Boron can also be produced at this time. This process is called nucleosynthesis for obvious reasons. In a matter of hours there are no more unbound neutrons left in the Universe, and the abundances of the elements are frozen until such time as fusion processes in stars can alter them.

Matter and radiation were in equilibrium while photon energy was large, but now there is very little mass left, and the radiation dominates the energy content of this primordial fireball. The radiation pressure continues to drive the expansion, but since photons are relativistic particles, their energy goes as the fourth power of the scale factor. As the Universe cools, the matter component becomes non-relativistic and its energy density will decrease as the cube of the scale factor. So, no matter what the amplitudes of

these functions, there must come an era when the energy density is matter-dominated. Radiation and matter are still in good thermal contact, though, due to Compton scattering of photons off all the free electrons, so the two populations have a common temperature. This picture is changed at recombination: the temperature drops below 13.6eV, the ionization temperature for Hydrogen, and the electrons can theoretically settle down into the shells of the hydrogen nuclei to produce atoms. This does not occur, in fact, until rather lower temperatures have been reached, since the radiation has an energy spectrum with a Planck distribution and photons in the high energy tail can still dissociate the atoms. The ratio of photons to baryons is so high ($\eta \sim 10^9$) that this continues to be significant at much lower energies. Bound electrons are much less efficient scatterers of light than free ones due to the restrictions on the wavelength of light they can absorb imposed on them by quantum mechanics. Thus the Universe rapidly changes from being opaque to light to being practically transparent. The photons are decoupled from the mass and the two components now follow separate thermal histories.

2.3.3 Structure

There is one obvious problem with the standard model of a homogeneous spacetime: it fails to provide a mechanism for the creation of the wealth of structure that we see around us in the Universe today, and indeed for our own existence.

Observations of the microwave background have revealed the presence of small fluctuations in this photon field. This is the only observable sign of structure other than that seen by surveys of the present-day Universe. To develop a theory of structure formation requires speculation to interpolate between these two epochs, and to extrapolate back before the surface of last scattering to explain the primordial nature of these fluctuations.

Starting in the beginning, we turn to the quantum world for an explanation. As the early Universe expanded, tiny but unavoidable perturbations in it caused by quantum fluctuations would also expand. These fluctuations would be Gaussian distributed with amplitude given by the Harrison-Zel'dovich power spectrum, $P(k) \propto k^n$ where n is unity (Zel'dovich 1972). This model is preferred because it is scale-invariant. As the Universe expands, the volume of space in causal contact with the observer increases. This volume is known as the observer's horizon, and for a scale-invariant power spectrum all the

modes have the same amplitude at the time they come inside this horizon, and there is no physical scale introduced other than that of the horizon itself.

Outside the horizon, in the radiation dominated era, the modes all grow with the square of the expansion factor, $d(t) \propto a(t)^2$. The power spectrum goes as the linear growth factor squared, $P(k,t) \propto d(t)^2$. Once the perturbations come within the horizon, they are decoupled from the expansion of the Universe and cease to grow. This behaviour stops at matter domination, when the growth factor behaves linearly with the expansion factor for modes both inside and outside the horizon, effectively maintaining the shape of the fluctuation spectrum. Thus we expect to see today the Harrison-Zel'dovich spectrum, $P(k) \propto k$, on the largest scales, with $P(k) \propto k^{-3}$ on small scales. The position of the turn-over between the two asymptotes provides useful information on the horizon size at recombination.

The fluctuations of the CMB are thus the signature of perturbations in the mass field, stamped on to the photon field at the time of decoupling.

After recombination, gravitational collapse means that areas with positive fluctuation attract more matter and become denser, whereas areas of negative fluctuation are gradually emptied of matter. The mathematics of linear evolution of the density modes is set out in Appendix A. Linear evolution is strictly only valid in the regime where the fields in question have amplitude much less than unity. Beyond this linear level the Press-Schecter formalism (Press & Schechter 1974) is often used to trace the evolution of the objects that will become galaxy haloes. This treatment assumes that, although the density field may be non-linear, the amount of matter going in the central, virialized halo is the same as that initially contained in its Lagrangian radius, and this flow is independent of the distribution of the mass within this radius. Alternatively, this regime is modelled using the method of computational *N*-body simulations.

2.3.4 Inflation

The inflationary paradigm is invoked to answer several key questions raised by the standard model, including:

- **Isotropy**. The size of the horizon at recombination was, when projected onto the sky, $\sim 1°$. How come the CMB is isotropic over much larger scales than the causality scale when it was formed?

- **Anisotropy**. Below the horizon scale, what caused the tiny anisotropies observed in the CMB that later seeded the formation of structure?

- **Flatness**. The Universe today is very close to flat. What *a priori* reason is there for the curvature to be less than or comparable to the energy density of matter?

Inflation models the vacuum energy of the Universe as the potential of a scalar field, ϕ. It is assumed that there is a spontaneous symmetry breaking transition in this field at a certain energy scale, T_c. At temperatures greater than this, ϕ is a symmetrical field with a minimum at the origin, $\phi = 0$. As the Universe cools, it eventually reaches temperatures comparable to T_c and the symmetry is broken; a secondary minimum in the potential comes about, say at $\phi = \sigma$. As the Universe continues to cool, this minimum becomes the global minimum potential for the field. The passage of the field from $\phi = 0$ to $\phi = \sigma$ is what drives inflation. This behaviour is illustrated in figure 2.2.

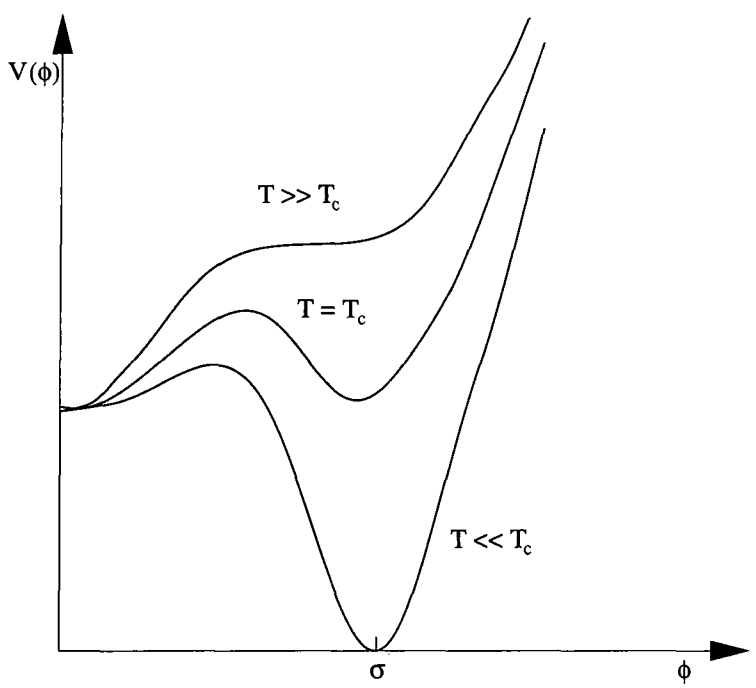

Figure 2.2: The behviour of the scalar field, $V(\phi)$, at three different temperature regimes, as discussed in section 2.3.4.

Firstly, quantum or thermal fluctuations allow ϕ to tunnel through the potential barrier separating it from the next "valley". Providing the potential is sufficiently shallow, the Lagrangian for ϕ is then dominated by a friction-like term, and this "slow-roll" inflation drives an exponential increase in the expansion factor of the Universe. After the slow-rolling era, ϕ proceeds to oscillate about its minimum, losing energy through particle production as it converges on $\phi = \sigma$. This energy re-heats the Universe to the temperature it was at before the exponential expansion took place. This model, then, resolves the shortcomings of the standard model mentioned above. The homogeneity problem is solved because, before inflation, the currently observable Universe was contained in a causally linked patch. Anisotropies are the result of inflation-amplified quantum fluctuations in the field, ϕ. The Universe after after inflation is necessarily very close to flat since the energy density has effectively remained the same, but the Universe has expanded enormously, wiping out the curvature component. For a more detailed introduction to inflation, see Kolb & Turner (1990), §8.

2.4 Observational evidence

What observational evidence is there for the Standard Model? What are its failings? And to what extent do we know the values of the parameters in the model? The parameters have left their signatures on the Universe in a number of different ways. None of them can be measured directly, and all require detailed physical models to relate them to observable quantities.

2.4.1 Expansion

As outlined in Chapter 1, Hubble's Law for relating galaxy redshifts to their distances from us is a key tool with which to examine cosmological models. There are several "standard candle" techniques for measuring the value of the Hubble constant, H_0, but large uncertainties in the calibration for most of these methods. This uncertainty leads to a wide variety in the measured value, though most groups find $40 < H_0 < 100 \mathrm{km\,s^{-1}\,Mpc^{-1}}$, with many recent determinations seeming to converge on a value of $\approx 65 \mathrm{km\,s^{-1}\,Mpc^{-1}}$. Apart from the normalization of the relation, the existence of a linear dependence of distance on redshift for close objects has been proved beyond doubt, and this result is a cornerstone

of the standard model. Many techniques are prone to systematic bias since they rely on calibrating distant standard candles at medium redshifts using other standard candle techniques that have been calibrated locally. Thus we have a picture of a cosmological "distance ladder", where higher redshift techniques stand on the shoulders of more local measurements.

Non-linear deviations from the relation, parameterized by a second order expansion of the relation such that

$$z = H_0 d_L + \frac{1}{2}(q_0 - 1)(H_0 d_L)^2, \tag{2.4}$$

are probes of spatial curvature. Current constraints on q_0 are very weak, since the signal at high redshift, where we would expect to see the departure from linearity, is contaminated by the possible evolution of the objects we are looking at with look-back time. The most sensitive current probe of this quantity is the flux from high-redshift supernovae, outlined in section 2.4.7. Certain techniques, eg. the Sunyaev-Zel'dovich effect which will be discussed in section 2.4.5, are capable of directly measuring the expansion rate over large distances, but at present the errors are large.

2.4.2 Age

Measurements of the age of the Universe can be directly tied into constraints on the cosmology and the value of H_0. The age is given by:

$$H_0 t_0 = \int_1^\infty \frac{dy}{y^2[1 + \Omega_0(y-1) - \Lambda_0(1 - 1/y^2)]^{1/2}} \tag{2.5}$$

where $y = 1 + z$. It can be seen that for the simple Einstein-de Sitter model with no curvature or cosmological constant, this equation results in simple expression $H_0 t_0 = 2/3$.

Measurements of the age of the Universe itself cannot be made independently of the cosmological framework, but this is not true for measurements of the objects within the Universe. It is generally considered reasonable to assume that the Universe must be older than the age of any objects in it. An immediate constraint on the age of the Universe can, then, be made on purely terrestrial grounds: by examining radioactivity in rocks, which decays with a known lifetime. For a variety of different isotope ratios, the results are

consistent with an age of the Earth of around $4\mathrm{Gyr}$. This result is confirmed by estimates of the age of the Solar System from isotope ratios in meteorites. The standard value for the age is now around $4.6 \pm 0.1\mathrm{Gyr}$ (Wasserburg et al. 1977). Using the observed abundances of heavy elements, an age limit of between 7 and $13\mathrm{Gyr}$ is found for material in our galactic disk, depending on how these elements formed. Stellar evolution models predict $16 \pm 2\mathrm{Gyr}$ for the oldest globular clusters in the galactic halo, (Renzini et al. 1996), although some more recent determinations point to rather lower results of a maximum age of $14\mathrm{Gyr}$ (Salaris, Degl'Innocenti, & Weiss 1997; Jimenez & Padoan 1998). To relate these ages to bounds on Hubble's constant or the cosmological model, we note that the units of Hubble's constant are $\mathrm{km\,s^{-1}\,Mpc^{-1}}$. It so happens that this unit is almost exactly one inverse terayear, so the relationship between time and Hubble's constant is simple if t_0 is expressed in units of $10^{12}\mathrm{yr}$. For an Einstein-de Sitter model, then, $t_0 = 16 \pm 2\mathrm{Gyr}$ implies a Hubble constant of $2/(3 \times 0.016) = 42 \pm 5\mathrm{km\,s^{-1}\,Mpc^{-1}}$. This result would seem in disagreement with the observed value mentioned in the section 2.4.1, so the simple Einstein-de Sitter model is excluded by this data.

2.4.3 Microwave background

The Cosmic microwave background (CMB) is, paradoxically, one of the most powerful arguments for isotropy and homogeneity in the Universe and simultaneously one of the most informative tools for examining the precise details of the anisotropies that we believe have led to the formation of the structure we see around us.

- **Homogeneity**. The CMB was discovered accidentally by Penzias and Wilson in 1965, as they were measuring microwave emission from our own galaxy and observed an isotropic source of detector noise in their radio antenna. This noise appeared to be at a temperature of around $4\mathrm{K}$, and did not change with direction, within the limited angular resolution of the experiment. The theoretical framework of a microwave background had been laid down a decade earlier by Gamow, who showed it to be a natural prediction of an expanding, cooling Universe. Once its significance was realized (by Dicke), a number of experiments set out to measure the temperature accurately and look for deviations from isotropy. A primary anisotropy was observed a decade later (Smoot, Gorenstein, & Muller 1977), a dipole term that is interpreted as representing

our motion with respect to a cosmic reference frame. Beyond this dipole, though, the CMB is smooth to a level of one part in a thousand.

No non-cosmological model is capable of producing the degree of isotropy observed in the CMB, and its observation is one of the cornerstones of the standard cosmology. Simultaneously, it is one of the models biggest deficiencies. In an expanding universe with a finite speed of light, objects can only be in causal contact if they are in within each other's particle horizon, the furthest distance a photon from one of the galaxies could have travelled if it set out at the moment of creation. If the CMB really is radiation left over from recombination, the particle horizon then was small compared to the distance between pockets of space that are observed in different directions by us now; only areas of separation $\sim 1^\circ$ could have been in contact at or before the formation of the CMB. If areas are not in causal contact, it is difficult to see why they should have the same properties, so the high level of isotropy is one of the chief failings of the standard model. This problem can be overcome, as mentioned earlier, by expanding the standard model to include inflation (section 2.3.4).

- **Anisotropies**. Anisotropy beyond the dipole term was first observed by the *COBE* satellite in the early 1990's (Smoot et al. 1992). This result has become a key tool in the understanding of cosmology and structure formation, since it is believed that the fluctuations observed in the radiation reflect the seeds that would grow into observable structure in the matter distribution.

  There are three primary sources of anisotropy:

  - *Gravity.* The gravitational field caused by an overdensity redshifts a photon climbing out of it.
  - *Doppler.* Matter with a peculiar velocity will Doppler shift the photons it scatters according to its direction.
  - *Temperature.* Denser matter is hotter, so photons from overdense areas are more energetic.

  On the largest scales, the kinetic energy effect is related linearly to the gravitational field. This results in a scale-independent fluctuation spectrum, known as the Sachs-Wolfe effect. The other effect that can be considered a primary one is the finite thickness of the last scattering surface (LSS). Anisotropies on scales smaller than this

thickness are washed out by the radial smoothing that is applied implicitly when data are averaged from a range of look-back times. These two very simple considerations (Sachs-Wolfe at large scales and finite thickness on small scales) are responsible for the asymptotic behaviour of the angular power spectrum, as demonstrated by the model spectrum (solid line) in the upper panel of figure 2.3.

On intermediate scales, the photon-baryon fluid undergoes damped oscillations. As perturbations enter the horizon, they all start with the same initial conditions, ie. the same phase. In the adiabatic case this corresponds to $\dot{\hat{\delta}} = 0$, $\hat{\delta} = -2\hat{\phi}$: like a pendulum at the top of its swing, it has all potential, and no kinetic, energy. The CMB we observe is a "cosmic snapshot" of these perturbations at a fixed time, at which shorter wavelength modes have been inside the horizon longer than large-scale perturbations, and hence have a more advanced phase. This leads to the nearly periodic behaviour in k seen in figure 2.3.

The amplitude of the oscillations depends on how tightly the photon field is coupled to the underlying mass distribution. The photons only interact with the baryonic component, so the peaks are higher in a model with a higher baryon fraction. The amplitude of CMB anisotropies is thus a useful probe of Ω_B.

The location of the peaks, in contrast, measures the geometry of the Universe. The power spectrum of the fluctuations has a fixed physical scale, but when observed in projection, the translation to l-space depends on geometry:

$$l = \eta k, \text{ where } \eta = \frac{2c}{H_0}\Omega_0^{-\alpha} \begin{cases} \alpha = 0.4 & \text{for a flat model} \\ \alpha = 1.0 & \text{for an open cosmology} \end{cases} \tag{2.6}$$

Measuring k in units of $h\,\mathrm{Mpc}^{-1}$, this becomes $\eta = 6000\Omega_0^{-\alpha}$ [1].

After recombination, the photon field is only coupled to the mass field via gravitational effects. In the time-independent case, if a photon travels into a potential well, the blue shift it gets is exactly cancelled out by the redshift it picks up as it climbs out again. However, if the potential evolves as the photon is travelling through it, this is not the case, and the photon may obtain a net blue or redshift. This effect is known as the integrated Sachs-Wolfe (ISW) effect, and there are three different ways in which the potential become time-dependent:

[1] $6000h^{-1}\,\mathrm{Mpc}$ is the comoving distance corresponding to the redshift of the epoch of recombination.

- *Early ISW.* At $z = z_{REC}$, the photon density is small but non-negligible, and as matter starts to dominate the energy density, its importance fades away, resulting in an evolving potential.

- *Late ISW.* Depending on the cosmology, at late times the Universe may become vacuum or curvature dominated. In this case, the potential will again become time-dependent.

- *Rees-Sciama.* At moderate redshifts, non-linear structures start to form, structures which evolve at a significant rate compared to the time taken for photons to cross them. Thus the potential a photon undergoes on climbing out of the potential well need not be the same as it experienced on the way in.

These effects also leave their mark on the CMB we observe today. Although they tell us little about the primordial density fluctuations themselves, they can act as useful cosmological probes in there own right. In general they result in only mild perturbations to the primary anisotropies; the late ISW affects only the largest scales, the early ISW affects only the first Doppler peak, and the Rees-Sciama effect has a negligible effect on the power spectrum for cold dark matter models of structure formation (Tegmark 1996).

Another gravitational effect that is thought to be of importance in the CMB signal is that of weak lensing of photons by structures close to the line of sight between emission and the observer. This effect leads to a smearing of the power spectrum since photons appearing to come from a certain patch of sky can, in reality, have originated from a wider area. A similar smoothing can be caused by a global reionization of the Universe. In this case, photons can Thomson scatter off a more recent surface than that at recombination, and information about their original points of origin is lost.

COBE gives us constraints on large-scale anisotropy, where the angular power spectrum has no features. The four-year *COBE* data is plotted in figure 2.4. It is readily apparent that the chief contribution to the anisotropy is the dipole caused by the Earth's motion relative to the CMB frame. Once this dipole is removed from the signal, the primordial anisotropies are clearly visible. The middle panel of this figure is still contaminated by emission from the Milky Way, seen as the strip across the middle of the projection. The corrected data can be used, given a particular cosmology, to predict the shape of the power spectrum. Further experiments have measured fluctuations on

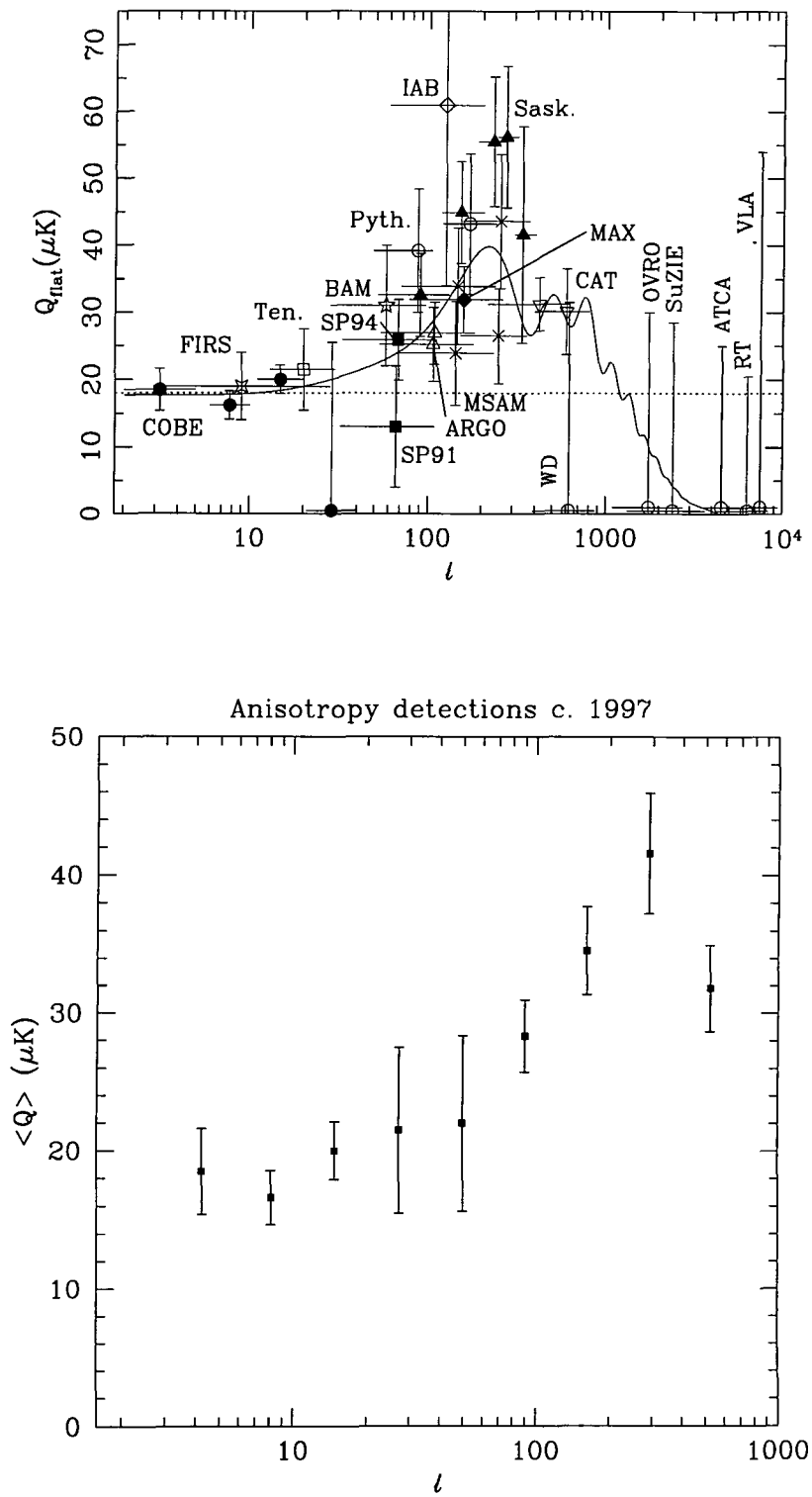

Figure 2.3: Plots of the multipole power spectrum, C_l, using results from various CMB experiments. The lower plot reflects the bounds obtained by averaging the individual experiments presented in the upper plot. Source: `http://www.astro.ubc.ca/people/scott/q_values_97.html`

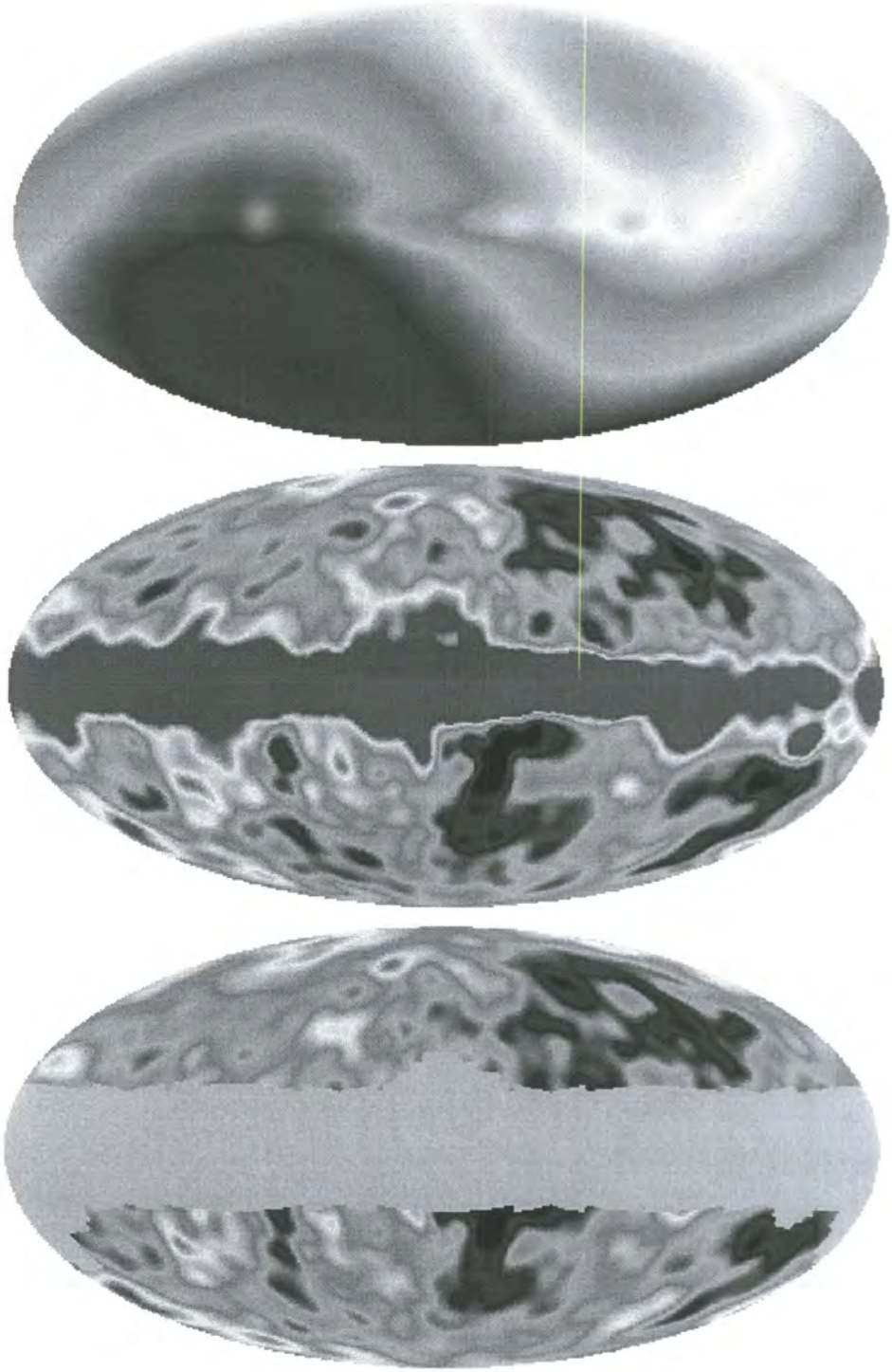

Figure 2.4: The microwave background from *COBE*. The upper panel shows the from the four year, uncorrected data in the 53GHz channel. The middle panel dhows the result of subtracting off the dipole. The lower panel shows the result of subtracting a model of the Galactic emission and masking out areas of high contamination. Source: `http://www.gsfc.nasa.gov/astro/cobe/dmr_image.html`

much smaller scales, either from ground-based or airborne experiments. At present, the consensus of opinion is that the existence of the first Doppler peak is fairly well established, but current measurements are not good enough to fix the peak or its amplitude. In figure 2.3 we show the current state of CMB observations as presented by Scott (1997). The averaged plot shows the Doppler peak quite clearly, putting it somewhere in the range $l = 200$-500.

Planned CMB experiments such as MAP [2] and Planck (Lawrence & Lange 1997) will be able to measure the CMB with far greater accuracy than any existing equipment, resulting in a wealth of data with which to constrain the cosmological parameters. Detailed studies of CMB polarization as well as temperature maps aim to break some of the inevitable degeneracy in fitting complex models to a single curve.

2.4.4 Galaxy surveys

The progress of three-dimensional redshift surveys has been described in Chapter 1. Redshift surveys have generally been confined to examining rather small volumes of space and this restriction has limited their use in looking at the linear part of the power spectrum, which is where much of the cosmological information is contained. Angular surveys can probe much larger volumes of space with good sampling rates, given the relative ease of measuring the position of an object on the sky rather than measuring its spectrum accurately enough to obtain a redshift. There is, of course, no information in an angular survey about the redshifts of the galaxies, but this problem can be circumvented given a redshift distribution in a statistical sense. Baugh & Efstathiou (1993 and 1994) show how the angular correlation function or power spectrum of galaxies in the APM Galaxy survey (Maddox et al. 1990) can be inverted, given a model for the distribution of galaxies with redshift, to produce the full three-dimensional power spectrum. This model is seen to be fairly robust to changes in the assumed galaxy distribution, and provides the most accurate currently available view of clustering on the largest scales, although there are uncertainties in tracing the power spectrum over the 'bump'; the APM survey is based on $6^\circ \times 6^\circ$ plates, and possible mismatches in the calibration of adjacent plates means the angular correlation function is prey to systematics on these scales, which is the region of interest as regards spotting a turnover in the power spectrum. Dust is also

[2] `http://map.gsfc.nasa.gov/`

a contaminant affecting the correlation function (Schlegel, Finkbeiner, & Davis 1998), an issue we will explore in greater depth in chapter 5. The quoted random errors, as well, are open to criticism, since they come from the simple technique of splitting the survey into four patches and measuring the variance between these parts of the sky. They are thus likely to be a serious underestimate of the true error, particularly on the largest scales, for which the amplitudes in adjacent patches will be highly correlated. Results from the APM survey point to a value of $\sigma_8^{\rm gal}$ (the variation in galaxy number counts in spheres of radius $8h^{-1}\,{\rm Mpc}$) of between 0.84 and 0.96. The conversion of angular data to constraints on the three-dimensional power spectrum is sensitive to assumptions about the evolution of clustering and cosmology, and hence this range of values represents the systematic uncertainty (Baugh, private communication). The power spectrum is assumed to evolve as

$$P(k,z) = P(k)/(1+z)^{3+\epsilon-\gamma}, \tag{2.7}$$

where $\gamma \approx 1.7$ is the slope of the correlation function, and ϵ parameterizes the clustering evolution. For $\epsilon = 0$, small scale clustering is fixed in physical coordinates, and the amplitude of the APM power spectrum is $\sigma_8 = 0.96 \pm 0.04$ (Maddox, Efstathiou, & Sutherland 1996). Redshift surveys have been employed to corroborate these values: the Stromlo-APM survey (Loveday et al. 1996) finds $\sigma_8 = 0.89 \pm 0.05$. If the shape of the power spectrum is parameterised by a CDM-like transfer function (Efstathiou, Bond, & White 1992), the value of Γ derived from the APM data is found to be $\approx$ 0.2-0.3. (Baugh & Efstathiou 1994; Maddox, Efstathiou, & Sutherland 1996). The relatively large error here reflects the uncertainty of the location of the turn-over and the large error-bars on points at small k. The CDM spectral shape is in fact not a good match to the APM data, if the errors can be trusted. In fact, the APM errors are calculated by looking at the variance in estimates from four adjacent quadrants. Especially on large scales, these measures will be correlated, and the APM errors are likely to be an underestimate of the true uncertainty. The poor quality of the fit is responsible in part for the variety of values for the estimated Γ.

Redshift surveys can also be used to constrain the β-parameter ($\approx \Omega_0^{0.6}/b$, where b is the bias parameter, the ratio of galaxy overdensity to the underlying mass overdensity). The galaxy power spectrum is distorted in redshift-space by the peculiar velocities of the galaxies, which depend on the density. β can be measured internally, by comparing the

quadrupole-to-monopole ratio of the distorted clustering, or by looking at the boost in the monopole power relative to the power spectrum of the parent angular catalogue. This latter technique has been used in the Stromlo-APM redshift survey (Loveday et al. 1996). Values for β range between 0.5 and 1 depending on the way the galaxies are selected. Some sample dependence is expected since different types of galaxies are expected to have different clustering properties, and different values of the bias and hence β. Current measurements are reviewed in Hamilton 1997. Dekel (1998) shows how a stochastic, non-linear model for bias can account for some of the scatter in estimates of β made using different techniques.

2.4.5 Clusters

Clusters of galaxies are the largest virialized systems in the Universe, and as such are a fertile hunting ground for information about structure on scales approaching the linear regime where cosmological parameters play an important role. Constraints from cluster measurements are not sensitive to the details of galaxy formation, making them a powerful and robust tool. There have been two chief methods using clusters to probe cosmology:

- **Abundance.** The Press-Schechter formalism (Press & Schechter 1974; Bond et al. 1991) can be used to predict the abundance of objects of a given mass if structure is caused by initial fluctuations with Gaussian random phases. Several authors (White, Efstathiou, & Frenk 1993; Eke, Cole, & Frenk 1996) have employed this method to constrain cosmology. The mass function thus derived is converted to a temperature function under the assumption that the gas is isothermal. Eke, Cole, & Frenk (1996) use the simulations we outline in Chapter 4 to assess the accuracy of the Press-Schecter results, and in general good agreement is found. This agreement is particularly good at the high-mass end, but the P-S treatment is known to disagree with simulations in the low-mass regime. In order to constrain cosmology, a comparison is made to the local abundance of clusters as a function of their X-ray temperature. That work uses a sample of twenty-five low redshift clusters compiled by Henry & Arnaud (1991). The best current results have

$$\sigma_8 = (0.52 \pm 0.04)\Omega_0^{\alpha} \begin{cases} \alpha = -0.46 + 0.10\Omega_0 & \text{for open cosmologies} \\ \alpha = -0.52 + 0.13\Omega_0 & \text{for flat models.} \end{cases} \tag{2.8}$$

These results are found to be quite insensitive to the shape of the power spectrum, so provide a direct and independent constraint on σ_8 for a given cosmology.

- **Evolution**. Having normalized the local cluster abundance, looking for evolution with redshift can be a powerful tool. The basic theorem used here is that, in models with low Ω_0, the Universe has not changed much in recent times: the rapid expansion of the Universe, caused by having a low energy density, acts to prohibit any further growth of structure, and evolution is suppressed relative to a model with $\Omega_0 = 1$. Adding a cosmological constant term causes structure to be frozen out at lower redshifts, producing slightly stronger evolution in a flat cosmology as opposed to an open one.

  In particular, the X-ray temperature of gas in a cluster is, by the virial theorem, a function of the mass of the cluster. This enables constraints to be placed on the value of Ω_0. It has been shown by Kay & Bower (1998) that X-ray luminosity evolution alone cannot constrain Ω_0, but that measurements are degenerate with the slope of the power spectrum on cluster scales. An independent measure of this local slope is thus needed to produce a good constraint. They conclude $\Omega_0 < 0.75$ using such a measurement. Eke et al. (1998) derive a constraint of $\Omega_0 = 0.45 \pm 0.25$ by examining the behaviour of the X-ray temperature function with redshift.

  A further technique involving cluster evolution is to look for the Sunyaev-Zel'dovich effect (Sunyaev & Zel'dovich 1972). CMB photons are scattered upwards in energy by collisions within a cluster with the hot electron plasma. The net effect is to produce a bump in the CMB spectrum along the line of sight to the cluster; photons are taken out of the distribution at one energy, and scattered out of the line of sight or into the line of sight but at a higher energy, causing a decrement at long wavelengths. The extent of this effect depends on the temperature of the electron gas, making it a useful probe of evolution.

  All current work on cluster evolution has a high level of uncertainty due to the lack of a large sample of well-measured clusters at high redshift, but will be a powerful tool when better data become available.

2.4.6 Big-bang nucleosynthesis (BBNS)

As already discussed, BBNS occurs during the epoch after the Universe has cooled sufficiently that it cannot pair-produce electrons and positrons. The light elements, deuterium, helium and lithium are produced. Today, deuterium abundance is measured along lines of sight through the interstellar medium. Deuterium has a very low binding energy, making it hard to produce in any astrophysical environment. Thus the ratio today should be a lower limit on the BBNS ratio. Most deuterium depletion occurs in stars, which generally convert the isotope to ^{3}He. We can estimate the difference between the pre-solar and processed ^{3}He abundance by comparing its concentration in dust on the Moon's surface with the nearly primordial amount found in the primitive meteorites known as carbonaceous chondrites. Assuming the difference to come from solar processing of deuterium allows us to measure the deuterium depletion and hence the total primordial abundance.

Helium is produced in stars, but not nearly enough to explain the $\sim 1{:}10$ ratio of ^{4}He to hydrogen. The ^{4}He abundance is a crucial test for the big bang model of cosmogony itself, but is in fact insensitive to cosmology. Observed in HII regions via its recombination line, the ratio appears to be universal. The abundance of deuterium, however, does depend on cosmology. Deuterium can be destroyed by proton collisions, and in a less dense universe, there is less chance of such collisions, so deuterium is preserved.

Walker et al. (1991) present a thorough examination of BBNS using recent data for the nuclear reaction cross sections, the half-life of the neutron, and the various astrophysical observations. They find that $\Omega_B h^2 = 0.0125 \pm 0.0025$, which is the value adopted in this work.

More recently, BBNS has become a controversial field with the development of techniques for accurately measuring the concentration of primordial elements in the absorption of light from QSOs by high-redshift clouds. These clouds have a very low metallicity, implying that there has been little stellar processing, and that the deuterium abundance is close to its primordial level. Rugers & Hogan (1996) show that the observed deuterium feature in the quasar Q0014+813 is a real feature, and the measured D/H abundance implies a rather lower value for the baryon fraction, $\Omega_B h^2 = 0.006 \pm 0.001$. In contrast, Tytler, Fan, & Burles (1996) use a similar technique with another quasar to show $\Omega_B h^2 = 0.024 \pm 0.006$, a shift in the opposite direction. The reason for this strong

systematic difference is not clear. Tytler et al. suggest that the result of Rugers & Hogan could be due to a hydrogen line appearing by chance at the expected deuterium position, causing the high estimate of deuterium abundance. Another uncertainty in this method includes the subtraction of the intrinsic quasar continuum spectrum, which is of course not known and has to be modelled.

2.4.7 Supernovae

Supernovae can be used as sensitive cosmological probes if they are treated as standard candles. These very luminous events are observable at high redshift, and measurement of their brightness constrains the relationship between luminosity distance and redshift. Thus we can directly measure the geometry of space-time. Two large collaborations are currently performing searches for the SNe. Observations are difficult since the objects must be observed as their light curve is on the way up, then monitored carefully to make detailed measurements of its shape.

The High-Z Supernova Search (Schmidt et al. 1998) use a sample of local supernovae ($z < 0.2$) and one at high redshift ($z = 0.479$) to show

$$\Omega_0 = \begin{cases} 0.2 \pm 1.0 & \text{for no cosmological constant} \\ 0.4 \pm 0.5 & \text{for a flat cosmology} \end{cases} \tag{2.9}$$

They estimate that with a sample of 30 high-z supernovae they should be able to get confidence limits of ± 0.2 on Ω_0 and Λ_0.

The Supernova Cosmology Project have recently shown (Perlmutter 1999), using forty-two type 1a supernovae with $0.18 < z < 0.83$,

$$\Omega_0 = 0.75\Lambda_0 - 0.25 \pm 0.12 \tag{2.10}$$

Assuming a flat model, this constraint becomes $\Omega_0 = 0.28 \pm 0.1$.

Many subtleties exist in this work, for instance the systematic errors from K-corrections, extinction, and selection effects. At some level, it is expected that the supernova population should evolve with look-back time, either through changing environment or simply because more massive stars will exhaust their fuel at earlier times. As more data come in, the random errors should be beaten down quite successfully, making supernovae promising tools for measuring geometry.

2.5 Summary

The key parameters of the standard cosmology, then, are:

- The mass density, Ω_0.
- The cosmological constant, Λ_0.
- The Hubble constant, H_0.

These three parameters also define the age of the Universe, t_0.

- the baryon fraction, Ω_B.
- The power spectrum of mass fluctuations, itself parameterized in a CDM framework by
  - The primordial slope, n.
  - The amplitude, σ_8.

  The shape, Γ, is generally determined by $\Gamma = \Omega_0 h$, with a weak dependence on Ω_B
- The bias factor, b, generally defined as the ratio of fluctuations of galaxies to mass in spheres of radius $8h^{-1}\,\mathrm{Mpc}$.

There is a strong theoretical prejudice for either a flat model ($\Omega_0 + \Lambda_0 = 1$), or an open model ($\Lambda_0 = 0$). This prejudice rests on the assumption that the cosmological constant is a rather arbitrary term in Einstein's equation, and it is only worth putting up with if it has the trade-off of providing an elegant, flat Universe.

In table 2.1 we summarize some of the main observational constraints that currently apply to these parameters, as detailed in the previous sections.

For the work in this thesis, we will generally be concerned with the power spectrum of the galaxy distribution, the function that measures the strength of clustering as a function of scale. Theoretical models of this statistic can be derived, and are dependent on the above parameters. We use the CMBFAST code of Seljak & Zaldarriaga (1996) to calculate this quantity under the assumption of adiabatic initial conditions for perturbations entering the horizon. In figure 2.5 we present some examples of power spectra for "reasonable" cosmologies, ie. ones that fit the data acceptably well. In each case the power spectra

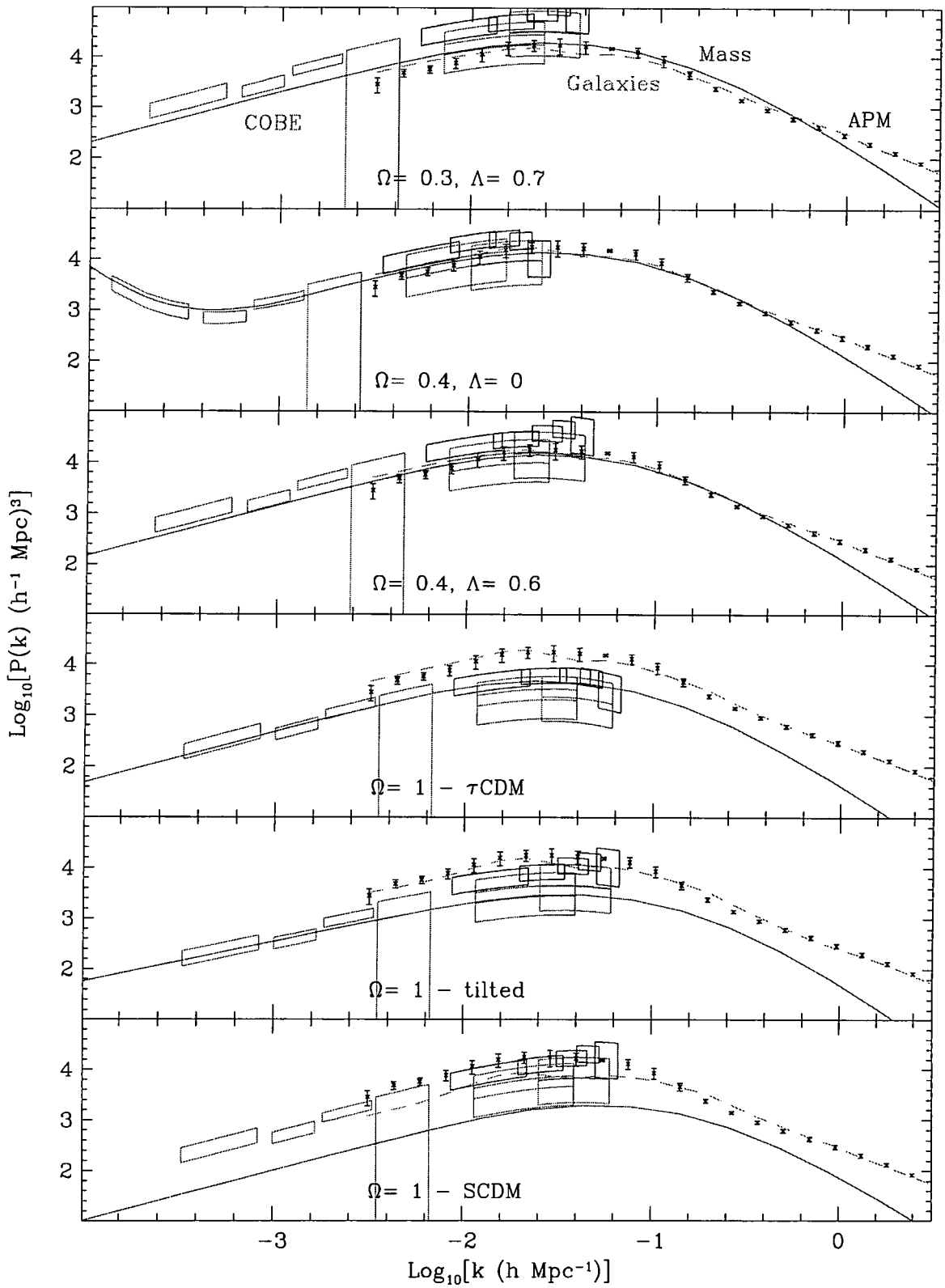

Figure 2.5: Mass power spectra (solid lines) for six different cosmologies, each with parameters chosen so as to be consistent with the summary of table 2.1. The dashed lines represent the corresponding galaxy power spectra, normalized such that they agree with the APM data (points with errorbars). The boxes represent constraints from CMB experiments, as described in the text.

Constraint	Source	Reference
$\Omega_B h^2 = 0.0125 \pm 0.0025$	BBNS	Walker et al. 1991
$H_0 = 69 \pm 8 \mathrm{km\,s^{-1}\,Mpc^{-1}}$	Cepheid variables	Tanvir et al. 1995
$t_0 = 16 \pm 2 \mathrm{Gyr}$	Globular clusters	Renzini et al. 1996
$n = 1.1 \pm 0.1$	CMB experiments	Hancock et al. 1997
$\Gamma = 0.21 \pm 0.03$	APM	Baugh & Efstathiou 1994
$\sigma_8^{\mathrm{mass}} \approx 0.5\Omega_0^{-0.55}$	X-ray clusters	Eke, Cole, & Frenk 1996
$\sigma_8^{\mathrm{gal}} = 0.96 \pm 0.04$	APM	Maddox, Efstathiou, & Sutherland 1996
$\beta = 0.6 \pm 0.1$	Stromlo-APM	Loveday et al. 1996

Table 2.1. Summary of current observational constraints on cosmological parameters.

have been obtained assuming σ_8 approximately from equation 2.8. For comparison, we also plot the galaxy power spectra from the *N*-body simulations that will be described in Chapter 4. These amplitudes are chosen to approximately replicate the clustering of galaxies in the APM catalogue (Baugh & Efstathiou 1994), shown by the points with errorbars. We also plot the constraints on the large-scale amplitude provided by *COBE* (the four error boxes on the left hand side of the plot), and the constraints at medium scales from two other CMB experiments, Saskatoon (Netterfield et al. 1997) and MSAM (Cheng et al. 1997).

It is clear from this figure that low-Ω_0 cosmologies can provide a good fit to all the data with very little galaxy biasing. The presence of a cosmological constant makes little difference to this fit. In $\Omega_0 = 1$ models, the story is very different; a high degree of biasing is required to match galaxy observations, and in the SCDM case it is clear that the *COBE* data outlaws a mass power spectrum consistent with cluster abundance at a high confidence level.

The $\Omega_0 = 1$ cosmology thus needs some extra work to rescue it, perhaps by assuming the existence of a massive neutrino species that decays, altering the shape of the power spectrum (the τCDM model), or by tilting the primordial power spectrum significantly ($n \approx 0.8$) to get an acceptable fit.

References

Baugh C. M., Efstathiou G., 1993, MNRAS, 265, 145

Baugh C. M., Efstathiou G., 1994, MNRAS, 267, 323

Bond J. R., Kaiser N., Cole S., Efstathiou G., 1991, ApJ, 379, 440

Cheng E. S. et al., 1997, ApJ Lett, 488, L59

Dekel A., 1998, in Wide Field Surveys in Cosmology, 14th IAP meeting held May 1998, Paris. Editions Frontieres., p. 47

Efstathiou G., Bond J. R., White S. D. M., 1992, MNRAS, 258, 1

Eke V. R., Cole S., Frenk C. S., 1996, MNRAS, 282, 263

Eke V. R., Cole S., Frenk C. S., Henry J. P., 1998, MNRAS, 298, 1145

Hamilton A. J. S., 1997, astro-ph/9708102

Hancock S., Gutierrez C. M., Davies R. D., Lasenby A. N., Rocha G., Rebolo R., Watson R. A., Tegmark M., 1997, MNRAS, 289, 505

Henry J. P., Arnaud K. A., 1991, ApJ, 372, 410

Jimenez R., Padoan P., 1998, ApJ, 498, 704

Kay S. T., Bower R. G., 1998, MNRAS, in press, astro-ph/9807240

Kolb E. W., Turner M. S., 1990, The early universe. Addison-Wesley

Lawrence C. R., Lange A. E., 1997, American Astronomical Society Meeting, 191, 4120

Loveday J., Efstathiou G., Maddox S. J., Peterson B. A., 1996, ApJ, 468, 1

Maddox S. J., Efstathiou G., Sutherland W. J., 1996, MNRAS, 283, 1227

Maddox S. J., Efstathiou G., Sutherland W. J., Loveday J., 1990, MNRAS, 242, 43P

Netterfield C. B., Devlin M. J., Jarolik N., Page L., Wollack E. J., 1997, ApJ, 474, 47

Perlmutter S. et al., 1999, ApJ, in press, astro-ph/9812133

Press W. H., Schechter P., 1974, ApJ, 187, 425

Renzini A. et al., 1996, ApJ Lett, 465, L23

Rugers M., Hogan C. J., 1996, ApJ Lett, 459, L1

Salaris M., Degl'Innocenti S., Weiss A., 1997, ApJ, 484, 986

Schlegel D. J., Finkbeiner D. P., Davis M., 1998, in Wide Field Surveys in Cosmology, eds. S. Colombi and Y. Mellier

Schmidt B. P. et al., 1998, ApJ, 507, 46

Scott D., 1997, `http://www.astro.ubc.ca/people/scott/q_values_97.html`

Seljak U., Zaldarriaga M., 1996, ApJ, 469, 437

Smoot G. F. et al., 1992, ApJ Lett, 396, L1

Smoot G. F., Gorenstein M. V., Muller R. A., 1977, Physical Review Letters, 39, 898

Steigman G., 1976, ARA&A, 14, 339

Sunyaev R. A., Zel'dovich Y. B., 1972, Comm. Astrophys. Space Phys., 4, 173

Tanvir N., Shanks T., Ferguson H., Robinson D., 1995, Nature, 377, 27

Tegmark M., 1996, in Dark matter in the universe: Proc. Enrico Fermi, Course CXXXII, astro-ph/9511148

Tytler D., Fan X.-M., Burles S., 1996, Nature, 381, 207

Walker T. P., Steigman G., Kang H.-S., Schramm D. M., Olive K. A., 1991, ApJ, 376, 51

Wasserburg G. J., Papanastassiou D. A., Tera F., Huneke J. C., 1977, Royal Society of London Philosophical Transactions Series, 285, 7

White S. D. M., Efstathiou G., Frenk C. S., 1993, MNRAS, 262, 1023

Zel'dovich Y. B., 1972, MNRAS, 160, 1P

Chapter 3

Power spectrum estimation with fast Fourier transforms

THE ARGUMENT. We show how the Power Spectrum of the spatial distribution of galaxies is defined, and why it is a useful quantity to measure. We present the fast Fourier Transform (FFT) technique for estimating the power and explore some subtleties of this method. We also review the treatment of Feldman, Kaiser, & Peacock (1994) to produce a minimum variance weighting scheme to measure the power spectrum as accurately as possible from a magnitude limited redshift survey.

3.1 Introduction

Having discovered the existence of galaxy clustering in three-dimensional redshift surveys, we must now define statistics with which to qualitatively measure the extent of this clustering. Our goal will then be to seek ways of theoretically deriving these statistics from cosmological and galaxy formation models. We will thus have a link between the theoretical background and observable quantities.

One statistic used to quantify the strength of clustering on different scales is the correlation function, $\xi(r)$ (Peebles 1980). This quantity measures the excess probability of finding a galaxy pair with a certain separation, r, over that expected for a purely random distribution. This two-point function cannot contain all the information about the galaxy distribution. In fact one can conceive pathological galaxy distributions that have similar

two-point clustering behaviour but are extremely different when higher order correlations are measured or when the distributions are examined visually. However, if the galaxies sample a Gaussian random field of density fluctuations, we know that the distribution is characterized solely by its two-point function. The Gaussianity of the initial density field is a direct prediction of inflationary models where cosmological perturbations are seeded by quantum fluctuations. The evolution of perturbations via gravitational instability causes this assumption to break down on small scales where the density field has become non-linear; strong evolution introduces a co-dependence between these non-linear modes. On larger scales, investigations have as yet shown no strong evidence of non-Gaussian behaviour. These have primarily concentrated on two techniques, the topology of the galaxy distribution via the genus statistic (Canavezes et al. 1998), and from looking directly at the fluctuations present in the CMB from the *COBE* maps (Kogut et al. 1996; Ferreira, Magueijo, & Gorski 1998). Given that the assumption of Gaussianity is broken only weakly (if at all) for initial, large-scale perturbations, the two-point statistics make a suitable starting place for the analysis of clustering.

The power spectrum, $P(k)$, is the Fourier transform of the two-point correlation function. Fourier space is less intuitive to work in, and harder to visualize than real-space, and yet in many ways the power spectrum is a more natural and fundamental quantity, and thus a more powerful tool for investigation than its real-space counterpart.

The shape of the power spectrum is characterized by several key scales relating to physical processes in the history of the Universe. As such, this shape is then a fundamental prediction of many theories of the early Universe and the formation of large-scale structure. Under the Gaussian assumption, modes with different wavelengths are initially completely uncorrelated, and in the linear regime they evolve independently and at the same rate. Thus this characteristic shape preserves the information about initial conditions, making it easy to relate theory to observation. The correlation function, on the other hand, contains contributions from a range of scales, for instance mixing linear and non-linear regimes. The statistical independence of modes makes error analysis in the Fourier domain a much simpler activity.

The shape of the power spectrum is also insensitive to errors in the mean galaxy density. This density in general has to be measured from the very sample of galaxies we are analyzing, and the error introduced can result in a bias in the correlation function, which

is particularly serious for small $\xi(r)$, ie. the realm of interest for cosmological physics. This "d.c." component of the density field appears only in the zero wavenumber bin of $P(k)$, and thus an error in this number will only propagate in the limit that modes close to this fundamental one are correlated with it. This is a very minor effect for cosmological simulations, where the largest modes are generally very linear and hence uncorrelated, but in a real galaxy survey with finite width window function it could be significant.

We summarize our definition of the Power spectrum and our Fourier transform convention in section 3.2. Section 3.3 presents the fast Fourier transform method for measuring the power, and explores some of the subtleties involved in making an estimate of $P(k)$ from such a technique. In section 3.4 we summarize the results of Feldman, Kaiser, & Peacock (1994) who have derived a minimum variance method of estimating the power.

3.2 Definitions

Throughout this work, we use the following convention for a Fourier transform pair: that, if f is a function of separation, r, then its Fourier transform, g, as a function of wavenumber, k, is given by

$$\begin{aligned} g(k) &= FT[f(r)] \\ &= \int f(r) e^{ikr} \mathrm{d}r. \end{aligned} \tag{3.1}$$

The inverse FT is defined

$$\begin{aligned} f(r) &= IFT[g(k)] \\ &= \frac{1}{2\pi} \int g(k) e^{-ikr} \mathrm{d}k. \end{aligned} \tag{3.2}$$

The extension to three dimensions is trivial;

$$\begin{aligned} G(\mathbf{k}) &= \int F(\mathbf{r}) e^{i\mathbf{k}.\mathbf{r}} \mathrm{d}^3\mathbf{r}, \\ F(\mathbf{r}) &= \frac{1}{(2\pi)^3} \int G(\mathbf{k}) e^{-i\mathbf{k}.\mathbf{r}} \mathrm{d}^3\mathbf{k}. \end{aligned} \tag{3.3}$$

The probability, dP, of finding a galaxy in a volume element dV, is given by $dP = ndV$, where n is the mean number density. The correlation function is then defined through the

joint probability of finding a galaxy in both elements dV_1 and dV_2 separated by a distance r,

$$dP = n^2[1 + \xi(r)]dV_1 dV_2. \tag{3.4}$$

For a continuous density field, $\rho(\mathbf{x})$, with mean $\bar{\rho}$, we define the overdensity, $\delta(\mathbf{x})$ as

$$\delta(\mathbf{x}) = \frac{\rho(\mathbf{x}) - \bar{\rho}}{\bar{\rho}} \tag{3.5}$$

the correlation function of this field is then given by

$$\begin{aligned} \xi(\mathbf{r}) &= \int \delta(\mathbf{x})\delta(\mathbf{x}+\mathbf{r})\mathrm{d}^3\mathbf{x} \\ &= \langle \delta(\mathbf{x})\delta(\mathbf{x}+\mathbf{r}) \rangle, \end{aligned} \tag{3.6}$$

where $\langle\rangle$ implies an ensemble average. This second expression is valid under the ergodic principle which states that an average over a sufficiently large volume is equivalent to an ensemble average over all possible universes.

The power spectrum is then the Fourier transform of $\xi(\mathbf{r})$,

$$P(\mathbf{k}) = \int \xi(\mathbf{r}) e^{i\mathbf{k}.\mathbf{r}} \mathrm{d}^3\mathbf{r} \tag{3.7}$$

Under the convolution theorem, the Fourier transform of the convolution of two functions is identically equal to the product of the Fourier transforms of those two functions. Now, the above expression for ξ is the convolution of the overdensity with itself. Thus its Fourier transform will be the square of the Fourier transform of the overdensity field. Mathematically:

$$\begin{aligned} P(\mathbf{k}) &= FT[\delta(\mathbf{r}) \otimes \delta(\mathbf{r})] \\ &= |\delta(\mathbf{k})|^2 \end{aligned} \tag{3.8}$$

3.3 The fast Fourier transform

The direct, continuous Fourier transform of a galaxy distribution on a set of scales can be found by calculating the complex exponential with period equal to the galaxy position for each galaxy at each wavenumber. This operation thus scales with the number of objects in the sample multiplied by the number the number of individual k-modes at which we

want to estimate the power. This is fine for the redshift surveys of ten years ago, but for a modern survey with $\sim 10^6$ galaxies, a faster technique must be used. In this case we apply the method of a discrete Fourier transform to the data. The assumption is that galaxies are tracers of an underlying galaxy density field, a profile of which can be constructed from placing the weights of these galaxies on a regularly sampled grid. At the loss of some small-scale sensitivity (obviously we cannot measure the power for wavelengths less than the size of one cell), the computation is thus made far more efficient. In fact, even more CPU time can be saved by using fast Fourier transforms (FFT's, see Press et al. 1992 Chapters 12 & 13). This technique efficiently performs the Fourier transform of a field discretely sampled on a regular grid by recursively splitting the transform into transforms of smaller length. It thus makes the number of operations increase as $O(N \log_2 N)$, rather than the $O(N^2)$ taken by a straightforward transform.

There are then several concerns :

3.3.1 Grid Size

The length of the cube used to perform the FFT analysis defines the longest wavelength mode we can examine. This requirement thus sets the resolution in k-space,

$$\Delta k = \frac{2\pi}{L_{\rm BOX}}. \tag{3.9}$$

3.3.2 Grid resolution

The grid resolution sets the small-scale limit to the power spectrum. The smallest wavelength that can be properly sampled is one where adjacent bins are at alternate minima and maxima of the wave, ie. $\frac{N}{2}\lambda = L_{\rm BOX}$, where N is the grid dimension. In k-space this maximum frequency is known as the Nyquist frequency, $k_{\rm Nyq} = \frac{N\pi}{L_{\rm BOX}}$.

3.3.3 Aliasing

Aliasing occurs whenever a distribution to be Fourier transformed has power at higher frequencies than the Nyquist frequency of the grid used for the analysis (Press et al. 1992, section 12.1). A component beyond the edge of the box in Fourier space will be reflected back ("aliased") into this frequency range. This is generally not a problem on cosmological

scales since the slope of the power spectrum is sufficiently steep ($-1 < n < -2$) that the aliased power can have little effect on any but the highest wavenumbers (Peacock & Dodds 1996).

3.3.4 Assignment schemes

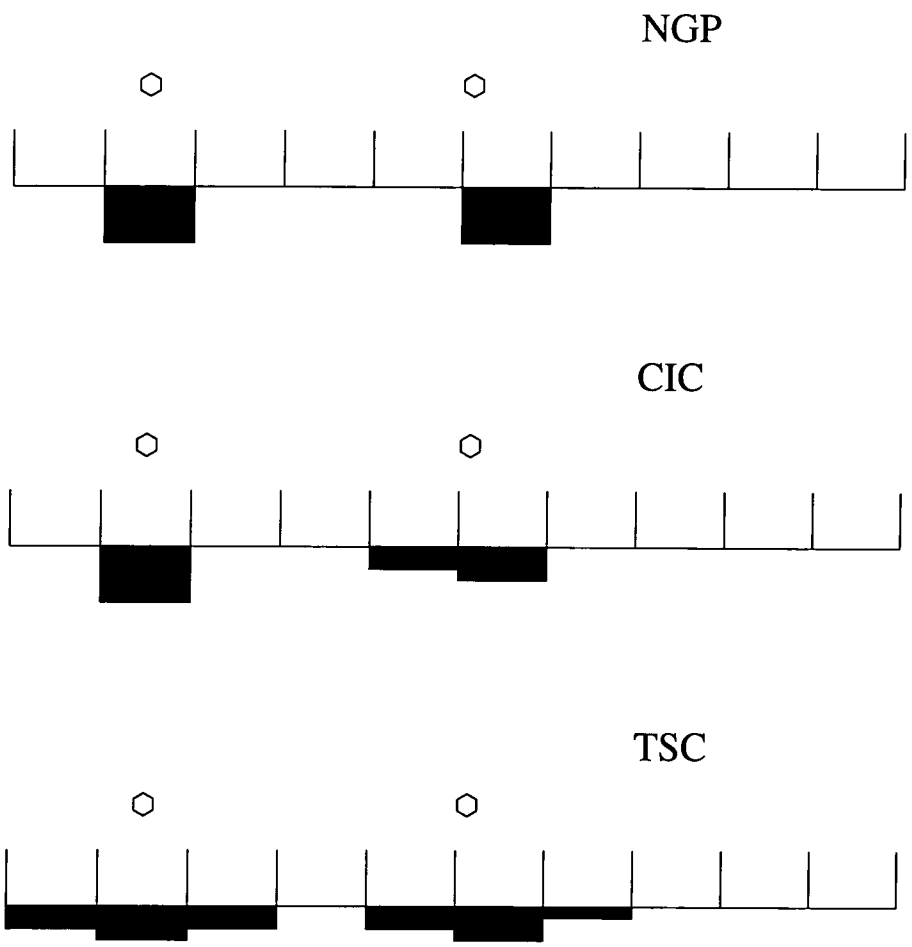

Figure 3.1: Schematic of the way the three different schemes (NGP, CIC, TSC) assign weights to grid points. In each case the particle on the left is in the centre of its cell, while the one on the right is close to the cell boundary.

Given a grid size and resolution, we construct a gridded density field, $\delta(\mathbf{r})$ from our galaxy distribution. We use three different algorithms to convert particle positions into local densities.

- **NGP.** Nearest Grid Point. In this, the simplest scheme, the weight of the galaxy is assigned entirely to the cell whose centre the galaxy is nearest.

- **CIC.** Cloud-in-Cell. The galaxy is given a "size" equal to one cell. Each neighbouring cell is then weighted in proportion to the amount that it overlaps with this galaxy 'cloud'.
- **TSC.** Triangular Shaped Cloud. Instead of a constant density profile over one cell-width, the galaxy has a triangular profile with a base stretching two cell-widths, and adjacent cells are given mass according to the amount of this profile they contain.

Figure 3.1 is a schematic representation of the way the different assignments share the weight of a galaxy between bins.

Figure 3.2 shows a comparison of power spectra derived from a simulation using each of the three schemes. As expected, the NGP scheme contains rather more small scale power, since the distribution is lumpier. For comparison we also show the same plot for the power spectrum definition advocated by Peacock & Dodds (1994,1996). This quantity, $\Delta^2(k)$, is the contribution to the fractional density variance per bin of $\ln k$. In our notation, $\Delta^2(k) = 4\pi/(2\pi)^3 k^3 P(k)$. Graphically, this statistic is useful for drawing attention to differences in the non-linear power spectrum, but since most of this work will concentrate on the linear and quasi-linear regimes, we will generally use the simple power spectrum, $P(k)$.

In figure 3.3 we compare the accuracy of the different schemes at recovering the true power spectrum of the galaxy distribution. As mentioned in the previous section, the maximum frequency we can recover is given by the Nyquist frequency of the box. In practice, the assignment scheme acts as a convolution to the density field, and it is impossible to fully recover the power spectrum on small scales when we deconvolve. We would like to know out to what scale we can trust our estimator. We do this by examining the ratio of the power derived from a grid of N^3 cells (where $N = 32, 48, 64, 96, 128$) with the power on a finer grid with twice the resolution. We then plot this ratio as a function of $k/k_{\rm Nyq}$, where $k_{\rm Nyq}$ is the Nyquist frequency of the lower resolution grid. To compare the different schemes, we define a limiting scale at which the treatment is considered reliable, $k_{\rm lim}$, such that the discrepancy between the two estimates is at the 2% level, ie. $P_{2N}(k_{\rm lim})/P_N(k_{\rm lim}) = 0.98$. This criterion seems quite conservative. Applying it, and averaging over the five different N values, we find that the NGP scheme is reliable up to around one half the Nyquist frequency, CIC up to three quarters, and TSC up to around 85%. There is also a systematic trend of the recovery to get worse as we go to finer resolution, for all the assignment schemes. We will generally use the CIC scheme for the

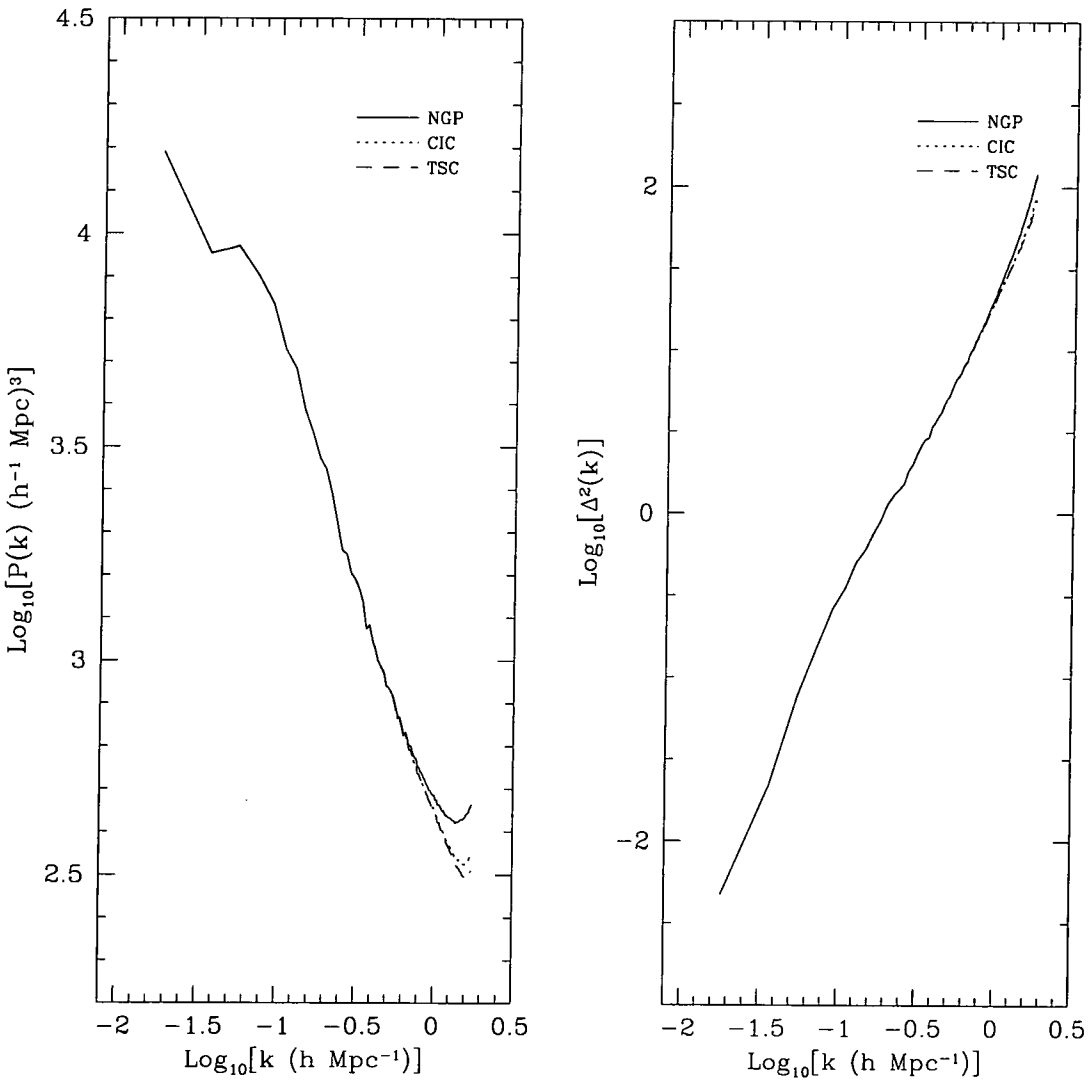

Figure 3.2: Power spectra from one simulation using the three different assignment schemes (NGP, CIC, TSC) for the density field, as outlined in section 3.3.4. The simulation used is $\Omega = 1$, normalized to reproduce the local abundance of galaxy clusters. We plot the power spectrum definition used throughout this work in the panel on the left, whilst the panel on the right shows the same data with the Peacock & Dodds (1994) definition, $\Delta^2(k) = 4\pi/(2\pi)^3 k^3 P(k)$.

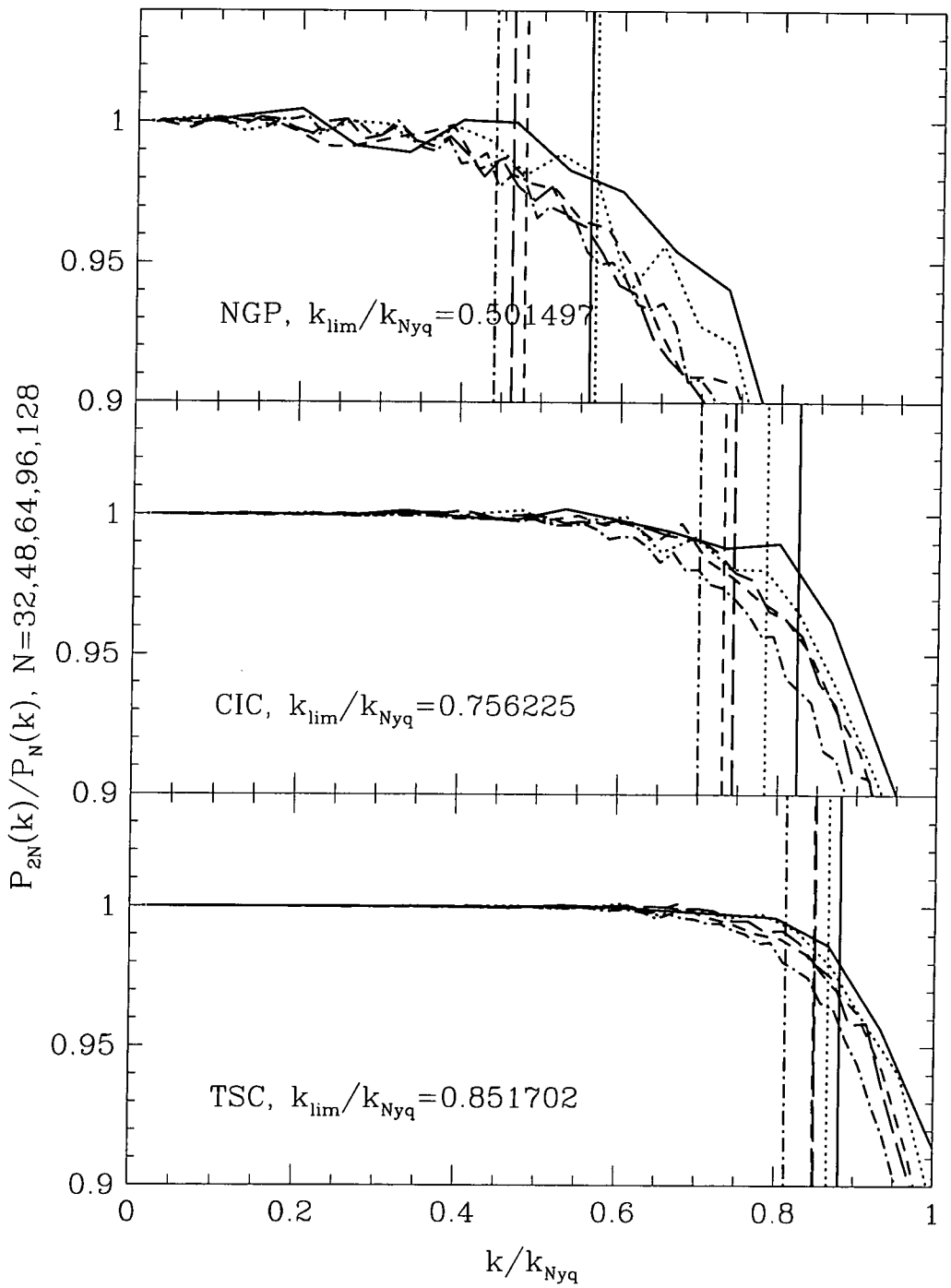

Figure 3.3: Comparison of the power spectra from one simulation using the three different assignment schemes (NGP, CIC, TSC) for the density field, as outlined in 3.3.4. In each case, we show the ratio of the power spectrum measured using a grid of dimension N divided by the power obtained using a grid of twice the resolution. The x-axis is the ratio of k to the Nyquist frequency of the coarser grid. Vertical lines intersect the curve at the point where the ratio goes below 0.98, and we use the average to obtain the value of k_{lim} quoted. Solid lines are $N = 32$, dotted are $N = 48$, short-dashed $N = 64$, long-dashed $N = 96$, dot-dashed $N = 128$.

rest of this work, and adopt the extremely conservative view that we can go out to one half the Nyquist frequency.

3.3.5 Shot noise subtraction

The galaxy density field may have a power spectrum given by $P(k)$, but in our analysis we are looking at galaxies that sample this field in a stochastic sense. A Poisson distribution has its own, scale independent power spectrum, $P(k) = P_{\rm shot}$. This "shot-noise" power will be added to the power spectrum of the underlying field in our measurements, biasing our estimate high. Thus we need to subtract the shot-noise power from our estimator. In the specific case of a Volume limited redshift survey with constant number density, the shot-noise power is given by $1/\bar{n}$.

3.3.6 Sampling convolution

When the particle distribution is assigned to the grid by one of the schemes described above, we must be careful to take into account the effect that the assignment has on the measurement of the power spectrum. Each of the schemes represents a smoothing of the galaxy density field, and has a convolving effect on the power spectrum. The field is generally smoothed on the same scale as the cell size of the FFT grid. The convolution is with the window function for a single grid-cell, ie. a cubical top-hat function of width $d = L_{\rm BOX}/N$. Thus, in a one dimensional case, we have:

$$\begin{aligned} FT[\delta_r \otimes W(r)] &= FT[\delta_r] \times FT[W(r)] \\ &= \delta_k \times \mathrm{sinc}\left(\frac{kd}{2}\right) \end{aligned} \tag{3.10}$$

where

$$\mathrm{sinc}\, x = \frac{\sin x}{x}. \tag{3.11}$$

To correct for this convolution in three dimensions, we must divide $\delta(k_x, k_y, k_z)$ by the Fourier transform of the cubical top hat,

$$\delta(k_x, k_y, k_z) \Longrightarrow \frac{\delta(k_x, k_y, k_z)}{\mathrm{sinc}(\frac{k_x d}{2})\mathrm{sinc}(\frac{k_y d}{2})\mathrm{sinc}(\frac{k_z d}{2})} = \frac{\delta(\mathbf{k})}{S(\mathbf{k})} \tag{3.12}$$

The effect of the CIC assignment is to convolve the galaxy density field with an additional cubical top hat of width d to obtain a smoothed field. In Fourier space this is

equivalent to multiplying the k-space overdensity by another sinc function, so we must again divide by this sinc function in order to deconvolve.

In the TSC case, we note that the triangle function is just the convolution of a top hat with itself, so we have to divide the k-space overdensity by the square of the sinc function. For the rest of this work we will employ the CIC scheme since it is more accurate than simple NGP. The TSC scheme would be just as good a choice.

3.3.7 Resolving the shot noise

In figure 3.4 we show the recovered power spectrum for a Poisson distribution of particles. This distribution has no power, so subtracting the shot-noise term should result in $P(k) = 0$. The three panels show the NGP, CIC, and TSC schemes, from top to bottom. In each case, the solid line shows no convolution correction, the dotted line shows correction by one power of the sinc function, $S(\mathbf{k})$, the short-dashed line two powers and the long-dashed three. From what we have just stated, we would expect to recover the true, constant shot-noise power spectrum by dividing by one, two and three powers of the sinc function for NGP, CIC, and TSC respectively. We see this is accurate for CIC and TSC, but not for NGP. In this case it seems that making no correction provides the most accurate estimate.

Under the NGP scheme, the binned density field has no knowledge of the original particle positions on a scale less than the size of one grid cell. The CIC and TSC schemes, on the other hand, do retain this information: for the case of particles separated by more than a few cell lengths, the galaxy positions can be perfectly reconstructed from the field on the grid.

In the NGP case, the shot-noise itself is convolved with the window function of a single cell, and thus we should subtract a corrected shot-noise in order to get $P(k) = 0$.

We demonstrate this in figure 3.5, where we analyze the case in which the field is smoothed on a scale of twice the cell length. We present NGP and CIC results for doing this. In the bottom panel we see, as expected, that the CIC scheme again works when we correct with the sinc function squared. In the top panel, however, we see that none of the four choices of correction work.

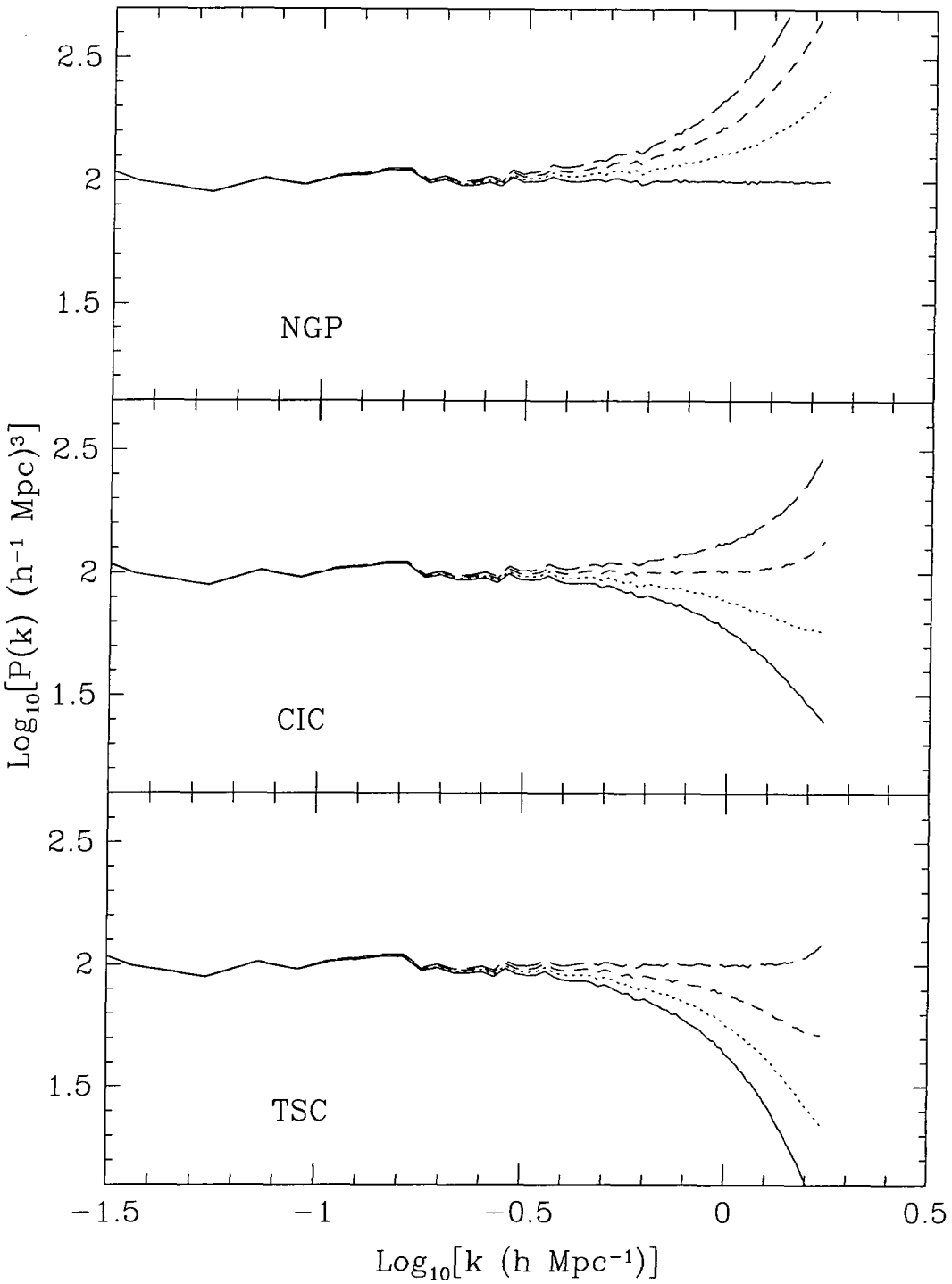

Figure 3.4: Recovered power spectrum for a Poisson distribution of particles. The density has been chosen such that the expected shot-noise is $P(k) = 100h^{-3}\,\mathrm{Mpc}^3$. Panels are for NGP, CIC, TSC from top to bottom. The solid line shows no convolution correction, the dotted line shows correction by one power of the sinc function, the short-dashed line two powers and the long-dashed three.

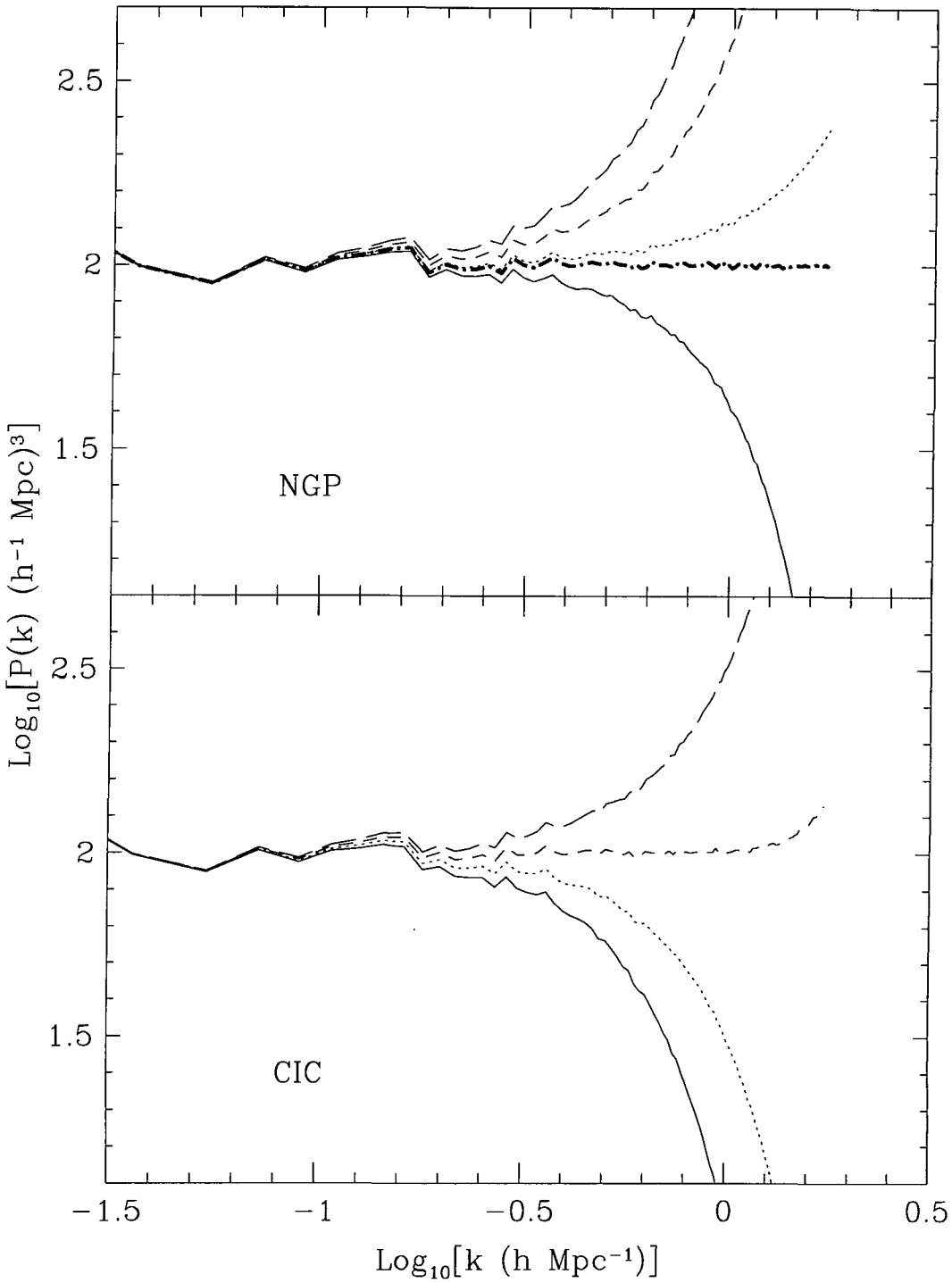

Figure 3.5: Recovered power spectrum for a Poisson distribution of particles, with twice normal smoothing length. Panels are for NGP (top) and CIC (bottom). Line types are the same as for figure 3.4, except in the upper plot where the heavy dot-dashed line is as explained in the text.

With the previous smoothing length, the convolution was cancelled out because the particle location was lost to within one cell length. With the double smoothing here, the particle location is still unknown to one cell length. So the power spectrum should be divided by $S(2\mathbf{k})$, double the usual period, but the shot-noise should only be corrected in the same way as it was previously. The result of doing this is shown by the thick dot-dashed line in figure 3.5, and we see that the original power spectrum is fully recovered.

In summary, then, we find empirically that the corrections that should be applied are:

- **NGP:** $P(\mathbf{k}) = \dfrac{\langle\delta(\mathbf{k})^2\rangle}{S(\mathbf{k})^2} - \dfrac{P_{\rm shot}}{S(\mathbf{k})^2}$ (3.13)
- **CIC:** $P(\mathbf{k}) = \dfrac{\langle\delta(\mathbf{k})^2\rangle}{S(\mathbf{k})^4} - P_{\rm shot}$ (3.14)
- **TSC:** $P(\mathbf{k}) = \dfrac{\langle\delta(\mathbf{k})^2\rangle}{S(\mathbf{k})^6} - P_{\rm shot}$ (3.15)

3.4 The FKP technique for power spectrum estimation

For a real galaxy survey, there are several extra complexities that arise due to our imperfect knowledge of the galaxy distribution. Feldman, Kaiser, & Peacock (1994) outline a method for dealing with real galaxy catalogues, and of measuring the power spectrum from a magnitude limited sample in an optimal way.

The weighted galaxy fluctuation field is defined as

$$F(r) \equiv \frac{w(\mathbf{r})[n_g(\mathbf{r}) - \alpha n_s(\mathbf{r})]}{[\int \mathrm{d}^3 r \bar{n}^2(\mathbf{r}) w^2(\mathbf{r})]^{1/2}} \tag{3.16}$$

where $n_g(\mathbf{r})$ is the number density of galaxies at position $\mathbf{r}$, α is the ratio (n_g/n_s) of real to random galaxies, and $w(\mathbf{r})$ is a radial weighting function chosen to minimize the variance in $P(k)$. The "random" galaxies are drawn from a mock galaxy catalogue having exactly the same radial and angular selection criteria as the real survey, but where galaxies are placed at random within this space.

The Fourier transform of this function is taken and squared to give:

$$\langle|F(\mathbf{k})|^2\rangle = P(\mathbf{k}) \otimes |G(\mathbf{k})|^2 + P_{\rm shot} \tag{3.17}$$

where

$$G(\mathbf{k}) \equiv \frac{\int \mathrm{d}^3 r \bar{n}(\mathbf{r}) w(\mathbf{r}) e^{i\mathbf{k}\cdot\mathbf{r}}}{[\int \mathrm{d}^3 r \bar{n}^2(\mathbf{r}) w^2(\mathbf{r})]^{1/2}} \tag{3.18}$$

is the Fourier transform of the mask defining the shape of the survey, and

$$P_{\rm shot} \equiv \frac{(1+\alpha)\int {\rm d}^3 r \bar{n}(\mathbf{r}) w^2(\mathbf{r})}{[\int {\rm d}^3 r \bar{n}^2(\mathbf{r}) w^2(\mathbf{r})]^{1/2}} \tag{3.19}$$

is the shot-noise component that arises due to the discreteness of the Poisson-distributed galaxies, as described in 3.3.5. The appearance of the $G(\mathbf{k})$ term has the effect of smoothing the power spectrum, ie. introducing correlation between adjacent k-modes. This correlation has no effect on the mean power if the slope of this window function term is much steeper than that of the power spectrum being measured. The function has a width of order $1/D$ where D is the length of the smallest dimension of the survey, so, in the limit of large k we can assume

$$\langle |F(\mathbf{k})|^2 \rangle \simeq P(\mathbf{k}) + P_{\rm shot} \tag{3.20}$$

Our estimator of $P(\mathbf{k})$ is thus

$$\hat{P}(\mathbf{k}) = |F(\mathbf{k})|^2 - P_{\rm shot} \tag{3.21}$$

FKP go on to construct an expression for the variance in the power spectrum, which we will use extensively in Chapter 7. They also use this variance estimate to derive a weighting scheme, $w(\mathbf{r})$, that minimizes the error in $P(k)$:

$$w(\mathbf{r}) = \frac{1}{1+\bar{n}(\mathbf{r})P(k_{\rm R})}, \tag{3.22}$$

where $k_{\rm R}$ is the physical scale for which we require the most optimal estimate of $P(k)$.

References

Canavezes A. et al., 1998, MNRAS, 297, 777

Feldman H. A., Kaiser N., Peacock J. A., 1994, ApJ, 426, 23

Ferreira P. G., Magueijo J., Gorski K. M., 1998, ApJ Lett, 503, L1

Kogut A., Banday A. J., Bennett C. L., Gorski K. M., Hinshaw G., Smoot G. F., Wright E. L., 1996, ApJ Lett, 464, L29

Peacock J. A., Dodds S. J., 1994, MNRAS, 267, 1020

Peacock J. A., Dodds S. J., 1996, MNRAS, 280, L19

Peebles P. J. E., 1980, The large-scale structure of the universe. Princeton University Press, Princeton, N.J.

Press W. H., Teukolsky S. A., Vetterling W. T., Flannery B. P., 1992, Numerical Recipes in FORTRAN, 2nd edition. Cambridge University Press, Cambridge

Chapter 4

Mock galaxy redshift surveys

THE ARGUMENT We present a comprehensive set of mock 2dF and SDSS galaxy redshift surveys constructed from a set of large, high-resolution cosmological *N*-body simulations. The radial selection functions and geometrical limits of the catalogues mimic those of the genuine surveys. The simulations span a wide range of cosmologies, including both open and flat universes. In all the models the galaxy distributions are biased so as to approximately reproduce the observed galaxy correlation function on scales of $1\text{-}10h^{-1}\,\mathrm{Mpc}$. In some cases models with a variety of different biasing prescriptions are included. All the mock catalogues are publicly available on the World Wide Web. We expect these catalogues to be a valuable aid in the development of the new algorithms and statistics that will be used to analyse the 2dF and SDSS surveys when they are completed in the next few years. Mock catalogues of the PSCz survey of *IRAS* galaxies are also available at the same WWW location.

4.1 Introduction

Our knowledge of large scale structure in the Universe will change dramatically as a result of the new generation of galaxy redshift surveys now underway. The Anglo-Australian Two-degree Field (2dF) survey will measure redshifts for 250,000 galaxies selected from the APM catalogue (Maddox et al. 1990b), and the Sloan Digital Sky Survey (SDSS) will obtain a redshift sample of one million galaxies. These surveys will be more than one order of magnitude larger than any existing survey and will allow measurements of large-scale structure of unprecedented accuracy and detail. Precise estimates of the standard statistics that are used to quantify large-scale structure (eg. the galaxy correlation function $\xi(r)$ and power spectrum $P(k)$) will be possible, and the surveys will provide the first opportunity to examine more subtle properties of the galaxy distribution. Getting the best

use out of this wealth of data will demand the development of faster algorithms capable of dealing with the very large numbers of galaxies involved, and the development of new statistical measures. Before the surveys themselves are completed, then, we require synthetic data sets on which the techniques can be tested.

In this chapter we present an extensive set of mock 2dF and SDSS galaxy catalogues. These artificial galaxy redshift catalogues have been constructed from a series of large, high-resolution cosmological *N*-body simulations. The *N*-body simulations span a wide range of cosmological models, with varying values of the density parameter, Ω_0, and the cosmological constant, Λ_0, and with varying choices of the shape and amplitude of the mass fluctuation power spectrum, $P(k)$. For some models several different catalogues have been produced, each employing a different biasing algorithm to relate the galaxy distribution to the underlying mass distribution. All the mock galaxy catalogues have selection functions that mimic those expected for the real surveys. The details of the construction of the catalogues and their basic properties are described here. The catalogues themselves can be obtained from the web address:

`http://star-www.dur.ac.uk/~sjh/mocks/main.html`

The mock redshift catalogues are the principal scientific product of this chapter. We will employ them later in this work, in Chapter 5 where we examine the effect of interstellar dust on the observed clustering of galaxies, and in Chapters 7 and 8 where we develop some new methods for the analysis of large-scale structure in the 2dF and SDSS redshift surveys. We are making them publicly available in the hope that they will be useful to other researchers, both inside and outside the 2dF and SDSS collaborations. Our illustrative plots also provide a qualitative prediction of the structure expected in these redshift surveys if the leading scenario for structure formation, based on Gaussian primordial fluctuations and a universe dominated by cold dark matter, is basically correct. The mock catalogues have a number of limitations (discussed in section 4.7 below): for example, the $345.6h^{-1}\,\mathrm{Mpc}$ simulation cubes are not as large as one might like, and we do not model some of the detailed selection biases that will affect the real surveys, such as loss of members of close galaxy pairs because of a minimum fibre separation. The strength of this collection of catalogues is that it covers a wide range of theoretically interesting cosmological models in a systematic, homogeneous, and documented fashion. We anticipate that these catalogues will be especially helpful to researchers who want to test

the discriminatory power of statistical techniques that probe intermediate scale clustering ($\sim$ 1-100h^{-1} Mpc) and/or to develop practical implementations of these techniques for large data sets. Eventually, mock catalogues like these, or improved versions of them, will be a valuable tool for comparing the survey data against the predictions of cosmological theories.

The cosmological models we have selected fall into two sets, which we refer to as "*COBE* normalized" and "structure normalized" (or "cluster normalized"). In the *COBE* normalized models, the amplitude of the density fluctuations is set by the amplitude of the cosmic microwave background temperature fluctuations measured by the *COBE* satellite and extrapolated to smaller scales using standard assumptions. The shape of the spectrum of density fluctuations is fixed by applying additional constraints on the age of the universe and the baryon fraction. The structure normalized models are, on the other hand, intended to produce approximately the observed local abundance of rich galaxy clusters, and all of them have the same shape for the density fluctuation spectrum, chosen to be consistent with existing observations of large-scale structure. Each set contains both open ($\Lambda_0 = 0$, $\Omega_0 < 1$) and flat ($\Omega_0 + \Lambda_0 = 1$) models with a range of values of Ω_0. Some of the models considered come close to satisfying simultaneously the *COBE* and cluster abundance constraints. For each simulation we apply a "biasing" algorithm to select galaxies from the *N*-body particle distribution, choosing its parameters so that the simulated galaxy population approximately reproduces the amplitude and slope of the observed galaxy correlation function on scales $\sim$ 1-10h^{-1} Mpc. For a few of the models we create multiple catalogues using several different biasing schemes, so that the sensitivity of methods to the detailed properties of biased galaxy formation can be investigated. The *COBE* normalized models arguably have a stronger theoretical motivation, since they represent the predictions of models that assume inflationary primordial fluctuations and cold dark matter with the specified values of Ω_0, Λ_0, Ω_B, and the Hubble constant. Since the structure normalized CDM models all have the same spectral shape, they are particularly useful for testing techniques designed to measure Ω_0 or Λ_0 independently of an assumed shape of the primordial mass power spectrum. Analysis of various aspects of these simulations have appeared elsewhere (Eke, Cole, & Frenk 1996; Cole et al. 1997).

The choice and parameterization of the cosmological models is discussed in section 4.2. Section 4.3 is a full description of all the details of the *N*-body simulations. The

construction of the initial conditions and their evolution are described in sections 4.3.1 and 4.3.2. The biasing prescriptions are explained in section 4.4. The method by which the biased distributions are converted into mock galaxy catalogues is presented in section 4.5. Our modelling of the survey geometries and selection functions is detailed in section 4.5.2. Section 4.6 presents plots showing slices of the galaxy distributions in a selection of the mock galaxy catalogues. The qualitative differences that are discernible in these distributions and the processes that give rise to them are discussed. In section 4.7 we discuss the limitations of this approach. Section 4.8 gives instructions on how to obtain and manipulate the mock galaxy catalogues. We conclude in section 4.9 .

4.2 Cosmological models

All our cosmological models are variants of the cold dark matter (CDM) scenario. The functional form we adopt for the matter power spectrum is that given by Bardeen et al. (1986),

$$P(k) \propto \frac{k^n}{[1+3.89q+(16.1q)^2+(5.46q)^3+(6.71q)^4]^{1/2}} \times \frac{[\ln(1+2.34q)]^2}{(2.34q)^2}, \tag{4.1}$$

where $q = k/\Gamma$ and $k = 2\pi/\lambda$ is the wavenumber in units of $h\mathrm{Mpc}^{-1}$. The index n is the slope of the primordial power spectrum, and in all but one case we adopt $n = 1$, as predicted by the simplest models of inflation, and in good agreement with the *COBE* constraint outlined in Chapter 2. Two further parameters complete the description of the matter power spectrum. These are the shape parameter Γ and the amplitude of the power spectrum, which we specify through the value of σ_8, the linear theory rms fluctuation of the mass contained in spheres of radius $8h^{-1}\,\mathrm{Mpc}$. The background cosmological model in which these fluctuations evolve is specified by the density parameter Ω_0 and the cosmological constant Λ_0, which we express in units of $3H_0^2/c^2$, where H_0 is the present value of the Hubble parameter. Thus, with the exception of the one tilted model with $n \neq 1$, our models are fully specified by the values of four parameters, Ω_0, Λ_0, σ_8 and Γ. For each of the twenty models, table 4.1 lists the values of these parameters along with other parameters that are described below. The names we have listed for the cosmological models are consistent with the convention used in Cole et al. 1997, but in

addition we have included (in parentheses) some more descriptive names for the various $\Omega_0 = 1$ models.

The *COBE* normalized set of models consists of:

- an Einstein-de Sitter,$\Omega = 1$, model (labelled E1 or CCDM for *COBE* normalized CDM),
- three open models with $\Omega_0 = 0.3$, 0.4 and 0.5 (labelled O3-O5), and
- five flat models with $\Omega_0 = 0.1$-0.5 and $\Omega_0 + \Lambda_0 = 1$ (labelled L1-L5).

We do not include *COBE* normalized open models with $\Omega_0 = 0.1$ or 0.2 because they are hopelessly inconsistent with the observed abundance of rich galaxy clusters (Cole et al. 1997). For each of the open models we choose the value of the Hubble parameter h[1] that gives a universe of age $t \approx 12\mathrm{Gyr}$, ie. the largest value of h that is consistent with standard globular cluster age estimates (Chaboyer et al. 1996; Renzini et al. 1996; Salaris, Degl'Innocenti, & Weiss 1997). For each of the low-Ω_0, flat models we choose the value of h that gives $t \approx 14\mathrm{Gyr}$. For $\Omega_0 = 1$ we take $h = 0.5$. Having chosen these values of h, we fix the baryon fraction in these models using the constraint from primordial nucleosynthesis of $\Omega_B = 0.0125h^{-2}$ (Walker et al. 1991). We then use the following expression for the shape parameter Γ,

$$\Gamma = \Omega_0 h \exp(-\Omega_B - \Omega_B/\Omega_0), \tag{4.2}$$

which approximately accounts for the effect of baryons on the transfer function (Sugiyama 1995)[2]. One prediction of theoretical models of adiabatic density perturbations is the existence of oscillations in the power spectrum (Peebles 1981). These "wiggles" are particularly noticeable when the matter and radiation fields are tightly coupled, ie. in the case of a high baryon fraction. More recent work (Eisenstein & Hu 1998) has demonstrated that, in the case of a high baryon fraction, simple adjustments to Γ do not provide good fits to the transfer function, as it is suppressed below the sound horizon scale. We note that the majority of our models have $\Omega_B/\Omega_0 \leq 10\%$, and so these effects are not significant. Finally, in each of these models the amplitude of the

[1] We use the convention that h is the value of the Hubble parameter in units of $100\,\mathrm{km\,s^{-1}Mpc^{-1}}$

[2] The expression for Γ that we have adopted is from the original version of the Sugiyama (1995) paper, and differs slightly from the expression in the published version of that paper, which was modified to improve its accuracy for high values of Ω_B.

density perturbations is set so as to be consistent with the *COBE* measurements of fluctuations in the cosmic microwave background (Smoot et al. 1992; White & Bunn 1995; White & Bunn 1996). Further details of these models can be found in Cole et al. 1997, which examines the abundance of galaxy clusters in *COBE* normalized CDM and presents some analysis of clustering of the mass distributions.

For the set of structure normalized models, we adopt a fixed value of $\Gamma = 0.25$, as suggested by observations of the large-scale structure traced by galaxies (eg. Maddox, Efstathiou, & Sutherland 1996). The amplitude of the power spectrum is set according to the formula $\sigma_8 = 0.55\Omega_0^{-0.6}$, which results in an abundance of rich galaxy clusters in reasonably good agreement with observations (White, Efstathiou, & Frenk 1993). These models include:

- the Einstein-de Sitter model, E3S. In this chapter we consider two independent realizations of this model, E3S A and E3S B. A further eight realizations (C-J) can be found on our web-site.
- a series of open models with $\Omega_0 = 0.2$-0.5 (labelled O2S-O5S), and
- a series of flat models with $\Omega_0 = 0.2$-0.5 and $\Omega_0 + \Lambda_0 = 1$ (labelled L2S-L5S).

Physically, these models could be produced either by having $h = \Gamma/\Omega_0$ or by a change from the standard model of the present energy density in relativistic particles. For example the E3S model is very similar to the τCDM model of Jenkins et al. (1998), which is motivated by the decaying particle model proposed by Bond & Efstathiou (1991), where late decay of the τ-neutrino results in the epoch of matter-domination being delayed, and hence the effective value of Γ being reduced. The final model listed in table 4.1, E4 (SCDM), is the "standard" CDM model, (Einstein-de Sitter with $\Gamma = h = 0.5$), normalized by the abundance of galaxy clusters.

We consider one further model that falls into both the *COBE* and structure normalized categories: the tilted Einstein-de Sitter model, E2 (tilted). For this model, the above constraints have been applied in relating the baryon fraction Ω_B, the Hubble parameter h, and the shape parameter Γ. In addition, the slope, n, of the primordial power spectrum has been adjusted so that the clustering amplitude matches *COBE* observations at large scales while simultaneously achieving $\sigma_8 = 0.55$, as required for consistency with the observed cluster abundances.

This procedure results in a tilted primordial spectrum with $n = 0.803$ and a transfer function with $\Gamma = 0.4506$ as given by equation 4.2. In normalizing to the *COBE* observations, we have included a gravitational wave contribution as predicted by the power-law model of inflation. For this model, gravitational waves contribute approximately 55% of the rms temperature fluctuations on the scales probed by *COBE*.

4.3 *N*-body simulations

We now describe how the initial conditions of the simulations were set up, how the simulated mass distribution was propagated to the present day, and how the particles labelled as galaxies were selected.

4.3.1 Initial conditions

Before imposing the desired perturbations, we set up a uniform density field using the technique described by White (1996) and Baugh, Gaztañaga, & Efstathiou (1995) to generate a particle distribution with a "glass" configuration. Particles are placed randomly throughout the simulation box and then evolved with the *N*-body code, but with the sign of the gravitational forces reversed. We used large timesteps that were approximately logarithmically spaced in expansion factor and evolved the distribution until the gravitational forces on all particles practically vanished. With this approach, the initial particle distribution is not regular, but the small random fluctuations in the particle density field do not seed the growth of spurious structures. Simulations with glass and grid initial conditions have been found to give very similar statistical results once they are evolved into the nonlinear regime (White 1996; Baugh, Gaztañaga, & Efstathiou 1995), but the simulations with glass initial conditions have the advantage that they do not retain an unseemly grid signature in uncollapsed regions.

Each of the simulations was of a periodic box of side $345.6h^{-1}\,\mathrm{Mpc}$ (192 cells of length $1.8h^{-1}\,\mathrm{Mpc}$). For each, we created a Gaussian random density field on a 192^3 grid, using the same Fourier phases from one model to the next, but varying the mode amplitudes according to the model power spectrum. We applied the Zel'dovich approximation (Appendix A) to this density field to compute displacements and peculiar velocities at each grid point. Each particle is displaced from its glass position according to the displace-

ments interpolated from the grid values. The initial expansion factors of the simulations a_i, listed in table 4.1, were determined by setting the amplitude of the initial power spectrum at the Nyquist frequency of the particle grid to be 0.3^2 times that for an equivalent Poisson distribution of particles. The Nyquist frequency is the minimum resolvable wavelength of the distribution,

$$k_{\rm Nyq} = \pi \bar{n}^{1/3} = \frac{2\pi}{3.6 h^{-1}\,{\rm Mpc}} \tag{4.3}$$

where $\bar{n}$ is the mean particle density. Thus, $P_{\rm initial}(k_{\rm Nyq}) = 0.3^2/\bar{n}$. The residual power in the glass configuration is only 0.5% of that in a Poisson distribution at the Nyquist frequency and drops very rapidly at longer wavelengths (see figure A2 of Baugh, Gaztañaga, & Efstathiou 1995). This choice is safely in the regime where:

- the initial density fluctuations are large compared to those present in the glass, but
- the Zel'dovich approximation remains accurate.

In particular, no shell-crossing has occurred.

4.3.2 Evolution

We evolved the simulations using a modified version of Hugh Couchman's Adaptive Particle-Particle-Particle-Mesh (AP^{3}M, Couchman 1991) *N*-body code. We set the softening parameter of AP^{3}M's triangular-shaped cloud force law to $\eta = 270 h^{-1}\,{\rm kpc}$, 15% of the grid spacing. The softening scale is fixed in comoving co-ordinates. This choice corresponds approximately to a gravitational softening length $\epsilon = \eta/3 = 90 h^{-1}\,{\rm kpc}$ for a Plummer force law, and we adopt ϵ as our nominal force resolution. The size of the timestep Δa was chosen so that the following two constraints were satisfied throughout the evolution of the particle distribution. First, the rms displacement of particles in one timestep was less than $\eta/4$. Second, the fastest moving particle moved less than η in one timestep. Initially these two constraints are comparable, but at late times the latter constraint is more stringent, particularly in low Ω_0 simulations. We monitored energy conservation using the Layzer-Irvine equation (equation 12b of Efstathiou et al. 1985) and found that, for this choice of timestep, energy conservation with a fractional accuracy of better than 0.3% was achieved. We also tested the inaccuracy incurred by these

Table 4.1. Simulation Parameters: the first column gives the label of each of the cosmological models; alternative, more descriptive names for the $\Omega_0 = 1$ models are given in parentheses. The following seven columns give the corresponding values of the density parameter Ω_0, cosmological constant Λ_0, Hubble parameter h, age of the universe t, baryon content Ω_B, power spectrum shape parameter Γ, and normalization σ_8 respectively. The final two columns give the initial expansion factors, a_i, and number of timesteps, $N_{\rm steps}$, used in the simulation.

Model	Ω_0	Λ_0	h	t/Gyr	Ω_b	Γ	σ_8	a_i	$N_{\rm steps}$
O3	0.3	0.0	0.65	12.2	0.030	0.172	0.5	0.15	93
O4	0.4	0.0	0.65	11.7	0.030	0.234	0.75	0.1	168
O5	0.5	0.0	0.6	12.3	0.035	0.27	0.9	0.08	254
L1	0.1	0.9	0.9	13.9	0.015	0.076	0.7	0.15	150
L2	0.2	0.8	0.75	14.0	0.022	0.131	0.9	0.12	220
L3	0.3	0.7	0.65	14.5	0.030	0.172	1.05	0.101	266
L4	0.4	0.6	0.6	14.5	0.035	0.213	1.1	0.09	275
L5	0.5	0.5	0.6	13.5	0.035	0.27	1.3	0.07	331
O2S	0.2	0.0	–	–	–	0.25	1.44	0.028	447
O3S	0.3	0.0	–	–	–	0.25	1.13	0.050	313
O4S	0.4	0.0	–	–	–	0.25	0.95	0.073	258
O5S	0.5	0.0	–	–	–	0.25	0.83	0.096	212
L2S	0.2	0.8	–	–	–	0.25	1.44	0.057	405
L3S	0.3	0.7	–	–	–	0.25	1.13	0.080	287
L4S	0.4	0.6	–	–	–	0.25	0.95	0.102	224
L5S	0.5	0.5	–	–	–	0.25	0.83	0.122	184
E1 (CCDM)	1.0	0.0	0.5	13.1	–	0.5	1.35	0.061	327
E2 (tilted)	1.0	0.0	0.5	13.1	0.05	0.45	0.55	0.20	200
E3S (τCDM)	1.0	0.0	–	–	–	0.25	0.55	0.21	103
E4 (SCDM)	1.0	0.0	0.5	13.1	–	0.5	0.55	0.15	170

choices of starting amplitude and timestep by comparing the final particle positions with two additional versions of the E1, $\Omega_0 = 1$ simulations, which were run starting from a fluctuation amplitude a factor of two lower and using timesteps a factor of two smaller. In each case we found that the final particle positions agreed very accurately, with rms differences of less than ϵ. More importantly, the correlation functions of the particle distributions in all cases were indistinguishable at scales larger than $\epsilon = 90h^{-1}\,\mathrm{kpc}$. Thus, the statistical clustering properties of these simulations have a resolution that is limited by the particle mass and force softening and not by the choice of timestep or starting redshift.

4.4 Biasing the galaxy distribution

In this section we describe the methods used to select the particles labelled as galaxies from the distributions of mass produced in the *N*-body simulations. A one-to-one correspondence of the galaxy field to the mass field is unlikely. For galaxies to be unbiased tracers of the underlying mass distribution, the ability to form a galaxy must be independent of the properties of the surrounding density field, so that each mass particle, no matter where it resided, was equally likely to be associated with a galaxy. Simple, physically motivated models such as the high peaks model (Davis et al. 1985; Bardeen et al. 1986) illustrate how a dependence of galaxy formation on the properties of the local density field can make the galaxy distribution more strongly clustered than the underlying mass distribution. This effect can be quantified in terms of a bias factor $b_R = \sigma_R^{\mathrm{gal}}/\sigma_R^{\mathrm{mass}}$, relating the fractional rms fluctuation in the number of galaxies in spheres of radius $Rh^{-1}\,\mathrm{Mpc}$ to the corresponding variation in the mass. For any model in which galaxies form in the collapse of dark-matter haloes, this relationship must break down on the very smallest scales simply because a galaxy has much smaller spatial extent than its halo. The processes of galaxy formation, locally extremely complex, can still result in a large-scale bias factor of unity.

Observational evidence for bias is presented by Peacock & Dodds (1994). They assume a simple, constant linear bias model in which a perturbation in the mass distribution is accompanied by an amplified perturbation in the galaxy distribution, $\delta_{\mathrm{gal}} = b\delta_{\mathrm{mass}}$. They find that the power spectra of differently selected galaxy samples require a bias relative to the power spectrum of *IRAS* galaxies, b/b_{IRAS}, given by:

$b/b_{\rm IRAS} = 1.3$ for optically selected galaxies

$b/b_{\rm IRAS} = 1.9$ for radio galaxies

$b/b_{\rm IRAS} = 4.5$ for Abell clusters.

Since a relative bias exists between any two of these differently selected samples, it seems natural to assume that all galaxy samples will be subject to some degree of bias relative to the underlying mass. We note that bias is also important in interpreting the estimates of the mass-to-light ratio of galaxies in clusters. These have been used in conjunction with estimates of the galaxy luminosity function to infer $\Omega_0 \approx 0.2$ (Carlberg, Yee, & Ellingson 1997). This inference assumes that galaxies are unbiased tracers of the mass distribution. If galaxies form preferentially in proto-cluster environments, then this estimate translates to $\Omega_0/B \approx 0.2$, where B is the factor by which the efficiency of galaxy formation is enhanced in regions destined to become clusters, relative to the field.

Since the physics of galaxy formation is very complex, we cannot yet determine the function that relates the probability of forming a galaxy to the properties of the mass density field, though first steps towards this goal have been taken using cosmological simulations with gas dynamics (Cen & Ostriker 1992; Katz, Hernquist, & Weinberg 1992; Summers, Davis, & Evrard 1995; Frenk et al. 1996) and with semi-analytic models of galaxy formation (Benson et al. 1999; Kauffmann, Nusser, & Steinmetz 1997). For this reason we take the approach of defining the biasing algorithm in terms of a simple parametric function. Then for each cosmological model we constrain the values of the function's parameters using estimates of observed small and intermediate scale galaxy clustering. For a subset of the cosmological models we repeat this procedure for several different biasing algorithms. Making this repetition, one can quantify the extent to which the properties of the catalogues depend on the choice of adopted biasing algorithm.

For optically selected galaxies in the APM survey the clustering amplitude is found to be $\sigma_8^{\rm gal} = 0.96$ (Maddox, Efstathiou, & Sutherland 1996). Many of our simulations have higher amplitudes than this, and therefore require an anti-bias ($b < 1$) on the $8h^{-1}\,{\rm Mpc}$ scale. Anti-bias seems less physically motivated than bias because it requires negative feedback processes to suppress galaxy formation in high-density regions. Such an anti-correlation, however, might be produced even if the production rate of galaxies in proto-

clusters is higher than in low-density regions, so long as galaxy merging in the proto-clusters is sufficiently efficient to suppress the overall number of galaxies in clusters. Alternatively, in an *N*-body treatment where haloes are assumed to be spatially exclusive, if each collapses to produce a single galaxy then the galaxies cannot be closer together than the radii of the haloes, so the galaxy distribution cannot match the mass distribution in high density regions. This leads to an anti-bias on scales of order the halo size.

The biasing schemes we consider are, with one exception, local, in the sense that the probability of a mass particle being selected as a galaxy is a function only of the neighbouring density field, eg. the density field smoothed on a scale $3h^{-1}\,\mathrm{Mpc}$. Such models have the property that, on scales (in the linear regime) that are much larger than that defining the local neighbourhood, they produce a constant, scale independent bias (Scherrer & Weinberg 1998). A derivation of an expression for this asymptotic bias is given in section 4.4.2 below. Our algorithms include both Lagrangian models, in which the selection probability is a function of the initial density field, and Eulerian models, in which the probability is a function of the final mass density field. For a consideration of the differences between these approaches see Mann, Peacock, & Heavens 1998.

We use seven different prescriptions for creating the biased galaxy samples. All of them involve defining a probability field from either the initial or the final density distribution, and then Poisson sampling the simulation particles using this field to define the selection probability. The probability is normalized such that a mean of 128^3 out of the original 192^3 particles are selected. The corresponding galaxy number density is $\bar{n}_{\mathrm{g}} \approx 0.05h^3\mathrm{Mpc}^{-3}$, which approximately equals that of galaxies brighter than $L_\star/80$. Although this density is less than that of the original simulation, occasionally the bias may demand that in certain regions there is a greater galaxy density than the original particle density. The Poisson sampling achieves this by allowing some particles to be selected more than once. This double sampling is generally rare but does occur, especially in the highly biased models. The functions defining the selection probability have one or two free parameters. In the case of those with just one free parameter, we fix its value by demanding that $\sigma_8^{\mathrm{gal}} = 0.96$, in agreement with the value estimated from the APM galaxy survey. The models with two parameters enable us to control both the amplitude of galaxy clustering on large scales and, to some extent, the slope of the galaxy correlation function on small scales. We set their parameters by attempting to match simultaneously the observed variance

of the galaxy density field in cubic cells of 5 and $20h^{-1}\,\mathrm{Mpc}$ on a side. We assume $\sigma_{\mathrm{cell}\,5} = 2.0$ and $\sigma_{\mathrm{cell}\,20} = 0.67$, the values from the power spectrum shape estimated for APM galaxies by Baugh & Efstathiou (1994), scaling its amplitude for consistency with the more recent estimate of $\sigma_8^{\mathrm{gal}} = 0.96$. In some cases, where, for instance, the small scale mass correlation function is very much steeper than the observed galaxy correlation, it does not prove possible to simultaneously satisfy these two constraints. For computational simplicity and to avoid any ambiguity, we choose, in all cases, to fit the observed values by minimizing the cost function

$$C(\alpha,\beta) = \left(\frac{(\sigma_{\mathrm{cell}\,20} - 0.67)}{0.67}\right)^2 + \left(\frac{(\sigma_{\mathrm{cell}\,5} - 2.0)}{2.0}\right)^2 + \epsilon_c(\alpha^2+\beta^2), \tag{4.4}$$

where α and β are the two model parameters. The third term has $\epsilon_c = 4\times10^{-7}$, and is included to avoid extremely large values of $|\alpha|$ and $|\beta|$ being selected for very little improvement in the values of $\sigma_{\mathrm{cell}\,5}$ and $\sigma_{\mathrm{cell}\,20}$.

4.4.1 Biasing algorithms

Here we define the selection probability functions, $P(\nu)$, which define each of our biasing algorithms. The resulting biased galaxy correlation functions, $\xi(r)$, and power spectra, $P(k)$, are shown in Figs. 4.1, 4.2, and 4.3 and discussed below. The biasing algorithm that we apply to all of the cosmological models is model 1; the other biasing models are used only to create additional mock catalogues for the O4S, L3S, and E3S simulations.

1. **Exponential method: Lagrangian.** This model bases the selection probability on the value of the smoothed initial density. We use a Gaussian smoothing of $\exp(-r^2/2R_S^2)$, with width $R_S = 3h^{-1}\,\mathrm{Mpc}$ to define a smoothed density field, $\rho_S(\mathbf{r})$, at the initial particle position. We find this field by taking the initial density field, which is defined on a grid convolving with the smoothing function using an FFT method.

   A dimensionless variable, ν, is defined: $\nu(\mathbf{r}) = \delta_S(\mathbf{r})/\sigma_S$, where δ_S is the smoothed overdensity field and $\sigma_S^2 = \langle|\delta_S|^2\rangle$. We then adopt

   $$P(\nu) \propto \begin{cases} \exp(\alpha\nu + \beta\nu^{3/2}) & \text{if } \nu \geq 0 \\ \exp(\alpha\nu) & \text{if } \nu < 0 \end{cases}, \tag{4.5}$$

   as the selection probability. The model has two free parameters α and β. This choice of functional form is essentially selected for its simplicity. Its exponential behaviour

ensures that the probability cannot be negative. The dependence on β for $\nu > 0$ enables the selection probability to be enhanced ($\beta > 0$) or suppressed ($\beta < 0$) in the densest regions. This property gives some control over the slope of the small scale correlation function. The choice of a $\nu^{3/2}$ dependence is made so that the probability converges when integrated over a Gaussian distribution of ν.

2. **Exponential method: Eulerian**. For this model the same functional form (equation 4.5) is used to define the selection probability, but this time the variable ν is defined in terms of the smoothed *final* density field around each particle. Again, a Gaussian smoothing with $R_{\rm S} = 3h^{-1}\,{\rm Mpc}$ is adopted.

3. **High peaks model**. The standard high peaks model of Bardeen et al. (1986) is used to predict the number of peaks of amplitude $\nu > \nu_{\rm p}$ defined on the scale of a galaxy as a function of the density smoothed on a larger scale that *is* resolvable in our simulation. In this case we choose the larger scale to be defined by applying a sharp cutoff to the power at a wavelength $\lambda \lesssim 4h^{-1}\,{\rm Mpc}$, which is quite well resolved in the initial conditions of the simulation. We define the galaxy mass scale by a Gaussian smoothing with $R_{\rm S} = 0.54h^{-1}\,{\rm Mpc}$, as adopted by White et al. (1987). Here the model parameter is $\nu_{\rm p}$. An unavoidable property of assuming that galaxies form in peaks of the density field is that they are more clustered than the mass distribution ($b > 1$). Thus this method cannot be applied in cases where an anti-bias is required.

4. **Threshold bias**. In this model a sharp cut-off is applied to the final smoothed density field, so that galaxies are entirely prohibited from forming in very underdense regions, but have an equal chance of forming wherever the overdensity rises above a certain threshold, $\rho_{\rm T}$. Thus

$$P(\nu) \propto \begin{cases} 1 & \text{if } \rho(\mathbf{r}) \geq \rho_{\rm T} \\ 0 & \text{if } \rho(\mathbf{r}) < \rho_{\rm T} \end{cases} . \tag{4.6}$$

This is the case if a bias greater than unity is required. For an anti-bias, the conditions are reversed and galaxies are prohibited from forming in the very densest regions. Note that this prescription for producing anti-bias has unphysical consequences, as it implies that the highest mass density regions have no galaxies in them at all.

5. **Power-law method**. As in model 2 the selection probability is defined in terms of the smoothed final density, but this time the functional form adopted is a power law,

$$P(\nu) \propto \nu^{\alpha}. \tag{4.7}$$

Here a positive value of the parameter α will induce a bias ($b > 1$) and a negative value an anti-bias ($b < 1$). The bias inferred by Cen & Ostriker (1993) from their hydrodynamic cosmological simulations has roughly this form, with $\alpha \approx 1.5$.

6. **Exponential bias: adaptive smoothing**. This algorithm is a variation of model 2 and again uses the formula (4.5), but with a different definition of the overdensity parameter ν. Instead of smoothing on a fixed scale of $3h^{-1}\,\mathrm{Mpc}$, the distribution was adaptively smoothed by setting the density at the position of each particle, $\rho \propto 1/r_{10}^3$, where r_{10} is the distance to the tenth nearest neighbour of that particle. It is hoped that this adaptive definition of the smoothing scale will result in the better definition of high-density areas, giving more control of the slope of the bias function on small scales.

7. **Non-local bias**. All the above models allow the degree of bias only to be affected by the locally smoothed density fields, on fairly modest scales. As pointed out by Bower et al. (1993) longer range effects (eg. positive or negative feedback effects from nearby proto-galaxies) could mean that the neighbouring density field at rather larger distances could have an effect on galaxy formation, the so-called "co-operative" model. We implement a simple, two parameter version of this model, where the bias probability is defined by a power-law,

$$P(\nu) \propto (\nu + \beta\nu_{\mathrm{s}})^{\alpha}. \tag{4.8}$$

Here, ν is the usual, locally smoothed density field, and ν_{s} the field smoothed on a larger scale ($10h^{-1}\,\mathrm{Mpc}$). We fit the parameters α and β so as to match the APM clustering amplitudes, as described above.

The parameters used in the first six, local biasing schemes are shown in table 4.2.

The various galaxy correlation functions and power spectra that result from applying bias model 1 to each of the cosmological simulations are shown in figures 4.1 and 4.2 respectively. The solid data points show the estimates of the correlation

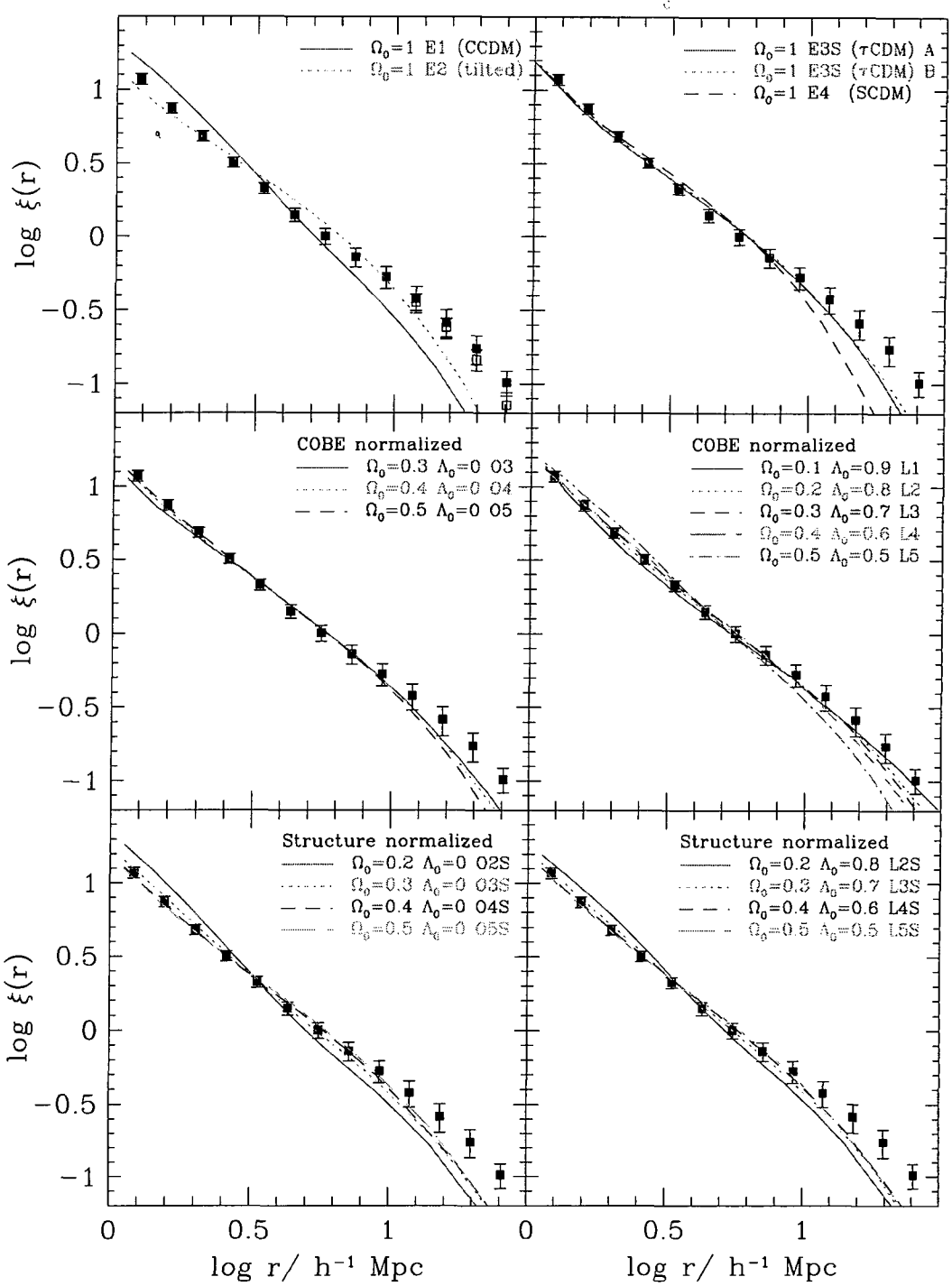

Figure 4.1: The galaxy correlation functions, $\xi(r)$, for each of our cosmological models when biased using model 1. Each of the lines corresponds to a different cosmological model as indicated on the legend. The solid data points are the same on each panel and are an estimate of the galaxy correlation function from the APM survey (Baugh 1996). The open data points, shown on the first panel, show an alternative estimate of the APM correlation function obtained by Fourier transforming the Baugh & Efstathiou (1993) estimate of the APM power spectrum.

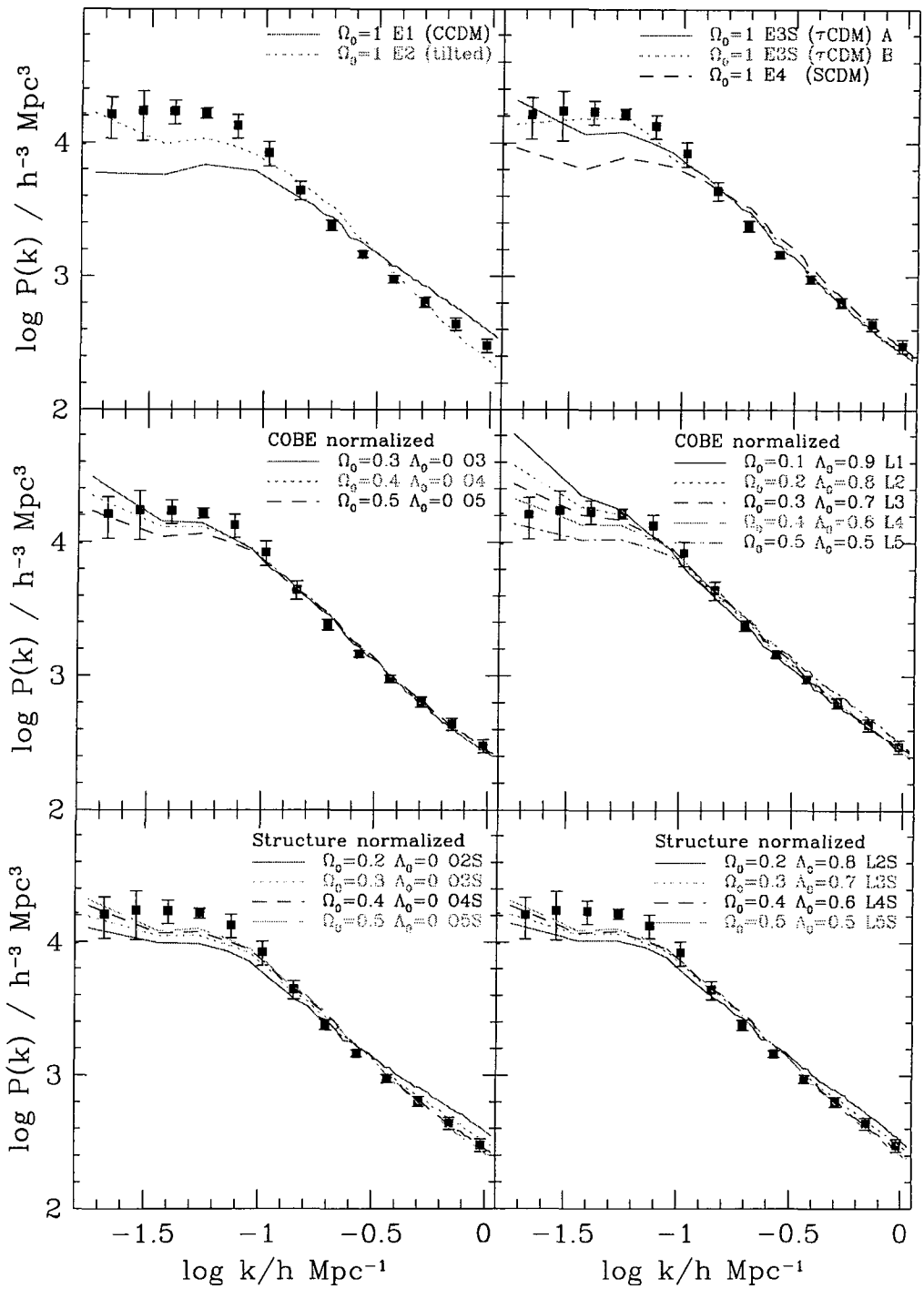

Figure 4.2: The galaxy power spectrum, $P(k)$, for each of our cosmological models when biased using model 1. Each of the lines corresponds to a different cosmological model as indicated on the legend. The data points are the same on each panel and are an estimate of the galaxy power spectrum from the APM survey (Baugh & Efstathiou 1993).

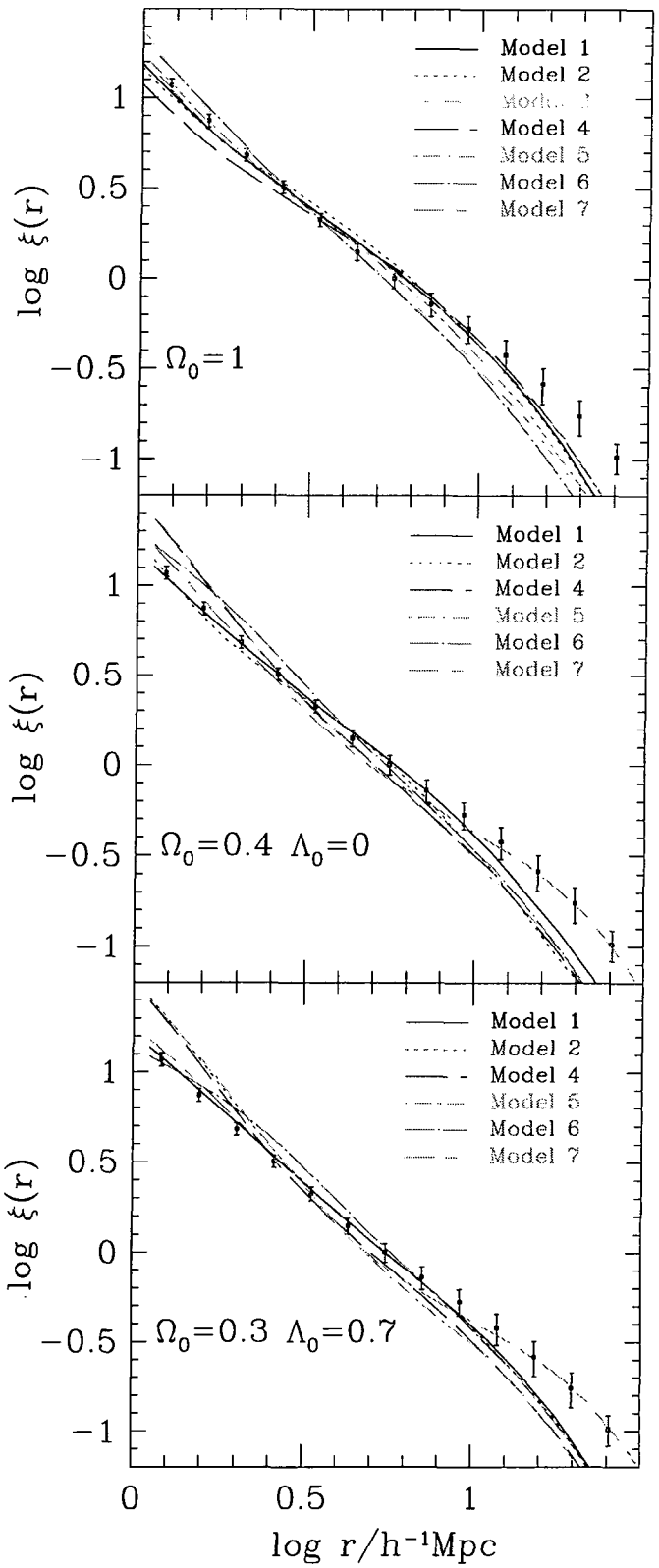

Figure 4.3: For three selected, structure normalized cosmological models (E3S,O4S and L3S), we show the galaxy correlation functions that result from each of the bias models. Note that both of the $\Omega_0 < 1$ models require anti-bias and therefore cannot be biased using peaks bias, model 3. The line types corresponding to each of the bias models are indicated on the legend. The data points again show the estimate of the galaxy correlation function from the APM survey.

Table 4.2. Bias model parameters. For the three selected cosmological models we list the parameter values required in each of the six local bias models. The resulting galaxy correlation functions are compared in figure 4.3.

Identifier	Model 1		Model 2		Model 3	Model 4	Model 5	Model 6	
	$\alpha_{\rm i}$	$\beta_{\rm i}$	$\alpha_{\rm f}$	$\beta_{\rm f}$	$\nu_{\rm p}$	$\rho_{\rm T}$	α	$\alpha_{\rm f}$	$\beta_{\rm f}$
O4S	3.60	-9.05	2.17	-1.31	–	<19.7	-0.02	3.96	-2.69
L3S	2.55	-17.75	0.15	-0.06	–	<15.5	-0.13	7.11	-7.15
E3S	1.10	-0.56	1.26	-0.51	1.005	>0.98	0.56	2.98	-1.25

function (Baugh 1996) and power spectrum (Baugh & Efstathiou 1993) of APM galaxies, scaled in amplitude to match the estimate of $\sigma_8^{\rm gal} = 0.96$ for the APM survey (Maddox, Efstathiou, & Sutherland 1996). The data points plotted as open symbols on the top left panel of figure 4.1 show the APM correlation function as estimated from the Fourier transform of the estimated APM power spectrum. There is a slight difference between this and the direct estimate at large separations, which arises because both $\xi(r)$ and $P(k)$ are estimated using non-linear inversions of the measured angular correlation function. The difference is an indication of one of the systematic errors involved in estimating $\xi(r)$ on large scales.

In general, the two-parameter biasing model is successful in matching both the amplitude and the shape of the galaxy correlation function on scales of $1\text{-}10h^{-1}\,{\rm Mpc}$, as can clearly be seen in figure 4.1. For a few cases, such as E1, O2S, and L2S, which have high values of $\sigma_8^{\rm mass}$ and consequently steep non-linear mass correlation functions, the bias model cannot reduce the slope of the correlation function enough to accurately match the observed value. The behaviour of the correlation functions on large scales reflects each model's value of the power spectrum shape parameter Γ. The APM data, if fitted with a Γ-model with no bias, prefer $\Gamma = 0.15\text{-}0.2$ (eg. Efstathiou, Sutherland, & Maddox 1990), so even our structure normalized, $\Gamma = 0.25$ models fall short of the amount of large-scale power evident in the APM correlation function. This short-fall is also exaggerated by a statistical fluctuation in our simulation initial conditions. As can be seen in the top-right-hand panel of figure 4.2, the first realization (A) of model E3S has less power on scales $0.03 \lesssim k \lesssim 0.06\,h{\rm Mpc}^{-1}$ than the second realization (B) of the same model. This downward fluctuation in the power is present in all the other cosmological models, since

all the initial density fields were generated from the same basic Gaussian random field but with expected mean amplitudes rescaled according to the model power spectrum. We also note that the longest wavelength modes, with $k = 2\pi/L_{\rm BOX}$, are noisy because of the small number of such modes contained in the simulation box. The comparison of model and APM galaxy power spectra on small scales (high k) is in accord with the small scale behaviour of the correlation functions.

The manner in which the galaxy clustering statistics vary with the form of the biasing is illustrated in figure 4.3. The one-parameter bias models (models 3, 4 and 5) do not have the flexibility to control both the amplitude and slope of the galaxy correlation function. Thus, in general, these models do not match the APM galaxy correlation function over a wide range of scales. In particular, the galaxy correlation functions of the three models selected for figure 4.3 are steeper than the correlation function of APM galaxies, reflecting the steepness of the underlying mass correlation functions. The $3h^{-1}\,{\rm Mpc}$ filter used in bias model 2 smooths over the structure of groups and clusters in the *final* density field. As a result, the small-scale slope of the galaxy correlation function ends up being insensitive to the bias model parameters in this case. In model 6, on the other hand, the use of an adaptive smoothing results in better resolution on the scale of groups and clusters. In some cases this is enough to enable the required adjustments to the slope of the correlation function on small scales. Model 7 is substantially better at obtaining the correct large-scale slope, especially in the low-Ω_0 cases. This is unsurprising since this method depends on the large-scale density field, giving it more "leverage" than the other models.

4.4.2 The asymptotic bias

In general all the biasing algorithms discussed above give rise to a bias that is scale dependent. However, since the biasing algorithms used in models 1-6 only depend on local properties of the density field, the bias should tend to a constant on large scales (Mann, Peacock, & Heavens 1998). Where the selection probability is a function of the initial density field, the value of this asymptotic bias can be computed analytically. The probability that a mass particle is selected as a galaxy is taken to be $P(\nu)$, where ν is the

amplitude of the initial density fluctuation in units of the rms, σ_s. The normalization of $P(\nu)$ is determined by the integral over the Gaussian distribution of initial density fluctuations,

$$\frac{1}{\sqrt{2\pi}} \int P(\nu)\, e^{-\nu^2/2}\, d\nu = 1. \tag{4.9}$$

The density of galaxies selected in a region in which a large scale perturbation Δ is added will be given by

$$\rho_{\rm gal} = \bar{\rho}_{\rm gal} \frac{(1+\Delta)}{\sqrt{2\pi}} \int P(\nu')\, e^{-\nu^2/2}\, d\nu, \tag{4.10}$$

where $\nu' = \nu + \Delta/\sigma_s$. In the regime where $\Delta/\sigma_s \ll \nu$, we can accurately approximate $P(\nu)$ with its first order series expansion, yielding

$$P(\nu') = P(\nu) \left(1 + \frac{d\ln P}{d\nu} \frac{\Delta}{\sigma_s}\right). \tag{4.11}$$

Hence

$$\frac{\rho_{\rm gal}}{\bar{\rho}_{\rm gal}} = \frac{(1+\Delta)}{\sqrt{2\pi}} \int P(\nu) \left(1 + \frac{d\ln P}{d\nu} \frac{\Delta}{\sigma_s}\right) e^{-\nu^2/2} d\nu, \tag{4.12}$$

which simplifies to

$$\frac{\rho_{\rm gal}}{\bar{\rho}_{\rm gal}} = (1+\Delta) \left(1 + \frac{\Delta}{\sqrt{2\pi}\sigma_s} \int \frac{dP}{d\nu} e^{-\nu^2/2}\, d\nu\right). \tag{4.13}$$

We can thus define an asymptotic bias factor, ie. the ratio of the galaxy to the mass perturbations on large scales, as

$$b_{\rm asymp} = \frac{\rho_{\rm gal} - \bar{\rho}_{\rm gal}}{\bar{\rho}_{\rm gal}} \Big/ \Delta = 1 + \frac{1}{\sqrt{2\pi}\sigma_s} \int \frac{dP}{d\nu} e^{-\nu^2/2}\, d\nu. \tag{4.14}$$

This result is compared to the bias estimated from the simulations in figure 4.4. The figure clearly shows that the bias does indeed tend towards its asymptotic value, as calculated above, on large scales.

4.5 The mock catalogues

The previous section described the procedure by which we create a galaxy distribution within each simulation cube. We now outline how these are manipulated and sampled to create the mock galaxy catalogues. It should be noted that we do not attempt to

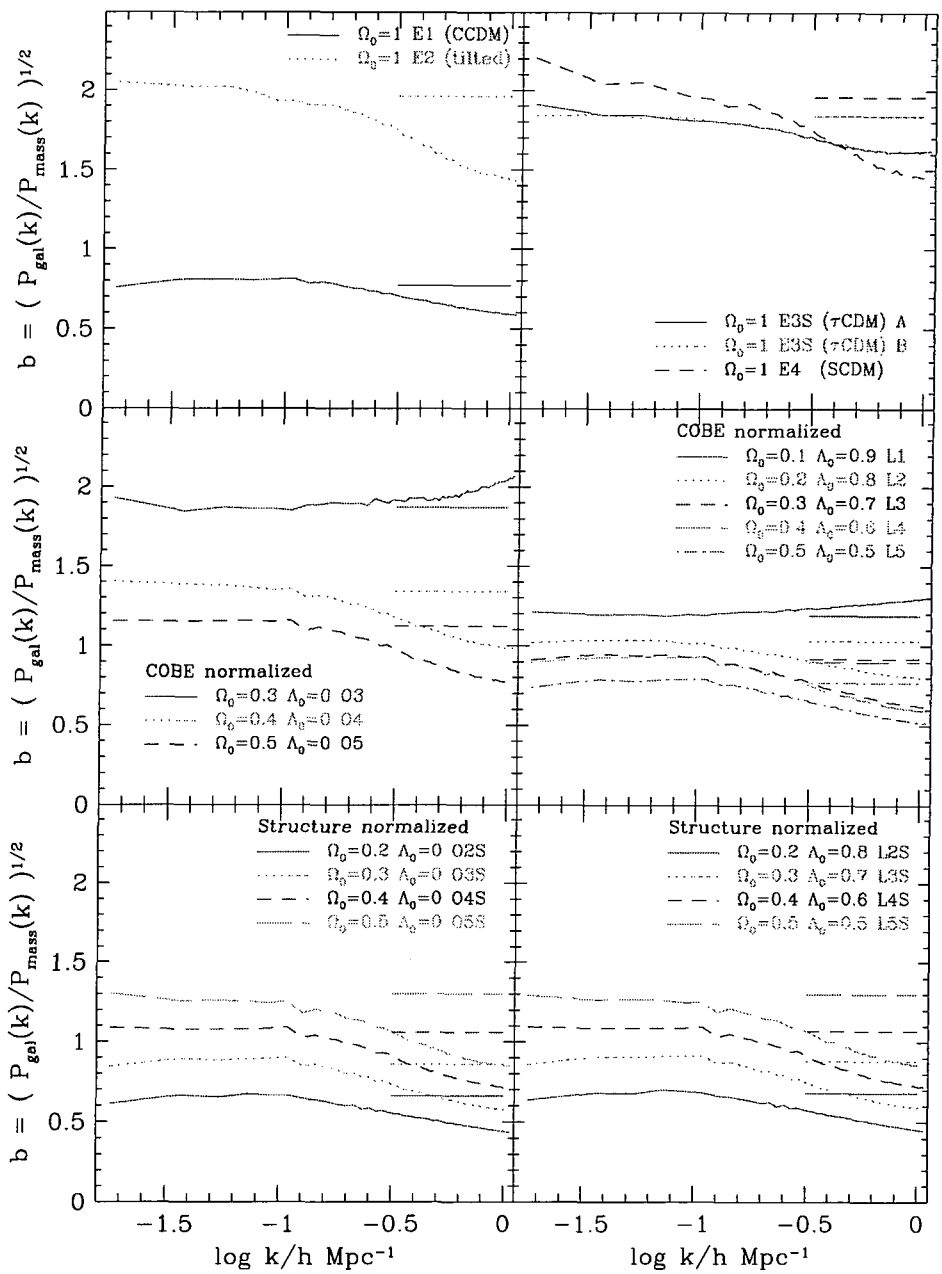

Figure 4.4: The scale-dependent bias, $b(k) = [P_{\rm gal}(k)/P_{\rm mass}(k)]^{1/2}$, for each of our cosmological models when biased using bias model 1. Each of the lines corresponds to a different cosmological model as indicated on the figure. To the right of each panel we show the value of the expected asymptotic bias on large scales, as explained in section 4.4.2.

mimic the imperfections that will inevitably be present in the genuine catalogues, eg. Galactic extinction, excluded regions around bright stars, or missing members of galaxy pairs separated by less than the minimum fibre spacing. Our goal is instead to create idealized catalogues with the expected redshift distributions and geometrical properties of the genuine surveys. We anticipate that members of the 2dF and SDSS collaborations will create mock catalogues that incorporate the finer details of the survey properties.

4.5.1 Survey geometry

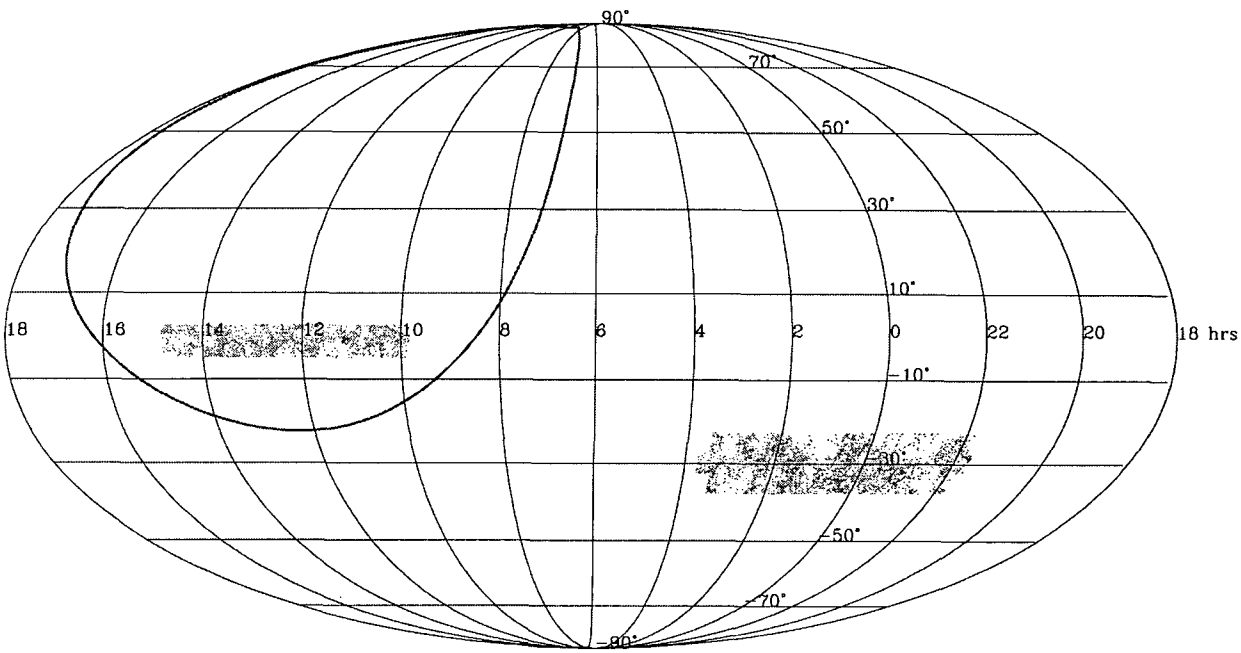

Figure 4.5: An equal area (Mollweide) projection of the whole sky showing the regions covered by the 2dF and SDSS galaxy redshift surveys. The regions covered by the 2dF survey are indicated by the areas populated by points. These are the galaxy positions for a narrow range in redshift from one of our mock catalogues. The 2dF consists of two strips. The larger crosses the SGP while the small one runs close to the NGP. The solid curve marks the boundary of the SDSS survey, which is an ellipse centred close to the NGP. We do not include the SDSS southern strips. The grid indicates the RA and dec. coordinates.

The specifications of both the 2dF and Sloan surveys may be slightly modified after evaluating the results from the current period of test observations. The areas that we have adopted are shown in figure 4.5 and defined below.

The main SDSS area is an elliptical region centred at $\alpha = 12^{\rm hr}20^{\rm m}$, $\delta = 32.8°$, close to the North Galactic Pole (NGP) and covering π steradians, one quarter of the sky. The

minor axis of the ellipse spans $110°$ and runs along a line of constant RA. The major axis spans $130°$. Our mock catalogues do not include the strips in the Southern Galactic Cap that will also be part of the SDSS redshift survey; larger simulation volumes are needed to model simultaneously the Northern and Southern SDSS.

The main 2dF survey consists of two broad declination strips. The larger is approximately centred on the SGP and covers the declination range $-22.5° > \delta > -37.5°$. This declination range breaks into three contiguous, $5°$ wide strips, each with slightly different ranges in RA, which, from north to south are:

1. $21^{\rm hr}48^{\rm m} < \alpha < 3^{\rm hr}24^{\rm m}$,

2. $21^{\rm hr}39.5^{\rm m} < \alpha < 3^{\rm hr}43.5^{\rm m}$ and

3. $21^{\rm hr}49^{\rm m} < \alpha < 3^{\rm hr}29^{\rm m}$.

The smaller strip in the northern galactic hemisphere covers $-7.5° < \delta < 2.5°$ with right ascension

4. $9^{\rm hr}50^{\rm m} < \alpha < 14^{\rm hr}50^{\rm m}$.

Together, the strips cover a solid angle of 0.51 steradians. There is considerable overlap between the northern slice and the area covered by the SDSS.

4.5.2 The radial selection function

The galaxies of the 2dF survey are selected from the APM galaxy survey and will be complete to an extinction corrected apparent magnitude of $b_{\rm J} < 19.45$. The SDSS will have galaxies selected from its own multi-band digital photometry. The primary selection will be made in the r'-band, and it will include a surface brightness threshold to ensure that an adequate fraction of the galaxy light goes down a $3''$ fibre (see Gunn & Weinberg 1995 for details). For simplicity, and because our goal is merely to match the geometry and depth of the two surveys, we make our selection for both catalogues in the $b_{\rm J}$-band. For the SDSS we adopt a magnitude limit of $b_{\rm J} < 18.9$ so as to approximately reproduce the SDSS target of 900,000 galaxies in the survey area. A mock catalogue from a $(600h^{-1}\,{\rm Mpc})^3$ *N*-body simulation that mimics the SDSS selection function in greater detail is also underway (Gott et al. in preparation; see also Gunn & Weinberg 1995). In

addition to its primary galaxy sample, the SDSS will target a set of $\sim 100,000$ luminous red elliptical galaxies, to create a deep, sparse sample that is approximately volume-limited to $z \sim 0.4$. Similarly, the 2dF programme includes a deep extension to $R \sim 21$ that will contain ~ 10000 galaxies. We do not attempt to model these samples because their median depths are larger than the simulation cubes.

In order to compute the radial selection functions of the surveys, we adopt a Schechter (1976) function description of the $b_{\rm J}$-band luminosity function,

$$\frac{d\phi(L)}{dL}\,dL = \phi_\star\,(L/L_\star)^{\alpha_\star}\,\exp(-L/L_\star)\,dL/L_\star, \tag{4.15}$$

with absolute magnitude $M_{b_{\rm J}} = M^{\odot}_{b_{\rm J}} - 2.5\log_{10}(L/L_\odot)$. We relate the apparent magnitude $b_{\rm J}$ of a galaxy at redshift z to the corresponding absolute magnitude $M_{b_{\rm J}}$ at redshift $z = 0$ using

$$b_{\rm J} = {\rm e} + {\rm k} + 5\log_{10}(d_L/h^{-1}\,{\rm Mpc}) + 25 + (M_{b_{\rm J}} - 5\log_{10} h). \tag{4.16}$$

Here d_L is the luminosity distance to redshift z in the appropriate cosmological model. The term "k" denotes the so called k-correction, which arises from the Doppler shift to the wavelength of the galaxy's spectral energy distribution when viewed in the observer's frame. The term "e" describes the effect of luminosity evolution in the galaxy as a result of a combination of passive evolution of the stellar populations and star formation. This model therefore allows for luminosity evolution, but not for any change in the shape of the galaxy luminosity function, which might occur as a result of galaxy merging or luminosity dependent evolution.

Even over the relatively limited range of apparent magnitudes covered by the APM survey, the galaxy number counts are a significantly steeper function of apparent magnitude than is predicted by non-evolving models (Maddox et al. 1990). In contrast, the K-band galaxy counts have shown no evidence for such a steep slope (Gardner et al. 1997), but recently Philips & Turner (1998) have used a compilation of survey data to argue that at the brightest magnitudes the K-band slope is as steep as that seen in the B-band. Unless we live in a very large underdense region or there exists some as yet unidentified systematic error in the bright galaxy counts (Bertin & Dennefeld 1997; Metcalfe et al. 1991), some form of rapid galaxy evolution is necessary. The counts can be reproduced by a model with strong luminosity evolution such as can be accommodated in equation 4.16,

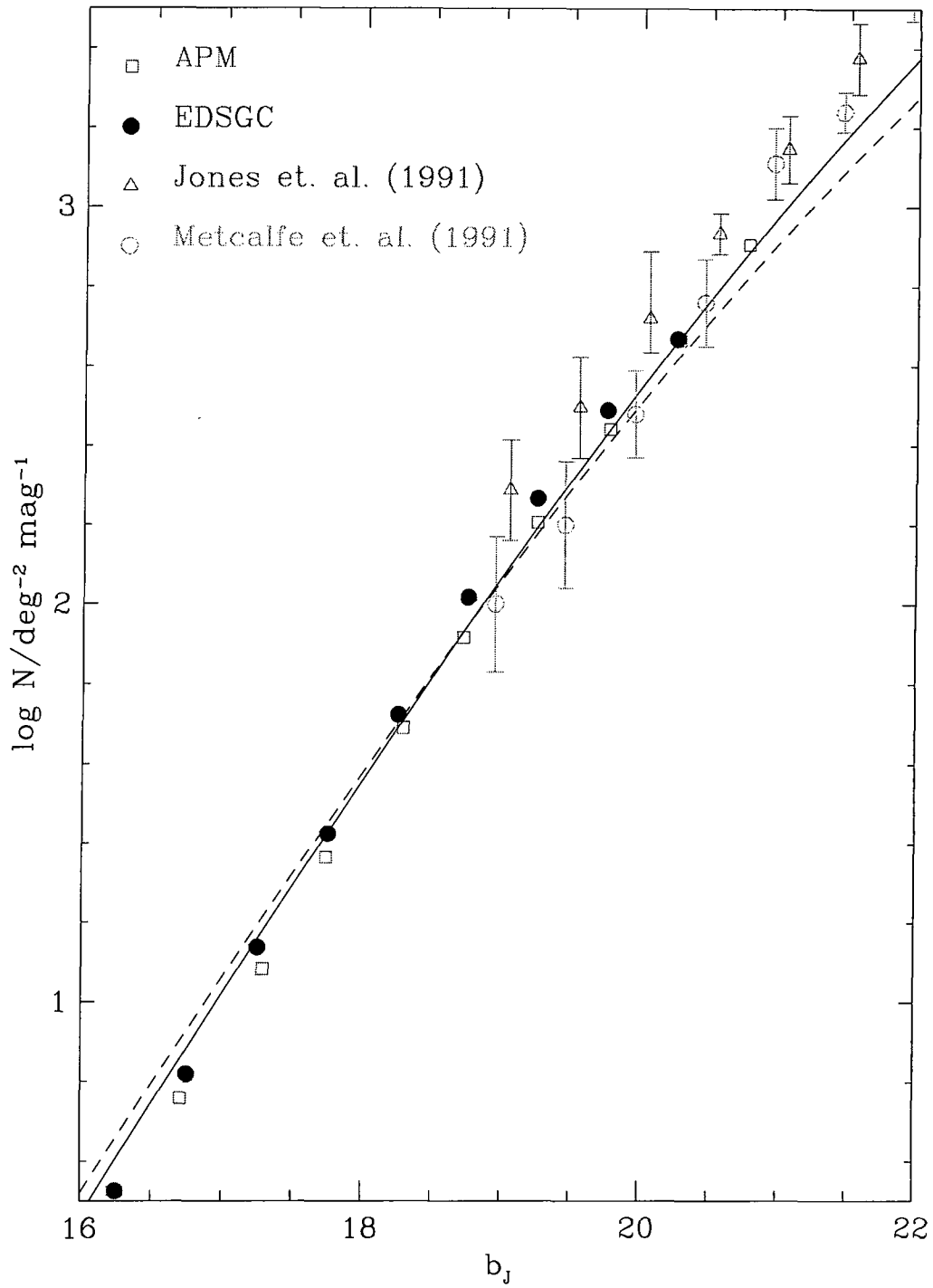

Figure 4.6: Galaxy number counts in our two evolution models compared with observational data. Over this range of magnitudes, the counts are weakly dependent on cosmology and are plotted here for $\Omega_0 = 1$. The solid line corresponds to our standard model in which luminosity evolution cancels the k-corrections. The dashed line corresponds to the less extreme model in which k-corrections are larger than the luminosity evolution. The data points are taken from Maddox et al. (1990b) (APM), Heydon-Dumbleton, Collins, & Macgillivray (1989) (EDSGC), Jones et al. (1991) and Metcalfe et al. (1991). The Poisson errorbars for the EDSGC sample are smaller than the point size used, although these are underestimates of the true uncertainty if clustering is significant in this sample.

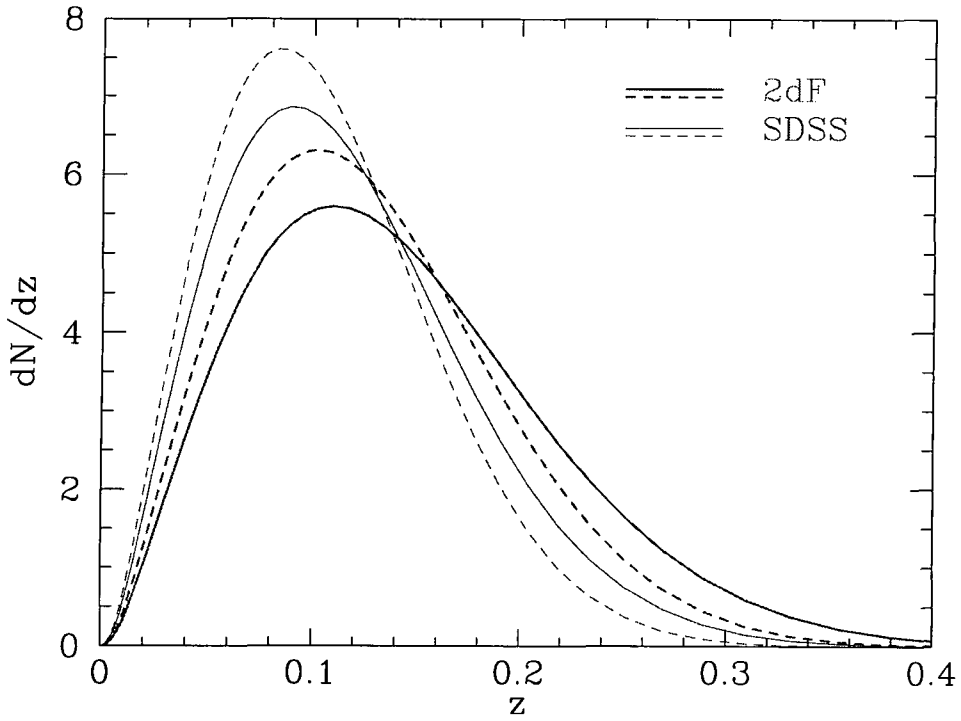

Figure 4.7: The model galaxy redshift distributions. These distributions are weakly dependent on cosmology and are plotted here for $\Omega_0 = 1$. The heavy curves, peaking at the higher redshifts, correspond to the magnitude limit of $b_J < 19.45$ of the 2dF survey and light lines to the $b_J < 18.9$ of the SDSS. As in figure 4.6, the solid curves are for our standard selection function and the dashed curves for the alternative model with weaker luminosity evolution. The median redshifts are $z_m = 0.13$ and 0.12 for the 2dF catalogues and $z = 0.11$ and 0.10 for the SDSS catalogues.

but, at fainter magnitudes than those covered by the SDSS and 2dF surveys, such a model predicts a tail of high redshift galaxies that is not seen in deep spectroscopic galaxy samples (eg. Colless et al. 1990). Thus, a more complicated form of evolution is required, either one in which different galaxies evolve at different rates or one in which galaxies merge so that their number is not conserved. The new redshift surveys themselves will give important information on evolution of the galaxy luminosity function. However, for the purposes of quantifying large structure this is not a problem provided that the selection function can be accurately determined. We have therefore adopted a simple model that produces a selection function with similar depth to that which we expect the surveys to have.

In our standard model we adopt the parameters found by Loveday et al. (1992) for the APM-Stromlo bright galaxy survey:

$$M^{\star}_{b_J} - 5\log_{10} h = -19.5 \ ,$$

$$\alpha_{\star} = -0.97 \ ,$$

$$\phi_{\star} = 1.4 \times 10^{-2} h^3 \mathrm{Mpc}^{-3} \ .$$

We also set $\mathrm{k} + \mathrm{e} = 0$, ie. we assume that strong luminosity evolution occurs, cancelling the k-correction. While this cancellation seems coincidental, figure 4.6 shows that this simple choice gives reasonable agreement with the observed galaxy number counts at $B_J \approx 19.5$ and so will produce mock galaxy catalogues with approximately the number of galaxies expected in the 2dF survey.

As a variation, we have also produced a selection of mock catalogues in which the artificial assumption that $\mathrm{k} + \mathrm{e} = 0$ has been dropped. For these we use the evolution law $\mathrm{k} + \mathrm{e} = 2.5\log_{10}(1+z)$, which corresponds to weaker luminosity evolution than in our standard model. To compensate for this we increase the value of $\phi_{\star}$ by 24% to keep the total number of galaxies in the survey approximately the same as in our standard model. This model's galaxy counts and redshift distributions (for the case of $\Omega_0 = 1$) are shown by the dashed lines in figures 4.6 and 4.7.

More recent observational data now exists concerning the faint end of the luminosity function. The ESO slice project, a redshift survey of three thousand galaxies with magnitude limit $b_J = 19.4$, find a steeper function, parameterized by $\alpha_{\star} = -1.22$ (Zucca et al. 1997). This would result in more objects at lower redshift, and a lower median redshift for the surveys.

4.5.3 Survey construction

The task of generating a mock galaxy catalogue now consists of two steps: choosing the location of the observer, and selecting galaxies subject to the geometrical constraints and radial selection function specified above.

To aid in the comparison between the different cosmological models, we choose to place the observer at the same position in each of the galaxy catalogues. The observer's position was essentially chosen at random, although we did apply the weak constraint that the velocity dispersion of particles within $5h^{-1}\,\mathrm{Mpc}$ of the observer should be less than $350\mathrm{km\,s}^{-1}$ in the $\Omega = 1$ model, in order to avoid observers placed in rich galaxy clusters.

This constraint was only directly applied in model E3S, but by virtue of the fact that all the simulations have the same phases it is effectively satisfied in all the structure normalized models. However, for the *COBE* normalized simulations that have σ_8 greater than that required to match the observed abundance of rich clusters, the galaxy velocity dispersion is typically higher, and the constraint may be violated. For most analyses of the 2dF and Sloan surveys the choice of the observer should not be important, as the volumes of the surveys are large compared to the local region whose properties are constrained by the choice of observer.

Having chosen the observer's location, we replicate the periodic cube of the *N*-body simulation around the observer to reach a depth of $z = 0.5$. We choose the same position for the observer in both the 2dF and SDSS surveys, but the relative orientations were not chosen to be consistent with the true angular positions of the two surveys. We then loop over all the galaxies within the geometrical boundaries of the survey. From the model luminosity function and cosmology we compute the expected mean number density $\bar{n}_{\rm s}(r)$ of galaxies brighter than the survey magnitude limit at the distance r of each of these galaxies. We then select the galaxy zero, one or more times according to a Poisson distribution with mean $\bar{n}_{\rm s}(r)/\bar{n}_{\rm g}$, where $\bar{n}_{\rm g}$ is the mean galaxy number density in the biased galaxy distribution described in section 4.4. In this process, approximately 1% of the galaxies are selected more than once and appear with identical positions and velocities in the mock catalogue. This double sampling essentially never occurs at $z > 0.02$, where the selection function drops to a space density less than $n_{\rm g}$. For each selected galaxy we generate an apparent $b_{\rm J}$ magnitude consistent with the selection function, and also a value of $z_{\rm max}$, defined as the redshift corresponding to the maximum distance at which the younger counterpart of the galaxy would still be brighter than the survey apparent magnitude limit. In computing this redshift we include the effect of both the k-correction and evolution on the galaxy's luminosity. As our idealized models assume that galaxy mergers do not take place, this definition of $z_{\rm max}$ makes it easy to construct volume limited catalogues in which the mean galaxy density is independent of redshift. For the genuine surveys, removing the effect of evolution from the radial dependence of the galaxy density field will be more problematic; evolutionary corrections for each galaxy will be uncertain, and, even over the limited redshift range probed by these surveys, galaxy merging may also play a small role. In our catalogues we record the galaxy redshift, its angular coordinates, the redshift it would have if it had no peculiar velocity, its

apparent b_J magnitude, and z_{max}. We also record an index that can be used to identify the particle to which it corresponded in the original *N*-body simulation. These records are explained in detail in section 4.8.

4.5.4 Adding long wavelength power

For a subset of simulations we have applied a technique that allows the spectrum of density fluctuations present in the final galaxy catalogues to be extended to wavelengths longer than those included in the original *N*-body simulation. This method, dubbed the Mode Adding Procedure (MAP), was proposed by Tormen & Bertschinger (1996) and discussed further by Cole (1997). Essentially, one uses the Zel'dovich approximation with a change of sign to remove from the initial *N*-body particle distribution the displacements caused by the longest wavelength modes in the original simulation. This procedure is accurate if the modes in question are still in the linear regime. One then generates a new large scale density field in a much larger box, which samples this same region of k-space more finely. Displacements are computed by the Zel'dovich approximation from this new field and used to perturb both the original simulation cube and the adjacent replicas. The displacements applied to each of the replicas differ, as the new large scale density field is not periodic on the scale of the original simulation cube. We choose to remove the inner 5^3 modes from the original simulations and generate the large scale density field in a box with edge seven times that of the original simulation ($N_S = 2$ and $L/S = 7$ in the notation of Cole 1997).

As pointed out by Cole (1997), the biasing algorithm must take account of the effect of the added long wavelength power. This is most easily done for algorithms such as model 1, which are a function of the initial linear density field. One simply replaces the original linear density field by a new one constructed by removing the original long wavelength power and adding the new large scale density field. It is more complicated to correctly apply a biasing algorithm that is a function of the final density field, because the final density field is non-linear, and its short wavelength modes are coupled to the linear long wavelength modes. With this in mind, we applied the MAP only in combination with bias model 1. In order to keep computer storage requirements within reasonable bounds, it is necessary to combine into a single program the application of the MAP, the biasing prescription, and the survey selection criteria.

4.5.5 Inventory

For each of the cosmological simulations listed in table 4.1 (21, including the second realization of model E3S), we have created mock SDSS and 2dF surveys using bias model 1 and the standard selection function, in which the evolution and k-corrections cancel. The MAP was not used to add long wavelength power to these catalogues. For four structure-normalized cosmological simulations (the open $\Omega_0 = 0.4$ model (O4S), the flat $\Omega_0 = 0.3$ (L3S), and the A and B realizations of the Einstein-de Sitter model (E3S)) we constructed a number of variants: changing the bias model to models 2, 3, 4, 5, 6, and 7; without bias; using the variation of the selection function described in section 4.5.2, in which luminosity evolution is weaker than the k-corrections; and using bias model 1 with long wavelength power added using the MAP.

4.6 Illustrations

We now compare and contrast the visual properties of the galaxy distributions in each of the mock catalogues using a series of redshift space wedge diagrams.

Figures 4.8 and 4.9 show the galaxy distribution in redshift space slices extracted from the mock 2dF and SDSS catalogues constructed from the cluster-normalized *N*-body simulations. Each of the catalogues was biased using model 1 of section 4.4. The 2dF slices (figure 4.8) are $90°$ wide in RA, $3°$ thick in declination and plotted out to a redshift of $z = 0.3$. By contrast, the SDSS slices (figure 4.9), which are $130°$ wide (corresponding to the full length of the long axis of the SDSS ellipse) are $6°$ thick but plotted only to $z = 0.2$. A visual inspection reveals that the structure in all six models looks remarkably similar. This is essentially a reflection of the facts that all the simulations were started with the same phases and that the observer is alway located at the same position. Also, because these models are designed to produce similar abundances of rich galaxy clusters, the strength of the "fingers-of-god" effect is also similar. The 1-dimensional galaxy velocity dispersions in all the cluster-normalized models is in the range 440-$465 \mathrm{km\,s^{-1}}$. The visible effects on the galaxy distribution that result from varying Ω_0, Λ_0, and the amount of large scale power (Γ) are quite subtle. Of the two $\Omega_0 = 1$ models, E3S (τCDM) has more large scale power than E4 (SCDM). A manifestation of this is that structure in E3S (τCDM) appears more connected and less choppy than that of E4 (SCDM). The changes that

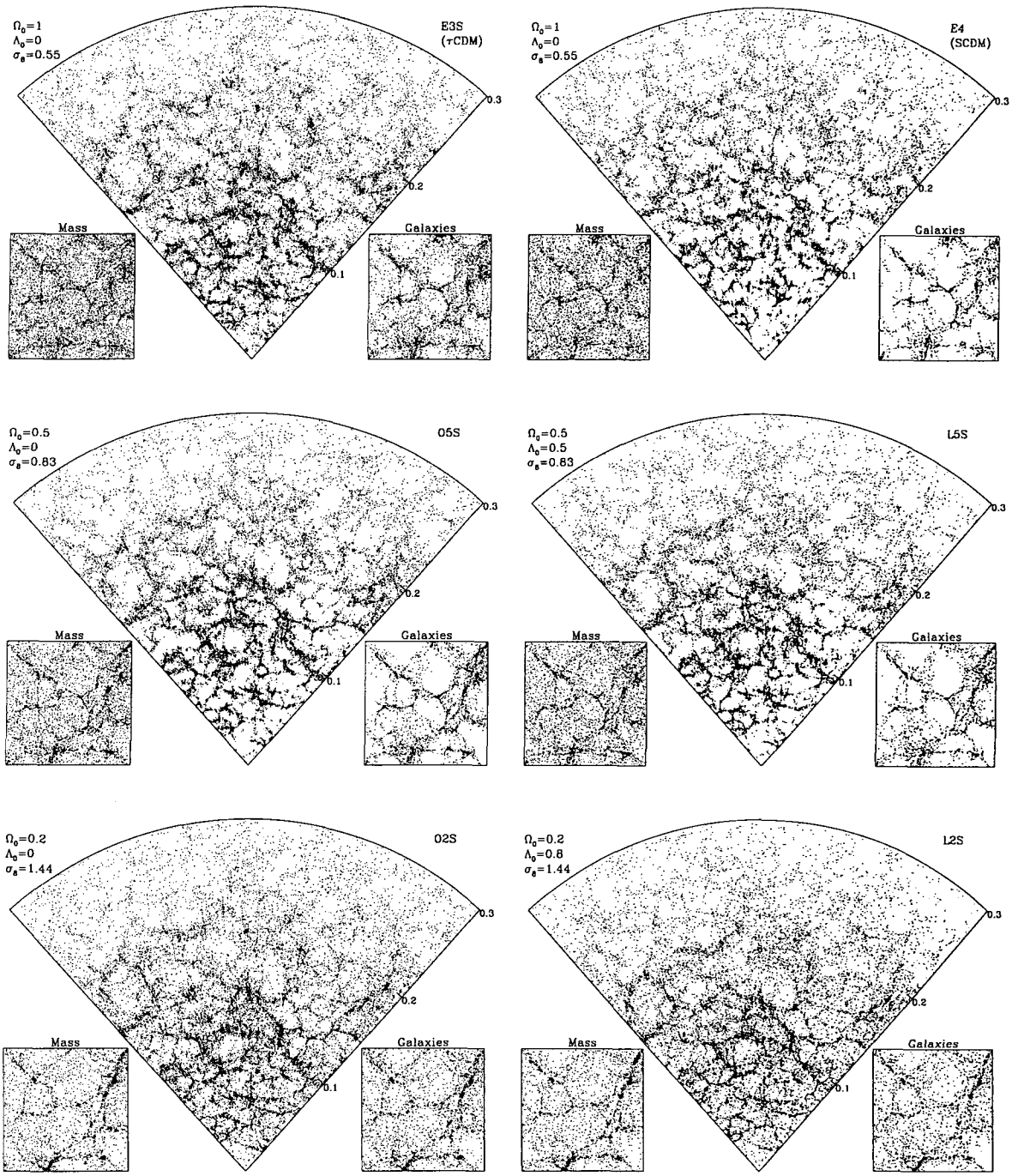

Figure 4.8: Redshift space slices showing galaxy positions from a variety of the mock 2dF galaxy catalogues. Each wedge shows a strip $90°$ wide in R.A. and $3°$ thick in declination, extending to $z = 0.3$. Each of the six models shown is normalized by the present abundance of galaxy clusters and biased using model 1 (see section 4.4). The inset square panels illustrate the effect of bias by showing the real space particle and galaxy distributions in a $100 \times 100 \times 20h^{-1}\,\mathrm{Mpc}$ slab. The top panels show $\Omega_0 = 1$ models: E3S (τCDM) on the left and E4 (SCDM) on the right. Below these are the open and flat $\Omega_0 = 0.5$ models, O5S and L5S, and, at the bottom, the open and flat $\Omega_0 = 0.2$ models, O2S and L2S.

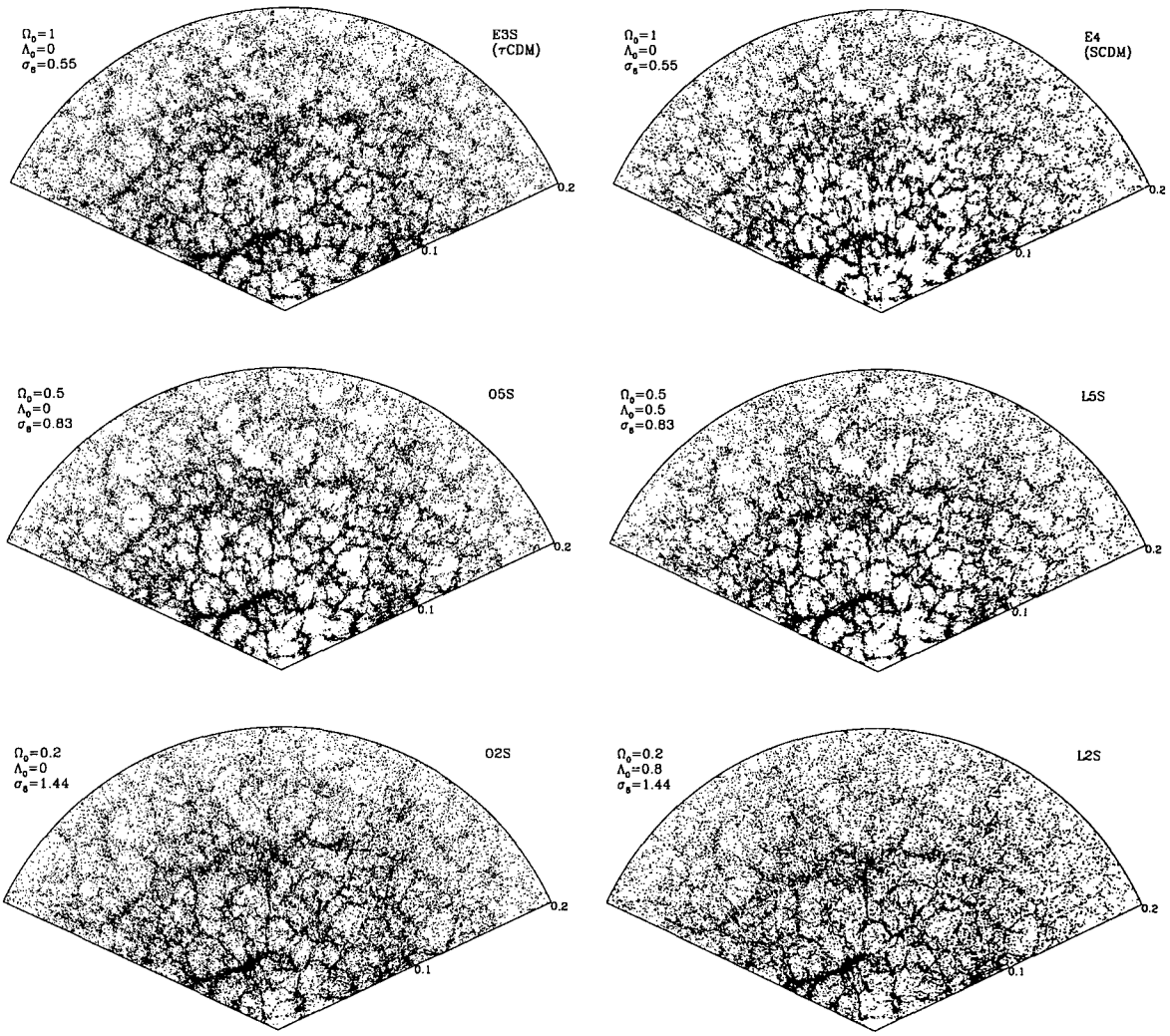

Figure 4.9: Redshift space slices from the cluster normalized mock SDSS catalogues. The correspondence between model and panel is the same as for figure 4.8. The slices are $130°$ wide by $6°$ thick and extend to $z = 0.2$. The qualitative differences between the structure visible in these slices and in the corresponding 2dF slices of figure 4.8 are due to the choice of slice thickness and depth rather than any intrinsic difference in the 2dF and SDSS selection functions.

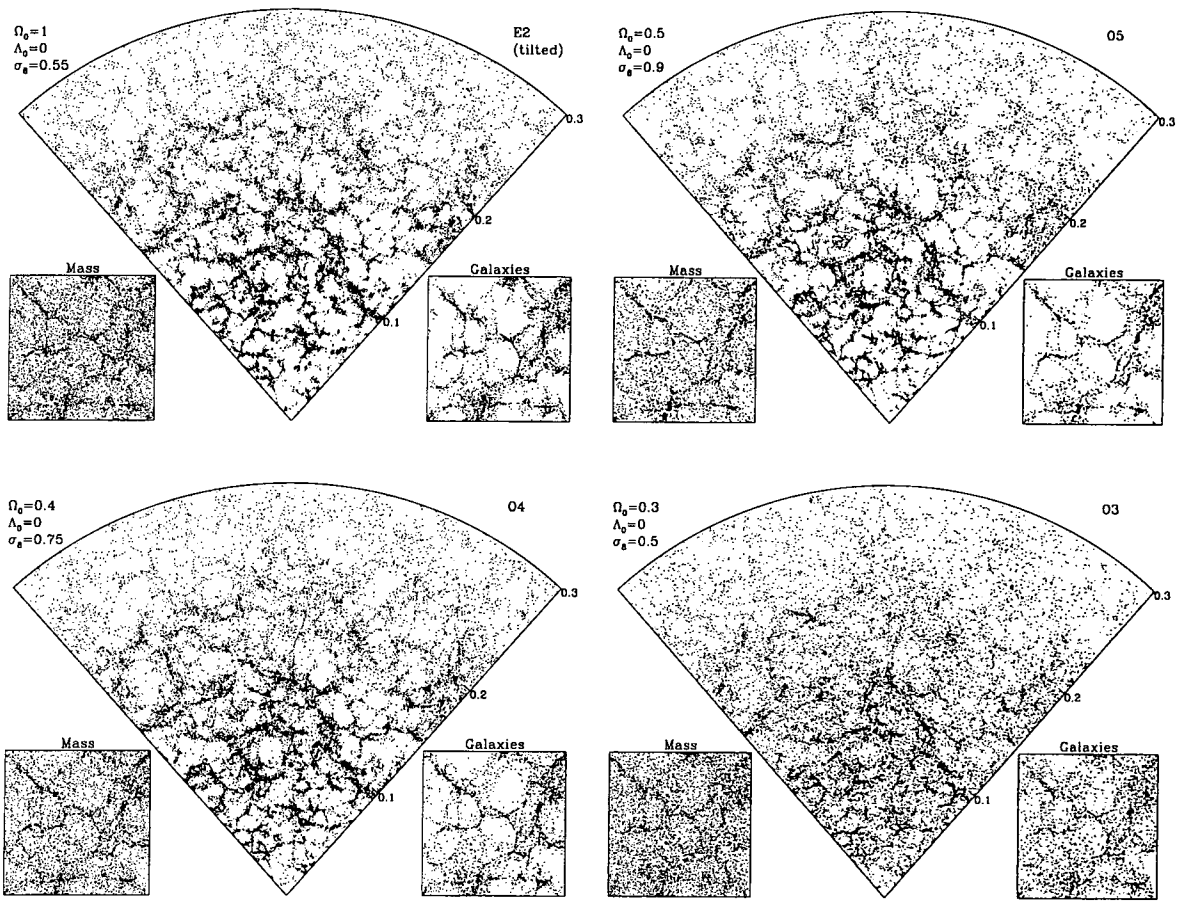

Figure 4.10: Redshift space slices from the mock 2dF catalogues for the tilted CDM model E2 (top left) and the open *COBE* normalized models, O5, O4, and O3. The corresponding value of Ω_0 and the normalization σ_8 are indicated on each panel. The geometry of the slices and inset plots of the real space mass and galaxy distributions is the same as in figure 4.8.

occur when Ω_0 is varied are related to the strength of galaxy biasing. For models that are normalized to produce the observed abundance of rich clusters, the amplitude of mass fluctuations, σ_8, increases as Ω_0 is decreased. Thus, the $\Omega_0 = 1$ models require a strong bias, the $\Omega_0 = 0.5$ models a weak bias, and the $\Omega_0 = 0.2$ models an anti-bias. The effect of this can be seen most clearly in the inset square panels of figure 4.8. These show, in real space, a $100 \times 100 \times 20h^{-1}\,\mathrm{Mpc}$ slab of the mass and corresponding galaxy distribution, both sampled to the same density of $\bar{n}_g \approx 0.05h^3\mathrm{Mpc}^{-3}$. In the $\Omega_0 \geq 0.5$ models, the biasing algorithm clearly has the effect of mapping underdense regions in the mass distribution to completely empty voids in the galaxy distribution. In the anti-biased, $\Omega_0 = 0.2$ models, galaxies continue to trace the mass in the underdense regions. Finally,

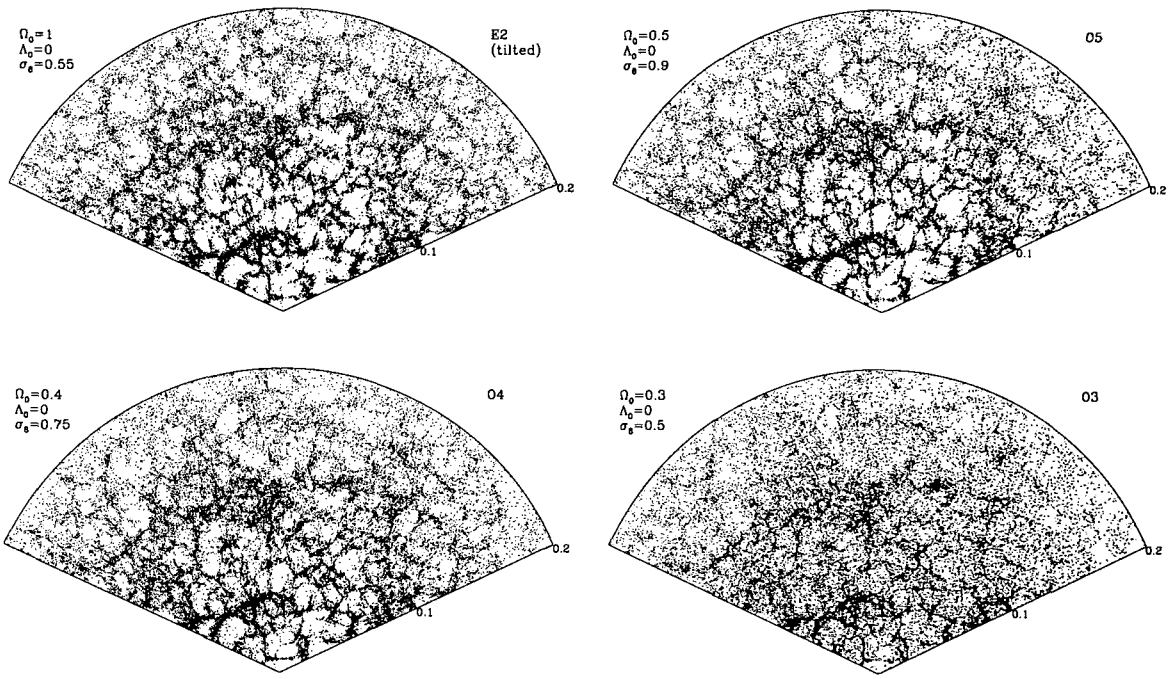

Figure 4.11: Redshift space slices from the mock SDSS catalogues for the same models as figure 4.10, the tilted CDM model E2 and the open *COBE* normalized models, O5, O4, and O3. The geometry of the slices is the same as in figure 4.9.

comparison of the open and flat models indicates that the value of the cosmological constant, Λ_0, has virtually no detectable effect on the galaxy distribution.

Figures 4.10 and 4.11 show redshift space slices with the same geometry as those of figures 4.8 and 4.9. The top left hand panels in each figure show the tilted $\Omega_0 = 1$ model, E2, which by virtue of the tilt is both cluster and *COBE* normalized. These distributions should be compared with those in the upper panels of figures 4.8 and 4.9, which show corresponding slices for our other two cluster normalized, $\Omega_0 = 1$ models. The tilted (E2) model appears intermediate in character between the τCDM (E3S) and SCDM (E4) models. This is consistent with the relative amounts of power on scales of $50\text{-}100h^{-1}$ Mpc in these models. The tilt ($n \approx 0.8$, $\Gamma \approx 0.45$) produces more power on these scales than in SCDM ($n = 1$, $\Gamma = 0.5$), but less than τCDM ($n = 1$, $\Gamma = 0.25$). The remaining three panels in figures 4.10 and 4.11 are for the open ($\Lambda_0 = 0$) *COBE* normalized models. In this sequence, as Ω_0 is decreased σ_8 decreases, the bias increases, and Γ decreases. The most visible effect comes from the variation of σ_8. There is a clear trend such that the mass distribution looks more evolved, with more crisply defined filaments and voids,

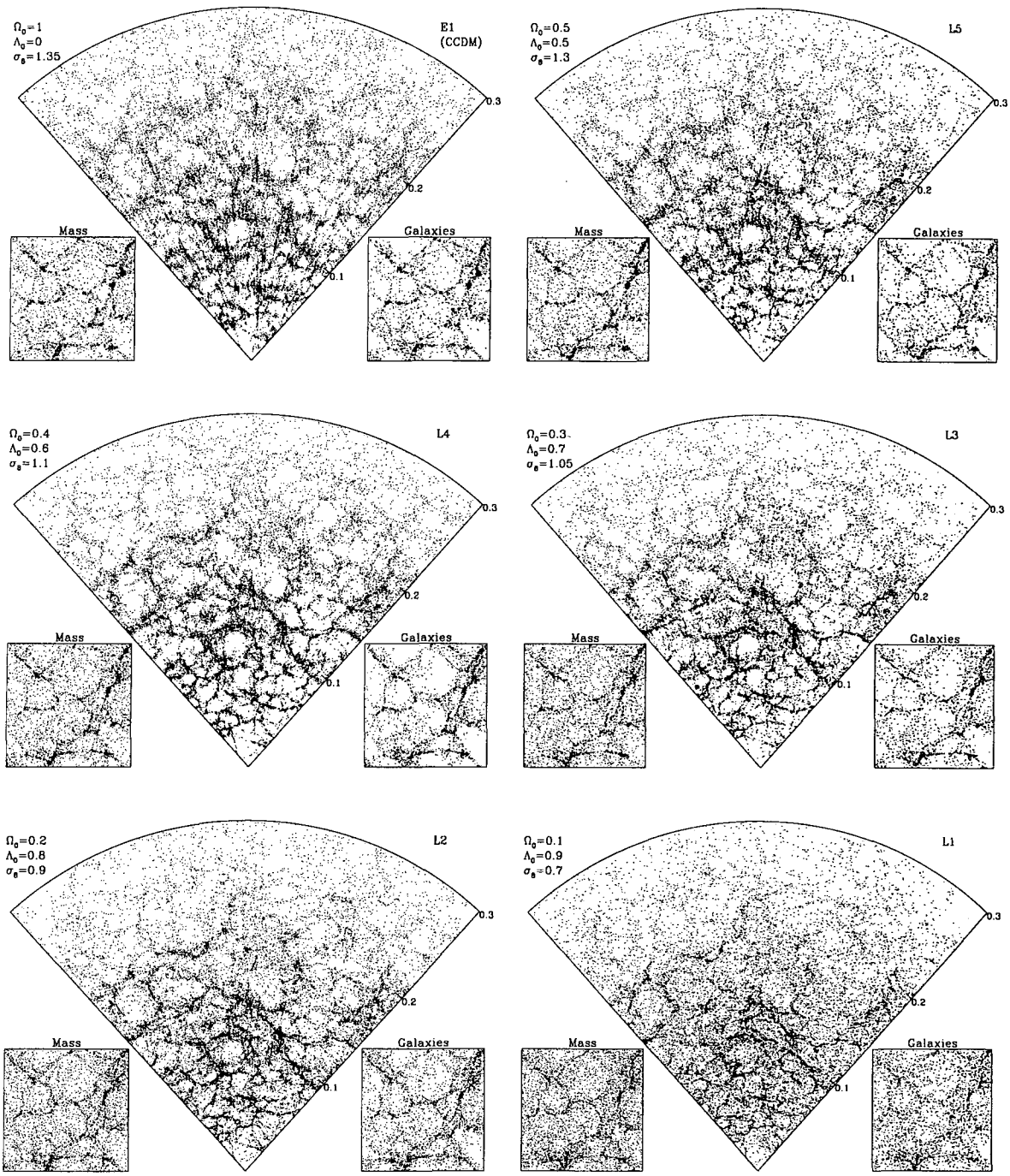

Figure 4.12: Redshift space slices from the mock 2dF catalogues for the flat *COBE* normalized models, E1 (CCDM), L1, L2, L3, L4, and L5. The corresponding values of Ω_0, Λ_0 and the normalization, σ_8, are indicated on each panel. The geometry of the slices and inset plots of the real space mass and galaxy distributions are the same as in figure 4.8.

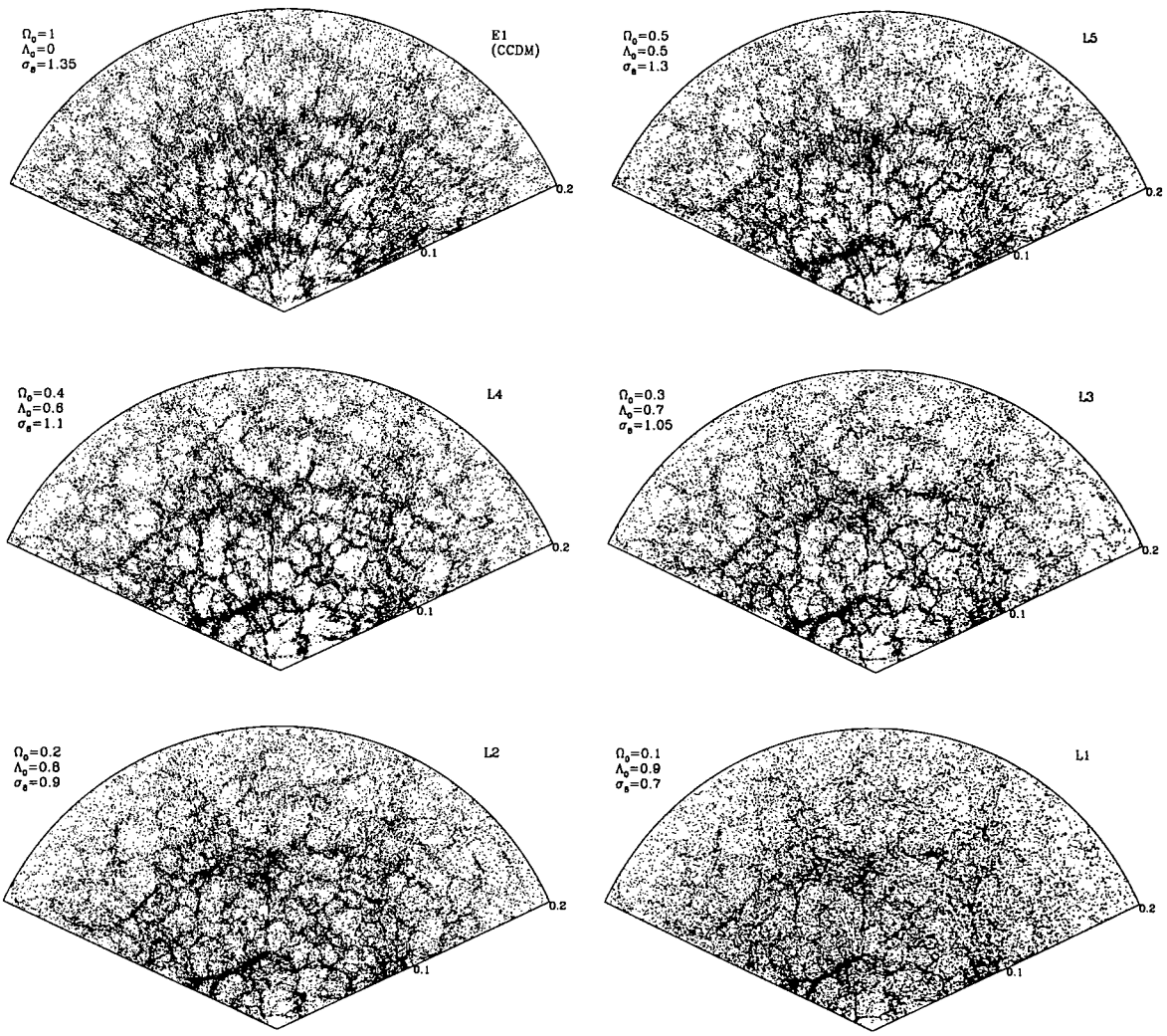

Figure 4.13: Redshift space slices from the mock SDSS catalogues for the same models as figure 4.12, the flat *COBE* normalized models, E1 (CCDM), L1, L2, L3, L4, and L5. The geometry of the slices is the same as in figure 4.9.

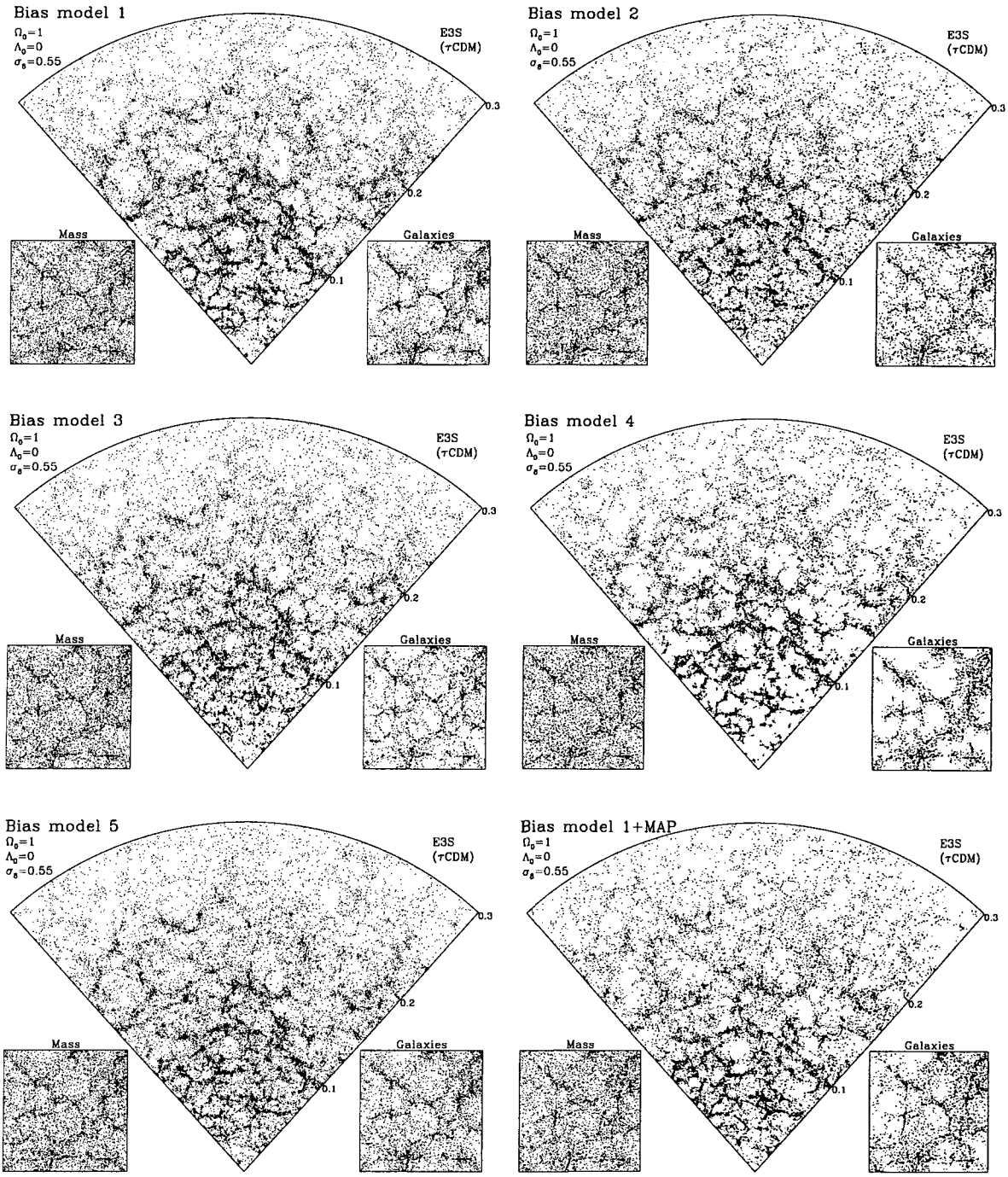

Figure 4.14: Redshift space slices from the mock 2dF catalogues showing the effect of varying the choice of biasing algorithm. Each slice was constructed from the same cosmological model E3S (τCDM), but with a variety of biasing algorithms as indicated on each panel. The panel at the bottom right shows the effect of using the MAP in conjunction with bias model 1 to add long wavelength power to the mock catalogue. The geometry of the slices and inset plots of the real space mass and galaxy distributions are the same as in figure 4.8.

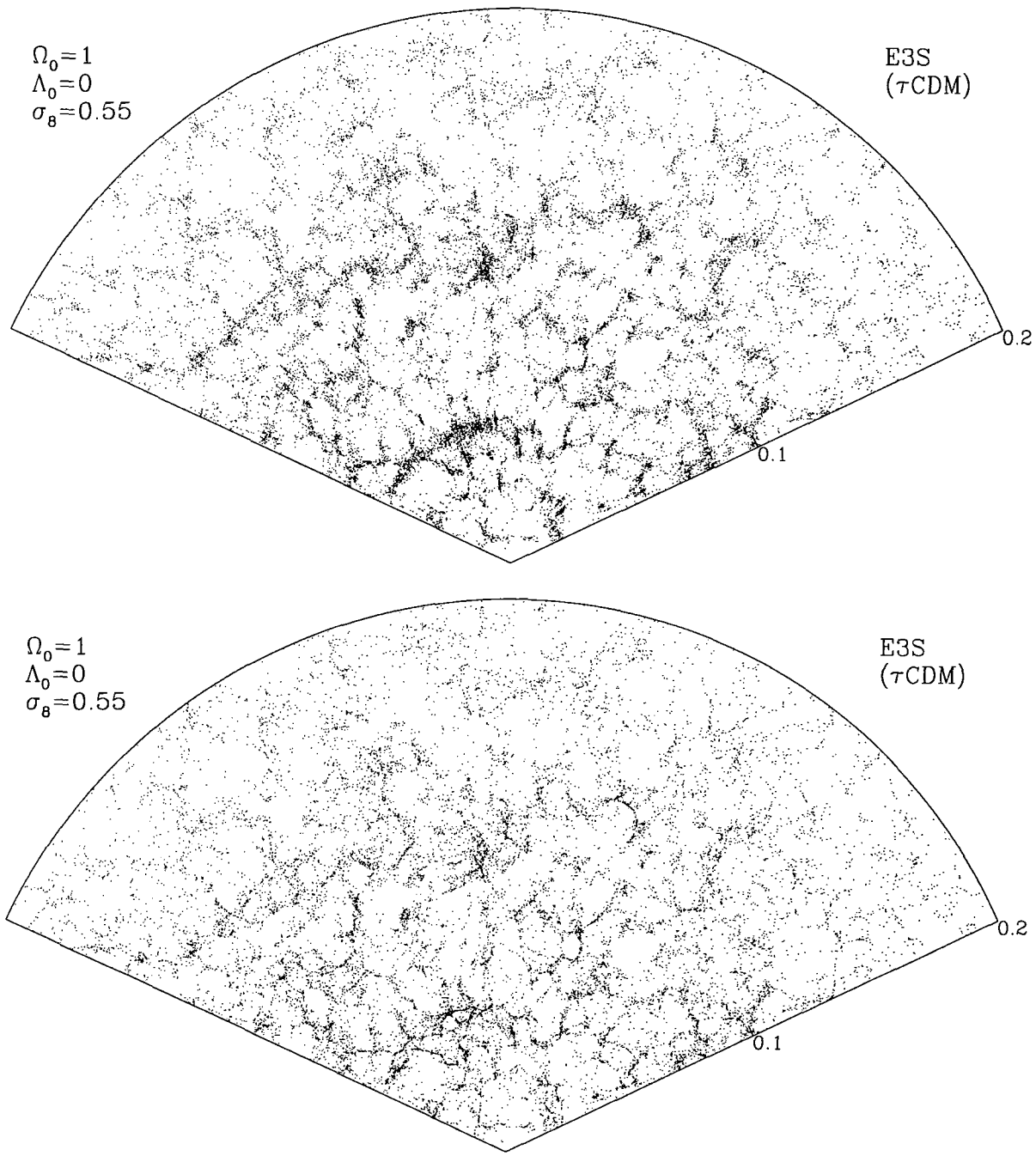

Figure 4.15: A comparison of the galaxy distribution in redshift space (upper panel) and real space (lower panel) for a 2° thick slice from a SDSS mock catalogue constructed from model E3S (τCDM).

as σ_8 is increased. This trend is also visible in the galaxy distribution, but here the bias partially compensates for the changing σ_8, and the relationship appears weaker. On small scales the effect of the random velocities within galaxy clusters is just discernible. The "fingers-of-god" are largest in the $\Omega_0 = 0.5$ in which the galaxies have a mean 1-dimensional velocity dispersion of $485\mathrm{km\,s^{-1}}$ compared to only $225\mathrm{km\,s^{-1}}$ in the $\Omega_0 = 0.3$ model. Although these velocity dispersion are appealingly small in comparison to the structure normalized simulations, we stress that this is achieved only at the expense of a low amplitude of mass fluctuations, resulting in an underprediction of the density of rich clusters.

Figures 4.12 and 4.13 show 2dF and SDSS redshift space slices for the set of *COBE* normalized, flat ($\Omega_0 + \Lambda_0 = 1$) models. For this sequence of models, σ_8 decreases weakly as Ω_0 decreases. Thus we see a weaker version of the same trend we noted in the open *COBE* normalized models. The higher Ω_0 models have a more evolved density distribution with more sharply defined voids and filaments. Also there is a similar trend in the galaxy velocity dispersion and the resulting "finger-of-god" features. The one-dimensional velocity dispersion is $200\mathrm{km\,s^{-1}}$ for $\Omega_0 = 0.1$ and climbs to $665\mathrm{km\,s^{-1}}$ for $\Omega_0 = 0.5$. The 'fingers-of-god" are extremely pronounced in the $\Omega_0 = 1$ model, which has a one-dimensional velocity dispersion of $890\mathrm{km\,s^{-1}}$.

Figure 4.14 shows 2dF redshift space slices illustrating the effect of varying the choice of biasing algorithm. Each slice was constructed from the same cosmological model E3S (τCDM), but with a variety of biasing algorithms as indicated on each panel. The correlation functions of each of these galaxy distributions, shown in figure 4.3, are quite similar. Despite this some of the distributions are visually quite distinct. The most striking feature is variation in the size and number of voids. The voids are largest and most numerous in bias model 4 as a result of its sharp density threshold. The models in which the bias is a more gradual function of density, such as the power law case of model 5, have far fewer voids. The panel at the bottom right shows the effect of using the MAP in conjunction with bias model 1 to add long wavelength power to the mock catalogue. The distortion of the small scale galaxy distribution is small as the perturbations are of very long wavelength, but their effect on measurements of large scale power can be appreciable.

Figure 4.15 contrasts the galaxy distribution in redshift space (upper panel) with what would be observed if true distances rather than redshifts were measurable (lower panel). The model that has been plotted here is the E3S (τCDM) model with galaxies selected using bias model 1. The thickness of the slice is just $2°$.

4.7 Limitations

We plan to use the mock catalogues presented in this chapter to help in the important task of testing and calibrating the algorithms and statistics that will be applied to the analysis of the 2dF and SDSS redshift surveys. We hope that they will be similarly useful to other researchers. However, it is important to be aware of the limitations of these catalogues.

- **Cosmetic problems.** The mock catalogues are idealized and do not suffer from certain problems that, at some level, are inevitable in the genuine surveys. These include systematic errors in the photometry used to select the target galaxies, cosmetic defects such as regions cut out around bright foreground stars, failure to measure redshifts for 100% of the target galaxies, redshift measurement errors, and the residual effects of extinction by foreground dust.

- **Selection functions.** The model selection functions are simplistic and do not allow for the effects of galaxy mergers. It will only become possible to adequately constrain evolution models that incorporate galaxy merging once the joint apparent magnitude-redshift distributions are accurately measured from the surveys themselves. Furthermore, we have not attempted to mimic the details of the SDSS target selection criteria, although we expect that the selection function of the SDSS will not differ substantially from that implied by the $b_{\rm J}$-magnitude limited criterion that we have used.

- **Clustering evolution.** Evolution of clustering over the redshift range of the surveys is ignored – each of the mock catalogues is constructed from a single output time from the *N*-body simulations. Clustering evolution is probably very weak over the depth of the SDSS and 2dF surveys but it may not be negligible for deeper surveys and will be important for some applications (eg. Nakamura, Matsubara, & Suto 1998). For many models it is found (Bagla 1998) that clustering evolution is partially cancelled out by evolution of the bias factor, and the assumption of no net evolution is valid out to quite high redshifts.

- **General relativity**. The *N*-body simulations solve the equations describing Newtonian gravity and therefore explicitly ignore space curvature across the simulation box. One consequence of this is that in the open models we are forced to use $4\pi r_c^2 dr_c$, where r_c is the comoving distance to redshift z, as the volume element rather than the correct relativistic expression. However, for the depth of the present surveys this is a very small effect.

- **Resolution**. The simulations have limited mass and force resolution. The spatial resolution in the initial conditions is limited to scales greater than the mean particle separation of $1.8h^{-1}\,\mathrm{Mpc}$. However, the power on these scales in the final configuration is dominated by non-linear transfer from large scales. Thus, the range of reliability of the estimated correlation functions and power spectra is determined by the force resolution, $\epsilon = 90h^{-1}\,\mathrm{kpc}$ (comoving), and the particle mass, $m_\mathrm{p} = 1.64 \times 10^{12}\Omega_0 \mathrm{h}^{-1}\mathrm{M}_\odot$. The smallest structures that are resolved are galaxy groups and clusters.

- **Mode sampling**. Because of the finite size of the *N*-body simulation volume, k-space is coarsely sampled and, in the absence of the MAP extension, the catalogues have no power in wavelengths $\lambda > 345.6h^{-1}\,\mathrm{Mpc}$. Since the depth of the surveys is comparable to the size of the *N*-body simulations, the coarse sampling could be problematic if one were to estimate the power spectrum from the mock catalogues using a high resolution estimator at values of $\mathbf{k}$ that do not match modes in the original simulation. There should be no problems for clustering statistics, such as the correlation function, which contain contributions from a broad range of wavenumbers.

- **MAP**. The application of the MAP extends the power coverage in the mock catalogues to wavelengths as large as $\lambda = 2420h^{-1}\,\mathrm{Mpc}$ and improves the sampling of k-space at low spatial frequencies ($k \lesssim 4\pi/L_\mathrm{BOX}$), but the sampling of k-space remains coarse at larger wavenumbers. Also, the MAP slightly modulates the frequencies of the existing high-k modes, with the result that although the power in this regime is still peaked around the modes present in the original simulation, some power is distributed to neighbouring values of k. Thus, narrow band estimates of the power spectrum at high frequency may still be slightly affected.

- **Velocity bias**. The mock catalogues assume galaxies trace the velocity field of the dark matter and thus that there is no velocity bias in the sense discussed, for example, by Carlberg, Couchman, & Thomas (1990).

- **Galaxy bias**. The adopted models of spatial bias are at best simplifications of the complex physics of galaxy formation. Since reliable *a priori* predictions of bias are not possible with current simulation techniques, we have given each of our adopted cosmological models a "good chance" by choosing bias parameters that force-fit the amplitude and (to the extent possible) the shape of the observed galaxy correlation function. Our logic is that if the cosmological model in question is to be consistent with current galaxy clustering data, then the "true" description of galaxy formation must somehow achieve the same thing that our biasing prescription does. In selected cases we have produced multiple mock catalogues with a variety of biasing algorithms, so that the sensitivity of methods to the details of biasing can be investigated.

4.8 Instruction manual

Each mock catalogue can be downloaded from our WWW site,
`http://star-www.dur.ac.uk/~sjh/mocks/main.html`

Included in these web-pages is a detailed description of the catalogue file format. Each of the SDSS catalogue files occupies 24 Mbytes. The smaller 2dF SGP and NGP catalogues occupy 5.4 and 2.7 Mbytes respectively. For each catalogue file there is an associated selection function file that tabulates the expected number of galaxies and the number density of galaxies as a function of redshift for each model. We have also made available a number of Fortran subroutines. The first can be used to read the mock catalogue files. A second reads one of the tabulated selection functions and can be used to used to generate random galaxy positions consistent with the survey radial selection function and geometric boundaries.

The main catalogue files list seven properties for each catalogued galaxy:

- x, y, z. The first three are Cartesian redshift coordinates, ie. the galaxy redshift is given by $z_{\rm gal} = (x^2 + y^2 + z^2)^{1/2}$, and two angular coordinates are defined by the relations $\sin\theta = z/z_{\rm gal}$ and $\tan\phi = y/x$. For the 2dF catalogues these angles are simply the declination, $\delta = \theta$, and Right Ascension, $\mathrm{R.A.} = \phi$. In the case of the SDSS they instead give a latitude, θ, and longitude, ϕ, relative to a pole at the centre of the SDSS survey region and with respect to the major axis of the SDSS ellipse. We

provide subroutines to convert between these two co-ordinate systems, and also to and from galactic co-ordinates.

- $z_{\rm rest}$. The quantity $z_{\rm rest}$ is the redshift the galaxy would have if it had no peculiar motion and was just moving with the uniform Hubble flow. The redshift space coordinates can thus be converted to real space coordinates by simply scaling each component by the ratio $z_{\rm rest}/z_{\rm gal}$.

- $b_{\rm J}$. The galaxy's apparent magnitude is given by the fifth co-ordinate, $b_{\rm J}$.

- $z_{\rm max}$ The maximum redshift at which the galaxy would enter into the catalogue taking account of the k-correction and luminosity evolution is $z_{\rm max}$. Thus selecting galaxies with both $z_{\rm rest} < z_{\rm cut}$ and $z_{\rm max} > z_{\rm cut}$ will produce a volume limited catalogue to redshift $z_{\rm cut}$. Note that such volume limited catalogues will have a mean comoving number density of galaxies that is independent of redshift. This occurs in our idealized models because we have assumed that galaxy merging can be ignored over the limited redshift range probed by the surveys and because we have included both the k-correction and evolutionary correction in our definition of $z_{\rm max}$.

- $i_{\rm ident}$. Finally, we give the integer, $i_{\rm ident}$, which is simply an index that relates the galaxy to a particle in the original *N*-body simulation.

4.9 Discussion

We have constructed, and made publicly available, a set of mock galaxy catalogues, constructed from *N*-body simulations, having the geometry and selection function appropriate to the forthcoming SDSS and 2dF redshift surveys. Our main intention has been to generate an extensive and flexible suite of artificial datasets that may be used to develop, test, and fine-tune statistical tools intended for the analysis of the real surveys and, eventually, for testing the real data against theoretical predictions. To this purpose we have generated mock surveys from simulations with a range of cosmological parameters and made a variety of (biasing) assumptions for extracting galaxies from the *N*-body simulations.

Our mock catalogues are restricted to CDM cosmologies with Gaussian initial fluctuations, but with a range of values for the cosmological parameters Ω_0, Λ, H_0, Γ, etc.

It will be interesting in future to extend this kind of work to other cosmological models, particularly models that do not assume Gaussian initial fluctuations. At present it remains somewhat unclear which non-Gaussian models will be the most profitable to investigate. In the CDM simulations, the fluctuation amplitude is set in two alternative ways: by matching the amplitude of cosmic microwave background fluctuations as measured by *COBE* (and extrapolated to smaller scales according to standard assumptions) or by matching the observed abundance of rich galaxy clusters. One of the models (tilted $\Omega_0 = 1$) is deliberately constructed so as to match both of these constraints while two others (open $\Omega_0 = 0.4$ and flat $\Omega_0 = 0.3$) come close to doing so in their own right. Although our suite of twenty models does not fully span this multi-dimensional parameter space, it does include many of the cosmological models currently regarded as acceptable.

We have implemented a variety of biasing prescriptions, all of which are designed to reproduce approximately the known APM galaxy correlation function over a limited range of scales. Alternative biasing schemes provide a testing ground for the statistics that attempt to infer properties of the mass from the measured properties of the galaxies, so that we can study how robust they are to the precise details of the bias.

In the absence of reliable theoretical predictions for the formation sites of galaxies, we have taken the pragmatic approach of using simple formulae, with one or two adjustable parameters, to characterise the probability that a galaxy has formed in a region where the density field has a given value. We have considered both Lagrangian and Eulerian schemes in which the galaxies are identified in the initial and final density fields respectively. The majority of our models contain "local biasing" where the probability depends solely on the value of the field smoothed in the local neighbourhood of a point. We also consider one example of a non-local biasing prescriptions, a variant of the cooperative galaxy formation model of Bower et al. (1993).

Over the range of scales adequately modelled by our *N*-body simulations ($\sim$ 1-$10h^{-1}\,\mathrm{Mpc}$), our two-parameter biased galaxy distributions match the APM data remarkably well in almost all the cosmological models we have considered, including those in which an anti-bias is required on small scales. In some cases, a one-parameter model suffices to obtain acceptable results. In all cases the bias in the galaxy distribution is scale-dependent, even over the relatively narrow range of scales covered in the simulations. As discussed by Jenkins et al. (1998), scale-dependent biasing is a requirement

of all viable CDM models, and it is encouraging that simple heuristic models that depend only on local density can achieve this, albeit over a limited range of scales. When using our mock catalogues it is important to bear in mind that while the locations of the galaxies are biased, the velocities are not; galaxies are assumed to share the velocity distribution of the associated dark matter.

A number of extensions of this work are possible. One that we have already implemented but not discussed in this chapter is the construction of mock catalogues with the properties of other surveys, particularly surveys of *IRAS* galaxies like the 1.2 Jy (Strauss et al. 1990) and the PSCz (Saunders et al. 1994). Mock catalogues of the latter are already available at the same web address as our 2dF and SDSS mock catalogues. There are several ways in which our catalogues could be improved to overcome at least some of the limitations discussed in section 4.5. For example, better *N*-body simulations are certainly possible with current technology. Larger simulations would be particularly advantageous, since the size of those we have used here is comparable to the depth of the real surveys. The 1-billion particle "Hubble Volume" simulation of a 2 Gigaparsec CDM volume recently carried out by the Virgo consortium (Evrard et al. in preparation) will certainly be large enough, and we plan to extract mock catalogues from it shortly. An interesting aspect of this simulation is that data are output along a light cone and so the evolution of clustering with look-back time can be incorporated into the mock catalogues. Clustering evolution is expected to be negligible in the main 2dF and SDSS surveys, but it will be important in the proposed faint extensions of these surveys and to QSO surveys.

A further improvement would be to construct ensembles of mock catalogues from independent simulations of each cosmological volume. These would help quantify the cosmic variance expected in the real surveys. As we discussed in section 4.4, sampling effects are still appreciable on large scales even with the huge volumes that will be surveyed with the 2dF and SDSS data. In fact, the fundamental mode in our simulations had a noticeable stochastic downward fluctuation that can confuse the comparison with data on large scales. Although this sort of effect can be quantified analytically to some extent, simulations are useful in order to check for the effects of biasing. For the case of the τCDM model, E3S, we have done this already with ten independent realizations. Finally, within a given *N*-body simulation, there are already better ways of identifying galaxies than the simple heuristic biasing formulae that we have used. These new methods consist of graft-

ing into an *N*-body simulation the galaxy formation rules of semi-analytic galaxy formation models (Kauffmann, White, & Guiderdoni 1993; Benson et al. 1999). Examples of this approach already exist (Kauffmann, Nusser, & Steinmetz 1997; Governato et al. 1998), but extensive mock catalogues are still to be constructed using this technique. The combined semi-analytic/*N*-body approach offers the advantage of producing realistic catalogues that include internal galaxy properties such as colours, star-formation rates, morphological types, etc. Such information would be particularly valuable to exploit the photometric data of the SDSS survey.

We are planning to implement several of the improvements just mentioned and to update our web page as we progress. In the meantime we hope that the gallery of mock catalogues already available will be of use to researchers interested in the 2dF and SDSS surveys.

References

Bagla J. S., 1998, MNRAS, 299, 417

Bardeen J., Bond J., Kaiser N., Szalay A., 1986, ApJ, 304, 15

Baugh C. M., 1996, MNRAS, 280, 267

Baugh C. M., Efstathiou G., 1993, MNRAS, 265, 145

Baugh C. M., Efstathiou G., 1994, MNRAS, 267, 323

Baugh C. M., Gaztañaga E., Efstathiou G., 1995, MNRAS, 275, 1049

Benson A. J., Cole S., Baugh C. M., Frenk C. S., Lacey C. G., 1999, MNRAS

Bertin E., Dennefeld M., 1997, A&A, 317, 43

Bond J., Efstathiou G., 1991, Phys. Lett. B, 265, 245

Bower R. G., Coles P., Frenk C. S., White S. D. M., 1993, ApJ, 405, 403

Carlberg R. G., Couchman H. M. P., Thomas P. A., 1990, ApJ Lett, 352, L29

Carlberg R. G., Yee H. K. C., Ellingson E., 1997, ApJ, 478, 462

Cen R., Ostriker J. P., 1992, ApJ, 399, 331

Cen R., Ostriker J. P., 1993, ApJ, 417, 415

Chaboyer B., Demarque P., Kernan P. J., Krauss L. M., 1996, Science, 271, 957

Cole S., 1997, MNRAS, 286, 38

Cole S., Weinberg D. H., Frenk C. S., Ratra B., 1997, MNRAS, 289, 37

Colless M., Ellis R. S., Taylor K., Hook R. N., 1990, MNRAS, 244, 408

Couchman H. M. P., 1991, ApJ, 368, 23

Davis M., Efstathiou G., Frenk C. S., White S. D. M., 1985, ApJ, 292, 371

Efstathiou G., Davis M., White S. D. M., Frenk C. S., 1985, ApJS, 57, 241

Efstathiou G., Sutherland W. J., Maddox S. J., 1990, Nature, 348, 705

Eisenstein D. J., Hu W., 1998, ApJ, 496, 605

Eke V. R., Cole S., Frenk C. S., 1996, MNRAS, 282, 263

Frenk C. S., Evrard A. E., White S. D. M., Summers F. J., 1996, ApJ, 472, 460

Gardner J. P., Sharples R. M., Frenk C. S., Carrasco B. E., 1997, ApJ Lett, 480, L99

Governato F., Baugh C. M., Frenk C. S., Cole S., Lacey C. G., Quinn T., Stadel J., 1998, Nature, 392, 359

Gunn J. E., Weinberg D. H., 1995, in proceedings of the 35th Herstmonceux workshop. Cambridge University Press, Cambridge, astro-ph/9412080

Heydon-Dumbleton N. H., Collins C. A., Macgillivray H. T., 1989, MNRAS, 238, 379

Jenkins A. et al., 1998, ApJ, 499, 20

Jones L. R., Fong R., Shanks T., Ellis R. S., Peterson B. A., 1991, MNRAS, 249, 481

Katz N., Hernquist L., Weinberg D. H., 1992, ApJ Lett, 399, L109

Kauffmann G., Nusser A., Steinmetz M., 1997, MNRAS, 286, 795

Kauffmann G., White S., Guiderdoni B., 1993, MNRAS, 264, 201

Loveday J., Peterson B. A., Efstathiou G., Maddox S. J., 1992, ApJ, 390, 338

Maddox S. J., Efstathiou G., Sutherland W. J., 1996, MNRAS, 283, 1227

Maddox S. J., Efstathiou G., Sutherland W. J., Loveday J., 1990, MNRAS, 243, 692

Mann R. G., Peacock J. A., Heavens A. F., 1998, MNRAS, 293, 209

Metcalfe N., Shanks T., Fong R., Jones L. R., 1991, MNRAS, 249, 498

Nakamura T. T., Matsubara T., Suto Y., 1998, ApJ, 494, 13

Peacock J. A., Dodds S. J., 1994, MNRAS, 267, 1020

Peebles P. J. E., 1981, ApJ, 248, 885

Philips L. A., Turner E. L., 1998, ApJ, submitted, astro-ph/9802352

Renzini A. et al., 1996, ApJ Lett, 465, L23

Salaris M., Degl'Innocenti S., Weiss A., 1997, ApJ, 484, 986

Saunders W. et al., 1994, in Proceedings of the 35th Herstmonceux workshop. Cambridge University Press, Cambridge

Schechter P., 1976, ApJ, 203, 297

Scherrer R. J., Weinberg D. H., 1998, ApJ, 504, 607

Smoot G. F. et al., 1992, ApJ Lett, 396, L1

Strauss M. A., Davis M., Yahil A., Huchra J. P., 1990, ApJ, 361, 49

Sugiyama N., 1995, ApJ Supp, 100, 281

Summers F. J., Davis M., Evrard A. E., 1995, ApJ, 454, 1

Tormen G., Bertschinger E., 1996, ApJ, 472, 14

Walker T. P., Steigman G., Kang H.-S., Schramm D. M., Olive K. A., 1991, ApJ, 376, 51

White M., Bunn E., 1996, ApJ, 460, 1071

White M., Bunn E. F., 1995, ApJ, 450, 477

White S. D. M., 1996, in Schaeffer R., ed, Cosmology and large scale structure : Les Houches, session LX, 1-28 August 1993. Elsevier Science, Amsterdam, astro-ph/9410043

White S. D. M., Efstathiou G., Frenk C. S., 1993, MNRAS, 262, 1023

White S. D. M., Frenk C. S., Davis M., Efstathiou G., 1987, ApJ, 313, 505

Zucca E. et al., 1997, A&A, 326, 477

Chapter 5

Dust extinction effects on clustering statistics

THE ARGUMENT The presence of dust grains in the Milky Way affects the propagation of light from extragalactic objects. Blue light can be scattered out of the line of sight, or absorbed and re-radiated at much lower (thermal) frequencies, causing a dimming in the apparent magnitude of the sources. The dust is distributed non-uniformly, concentrated at low galactic latitudes, and dust clouds are themselves clustered. Thus, if care is not taken, the clustering signal from galaxy catalogues can be contaminated by that of the Galactic dust. In this chapter we attempt to assess the effect of dust on the clustering signal in the power spectrum from the SDSS using mock redshift catalogues and maps for the dust distribution. The SDSS itself will be corrected for dust using the same maps we employ, and so we also attempt to assess the likely systematic errors that could be caused by inaccuracies in the corrections applied to the catalogues if there are errors in these maps. We compare the systematic effect on the three-dimensional power spectrum with the effect on the two-dimensional correlation function, $w(\theta)$.

5.1 Introduction

The disk component of the Milky Way contains a significant amount of dust in the form of small grains, which are effective optical absorbers over a range of wavelengths. Their ability to absorb starlight has a substantial effect on the magnitudes and colours of sources when viewed through clouds of dust, preventing us from seeing more than a

few kiloparsecs into the centre of the Galaxy in optical light. The distribution of dust column density around us is neither homogeneous nor random; there is a much higher concentration of dust in the galactic plane, and dust appears to be clumped into clouds, resulting in so-called "patchy obscuration".

The correlations that exist in the dust distribution can potentially contaminate the correlations we measure in the background galaxy density, since the number of galaxies seen down to a specific apparent magnitude depends on the column density of dust along the line of sight. The purpose of this chapter is to use the latest extinction maps to assess the effect of foreground dust on the clustering signal obtained from the future galaxy redshift surveys outlined in the previous chapter; we concentrate on the Sloan Digital Sky Survey as an example. In actual fact, the SDSS team will be using the very dust maps described here to *correct* the data from the survey, ie. by observing to fainter magnitudes in regions of high extinction and correcting the measured magnitudes accordingly. It is useful, therefore, to have an idea of how accurate the maps themselves are, and to what extent the clustering signal could be contaminated by errors in our ability to dust-correct. We estimate the systematic error in the dust map by putting dust into the mock catalogue using the best maps available, but correcting the catalogue using maps that derived around fifteen years ago.

In this chapter we will first outline the discovery of dust in the early part of this century, and go on to look at the way extinction is caused, and the key techniques that have been used in its measurement (section 5.2). In section 5.3 we briefly describe the construction of the best dust maps that currently exist, and explain how we apply them to the mock SDSS galaxy redshift catalogue. Section 5.4 contains our results in terms of the effect of dust on three different quantities: the angular correlation function, the power spectrum of the entire flux-limited survey with a particular weighting, and the power spectrum of a volume-limited sample of the survey . We conclude in section 5.5.

5.2 What is dust?

5.2.1 History

Dust has already made its presence felt in our established astronomical World View. In 1773, Sir William Herschel built his own $1.2\mathrm{m}$ telescope and counted stars in all directions.

Assuming that the fainter stars were farther away, using an inverse square law for the luminosity-distance relation, he concluded that the Sun is at the centre of the distribution of visible stars, and that stars are scattered farther from us along the Milky Way than in other directions. This view stood for well over a century, and was re-confirmed early in the 1900s by the work of Jacobus Kapetyn. Kapetyn used more star counts to show that the Sun was around $0.5\mathrm{kpc}$ from the centre of a stellar distribution around $10\mathrm{kpc}$ in diameter and $3\mathrm{kpc}$ thick. Kapetyn's Universe is compared with our current knowledge of the shape and size of the Milky Way in figure 2.1.

The existence of dust in the ISM was inferred by Trumpler (eg. Trumpler 1930) through studies of Galactic Clusters. Without accounting for dust, it was found that the inferred sizes of clusters increased with their distance from us. This result seems unphysical, unless an extra effect causes more dimming of starlight with distance than the inverse square law predicts. In this case, the clusters would have true distances greater than the derived ones, and the problem would be resolved.

This issue was resolved by Shapley through observations of globular clusters. Globulars are believed to have formed very early in the history of the Milky Way and reflect the initial shape of the cloud that formed the Galaxy and, as such, are distributed in a spherical distribution about the centre of the Galaxy. Using RR Lyrae stars as distance indicators, Shapley deduced the distribution of globular clusters in the Milky Way. He demonstrated that the Sun was in the disk of our Galaxy, and that the dusty material is concentrated along the Milky Way, explaining the large dark patches in the sky. Herschel & Kapetyn, it transpired, were only able to see the nearest stars, and underestimated the size of the Milky Way because they never saw the centre. In fact, current astronomical research puts the Sun around $10\mathrm{kpc}$ from the centre of a thin disk of stars of total diameter $25\mathrm{kpc}$ and thickness $1\mathrm{kpc}$. Stars are, on average, around one magnitude fainter in the visual band for every kiloparsec they are away from us, leading to approximately twenty-five magnitudes of visual extinction to the Galactic centre.

5.2.2 The cause

Reddening of starlight is caused by the presence of dust grains in the Interstellar Medium (ISM). Dust particles are agglomerations of billions of atoms, thought to be either silicate or graphite material, sometimes with a coating of water ice. Because they are composed

of the trace elements of the Universe, they are exceedingly rare compared to hydrogen and helium in the interstellar medium. There is roughly one hydrogen atom per cubic centimeter in the ISM while dust particles are approximately 10^{12} times scarcer. Despite their rarity, they are the principal absorbers and scatterers of radiation; hydrogen can only absorb at specific energies, and thus is transparent to the bulk of the radiation produced by stars. Dust, on the other hand, absorbs radiation over a large wavelength range very efficiently. The absorbed energy goes into heating of the dust particles, which proceed to radiate thermally at a temperature of 15-20K.

There are two distinct effects of dust on galaxy luminosities, extinction and reddening. Extinction describes the reduction in luminosity of light passing through a dust cloud. Reddening refers to the differential extinction between wave bands, and hence the change in apparent colour of the source. Dust grains of diameter d can only interfere with light of wavelength $\lambda \lesssim d$. Dust grains have a typical radius ~ 5000Å. In the Johnson magnitude system:

the B-band (Blue) has $\lambda \approx 4300 \pm 500$Å, whilst

the V-band (Visual) has $\lambda \approx 5500 \pm 600$Å.

Thus, extinction affects the blue more than the visual, and the colour index $B - V$ increases as the object becomes reddened. Reddening values are commonly quoted in magnitudes of $B - V$, E_{B-V}. The application to extinction in a specific waveband depends on the waveband; its relation to E_{B-V} is never certain, since it cannot be directly measured. Extinction is normally denoted by a capital 'A' with the waveband as a subscript, eg. A_B is the B-band extinction.

5.2.3 Measurement

If dust is concentrated in a slab in the galactic disk, the column density should behave as a simple co-secant law with galactic latitude, b. While studies have shown this model to be reasonably accurate for the dust averaged over galactic longitude (Boulanger & Perault 1988), so-called "patchy obscuration" is responsible for vast differences from this rule for individual lines of sight (Burstein & Heiles 1978).

Four chief techniques have been used to assess the dust distribution in our Galaxy.

- **Radio** HI 21cm. Radio observations are used to give the column density of HI along the line of sight. The assumption is then made that the dust and gas distributions are tightly correlated. The definitive survey of this kind was made using the Bell Labs 20ft horn reflector, which has a beam width of 2° (Stark et al. 1992). The simplest use of this information to estimate extinction is to assume the linear relationship:

$$N(\mathrm{HI}) = \eta E_{B-V}, \tag{5.1}$$

where η is thus the dust-to-gas ratio. Nichol & Collins (1993) use two different values of η to correct the angular correlation function of the EDSGC for dust using this simple relationship,

$$\eta = 5.2 \times 10^{21} \mathrm{cm}^{-2}\mathrm{mag}^{-1} \ (B\text{-band extinction, } A_B = 8.2 \times 10^{-22} N(\mathrm{HI})\mathrm{cm}^2\mathrm{mag}),$$

$$\eta = 4.0 \times 10^{21} \mathrm{cm}^{-2}\mathrm{mag}^{-1} \ (B\text{-band extinction, } A_B = 17.5 \times 10^{-22} N(\mathrm{HI})\mathrm{cm}^2\mathrm{mag}),$$

representing, respectively, a typical model and a reasonable upper limit based on examples in the literature. Dust correction in this way based on $N(\mathrm{HI})$ works well on aggregate, suggesting that dust and gas are reasonably well correlated, but for individual lines of sight, independent estimates of the reddening suggests that η can vary by up to a factor of three.

- **Galaxy counts**. Given that extinction causes a dimming in galaxy magnitudes, a galaxy survey with constant magnitude limit should see fewer galaxies per solid angle in areas of high extinction. This effect can be a useful tool for examining dust. The first large collection of galaxy counts was produced by Shane & Wirtanen (1967) at the Lick Observatory. Their survey covered approximately half the sky ($\approx 19,000$ square degrees), above $|b| = 20^\circ$. Analysis by Heiles (1976) suggests a good fit is given by $\log N_{\mathrm{gal}} = A + BN(\mathrm{HI})$. However, there are several problems with using the galaxy distribution in this way, namely:

  - poor statistics at low galactic latitudes leads to a high Poisson counting error in bins near the galactic plane.

  - for testing the behaviour of the relation at high galactic latitudes there is a "lack of sky", resulting in uncertainty about the zero-point of the relation, ie. to what extent lines of sight towards the galactic poles are dust-free.

- the intrinsic mottling of the sky due to large-scale structure imprints a false signature on the counts in cells in addition to that from the variation in the dust column density. This can be erased by smoothing, but the smoothing length must be quite large. For instance Heiles (1976) used bins of $13° \times 13°$ to remove the signal from clustering.

Having obtained average values of the constant in the relation $\log N_{\rm gal} = A + BN({\rm HI})$, the accuracy of this treatment is found to vary substantially over the sky, just as the extinction/HI relation does. Burstein & Heiles (1978) developed a much more successful model by combining the HI data with the galaxy counts, resulting in an expression of the form

$$E_{B-V} = y_1 + y_2 N({\rm HI}) + y_3 N({\rm HI})^2 + y_4 N({\rm HI}) \log N_{\rm gal} \tag{5.2}$$

- **Standard candles**. Another technique uses objects with known spectral properties to assess the dust column-density along their lines of sight by examining the effect on their spectra. In general, one would like to perform this analysis using extragalactic sources, as one cannot guarantee that stars within the Milky Way have no dust beyond them. This technique can generally only be applied to a small number of lines-of-sight, so it is of little use for compiling maps of dust extinction, but is a powerful tool for checking that maps produced by other methods are reliable. There are three chief methods of observation using standard candles:

  - *Globular clusters*. This method involves matching the colour-magnitude diagram of a globular cluster to that of a cluster with known reddening, thus obtaining a measure of the extra reddening in the observed cluster. Burstein & McDonald (1975) use globulars in M31 to calibrate a colour-magnitude relation for globulars and apply it to the integrated spectral properties of 74 disk and halo clusters in our own galaxy, providing a measure of the reddening caused by foreground dust.

  - *Elliptical galaxies*. Observations show that there exists a strong correlation between the absorption line strengths of elliptical galaxies and their intrinsic continuum colour. Once this relation is calibrated, the difference between true and observed colour can be estimated and the reddening deduced. Faber (1973) performed this analysis with a sample of 31 elliptical galaxies.

- *Stars*. Again, a similar technique involves the intrinsic colour relations for early-type (B,A,F) stars. Hilditch, Hill, & Barnes (1976) show how colour excesses in the Strömgen uvby-β photometry of these objects can be used to measure the amount of reddening, once the system is calibrated for objects in areas of very low extinction. Care must be taken to ensure that these are essentially background objects, in that all the dust along their lines of sight is in front of, rather than behind them.

All these methods generally suffer from the constraint that they can only be applied for low reddening, so that we can actually observe objects to measure the amount of extinction in a certain part of the sky. Thus they are generally confined to $|b| \gtrsim 30°$, and typically even higher latitudes for the stellar method.

- **Direct observation**. By observing in the far infra-red, we can actually see the re-radiated energy that has been absorbed out of starlight by the dust. Ground-based FIR astronomy has proven difficult due to absorption by water vapour in the atmosphere and the problems of shielding a telescope from local heat sources. Many of these problems were overcome with the launch of the *IRAS* satellite in 1983. This experiment provided detailed, full-sky maps (Wheelock et al. 1994) in four infrared bands ($12, 25, 60$, and $100\ \mu$m), with high resolution ($\sim 5'$ beam width). The emissivity of the dust depends very sensitively on its temperature, so it is crucial to observe in multiple wave-bands to allow the temperature to be measured. Difficulties still exist with using *IRAS* to accurately measure the extinction in the Milky Way, chiefly: the uncertainty in subtraction of zodiacal light (caused by scattering from material in the plane of the Solar System); contamination by extra- and intra-galactic point sources; and the possible existence of a diffuse extragalactic infra-red background. The DIRBE experiment on board the *COBE* satellite, which took data during 1989-90, provided a complementary survey, with much better control of calibration uncertainties despite the much poorer angular resolution compared with *IRAS* ($0.7°$).

5.3 Putting dust in the catalogues

5.3.1 The dust maps

For fifteen years, the treatment of Burstein & Heiles (1982) stood as the best parameterization of extinction from dust in our Galaxy. This model included a non-linear dependence on HI density and the use of the Shane & Wirtanen (1967) galaxy counts. Problems included: an uncertainty in the zero point of the relation; the lack of galaxy counts below $-23°$ in declination; and using only HI information for high galactic latitudes, $|b| > 65°$. However, the maps were found to be highly accurate when applied to most line-of-sight extinction measurements from standard candle techniques, and the authors claim an accuracy of $\Delta E_{B_V} = \pm 0.01$ mag or $\Delta E_{B_V} = \pm 0.1 E_{B_V}$, whichever is greater, for galactic latitude $|b| > 10°$.

The next significant step forward in mapping extinction took place with the work of Schlegel, Finkbeiner, & Davis (1998) (henceforth SFD). The key achievement of this work has been the coupling of *IRAS* resolution with the calibration accuracy of DIRBE. Great care has been taken to remove the zodiacal foreground and point sources. The DIRBE $100\ \mu$m and $240\ \mu$m data have been combined to map dust temperature in order that the $100\ \mu$m map be converted to a map of dust column density. There are still problems with these maps, namely certain areas that were not scanned by *IRAS*, or that were contaminated in some way (ie. a strip amounting to 3% of the sky and a small (radius $2°$) area in the Northern Galactic sky [$(l, b) = (326°, 52°)$] contaminated by Saturn). These areas have generally been filled in with the lower resolution DIRBE data. The overall normalization of column density to reddening has an uncertainty of 10%.

SFD find a zero point of 0.020 mag for the amount of reddening, in contrast to BH who conclude that there are areas of the sky with no reddening at all. Both the SFD maps and the BH maps, plus the software required to read them, can be found at

`http://astro.berkeley.edu/davis/dust/index.html`

`http://astro.princeton.edu/~schlegel/dust/index.html`

In figure 5.1 we show a pictorial representation of the SFD dust maps for the North and South Galactic hemispheres. In the lower panel we show the difference between the SFD maps and those of Burstein & Heiles. The generally close correspondence between the

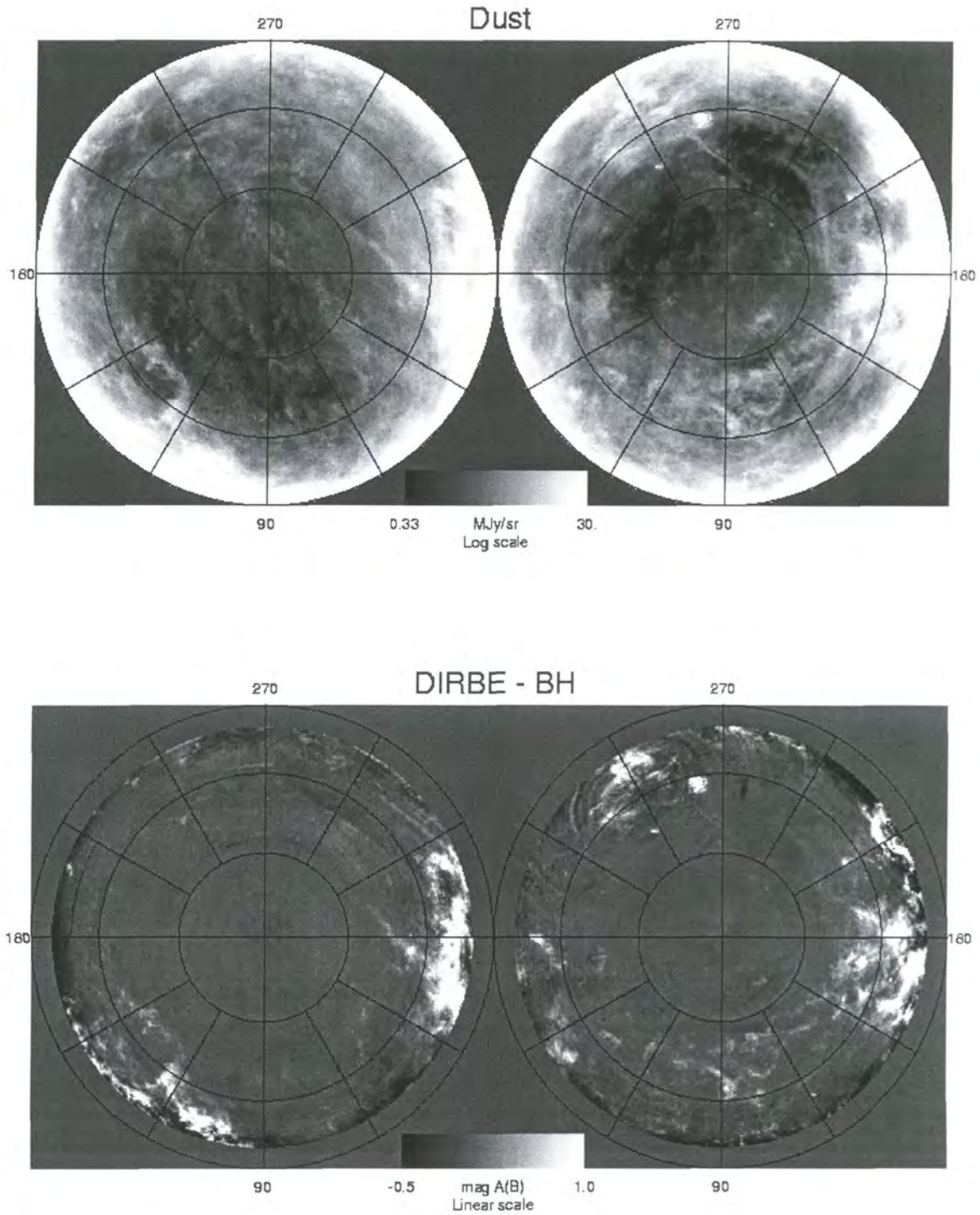

Figure 5.1: The SFD dust maps (upper panel) and the SFD - BH difference maps (lower panel). The maps are shown as equal area projections centred on the North and South Galactic Poles. Source: `http://astro.berkeley.edu/davis/dust/index.html`

maps is clearly visible, as are the differences at low galactic latitudes and the appearance of large patches nearer the poles with slightly discrepant values.

The real SDSS project will be using the SFD maps to correct the catalogue for dust as it goes along. So, for us to look at the effects on clustering statistics of a catalogue that contains dust but has no corrections is a needlessly pessimistic task. A more realistic target would be to examine a catalogue that is only dust-affected at the level of the errors in the SFD work. But the errors are of course highly systematic and coherent over the sky, so in order to get an idea of the errors involved we take the difference between these maps and those presented in BH. This approach will then give some sort of worst case indication of the systematics that could be present.

5.3.2 Application to mock catalogues

In order to apply dust to the mock SDSS catalogue, we use the same scheme for assigning random magnitudes as we do for the "clean" catalogues. We then determine the angular position of each galaxy in Galactic coordinates, and use the SFD maps to calculate its E_{B-V} extinction.

The SDSS will select galaxies from photometry in the r'-band. To correct the magnitude of the galaxy, we apply the relation (Schlegel, Finkbeiner, & Davis 1998, table 6)

$$A_{r'} = 2.751 E_{B-V}. \tag{5.3}$$

To perform the equivalent magnitude correction for a 2dF catalogue we would use a factor of 4.035, which reflects the larger extinction in the shorter wavelength $b_{\rm J}$-band used to select galaxies in the parent APM survey.

We note that a zero point in the extinction can have no effect on the clustering signal, so we subtract the SFD baseline of 0.020 mag in E_{B-V} before applying the correction. Having obtained the magnitude change, we add it to the magnitude of the galaxy, and throw the galaxy out of the survey if it is fainter than the magnitude limit. We also use the increased magnitude to lower the value of $d_{\rm max}$, the furthest distance that the galaxy could be seen at before it passes out of the apparent magnitude limit.

The luminosity function of this catalogue was chosen (Chapter 4) to obtain a reasonable match to galaxy number counts. Changing the galaxy magnitudes to account for redden-

ing has the effect of manipulating the selection function. We choose to compensate for this effect by boosting $\phi_\star$, the number density of $L_\star$ galaxies, in order to keep the total number of galaxies constant. To keep $N_{\rm gal} \approx 900,000$ we increase $\phi_\star$ by 8.6%. We note that the number counts, dN/dm, will not be the same as for the clean mock catalogues.

For the "corrected" mocks, we subtract the Burstein & Heiles (1982) reddening from the SFD reddening and add the corresponding magnitude change to the magnitude of the galaxy. This time, of course, there is potential for objects to be moved to brighter magnitudes. Since we want to avoid the potential for objects outside the original catalogue to be scattered into it, we have chosen to add the SFD zero-point, again noting that it cannot affect the clustering signal at all. Since the two maps are, in general, well correlated, the differences between them are normally quite small, and this magnitude shift should be enough to catch all the galaxies. This time, we need to increase $\phi_\star$ by 6.4% to conserve the number of galaxies.

We will thus end up with three mock SDSS catalogues: a "clean" one with no dust, or, equivalently, perfect dust correction; a "dusty" one; and a "corrected" one.

In figure 5.2 we show the resultant distribution of magnitude shifts in the corrected and uncorrected maps. As expected, the SFD correction now has a baseline of zero, and the SFD-BH peaks at 0.02 mag since the majority of galaxies have little correction except for the 0.02 mag zero point after applying an SFD magnitude shift and then correcting with BH. It can also be seen that very few galaxies have negative extinction in the corrected catalogue, so we can be reasonably sure that we are not significantly biased by failing to catch galaxies that would be scattered in to the tail-end of the magnitude distribution. This problem could certainly be eliminated altogether by increasing the offset by another 0.03 mag.

5.4 Results: systematic effects on clustering

Our chief interest in dust in this work involves possible bias in the measured clustering properties of the galaxy distribution caused by observing the galaxies through a dust layer that has its own correlations.

To assess the effect of dust, we look at three statistics: the power spectrum of a volume limited sample of galaxies selected from the full SDSS; the power spectrum of the whole,

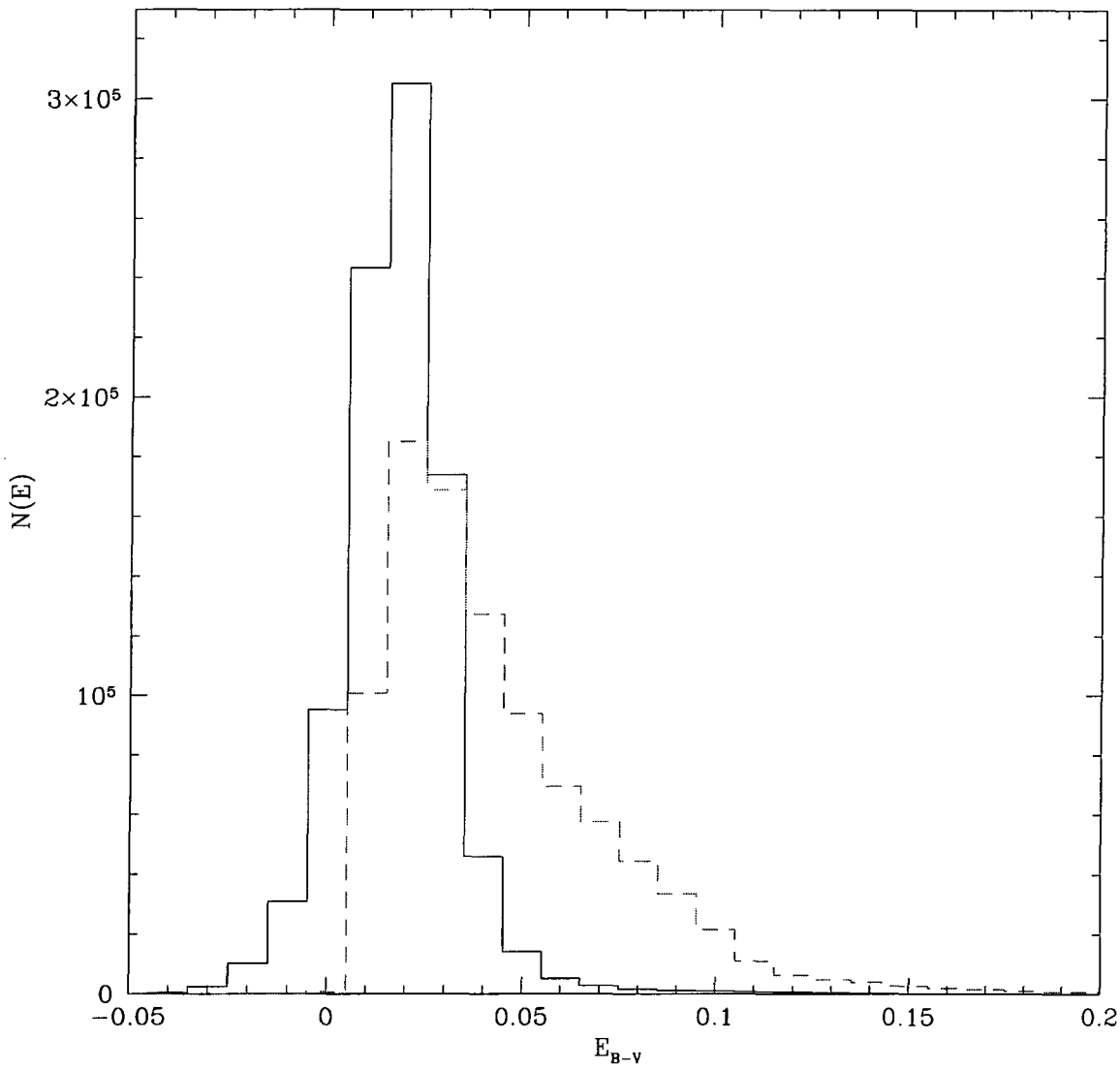

Figure 5.2: Histogram of extinction, E_{B-V}, for galaxies in the dusty sample (dashed line) and corrected sample (solid line).

magnitude limited SDSS catalogue; and the angular correlation function of the whole catalogue.

For each statistic, we examine the clean catalogue with no dust effects, the dusty catalogue with SFD dust and no correction, and the corrected catalogue with SFD dust and BH correction, as described in 5.3.

In order to measure the power spectrum, we must create a catalogue of random galaxies with the same window function and density distribution as the catalogue we are

measuring. Constructing this catalogue is trivial in the clean case as it simply involves the $n(z)$ function used in the creation of the original mock catalogue. In the dusty and corrected mocks, this $n(z)$ is no longer that which would be measured from the survey, since we have thrown galaxies out of the sample. In order to create realistic random catalogues for these realizations, we take galaxies from the distribution before throwing them out due to dust effects, and for each galaxy pick a random line of sight that is within the angular bounds of the SDSS window function. We then change the magnitude of the galaxy according to the amount of extinction along this random direction. In this way we model the correct distribution of reddening without introducing any correlations into the random catalogue.

5.4.1 The power spectrum – volume limited case

In the case of a volume limited sample of galaxies without dust, we are simply selecting a constant density wedge from the galaxy catalogue out to a fixed radius. Introducing dust has the effect of changing the $d_{\max}$ values of the galaxies, so, galaxies near the volume limit are scattered in and out of the sample. Effectively, then, we still have a wedge but its furthest edge is now ragged due to the different magnitude shifts along different lines of sight. Our technique for constructing the random catalogue with no clustering means that the edge of the random catalogue is at the average distance of galaxies at the edge of the real catalogue, but it still has a sharp cut-off with distance. A systematic bias will be introduced since the real and random catalogues do not have the same shape. If the dust has a characteristic clustering scale, θ_c, then we would expect to see biases in the power spectrum on scales of around $r\theta_c$, where r is the depth of the survey. In the example shown here, we use a volume limit of $z = 0.23$, which translates to a comoving distance $r = 590h^{-1}\,\mathrm{Mpc}$. For the fast Fourier transform analysis, we use a box size of $1036.8h^{-1}\,\mathrm{Mpc}$, three times the length of the simulation, and a 192^3 grid. We show results for the effect of dust on the power spectrum in figure 5.3. There is a large systematic problem with the dusty, uncorrected catalogue in the very long wavelength regime, in excess of the random errors associated with these points. It would therefore seem that failing to correct the SDSS redshift survey for dust extinction effects would result in a strong bias in measurements of large-scale power, entirely removing the turn-over we would expect to see in a CDM-type model.

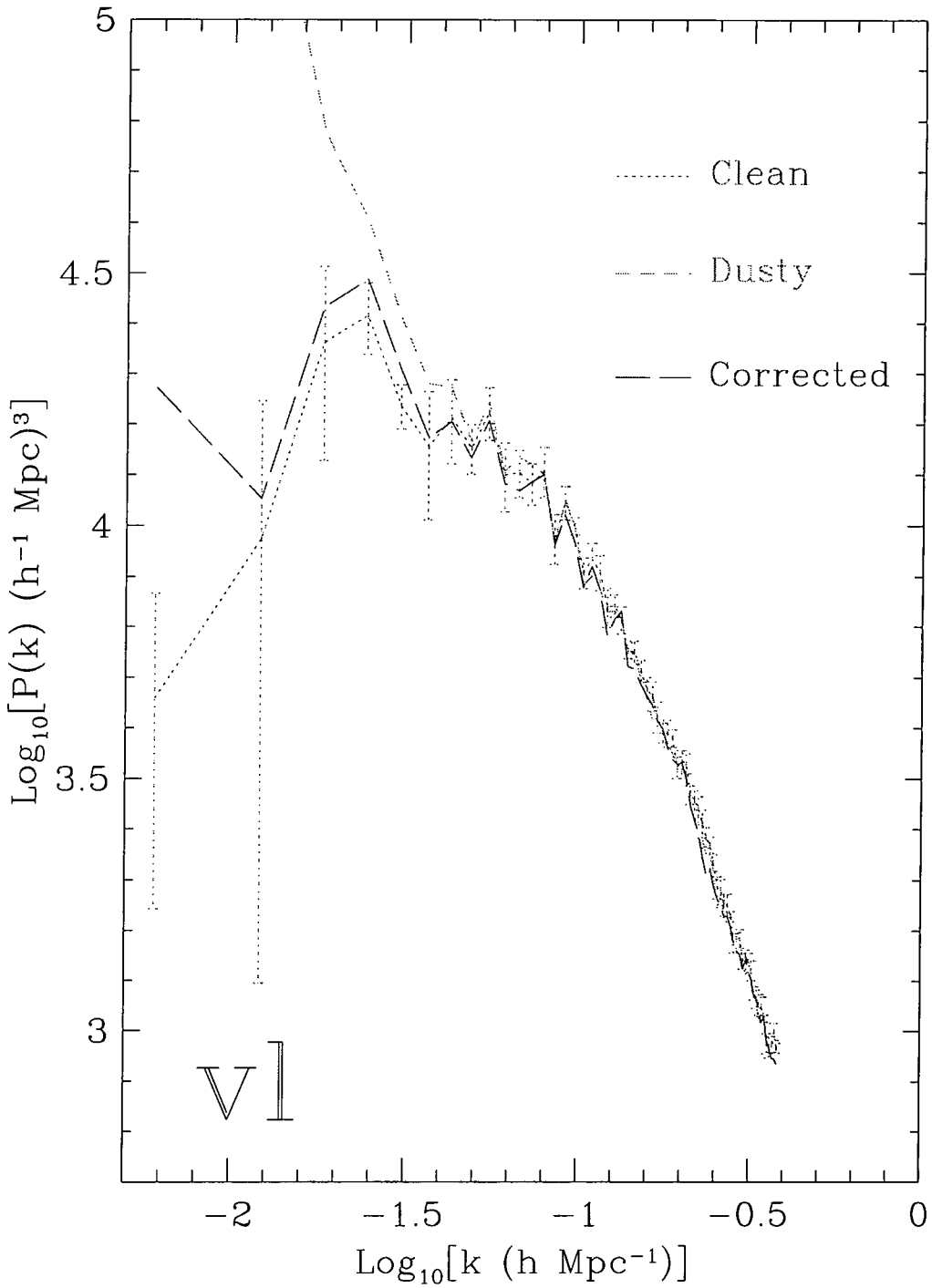

Figure 5.3: The three-dimensional power spectrum, $P(k)$, for a volume-limited subsample of the SDSS galaxies for the three cases of a clean catalogue (dotted line), a dusty catalogue contaminated according to the SFD maps (short-dashed line), and the dusty catalogue corrected with the BH maps (long-dashed line). Error-bars come from the variance between ten independent realizations of the clean SDSS mock catalogue. We plot the power spectrum out to two-thirds the value of the Nyquist frequency.

5.4.2 The power spectrum – magnitude limited case

For the case of the whole, magnitude limited sample, the same reasoning applies, except that a dust fluctuation on a certain angular scale has an effect on the density along that line of sight for the entire depth of the survey. Thus dust can introduce a bias between the real and random catalogues at smaller physical scales than in the volume limited case.

We weight the galaxy sample with the FKP minimum variance weighting method, as described in Chapter 3, with $P = 4000h^{-3}\,\mathrm{Mpc}^3$. As with the volume limited case, the analysis is performed on a 192^3 grid with length $1036.8h^{-1}\,\mathrm{Mpc}$.

In figure 5.4 we show results for the three-dimensional power spectrum in the case of the clean, dusty and corrected catalogues. As in the volume limited case, the corrected catalogue seems to recover the power extremely well out to large scales, whereas the uncorrected catalogue has significantly higher amplitude in this regime: well outside the range allowed by random errors on the power spectrum.

5.4.3 The angular correlation function,$w(\theta)$

The angular correlation function is a measure of the amplitude of clustering of objects on the sky as a function of angular separation, θ, and as such we expect it to be more sensitive to contamination by dust, which itself has power only in an angular sense. The angular correlation function carries less information than its 3D counterpart, since one dimension is projected out, so to calculate $w(\theta)$ for a redshift survey is rather a perverse use of the data. However, the SDSS survey will consist of an angular catalogue of 10^8 galaxies, of which the redshift survey is a subset. The survey, then, will provide extremely accurate data due to its high sampling rate, and we can use the mock SDSS to assess the systematic error introduced by failing to correct for dust or by plausible errors in the SFD dust-correction technique.

In figures 5.5, 5.6 and 5.7, we plot the angular correlation function from the mock SDSS catalogue with no dust, SFD dust and SFD-BH corrected dust, respectively.

In order to save computational time, we split the sample up into ten different apparent magnitude bins and calculate the correlation function for each one individually. Rather than applying fixed bounds on the magnitude range for each bin, we choose Δm such

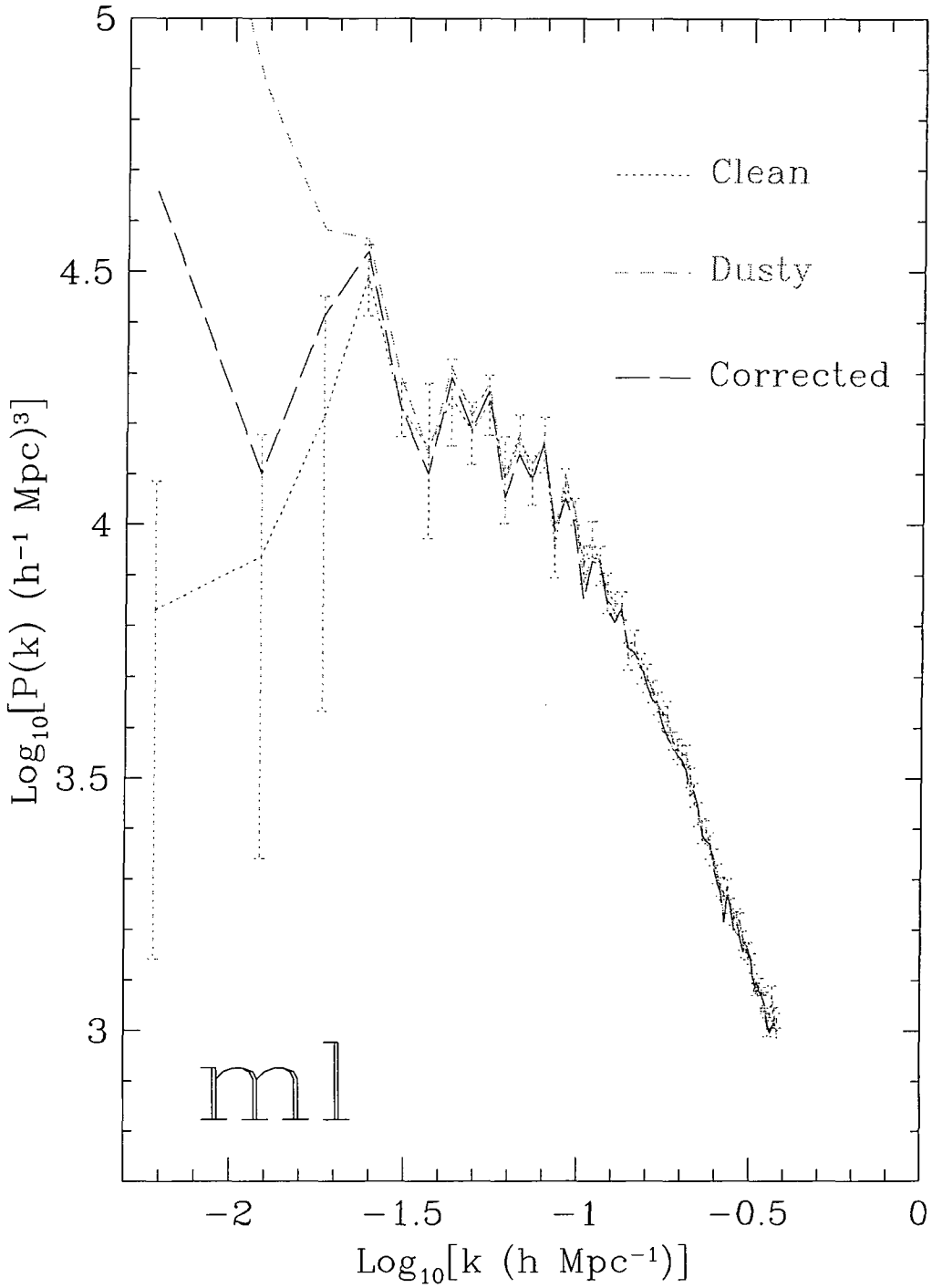

Figure 5.4: As for figure 5.3 but this time the galaxies are the whole, flux limited SDSS sample weighted with an FKP scheme, as described in section 5.4.2.

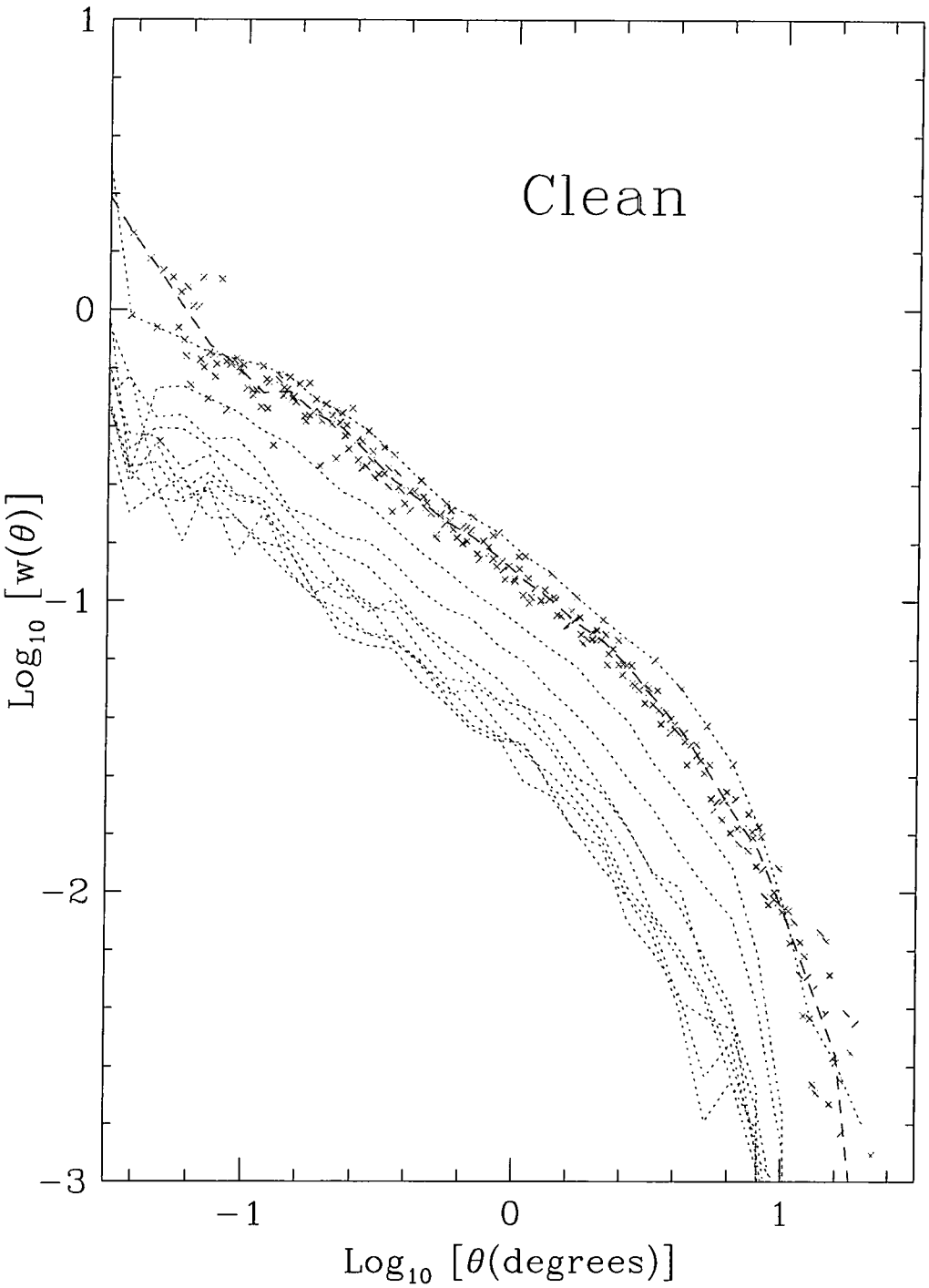

Figure 5.5: The angular correlation function, $w(\theta)$ for our SDSS mock catalogue with $\Omega_0 = 1, \Lambda_0 = 0$. The dotted lines show $w(\theta)$ for ten different magnitude bins out to the limiting SDSS magnitude, whilst the dots show the correlation function scaled using the relation described in section 5.4.3. The dashed line shows the average over the ten magnitude slices.

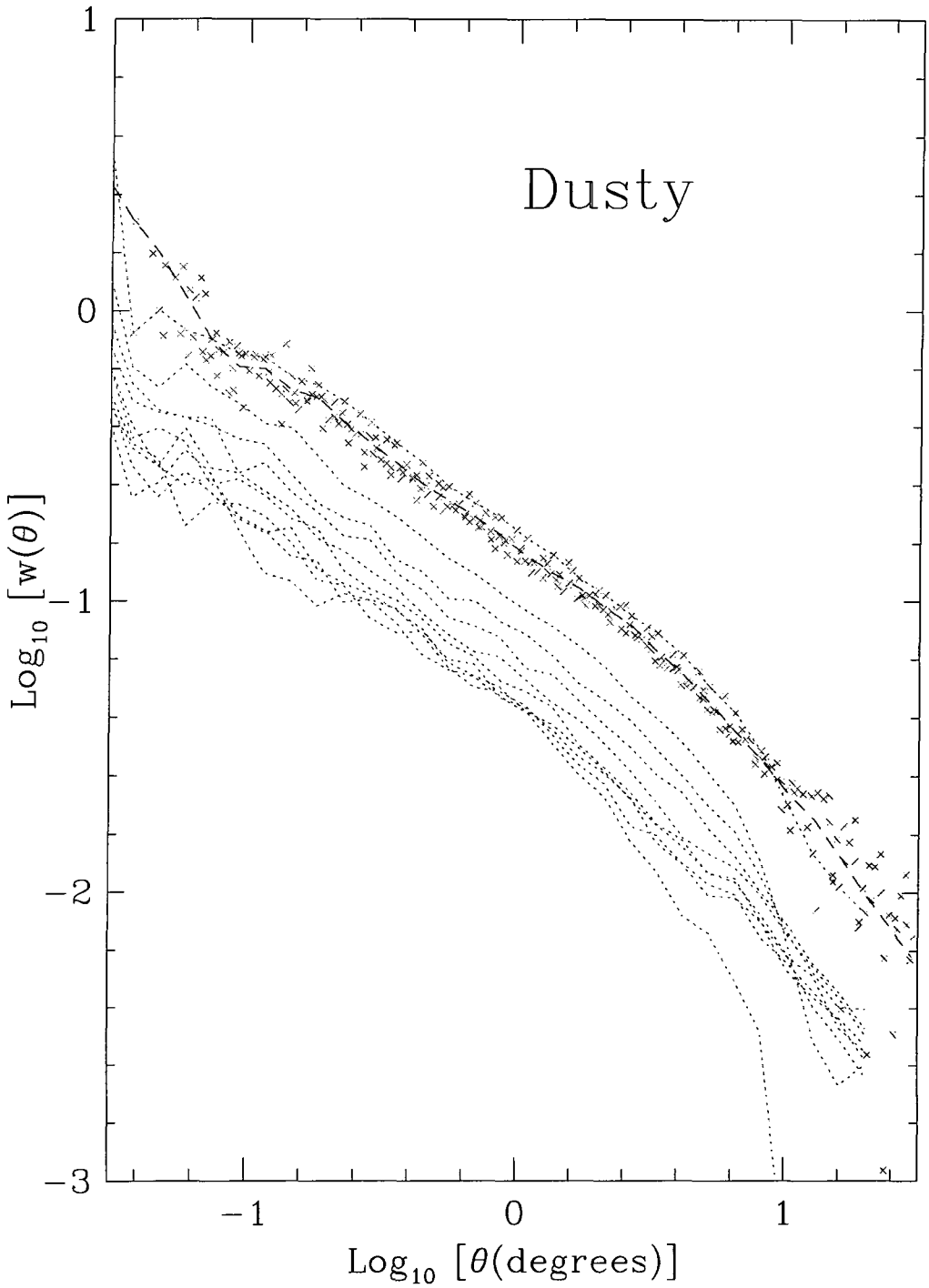

Figure 5.6: As for figure 5.5 but the correlation function is for the mock catalogue with dust introduced via the SFD dust maps.

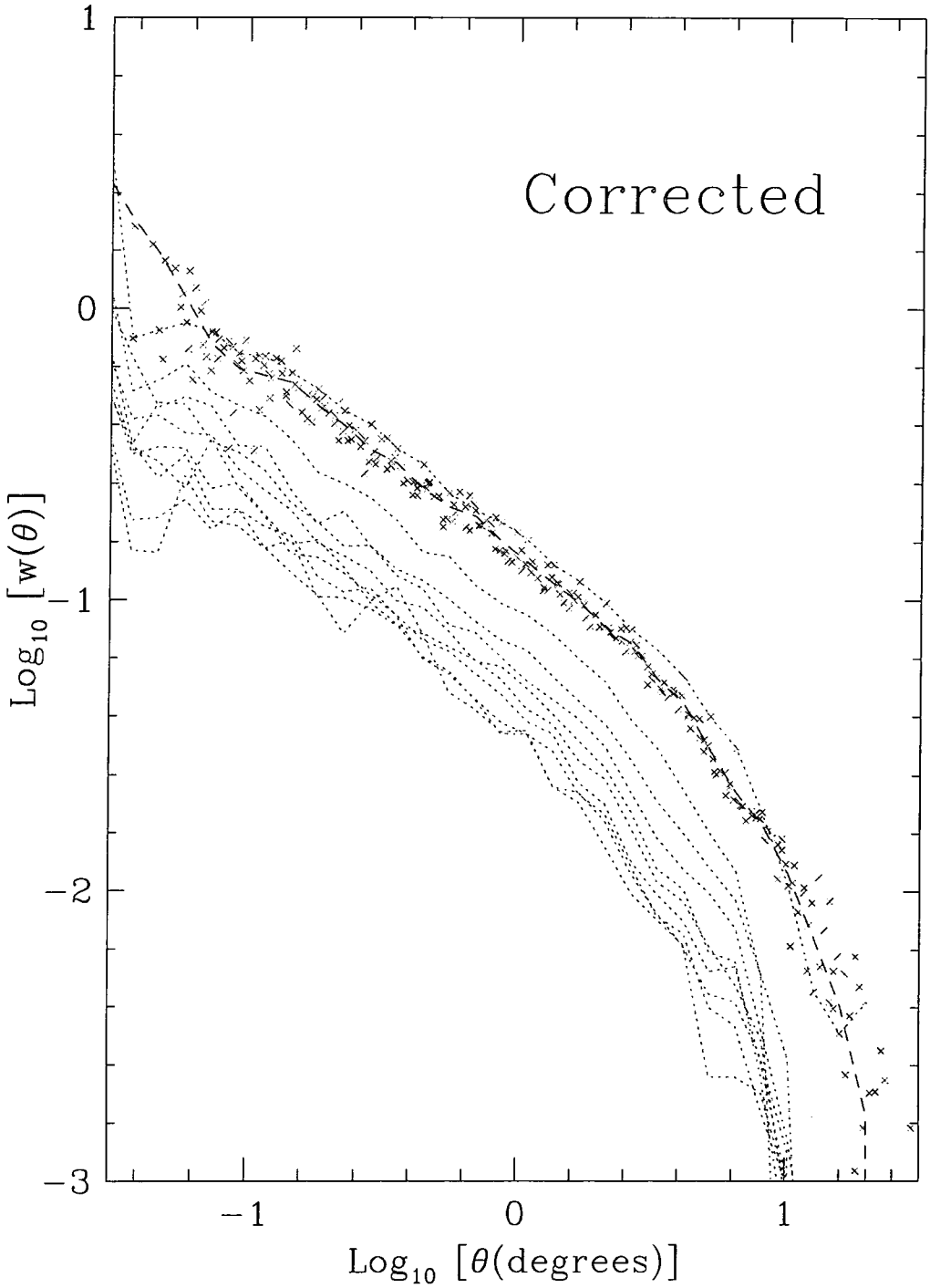

Figure 5.7: As figures 5.5 and 5.6, but this time the correlations are for dust that has been added using the SFD maps, and corrected for using the BH maps.

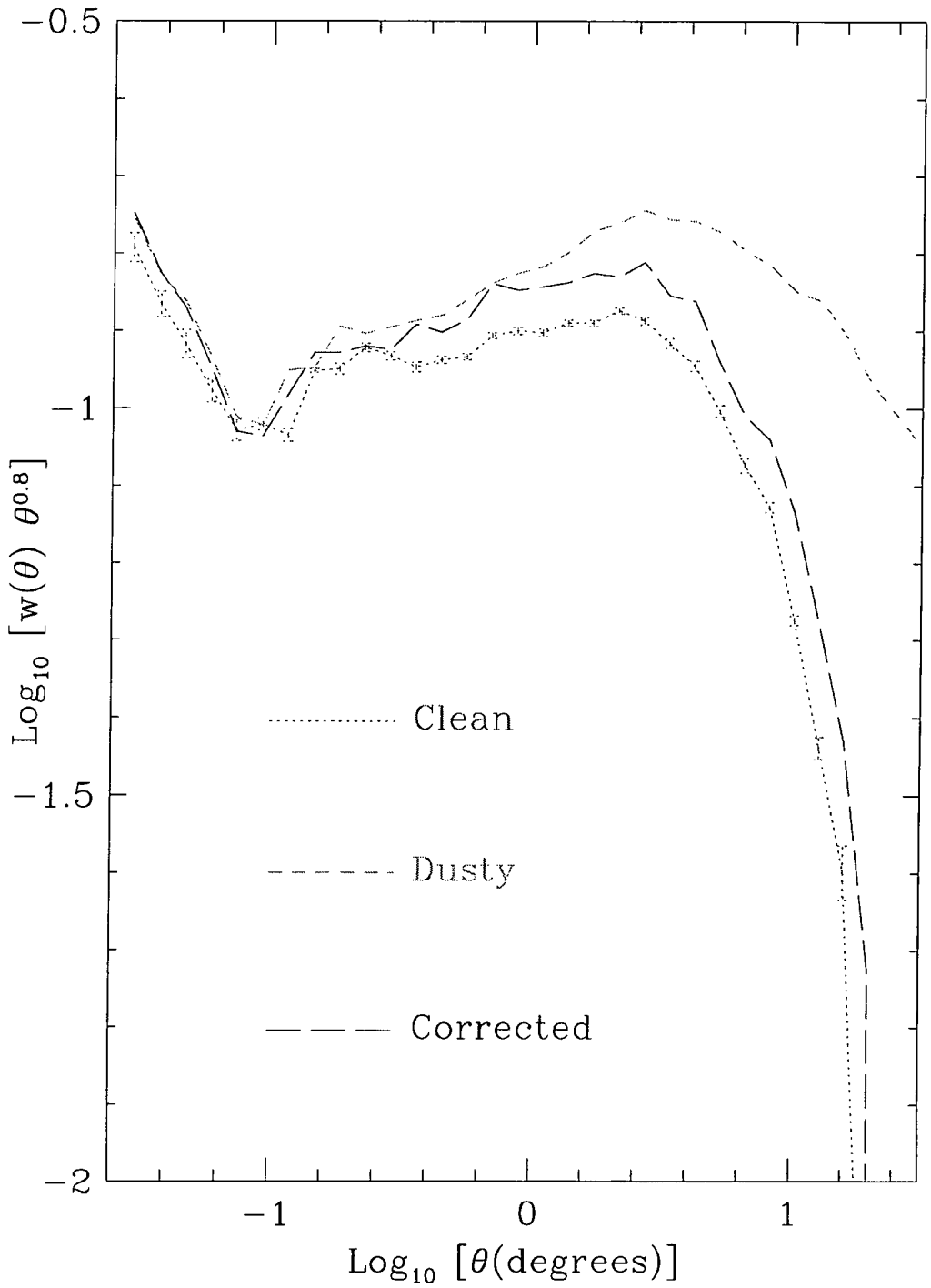

Figure 5.8: The three scaled correlation functions from figures 5.5, 5.6 and 5.7 plotted on the same axes. The $\theta^{-0.8}$ dependence has been taken out to amplify the differences at large separations. Error-bars show the standard error on the mean for the ten magnitude slices.

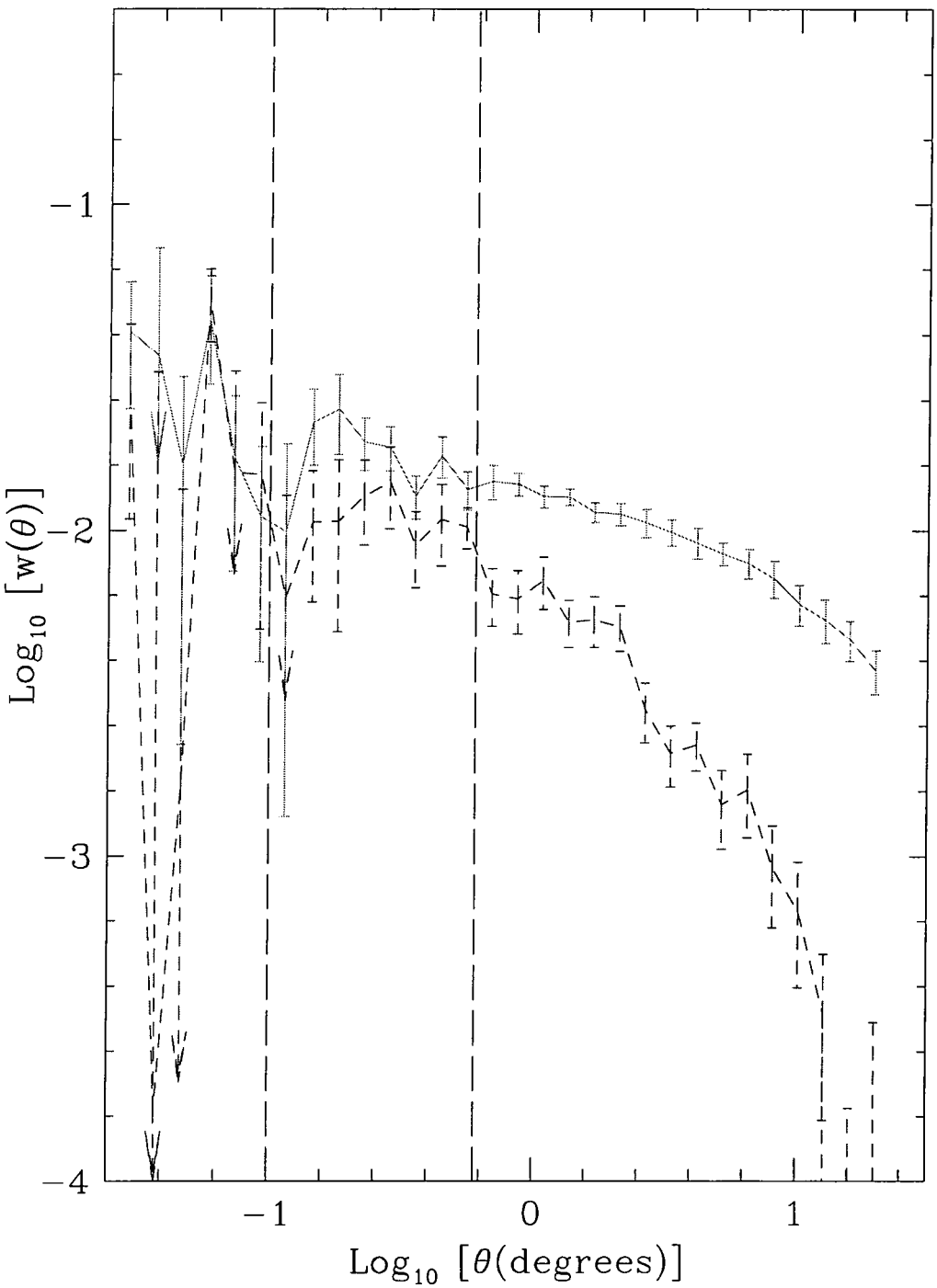

Figure 5.9: The correlation function of the SFD dust map (dotted line) and the SFD-BH difference map (dashed line). As explained in the text, we obtain the correlation function of the dust by subtracting the 'dusty' correlation function from that of the dust-free catalogue. The vertical, long-dashed lines give the angular resolution of the SFD maps (0.1°) and the BH maps (0.6°).

that each of the ten samples has a similar number of objects in it, this method being the most efficient use of resources.

The correlation function is expected to obey a simple scaling relation, where the angular scale and the amplitude are proportional to the inverse of $D_\star$, which is the distance at which an $L_\star$ galaxy would have magnitude equal to the limiting magnitude of the bin. Hence,

$$D_\star = \sqrt{\frac{L_\star}{4\pi f}}, \tag{5.4}$$

(Peebles 1993). Given that magnitude, m, is equal to $2.5 \log f$, it can be seen that

$$D_\star \propto 10^{-m/5}. \tag{5.5}$$

This relation provides an easy method for comparing the angular correlation function in different magnitude bins.

Table 5.1. Limiting magnitudes for our ten magnitude bins and the corresponding values of $D_\star$, the characteristic depth, as a fraction of the characteristic depth of the brightest (nearest) bin.

Limiting magnitude	$D_\star^0/D_\star$
17.07	1
17.61	0.7798
17.93	0.6730
18.16	0.6053
18.34	0.5572
18.49	0.5200
18.61	0.4920
18.72	0.4677
18.82	0.4467
18.90	0.4305

In table 5.1 we present the limiting magnitudes and corresponding relative values of $D_\star$ for the ten magnitude bins. In figures 5.5, 5.6 and 5.7 we plot as crosses the measured

values of the correlation function scaled up by the correct factor. The dashed line is the average over the ten different bins. It can be seen that the scaling relation works extremely well for the mock catalogues. There is a high level of scatter (indicated by the spread of the dots) in the relation for large θ in the dusty catalogue; this scatter is not random noise but rather exists because the dust distribution that contaminates the background signal has no scaling relation, but instead has a fixed scale length independent of the galaxies being observed.

It can be seen from these figures that the presence of underlying correlations in the foreground can strongly contaminate the galaxy clustering signal, resulting in an observed angular correlation function that is systematically biased. In figure 5.8 we plot the average curves from the previous three figures, ie. the correctly scaled angular correlation function for the clean, dusty and corrected catalogues. To enhance the difference between the curves on large scales, we divide $w(\theta)$ by the canonical dependence of the correlation function, $w(\theta) \propto \theta^{-0.8}$ (Groth & Peebles 1977). The error-bars show the standard error on the mean from the ten magnitude slices after scaling to the same effective depth. It can clearly be seen that the dusty catalogue is biased to a highly significant level on all scales above $0.2°$. The clustering in the dust distribution has the effect of adding a lot of power on these scales. The corrected catalogue is much healthier, with its shape much more similar to that of the clean catalogue, but comparison with the error-bars shows that it is still significantly biased compared to the level of random uncertainty in the measured $w(\theta)$. Since the ten slices occupy overlapping volumes, they are in fact rather correlated, and these error-bars reflect a certain underestimation of the true error. However, even in a worst-case scenario where we plot the standard deviation of the ten slices, rather than the error on the mean, the corrected line is biased at the 1-σ level for $\theta > 0.3°$.

Perhaps a more illustrative picture of the effect of dust comes if we subtract the clustering signal due to correlations in the background galaxy distribution. The observed correlation function is given by

$$w_{\rm obs} = w_{\rm dust} w_{\rm gal} + w_{\rm dust} + w_{\rm gal}, \tag{5.6}$$

assuming that the foreground and background distributions are entirely uncorrelated (see Geller, De Lapparent, & Kurtz 1984, although their application of this method is to study

correlations between plates). Thus we derive an expression for the correlation function of the dust,

$$w_{\rm dust} = \frac{w_{\rm obs} - w_{\rm gal}}{1 + w_{\rm gal}}. \tag{5.7}$$

This function is plotted in 5.9 for the case of no dust-correction and for correction via the BH maps. The plots are averaged over the ten magnitude bins, although in this case note that the above scaling relation has not be applied since the dust has fixed angular and physical clustering properties, independent of the depth of the survey. The error bars come from the variances between the different magnitude samples, which are of course not statistically independent, so they will tend to underestimate the true error on $w_{\rm dust}$.

Three distinct regimes can be identified from this graph:

1. **Very noisy signal at small separations**. We expect to see no clustering for small angular separations since the *IRAS*-derived SFD maps have angular resolution $\sim 6'$, so there is no real information about clustering on scales below this ($\log\theta \lesssim -1$). In fact we see a very noisy signal on these scales because the number of very close pairs is small.

2. **Similar correlations on intermediate scales**. Around $\theta = 1°$ both correlation functions are at a similar level. The HI survey (Heiles 1975) used to compile the BH dust maps has a beam width of $0.6°$, so in this regime we are between the angular resolution of the two maps. The small scale power, then, in both cases comes only from the SFD maps, and we should thus expect little difference in the angular correlation function on these scales.

3. **Long wavelengths**. For large separations, the BH correction is doing a good job of removing the dust contamination from the SFD maps, and even this worst case scenario view of systematic errors leads to leads to an order of magnitude less contamination of the intrinsic clustering signal at $\theta \approx 10°$.

5.5 Conclusions

In this chapter we have shown that, on small scales, dust is of little significance in the clustering statistics. Its most crucial effect is that of altering the power spectrum on large

spatial scales. Unfortunately, the dust power appears to affect the power spectrum in both the volume and magnitude limited cases at around the scale where we would expect to see the turnover in CDM-variant models. This coincidence is extremely irksome since the turnover is one of the key predictions of such models, and its precise location is an important parameter. Currently, we do not really know precisely how accurate the SFD recipe is, and we must stress that using the SFD-BH difference maps could lead to an over-prediction in the level of systematic error. However, it is apparent from this work that estimates of the shape parameter from the SDSS power spectrum could be significantly biased, even once dust has been corrected for to the best of our current ability.

Failing to correct for dust at all can obviously produce very high biases in measurements of large-scale power, and we speculate that recent work (Sylos Labini & Montuori 1998) claiming to see no evidence for a turnover to homogeneity in large galaxy samples like the Stromlo-APM redshift catalogue could be mistaking fluctuations in the dust distribution in our Galaxy for fractal clustering patterns in the large-scale structure of the Universe.

We intend to apply the SFD dust maps to the APM-selected galaxy catalogues, and hence investigate the likely effect on clustering in the Stromlo-APM and 2dF surveys. The effect is likely to be even more pronounced than for the SDSS, since the magnitude correction per unit of extinction is 50% higher (section 5.3.2). For the 2dF this will be countered by the fact that the South Galactic strip is located in a region of very low extinction, whereas the SDSS goes down to quite low galactic latitudes, where there is significant contamination.

The rest of the work in this thesis concerns estimation of the β-parameter ($\approx \Omega_0^{0.6}/b$) from redshift-space distortions to the power spectrum. We have shown that the power spectrum itself can be quite seriously contaminated by dust, but it will be interesting to investigate whether the magnitude of the measured anisotropy is more or less robust to dust extinction effects.

References

Boulanger F., Perault M., 1988, ApJ, 330, 964

Burstein D., Heiles C., 1978, ApJ, 225, 40

Burstein D., Heiles C., 1982, AJ, 87, 1165

Burstein D., McDonald L. H., 1975, AJ, 80, 17

Faber S. M., 1973, ApJ, 179, 731

Geller M. J., De Lapparent V., Kurtz M. J., 1984, ApJ Lett, 287, L55

Groth E. J., Peebles P. J. E., 1977, ApJ, 217, 385

Heiles C., 1975, A&A Supp, 20, 37

Heiles C., 1976, ApJ, 204, 379

Hilditch R. W., Hill G., Barnes J. V., 1976, MNRAS, 176, 175

Nichol R. C., Collins C. A., 1993, MNRAS, 265, 867

Peebles P. J. E., 1993, Principles of Physical Cosmology. Princeton University Press, Princeton

Schlegel D. J., Finkbeiner D. P., Davis M., 1998, ApJ, 500, 525

Shane C. D., Wirtanen C. A., 1967, Pub. Lick Obs., 22, 1

Stark A. A., Gammie C. F., Wilson R. W., Bally J., Linke R. A., Heiles C., Hurwitz M., 1992, ApJ Supp, 79, 77

Sylos Labini F., Montuori M., 1998, A&A, 331, 809

Trumpler R. J., 1930, Lick Observatory Bulletin, 420, 154

Wheelock S. L. et al., 1994, IRAS sky survey atlas: Explanatory supplement. JPL publication 94-11

Chapter 6

Redshift-space distortions

THE ARGUMENT. We use a set of large, high-resolution cosmological *N*-body simulations to examine the redshift-space distortions of galaxy clustering on scales of order 10-200h^{-1} Mpc. Galaxy redshift surveys currently in progress will, on completion, allow us to measure the quadrupole distortion in the 2-point correlation function, $\xi(\sigma, \pi)$, or its Fourier transform, the power spectrum, $P(k, \mu)$, to a high degree of accuracy. On these scales we typically find a positive quadrupole, as expected for coherent infall onto overdense regions and outflow from underdense regions, but the distortion is substantially weaker than that predicted by pure linear theory. We assess two models that may be regarded as refinements to linear theory, the Zel'dovich approximation and a velocity dispersion model. We find that neither provides an adequate physical description of the clustering pattern. If used to model redshift-space distortions on scales for $10 < \lambda < 200h^{-1}$ Mpc the estimated value of β ($\beta = f(\Omega_0)/b$ where $f(\Omega_0) \approx \Omega_0^{0.6}$ and b is the galaxy bias parameter) is liable to systematic errors of order ten per cent or more. We discuss how such systematics can be avoided by i) development of a more complete model of redshift distortions and ii) the direct use of galaxy catalogues generated from non-linear *N*-body simulations.

6.1 Introduction

In early galaxy redshift surveys (Jackson 1972; Gregory & Thompson 1978), some of the most striking artefacts observed were the so-called "fingers of God": ridges in the galaxy distribution pointing directly at the observer. The first evidence of the redshift-space distortion of galaxy clustering had been observed. If galaxy motions were perfectly described by the Hubble flow, then redshift would be an accurate indicator of distance, and the clustering pattern observed in redshift surveys would be statistically isotropic.

Peculiar velocities perturb the redshifts, and hence the inferred distances, of the galaxies, generating the observed anisotropic clustering pattern.

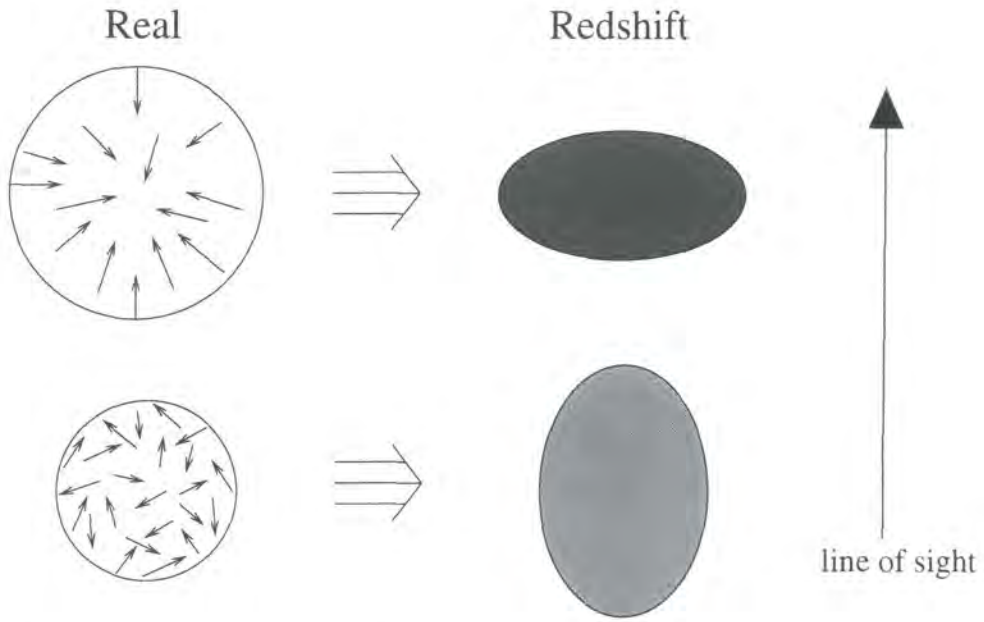

Figure 6.1: Qualitative picture of redshift space distortions. On the top is a linear perturbation, a galaxy cluster whose mass exerts gravitational force on nearby objects causing a collapse. Thus the cluster appears collapsed along the line of sight when viewed in redshift-space. On the bottom we show the non-linear case of a collapsed cluster whose members have thermal velocities. The cluster is smeared out along the line of sight when viewed in redshift-space.

Galaxy peculiar velocities can arise as a local effect, when the non-linear velocities of virialized groups and clusters create the fingers of God by stretching out these structures along the line of sight. On large scales, the clustering pattern is predicted (as suggested in Sargent & Turner 1977) to be compressed along the line of sight by coherent infall onto galaxy clusters and super-clusters, and outflow from voids and other underdense regions. Figure 6.1 is a simple representation of these two regimes and their effect on isotropy.

On both scales, the anisotropy of galaxy clustering encodes information about the galaxy velocity field and hence the underlying mass density field that gave rise to it. Measurements of redshift-space distortions can therefore be used to place constraints on the density parameter, Ω_0, and the bias parameter, b, which relates fluctuations in the galaxy distribution to those in the mass distribution. A comprehensive review of linear redshift-space distortions can be found in Hamilton (1997).

Redshift-space distortions directly measure the combination of parameters $\beta \equiv \Omega_0^{0.6}/b$. $\Omega_0^{0.6}$ is approximately the logarithmic derivative of the linear growth factor with respect to the expansion factor, and so relates particle velocities to the gradient of the mass distribution. β is thus the factor that relates particle velocities to the gradient of the galaxy overdensity field. Interesting constraints on this quantity have been obtained by analysis of optical redshift surveys (Loveday et al. 1996; Ratcliffe et al. 1998a) and *IRAS* surveys (eg. Hamilton 1993; Fisher et al. 1994; Cole, Fisher, & Weinberg 1995 and more recent papers such as Fisher & Nusser 1996; Bromley, Warren, & Zurek 1997). However, the statistical errors remain large and no consensus on the value of β has been reached (for a review see Strauss & Willick 1996). The next generation of large surveys, including the 2-degree-Field (2dF, Colless 1995) and Sloan Digital Sky Survey (SDSS, Gunn & Weinberg 1995), will enable redshift-space distortions to be measured with unprecedented accuracy. These surveys should allow β to be measured to an accuracy of better than 10% (see Chapters 7 and 8), and possibly for Ω_0 and b to be separately constrained. To achieve such accuracy and avoid systematic errors it is important that the theoretical modelling of redshift-space distortions be accurate. This is a non-trivial requirement, as these surveys will provide their most precise measurements of the distortions on scales of 30-$100h^{-1}\,\mathrm{Mpc}$, where the predictions of pure linear theory are not expected to hold exactly.

In this chapter we investigate the usefulness of existing models for the distortions using a set of high-resolution *N*-body simulations. These simulations accurately follow the evolution of clustering over the range of scales that will be probed by the next-generation surveys. Our aim is not to formulate a procedure for analysing real data, and so, rather than constructing mock galaxy catalogues, we instead use the full simulations to quantify the redshift-space distortions as accurately as possible. We thus assess the accuracy of the linear theory model and two proposed extensions to it. We make no attempt to examine the cosmological anisotropies that occur when the cosmological model adopted to map distance to redshift does not have the true values of Ω_0 or Λ_0 (Matsubara & Suto 1996; Ballinger, Peacock, & Heavens 1996). Neither do we investigate the validity of the "distant observer" approximation, which assumes that the scales of interest in the survey subtend a small angle at the observer.

In section 6.2 we define our notation convention and introduce the quadrupole statistic used to assess the level of redshift-space distortion. Section 6.3 details the parameters of the set of *N*-body simulations, and explains the methods we employ to construct biased galaxy samples. The linear theory prediction and the two other models are described in section 6.4. In section 6.5 we compare the analytic models with measurements of the redshift-space distortions in the *N*-body simulations. We discuss results in section 6.6.

6.2 Anisotropy in redshift-space

6.2.1 The power spectrum

Our method of analysis uses the power spectrum, $P(\mathbf{k})$, which is the Fourier transform of the correlation function,

$$P(\mathbf{k}) = \int \xi(\mathbf{r}) \mathrm{e}^{i\mathbf{k}.\mathbf{r}} \, d^3\mathbf{r}, \tag{6.1}$$

where we use the Fourier convention that the wavenumber, k, is the angular frequency corresponding to wavelength λ, ie. $k = 2\pi/\lambda$. The correlation function is given by

$$\xi(\mathbf{r}) = \langle \delta(\mathbf{x}+\mathbf{r}) \delta(\mathbf{x}) \rangle, \tag{6.2}$$

where $\delta(\mathbf{r})$ is the fractional overdensity,

$$\delta(\mathbf{r}) = \frac{\rho(\mathbf{r}) - \bar{\rho}}{\bar{\rho}}. \tag{6.3}$$

The power spectrum has been used by many authors to study the growth of gravitational clustering in simulations, and to quantify the clustering observed in redshift surveys (for recent examples, see da Costa et al. 1994; Tadros & Efstathiou 1995; Shectman et al. 1996).

When galaxy distances are measured in redshift space, their peculiar velocities (ie. relative to the pure Hubble flow) distort the pattern of galaxy clustering by displacing galaxy positions along the line of sight. Thus a galaxy whose true position is $\mathbf{r}$ appears in redshift space at the position:

$$\mathbf{s} = \mathbf{r} + U(\mathbf{r})\hat{\mathbf{r}}, \tag{6.4}$$

where the line-of-sight peculiar velocity $U(\mathbf{r}) = \mathbf{v}(\mathbf{r}).\hat{\mathbf{r}}$. Here we have adopted units in which the Hubble constant has unit value; distance is measured in units of $h^{-1}\,\mathrm{Mpc}$, where $h \equiv H_0/(100\mathrm{km\,s^{-1}Mpc^{-1}})$, and velocities in units of $100\mathrm{km\,s^{-1}}$.

In redshift space this displacement in a preferred direction causes the observed power spectrum to be anisotropic, with different values for wavevectors along the line of sight to those perpendicular to it. Thus, the redshift-space power spectrum can be thought of as a function of $k\,(= |\mathbf{k}|)$ and μ, the cosine of the angle between wavevector $\mathbf{k}$ and the line of sight,

$$P(\mathbf{k}) = P(k, \mu). \tag{6.5}$$

We use the convention that $P(\mathbf{k})$ or $P(k, \mu)$ refers to the redshift-space power spectrum, since this quantity depends on both the magnitude and direction of $\mathbf{k}$, whereas $P(k)$ represents the real-space power spectrum, depending only on the scalar k.

6.2.2 The quadrupole ratio

The redshift-space distortions can be conveniently quantified by a simple statistic. The anisotropy in $P(\mathbf{k})$ is symmetric in μ, ie. $P(k, \mu) = P(k, -\mu)$, so the distortion depends only on even powers of μ. To measure the extent of deformation from isotropy, we decompose the power spectrum into multipole moments using the Legendre polynomials, $L_l(\mu)$. Thus,

$$P(k, \mu) = \sum_{l=0}^{\infty} P_l(k) L_l(\mu), \tag{6.6}$$

where the sum is over even values of l. From the orthogonality relation for Legendre Polynomials, the multipole moments $P_l(k)$ can be found by evaluating

$$P_l(k) = \frac{2l+1}{2} \int_{-1}^{+1} P(k, \mu) L_l(\mu) \mathrm{d}\mu. \tag{6.7}$$

We find that estimates of $P_l(k)$ rapidly become noisy for multipoles with $l > 2$, so we choose to use as the key statistic for our analysis the quadrupole to monopole ratio, $P_2(k)/P_0(k)$.

We have chosen to carry out all analysis in k-space using power spectrum multipoles $P_l(k)$. However, our results can readily be translated into predictions of the multipole

moments of the correlation function, $\xi_l(r)$ using the identities derived in appendix B of Cole, Fisher, & Weinberg (1994).

6.3 Construction and analysis of galaxy catalogues

In order to study the effects of non-linear gravitational evolution on redshift-space clustering we examine a selection of *N*-body simulations with different values of the density parameter Ω_0 and the galaxy bias, b. These simulations are taken from the same set used to construct the mock galaxy catalogues described in Chapter 4.

The main cause of redshift-space distortion on small scales is the random velocities of galaxies in groups and clusters. Since our aim is to study deviations from linear theory on scales of $10\text{-}200h^{-1}\,\mathrm{Mpc}$, this important non-linear effect must be included at a realistic level. Therefore we have selected simulations from the series for which the fluctuations in the mass distribution are normalized to produce approximately the observed abundance of rich galaxy clusters.

To illustrate our results we focus mainly on two models, the $\Omega_0 = 1$ model and a low density $\Omega_0 = 0.3$, $\Lambda_0 = 0.7$ model. The key simulation parameters are summarized in the first two rows of table 6.1.

Ω_0	Λ_0	N_{gal}	σ_8^{gal}	b	β
1.0	0.0	192^3	0.55	1.0	1.00
0.3	0.7	192^3	1.13	1.0	0.48
1.0	0.0	128^3	0.96	1.8	0.55

Table 6.1. Summary of the parameters of the three simulations analysed. N_{gal} is the number of mass particles selected as galaxies. σ_8^{gal} is the variance in galaxy number counts in spheres of radius $8h^{-1}\,\mathrm{Mpc}$. b is the bias factor, defined as the ratio of σ_8^{gal} to the underlying *mass* variance in spheres, and β is the combination $\Omega_0^{0.6}/b$.

As discussed extensively in Chapter 4, a flat universe with zero cosmological constant requires a significant amount of biasing to match observations of the galaxy clustering amplitude. To this end, we employ three different methods of biasing the $\Omega_0 = 1.0$ simulation, in order to find out how robust our parameter estimation techniques are

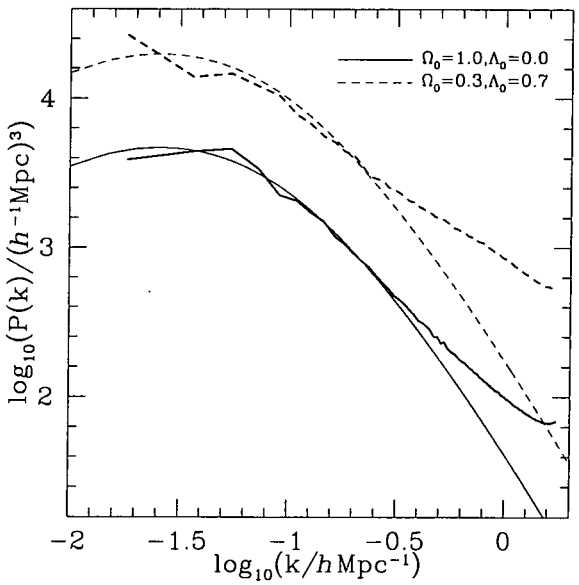

Figure 6.2: Power spectra of the real-space mass distributions of the *N*-body simulations described in section 6.3. In each case the thin line is the linear theory, $\Gamma = 0.25$ CDM spectrum (equation 4.1) which was used to set up the initial conditions of the simulations, extrapolated to the present day, and the thicker line is the evolved, non-linear power spectrum of the simulation measured at $z = 0$.

to the precise bias prescription. The methods used are similar to those described in Chapter 4, assigning selection probabilities to dark matter particles based on the value of the local mean density. In each case the bias is chosen to obtain a $\sigma_8^{\rm gal}$, the variance in galaxy counts in spheres of radius $8h^{-1}\,\mathrm{Mpc}$, consistent with the results of Maddox, Efstathiou, & Sutherland (1996), who find $\sigma_8^{\rm gal} = 0.96$ for the APM Galaxy Survey. Thus, the bias factor, defined as $\sigma_8^{\rm gal}/\sigma_8$, has value $b = 1.81$. The parameters of our biased simulation are given in the third row of table 6.1. The three methods used are:

- **High Peaks**. We bias the dark matter distribution with a high peaks model, as described in Chapter 4, section 4.4, model 3.

- **Exponential**. This model is a variant on the Lagrangian exponential model described in section 4.4, model 1. Since we only need to bias one simulation, with a moderate degree of bias, we use the same technique with a simpler form of the probability formula:

$$P(\nu) = A\,\exp(\alpha\nu + \beta\nu|\nu|). \tag{6.8}$$

- **Threshold**. This model is, again, as described in section 4.4, model 4. The particle distribution resulting from this scheme is expected to contain large voids since the sharp cut-off at the threshold is extremely effective at evacuating underdense regions (Weinberg & Cole 1992).

The three methods described here are intended to span a broad range of plausible biasing prescriptions that might occur in the real universe. If so, and if we can develop techniques that are unaffected by the choice of scheme, these techniques should be insensitive to the way in which bias really comes about.

The density of the biased catalogues is chosen to be one galaxy per $25(h^{-1}\,\mathrm{Mpc})^3$ volume, roughly four times $\phi_\star$, the observed number density of $L_\star$ galaxies (eg. Peebles 1993, §5; Ratcliffe et al. 1998b). The high sampling density has been adopted as we are interested in investigating systematic effects on the redshift-space distortions, and so want to minimize the statistical uncertainties produced by sparse sampling.

6.3.1 Zel'dovich approximation simulations

In section 6.5 we will compare the redshift-space distortions measured in the *N*-body simulations with a similar analysis of Monte Carlo implementations of the Zel'dovich approximation. Our Monte Carlo realizations have the same 192^3 particle grid and initial density field parameters as the corresponding *N*-body simulations. Exactly the same method is used to perturb the particles as that employed to set the initial displacements in the *N*-body simulation, only with a much larger perturbation amplitude corresponding to $z = 0$ rather than the starting redshift of the simulation. For the *N*-body simulations we populate all the modes in the 192^3 k-space grid including those in the corners of the cube. However for these realizations of the ZA, we make our treatment consistent with the analytic calculation that we outline in section 6.4.2, by smoothing the density field in the same way, ie. by truncating the power spectrum isotropically at the Nyquist frequency of the grid, $k_{\mathrm{Nyq}} = 2\pi/2L_{\mathrm{cell}}$, where L_{cell} is the length of one grid cell.

These realizations of the ZA can be biased using exactly the same prescriptions that we use for the *N*-body simulations. The catalogues thus created are then subjected to the same multipole analysis as our *N*-body simulations.

6.3.2 Estimation of multipole moments

We ensure that the distant observer approximation is satisfied by assigning redshift-space positions to galaxies based on their distance along the x-axis of the simulation. Effectively the simulation box is placed at infinity and the line of sight aligned with the x-axis. To minimise the noise in our estimates we repeat the analysis with the simulation rotated to align the line of sight with the y- and then z-axes and average the results.

We use a fast Fourier transform (FFT) analysis with a cloud-in-cell (CIC) assignment scheme to obtain the power spectrum from the particle distribution, as described in Chapter 3.

For the biased galaxy simulations a constant equal to the inverse of the number density of galaxies in the catalogue is subtracted at this point to account for the shot noise introduced by the Poisson sampling of the galaxies. This correction is not necessary in the unbiased cases as here we use all the particles from the original glass distribution rather than a Poisson sample.

The multipole moments of the power spectrum are estimated by approximating the integral of μ in equation 6.7 by a discrete sum over modes. This method works perfectly well at high-k, but for the first few shells, where the sampling of k-space results in poor sampling in μ, it leads to a small systematic error in $P_2(k)/P_0(k)$. An alternative method of estimating $P_2(k)$ and $P_0(k)$, which can readily be employed for low-k, is to make a least squares fit to the μ dependence of $P(k,\mu)$ using a basis of the Legendre polynomials L_0,L_2 and L_4. This second method produces a less noisy estimator but still suffers from a small systematic error due to the poor sampling in μ. Empirically we find this error to be independent of the input power spectrum, and so we choose to correct for it by applying a small (5% for the lowest wavenumber) correction to our first five bins in k.

The lowest k-mode probed using this method is the fundamental mode of the box, $k_{\rm F} = 2\pi/L_{\rm BOX}$, ie. when one wavelength spans the whole box. The highest is the Nyquist frequency, $k_{\rm Nyq} = k_{\rm F} \times (N/2)$, where N is the number of cells along one side of the simulation box. We do not expect our treatment to work all the way up to the Nyquist frequency, since the deconvolution correction can never recover all the information lost by assigning particles to a discrete grid. This effect can be seen in figure 6.2 where

the power spectrum turns up for the very highest k-values. For this reason we limit our analysis rather conservatively to modes with $k < k_{\rm Nyq}/2$, as explained in Chapter 3.

6.4 Analytic models

Assuming that the velocity field, $\mathbf{v}(\mathbf{r})$, is generated via gravitational instability, it can be related to the underlying mass density field. Here we consider three analytic models for the relationship of the velocity field to the density field, which lead to quantitative descriptions of the redshift-space distortion of galaxy clustering. The first is based purely on linear theory. In the second, the effect of non-linear velocities in galaxy clusters is modelled by adding a random velocity dispersion to the velocity predicted by linear theory. The magnitude of this dispersion, σ_v, is not predicted by the model, but is expected to bear some relation to the typical thermal velocity of galaxies within groups and clusters. The third model is the Zel'dovich approximation (ZA) (Zel'dovich 1970). This model provides a complete description of the evolved density and velocity fields, which is expected to be accurate in the quasi-linear regime where the overdensity predicted by linear theory is of order unity. Thus this model has the potential to give an accurate physical description of redshift-space clustering. These three models are described in detail below and compared in figure 6.3. In each case we assume that the distant observer approximation is well satisfied and that we are dealing with volume limited galaxy samples. The effects of relaxing these assumptions are discussed in Kaiser (1987).

6.4.1 Linear theory

In the regime of linear theory, Kaiser (1987) showed that the redshift-space power spectrum is related to the real-space power spectrum in a very simple way:

$$P(k,\mu) = P(k)(1+\beta\mu^2)^2, \quad \beta \equiv f(\Omega_0)/b \approx \Omega_0^{0.6}/b. \tag{6.9}$$

The function $f(\Omega_0) \approx \Omega_0^{0.6}$ is the logarithmic derivative of the fluctuation growth rate (Peebles 1993, §14 ; Bouchet et al. 1995). The bias factor, b, is an assumed constant relating fluctuations in the galaxy density to those in the mass. We derive this result in Appendix A. Applying equation 6.7 for the $l = 0$ and $l = 2$ modes results in

$$\frac{P_2}{P_0} = \frac{4\beta/3 + 4\beta^2/7}{1 + 2\beta/3 + \beta^2/5}. \tag{6.10}$$

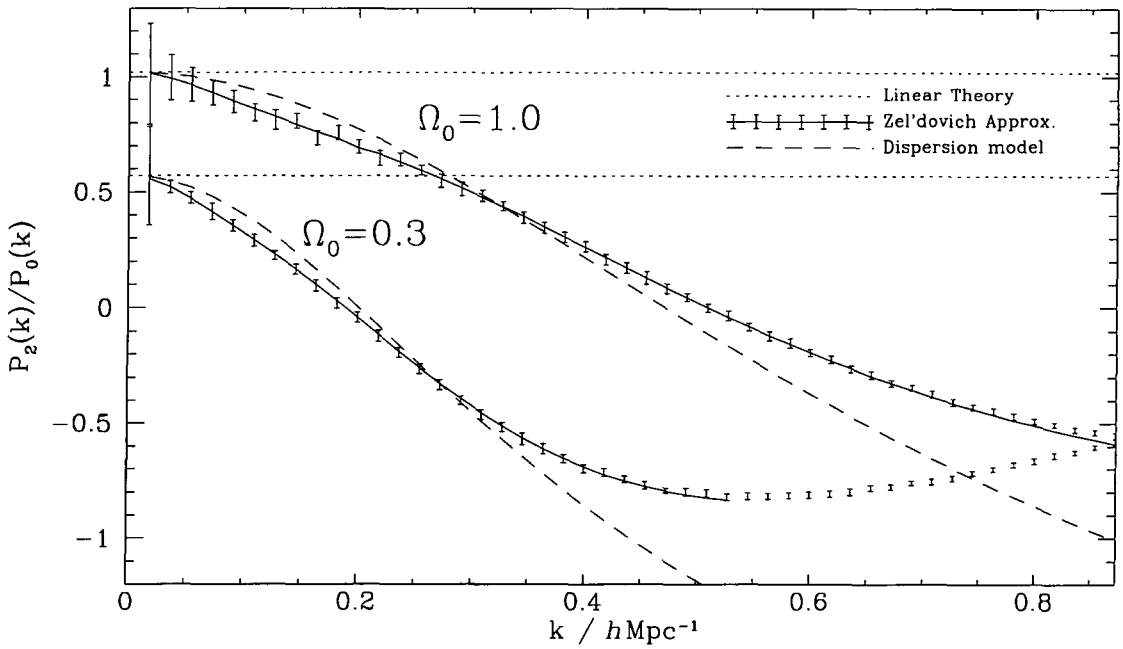

Figure 6.3: Model predictions for the redshift space power spectrum quadrupole to monopole ratio $P_2(k)/P_0(k)$. The two sets of curves are for two unbiased ($b = 1$) CDM models with $\Gamma = 0.25$ power spectra. The upper curves are for $\Omega_0 = 1.0$, $\sigma_8 = 0.55$, while the lower model is $\Omega_0 = 0.3, \Lambda_0 = 0.7$ and $\sigma_8 = 1.13$. In both cases the curves show the constant ratio predicted by linear theory (dotted), the analytic Zel'dovich Approximation result (solid), and examples of the dispersion model (dashed) with $\sigma_v = 300\mathrm{km\,s^{-1}}$ for $\Omega_0 = 1.0$ and $\sigma_v = 500\mathrm{km\,s^{-1}}$ for $\Omega_0 = 0.3$. The error bars are centred on the averages of forty random Monte Carlo realizations of the Zel'dovich approximation. These error bars indicate the standard deviation of the sample, and thus are typical of the error expected in a single realization. The analytic Zel'dovich Approximation curve only extends down to the scale at which our integration technique breaks down, as explained in section 6.4.2.

Thus linear theory predicts a constant quadrupole-to-monopole ratio, P_2/P_0, independent of scale. This model is shown by the dotted lines in figure 6.3. Linear theory is valid only so long as each of the four following constraints is satisfied, so that the corresponding form of non-linearity can be ignored (Cole, Fisher, & Weinberg 1994, section 2.2);

- **Dispersion.** Peculiar velocities in virialized systems affect the measured clustering at wavenumbers $k \gtrsim 1/\sigma_v$, where σ_v is the velocity dispersion. This effect must be small, hence $k\sigma_v \ll 1$.

- **Dynamical.** The linear relationship between velocity and overdensity, ie. the first order approximation of the continuity equation (A.19), must be accurate.

- **Gradient**. Second order terms in the gradient of the line-of-sight velocity field must be negligible, ie. $dU/dr \ll 1$.
- **Contrast**. Second order terms in the galaxy overdensity field must be small, ie. $\delta(\mathbf{r}) \ll 1$.

All these constraints will be satisfied on the very largest scales, but, depending on the present-day amplitude of galaxy clustering and on the values of Ω_0 and b, we expect some or even all of them to be violated on scales of less than $100h^{-1}\,\mathrm{Mpc}$.

6.4.2 The Zel'dovich approximation

The linear theory approach to modelling the growth of density perturbations is only valid if $\delta(\mathbf{r}) \ll 1$. The refinement to linear theory proposed by Zel'dovich (1970) was to formulate a Lagrangian approach. Here each particle is displaced from its original position along a straight line defined by the direction of the initial velocity field. In comoving co-ordinates, the final position, $\mathbf{r}$, is related to $\mathbf{q}$, the initial position, by

$$\mathbf{r} = \mathbf{q} + \mathbf{d}(\mathbf{q}, t), \quad \mathbf{d}(\mathbf{q}, t) = \frac{\mathbf{v}(\mathbf{q})}{f(\Omega_0)}. \tag{6.11}$$

The ZA is expected to break down at the stage when shell-crossing occurs ($\delta_r \sim 1$). This breakdown occurs because, under this model, the particles pass right through caustics as they continue to move in the direction of their original velocity. In contrast, in *N*-body simulations non-linear effects cause the particles to behave as if they were "sticky", and galaxies congregate in high density shells or walls. If the power spectrum is not truncated or filtered at high spatial frequencies, shell-crossing occurs on small scales, with the result that small-scale and some large-scale power is erased, and the degree of anisotropy is lower than expected. We choose to smooth the initial density field for the Zel'dovich realizations on small scales by applying a sharp cut-off to the power spectrum at the Nyquist frequency of the grid used in the *N*-body simulations.

Recent efforts (Fisher & Nusser 1996, henceforth FN96 ; Taylor & Hamilton 1996) have obtained an analytic result for the redshift-space distortion produced with the ZA. We present this lengthy calculation in Appendix B. One aspect of this result is that a first-order expansion yields the linear theory prediction (equation 6.9), so, whatever power spectrum or biasing method we use, we expect the two models to converge on very large

scales. The full end product of the analytical treatment is to produce an expression for P_0 and P_2 in terms of an awkward multi-dimensional integral. We perform this integration using an Euler technique (Press et al. 1992) to deal with diverging oscillations of the integrand. Over the range of k we are interested in, the method is quite stable, and avoids the complexity described in the appendix of Taylor & Hamilton (1996). However, our technique breaks down at a scale $k \gtrsim 0.6/\sigma_8$. At this point oscillations in the radial integrand become too rapid and of too great an amplitude for the method to cope.

This analytic calculation of the quadrupole ratio $P_2(k)/P_0(k)$ is compared with the results of averaging many Monte Carlo realizations of the ZA in figure 6.3. The close agreement of the two methods is very reassuring. It not only demonstrates the accuracy of our numerical integration technique, but also our implementation of realizations of the ZA and the entire procedure of estimating $P_2(k)/P_0(k)$ from particle distributions.

In figure 6.3 the P_2/P_0 ratio of the $\Omega_0 = 0.3$ model reaches a minimum at $k \approx 0.5h\,\mathrm{Mpc}^{-1}$ and then slowly increases. The ratio behaves in a similar manner for $\Omega_0 = 1.0$, but with a minimum at $k \approx 1.0h\,\mathrm{Mpc}^{-1}$, which lies off the right-hand side of figure 6.3. We attribute this behaviour to the breakdown of the ZA at scales on which substantial shell crossing has occurred. This effect occurs on larger scales in the $\Omega_0 = 0.3$ model as it has the larger amplitude of density fluctuations: $\sigma_8 = 1.13$, compared with $\sigma_8 = 0.55$ in the $\Omega_0 = 1.0$ model. In reality, one expects the ratio $P_2(k)/P_0(k)$ to become increasingly negative on small scales due to the fingers of god produced by the high random velocities in virialized groups and clusters.

The ZA has several advantages over pure linear theory. The velocity, $\mathbf{v}$, is given in terms of the density field at the *initial* position, $\mathbf{q}$, rather than the final position, $\mathbf{r}$. This dynamical relation remains quite accurate until shell crossing occurs, whereas the linear theory relation is only accurate for $\delta(\mathbf{r}) \ll 1$. In contrast to the linear theory derivation in Appendix A, no further assumptions regarding either the amplitude of the velocity gradient nor the density fluctuations are made in deriving the resulting power spectrum. Thus, in this respect, the Zel'dovich approximation is able to deal with both gradient and contrast non-linearity. For describing redshift-space distortions the main shortcoming of the ZA is that it does not model the random velocities produced in non-linear relaxed structures; instead it produces its own velocity dispersion on small scales due to the shell crossing. Thus it cannot make accurate predictions in the regime where dispersion non-linearity is

dominant. Also in the form described above it does not explicitly deal with the effects of biasing. The simplest modification to the ZA to account for bias would be to hope that, as in the linear theory case, to a good approximation we can simply replace $f(\Omega_0)$ with $\beta = f(\Omega_0)/b$. We investigate this modification in section 6.5.

6.4.3 Dispersion model

The velocity dispersion of galaxies in galaxy clusters is typically $800\mathrm{km\,s^{-1}}$ (White, Efstathiou, & Frenk 1993). Thus, from the constraint that $k\sigma_v \ll 1$, we would expect the linear theory result (equation 6.9) to apply only on scales where $k \ll 0.1h\,\mathrm{Mpc}^{-1}$. Since we are interested in clustering on scales from $10\text{-}200h^{-1}\,\mathrm{Mpc}$ (corresponding to wavenumbers $0.03 \lesssim k \lesssim 0.6h\,\mathrm{Mpc}^{-1}$), an accurate model will have to take into account these non-linear velocities.

On small scales the redshift-space correlation function has been found to be well modelled as a convolution of the real-space isotropic correlation function with an exponential probability distribution function for line-of-sight velocities (Bean et al. 1983; Davis & Peebles 1983; Fisher et al. 1994).

We follow Park et al. (1994) in taking the 1-dimensional, pointwise galaxy velocity distribution to be an exponential. Since this convolution with the velocity distribution in r-space is equivalent to a multiplication in k-space, the power spectrum is multiplied by the square of the Fourier transform of the (single particle) velocity distribution function. Peacock & Dodds (1994) show that the effects of linear clustering and this model of small-scale velocity dispersion can be combined to give a redshift-space power spectrum

$$P(k,\mu) = P(k)(1+\beta\mu^2)^2\left[1+\frac{(k\mu\sigma_v)^2}{2}\right]^{-2}. \tag{6.12}$$

For this expression the integration over μ (required in equation 6.7) is considerably harder than for the linear theory case, but an analytic expression for $P_2(k)/P_0(k)$ can easily be obtained with the aid of mathematics packages such as MAPLE. In Appendix C we present the results of applying MAPLE to this expression.

This model extends linear theory by relaxing the dispersion constraint listed in the previous section, but still implicitly assumes the other three. The model of the small-scale velocity dispersion is also simplistic, in that it takes no account of the fact that the

velocity dispersion is correlated with the density field, ie. the dispersion is higher in high density regions such as galaxy clusters. Thus the value of σ_v used in this model is only an *effective* velocity dispersion that depends on how galaxies populate the clusters, and thus on the bias parameter, b. Examples of this model are shown by the short dashed curves in figure 6.3. In these examples, σ_v is not a fitted parameter, but rather set to arbitrary values so as to approximately produce the correctly-shaped curve.

6.4.4 Fitting the models

Our objective is to illustrate the systematic differences between the *N*-body results and the models rather than to propose a methodology to estimate model parameters from real estimates of the redshift-space distortion. In order to analyze the data from our simulations on quasi-linear scales, we will perform χ^2 fits for the dispersion and ZA models to the *N*-body points and restrict the range of k to the regime over which each model can reasonably match the data. To perform these fits we need to put error bars on our *N*-body points. We will find in section 6.5 that, on large scales, the *N*-body and numerical Zel'dovich curves are identical for simulations with the same initial particle positions. Therefore, at least on these scales, repeated Zel'dovich runs with random initial conditions will mimic repeated *N*-body simulations, but at a tiny fraction of the computing time. Our error bars, then, reflect the variance in a set of forty random Zel'dovich runs.

The dispersion model provides a functional form for the shape of the quadrupole estimator, but says nothing about the clustering itself. Thus, in fitting to the data, no assumptions need be made about the shape or amplitude of the underlying power spectrum; we simply find the best fit model using β and σ_v as free parameters.

In contrast, the ZA is much more physically motivated in that it attempts to model both the clustering and the associated velocity field from first principles. We first attempt to utilize a simple fitting formula for the shape of $P_2(k)/P_0(k)$ presented in FN96. This formula depends on β and the zero-crossing of the quadrupole, $k_{\rm nl}$. We find that using this approximation introduces a significant offset between the best-fit and true values of β. We therefore opt to evaluate the full expression derived by FN96 for the expected quadrupole to monopole ratio at each stage in making the minimum-χ^2 fit. This expression gives the distortion as a function of β and the power spectrum shape and normalization (Γ and σ_8). Here we simply adopt the values of Γ and σ_8 used in the simulations and use β as the

single free parameter in the model. For real observations one could simultaneously fit for these parameters using estimates of the redshift-space power spectrum monopole, $P_0(k)$.

6.5 Results

In figure 6.4 we compare the model predictions for the quadrupole ratio, $P_2(k)/P_0(k)$, with the results of the two unbiased *N*-body simulations. The points with error bars show the *N*-body results. The model that produces the lower quadrupole ratios has $\Omega_0 = 0.3$, $\Lambda_0 = 0.7$ and $\sigma_8 = 1.13$, and that with the stronger quadrupole signal has $\Omega_0 = 1$ and $\sigma_8 = 0.55$. The error bars placed on the *N*-body results are indicative of the statistical error we expect on an estimate of the quadrupole ratio, from a single realization, and are obtained by taking the standard deviation of forty Monte Carlo realizations of the ZA. It is clear that, apart from the first few points with $k \lesssim 0.07h\,\mathrm{Mpc}^{-1}$, the deviation from the constant ratio predicted by linear theory is large.

The solid lines in figure 6.4 are each for one ZA realization starting from the same initial density field as the corresponding *N*-body simulation. This model reproduces the *N*-body results extremely accurately at low-k. For the $\Omega_0 = 0.3$ case the ZA and *N*-body results match well up to $k \approx 0.25h\,\mathrm{Mpc}^{-1}$, which is beyond the scale at which $P_2(k)/P_0(k)$ becomes negative. This result is in complete agreement with the findings of FN96. The only *N*-body results they studied were for a similarly normalized $\Omega_0 = 0.3, \Lambda_0 = 0.7$ model. In the case of $\Omega_0 = 1$ we find much less impressive agreement between the ZA and *N*-body simulations. The results begin to diverge at $k \gtrsim 0.15h\,\mathrm{Mpc}^{-1}$ and differ very significantly at $k = 0.425h\,\mathrm{Mpc}^{-1}$, where $P_2(k)/P_0(k) = 0$ for the *N*-body simulation.

Figure 6.5 shows another comparison between these *N*-body and ZA realizations. We show the ratio of their estimated final power spectra to the expected linear power spectra, ie. the initial power spectra evolved to $z = 0$ assuming linear theory. We see that in the *N*-body simulations the non-linear growth of structure leads to an increase in power on small scales. This effect is strongest for $\Omega_0 = 0.3$, which has the highest σ_8 and is therefore the most non-linear. In contrast, the behaviour of the ZA simulations is the exact opposite; shell crossing erases power on small scales. In this respect the agreement between ZA and *N*-body is particularly poor for the $\Omega_0 = 0.3$ model. Even at mildly non-linear scales the discrepancy is quite severe: evidently the accuracy of the ZA at modelling the ratio

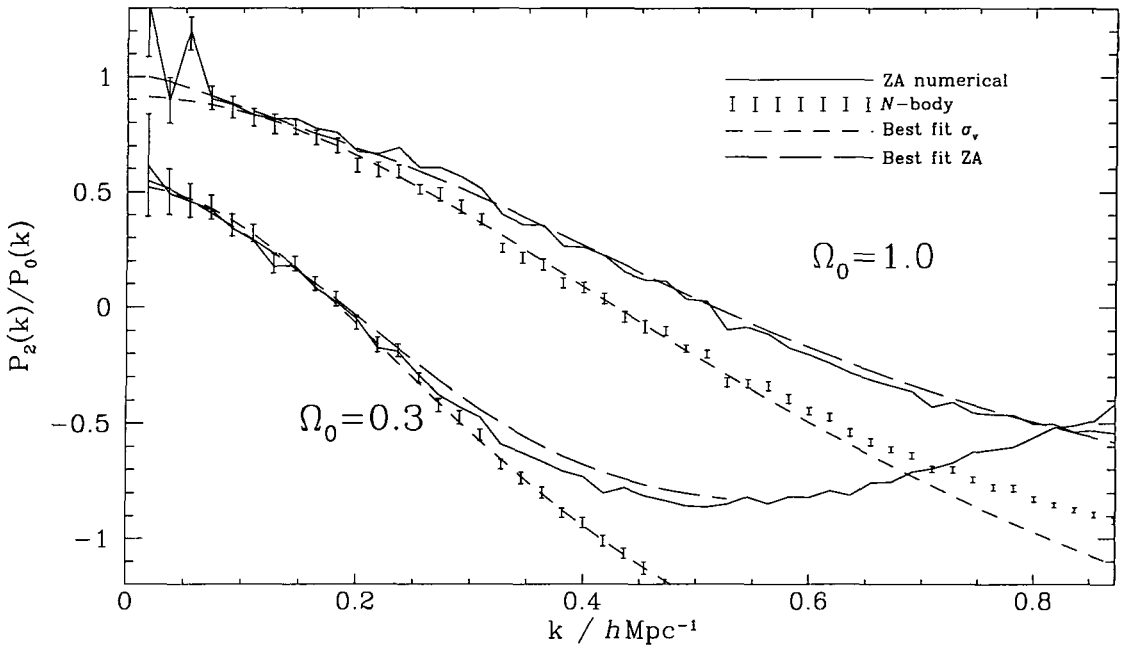

Figure 6.4: The quadrupole ratio $P_2(k)/P_0(k)$ for two unbiased *N*-body simulations compared with the corresponding Zel'dovich approximation simulations and two model fits. The upper curves are for $\Omega_0 = 1$ and $\sigma_8 = 0.55$ and the lower curves for $\Omega_0 = 0.3$, $\Lambda_0 = 0.7$ and $\sigma_8 = 1.13$. The error bars on the *N*-body results are indicative of the statistical error in our estimates and are estimated from the standard deviation between forty ZA realizations. The solid lines show the results from single ZA realizations starting from the same density fields as the *N*-body simulations. The long dashed and short dashed curves are model fits for the ZA and dispersion model respectively. Only the first ten points have been used in constraining the ZA fits, and the first thirty for constraining the dispersion model, as explained in section 6.5. The corresponding best fit parameters and confidence intervals are shown in figure 6.7.

$P_2(k)/P_0(k)$ is either a coincidence, or this statistic is less sensitive to the shortcomings of the method than the power spectrum itself is. Until this problem is investigated more thoroughly, we suggest that the success of the ZA should be treated with scepticism.

In our implementation of the ZA we have applied very little smoothing of the initial density field. We have simply truncated the input power spectrum at the Nyquist frequency of the particle grid used in the Monte Carlo realizations described in section 6.3.1 to facilitate inter-comparison. However, Melott, Pellman, & Shandarin (1994) have shown that, at least for some statistics, the correspondence between the ZA and *N*-body simulations

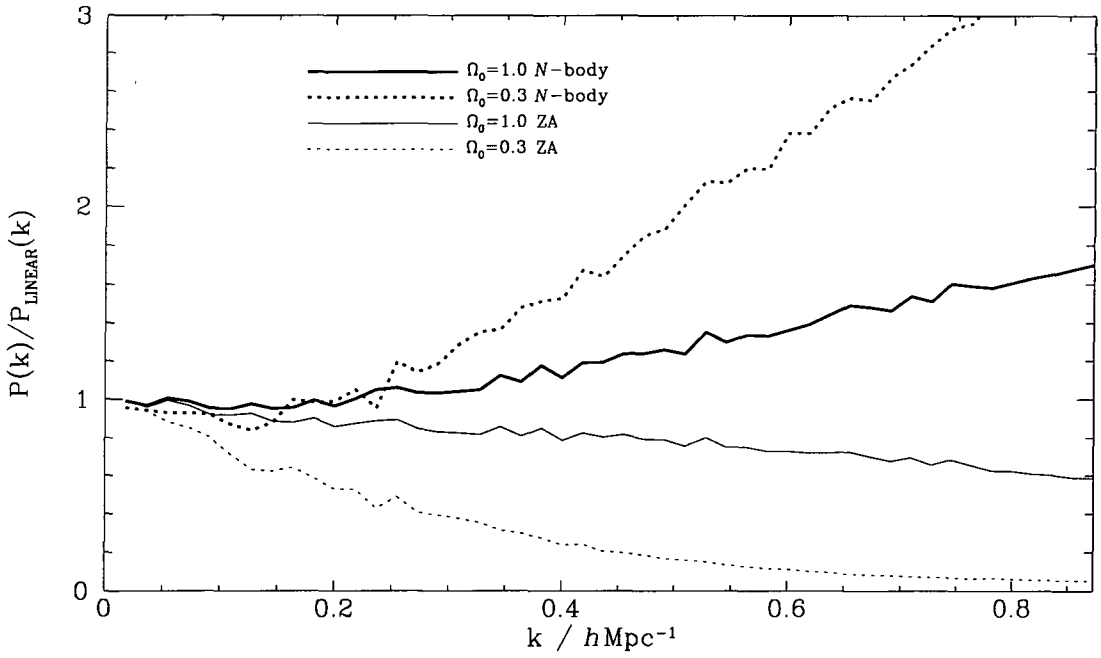

Figure 6.5: The ratio of estimates of the real-space evolved power spectra, $P(k)$, to the linear theory predictions, $P_{\rm LINEAR}(k)$, for the *N*-body simulations and the corresponding ZA simulations. The models are the same $\Omega_0 = 1$ and $\Omega_0 = 0.3$ models studied in figure 6.4.

can be improved by more severe smoothing of the initial density field. They define a non-linear wavenumber, $k_{\rm nl}$, by

$$4\pi \int_0^{k_{\rm nl}} P(k) k^2 {\rm d}k = 1 \qquad (6.13)$$

and then smooth the initial density field with a Gaussian window, $\exp(-k^2/2k_{\rm s}^2)$, with $k_{\rm s} = pk_{\rm nl}$. They find that the best choice of the parameter p depends only weakly on the shape of the power spectrum and is $p \simeq 1.25$.

The consequences of adopting such a Truncated ZA power spectrum for our distortion statistic are shown in figure 6.6. The introduction of additional smoothing worsens the agreement between the *N*-body results and those of the ZA. In particular, for the degree of smoothing advocated by Melott et al. ($p = 1.25$) the agreement between *N*-body and ZA is very poor. The smoothing applied is washing out the distortions we are trying to measure. However, we find that in real space a mild amount of smoothing can produce a power spectrum that is slightly closer to the *N*-body result, though this effect is rather small.

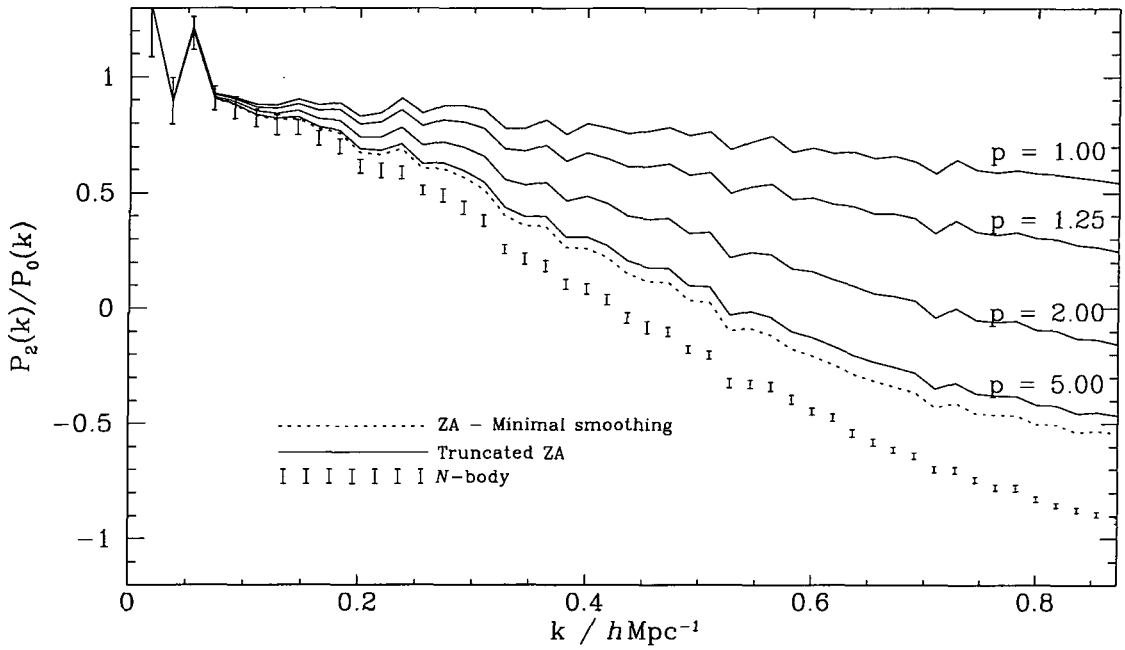

Figure 6.6: The dependence of the Zel'dovich approximation prediction for the ratio $P_2(k)/P_0(k)$ on the extent to which the initial density field is smoothed before applying the ZA. The error bars show the *N*-body result for the $\Omega_0 = 1.0$ model taken from figure 6.4. The dotted curve shows the ZA result for the minimal amount of smoothing, ie, truncation at the Nyquist frequency. The remaining curves show the effect of gradually increasing the smoothing using an additional Gaussian smoothing with $k_s = pk_{nl}$ (see equation 6.13) and $p = 5.0, 2.0, 1.25$ and 1.0.

The ZA and dispersion model fits are shown by the smooth long and short dashed curves in figure 6.4. The corresponding best fit model parameters and confidence intervals are shown in figure 6.7 and table 6.2. Here the horizontal lines bracket the 68% and 99.7% (1- and 3-σ) confidence intervals of β for the ZA fit. The ellipses show the corresponding confidence intervals for the two-parameter dispersion model. Both ZA fits give a best-fit β that is within 1-σ of the theoretical value, so there seems to be no appreciable systematic error in our estimate. However, this result is achieved by limiting the range of the fit to the first ten bins in k-space, ie. $k < 0.182h\,\mathrm{Mpc}^{-1}$, in both models. At smaller scales than this, particularly in the $\Omega_0 = 1$ model, the fits can be seen to strongly overestimate the redshift-space distortion. Thus if a fit were made to data covering a wider range of scales, β would be severely underestimated. In contrast, the dispersion model fits remain in reasonable agreement with the data up to much larger k. We fit our data up to the thirtieth data bin, corresponding to a length scale of $11.5h^{-1}\,\mathrm{Mpc}$. For

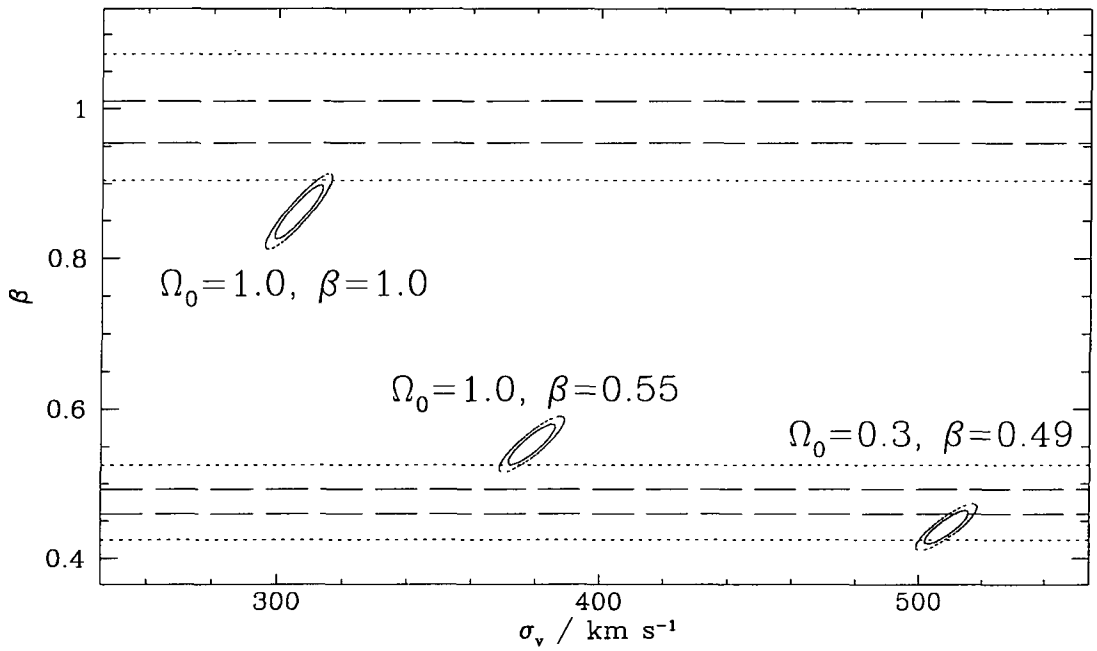

Figure 6.7: The 68% and 99.7% confidence intervals (1- & 3-σ) of the model parameters for the fits shown in figure 6.4 and figure 6.8. The ellipses are for the two-parameter dispersion model for the three different simulations, and the horizontal lines for single-parameter ZA model for the two unbiased models for which this provides a reasonably good fit. The best fit values of β and the χ^2 per degree of freedom for the best fit models are given in table 6.2.

$\Omega_0 = 0.3$, the dispersion model analysis seems to be offset towards a low estimate of β, but this effect is fairly small given the size of the error contours. The fit itself is a very good over the whole range of k in question. However, for $\Omega_0 = 1$, β is systematically underestimated by more than 10% at a high level of significance. This offset can be understood by reference to the models shown in figure 6.3. In comparison to the ZA, which is an accurate fit at low-k, the dispersion model curve changes slope too rapidly and is too shallow at low-k, leading to an underestimation of β. We found this behaviour to be the same for a variant of the dispersion model in which the small scale random velocity is assumed to be Gaussian rather than exponentially distributed. This alternative Gaussian dispersion model produces a worse fit overall, and a more biased estimate of β. The same effect is also expected to introduce an offset in the $\Omega_0 = 0.3$ simulation, but it is rather smaller for this case and so is not easily detected.

As shown in table 6.2, we have calculated the one-dimensional rms peculiar velocity of particles in each simulation, $\sigma_v^{\rm SIM}$, in an attempt to look for a physical significance of the

σ_v value found in the dispersion model fit. We do not expect this velocity to correspond to that obtained from the dispersion model fit, as this quantity should reflect the small-scale peculiar velocity, after velocities resulting from large-scale bulk flows have been subtracted. In order to compare like with like, we also calculate a small-scale dispersion, $\sigma_v^{\rm SS}$, in the following manner. A friends-of-friends algorithm is used to identify cluster membership for each galaxy, and each cluster galaxy has its velocity in the simulation replaced with its *relative* velocity with respect to the parent cluster. Galaxies not tagged as being in a cluster are thrown out of the sample. Thus, $\sigma_v^{\rm SS}$ should be closely related to the dispersion from the model fit. The results presented in table 6.2 clearly show that, in fact, this is not the case, and there is no simple relationship between the best fit dispersion and the true velocities of the galaxies over the range covered by our simulations.

Ω_0	β	model	$\beta_{\rm fit}$	χ^2/ν	$\sigma_v^{\rm FIT}$	$\sigma_v^{\rm SIM}$	$\sigma_v^{\rm SS}$
1.0	1.00	ZA	0.98	2.28			
1.0	1.00	disp	0.87	2.03	306	365	300
0.3	0.49	ZA	0.48	0.86			
0.3	0.49	disp	0.44	0.99	509	431	388
1.0	0.55	disp	0.56	1.39	379	425	331

Table 6.2. Best fit β and goodness of fit (χ^2 per degree of freedom) indicator for our simulations under the Zel'dovich and dispersion models. For the dispersion model we also show the best fit values of σ_v and compare with the one-dimensional velocity dispersion of the simulations, $\sigma_v^{\rm SIM}$, and the small-scale dispersion, $\sigma_v^{\rm SS}$, as explained in section 6.5. All velocities are measured in $\mathrm{km\,s^{-1}}$. Error contours for the fits are shown in figure 6.7.

6.5.1 Biased models

In figure 6.8 we show the model predictions for the quadrupole ratio, $P_2(k)/P_0(k)$, for a biased model with $\Omega_0 = 1.0$. The heavy curves show the results of selecting biased galaxy catalogues by the three methods described in section 6.5.1. The differences between the models at large scales are purely statistical, since different galaxies have been selected in the different samples. At high k the two Lagrangian methods agree well, but the Eulerian one systematically shows less distortion. This difference is to be expected as this method populates evenly all regions with density higher than the threshold, rather than giving

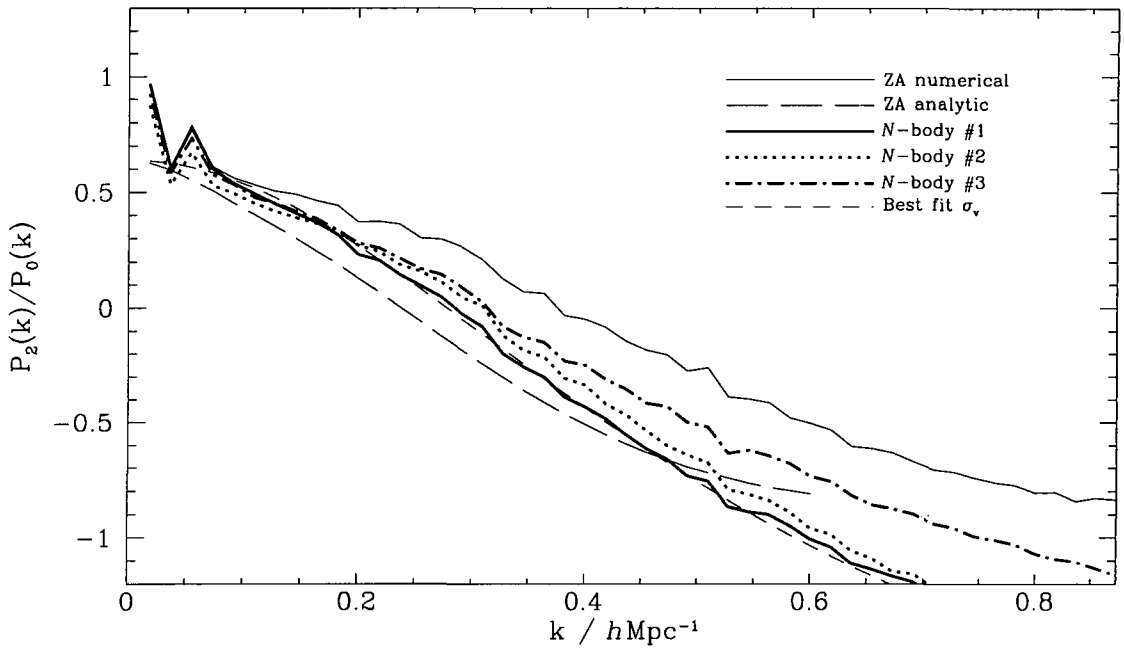

Figure 6.8: The quadrupole ratio, $P_2(k)/P_0(k)$, for biased $\Omega_0 = 1$ galaxy catalogues with $b = \sigma_8^{\rm gal}/\sigma_8 = 1.81$, $\beta = 0.55$. The *N*-body lines show the results for our three different methods of constructing biased galaxy catalogues from the *N*-body simulation, as outlined in section 6.5.1. The thin solid line shows the result of a ZA realization that has been biased in the same way as one of the *N*-body catalogues. The long dashed curve shows the prediction of the ZA made by assuming $\sigma_8 = \sigma_8^{\rm gal}$ and $\Omega_0^{0.6} = \beta$ as proposed by FN96. The short dashed line is a fit of the dispersion model to one of the *N*-body catalogues.

extra weight to the areas with higher density (and thus velocity dispersion), as the other two models do.

The long dashed curve shows the prediction for the analytic ZA where, as suggested by FN96, the model adopted assumes that galaxies are unbiased, $\sigma_8 = \sigma_8^{\rm gal}$, but with $\Omega_0^{0.6} = 1/1.81$ to match the value of $\beta = 1/b$. This curve should be compared with the results from a biased catalogue constructed from a realization of the ZA (thin solid curve). Clearly these two curves do not agree, except at the very largest scales. We cannot, then, use the simple linear theory modification to the ZA to account for bias if we want to use data in any but the most linear regime. This result is perhaps to be expected as bias will not only boost the galaxy density fluctuations with respect to the underlying mass distribution, but will also preferentially place galaxies in dense structures where random velocities produced by virialized structures are largest. The small scale velocity field produced by shell crossing in the ZA is not a good model of the random velocities

produced in non-linear regions. For this reason the biased ZA realization is a poor fit to the *N*-body results. It diverges from the *N*-body result more rapidly than the corresponding model for the unbiased $\Omega_0 = 1$ simulation.

The short dashed curve is a fit of the dispersion model to the *N*-body peaks biased galaxy catalogue. This model, with an exponential velocity distribution, determines β very accurately and is a good fit to the data over this range of scale. The fitted velocity dispersion is $\sigma_v = 380\mathrm{km\,s^{-1}}$, $70\mathrm{km\,s^{-1}}$ higher than the unbiased version of the same *N*-body simulation, which illustrates how bias preferentially places galaxies in environments with higher thermal velocities.

6.6 Discussion

We have used a set of high resolution *N*-body simulations to investigate the accuracy of two models of the redshift-space distortion of galaxy clustering on scales of $10\text{-}200h^{-1}\,\mathrm{Mpc}$. We conclude that neither the Zel'dovich approximation (Fisher & Nusser 1996; Taylor & Hamilton 1996) nor the linear theory plus random velocity dispersion model (Peacock & Dodds 1994) provides an accurate description of redshift-space clustering. In general both models could lead to significant systematic errors in the estimation of $\beta \equiv \Omega_0^{0.6}/b$ when applied to the high precision data that will be available from the large 2dF and SDSS galaxy redshift surveys.

The ZA provides a good fit in the unbiased cases on the very largest scales that we have investigated. However, only for the low Ω_0 cosmology considered does this model remain accurate over the full range of scales for which the quadrupole distortion is positive ($P_2(k)/P_0(k) > 0$). In the case of biased galaxy catalogues, the ZA is a very poor description of redshift clustering apart from on the very largest scales, where it tends to the linear theory result.

Smoothing the initial density field prior to applying the ZA, as in the Truncated ZA, was found to further worsen the agreement with the *N*-body results of redshift-space distortions. In general, then, we would only advocate using the ZA for analysis of unbiased universes on scales down to $\sim 40h^{-1}\,\mathrm{Mpc}$.

The two-parameter dispersion model was found to produce more acceptable fits to the *N*-body results. However, only in the cases in which the small scale velocity dispersion

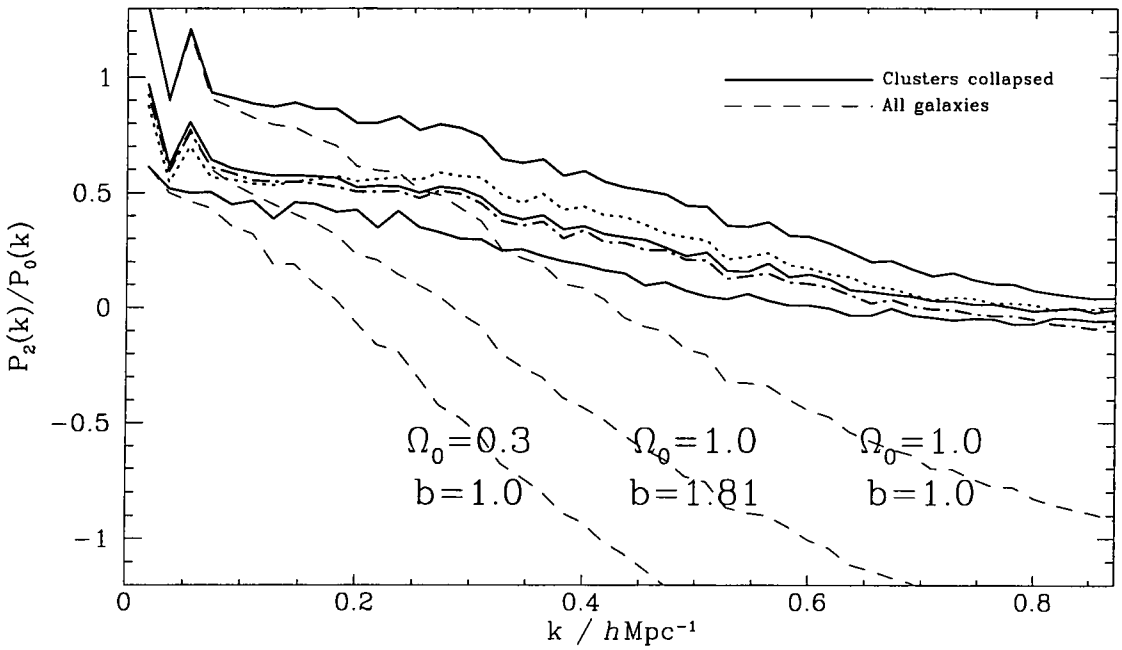

Figure 6.9: A comparison of the quadrupole ratio, $P_2(k)/P_0(k)$ before and after identifying and collapsing the galaxy clusters. The dashed lines show the original shape for the three simulations, where we have used the peaks biasing method for the biased case. The solid lines show the result after cluster collapse for the three models. We also plot the other two variants of the biasing model in the collapsed case, using a dotted line for method 2 and dot-dashed for method 3.

was large did these fits yield values of β that were not significantly biased with respect to the true values. This model also yields a value for the velocity dispersion parameter σ_v, but this depends on the degree and form of galaxy bias and so is difficult to directly relate to an interesting physical quantity. Note that, although the dispersion model was unable to deal with the unbiased $\Omega_0 = 1.0$ simulation, and in fact extracted a value of β offset from the true value by several-sigma, results from a variety of cosmological methods are making it seem increasingly unlikely that we live in such a universe; constraints from the observed σ_8 and current β estimates require a low-Ω_0 or biased cosmology, as explained in Chapter 2. Thus the dispersion model may well prove to be a useful tool for extracting information from redshift surveys on intermediate scales.

There appear to be two distinct ways to proceed to remedy or by-pass the above shortcomings:

- Improve the analytic models so as to produce accurate predictions over the full range of scales that will be probed by the redshift surveys.

- As our computers increase in memory and CPU power, the "brute force" approach of simply running *N*-body simulations for the whole range of parameter space becomes increasingly plausible. Here the dispersion model may be very useful in fitting and suggesting the approximate value of β, and thus putting restrictions on the combinations of parameter values worth investigating.

A promising approach following the first method is an extension of the model discussed in Fisher (1995), where linear distortion effects on $\xi(\sigma,\pi)$ are modelled as a convolution with a Gaussian velocity distribution with scale- and orientation-dependent velocity dispersion. Fisher suggests that this model may be adapted to deal with distortions in the highly non-linear regime by replacing the Gaussian with a generalized distribution function. This function should behave asymptotically as a Gaussian on large scales but tending to an exponential with isotropic and constant velocity dispersion on small scales. Hamilton et al. (1991) developed an accurate method of obtaining the non-linear correlation function in real space, $\xi(r)$, using a universal scaling relation. This work has been extended to the non-linear power spectrum for a range of initial power spectra and cosmologies (Peacock & Dodds 1994; Jain, Mo, & White 1995). Mo, Jing, & Borner (1996) outline a technique by which the quantities that define the velocity field (ie. mean pairwise peculiar velocity, $v_{12}(r)$, pairwise peculiar velocity dispersion, $\langle v_{12}^2(r)\rangle$, and mean square peculiar velocity, $\langle v_1^2\rangle$), can be modelled for a given cosmology and initial power spectrum. Given reliable models for these quantities, Fisher's treatment should provide a way of translating $\xi(r)$ into the redshift-space statistic $\xi(\sigma,\pi)$, and thus calculating precisely the anisotropy expected on any given scale. However, this method is still subject to problems: namely, finding out exactly how the velocity distribution function behaves on intermediate scales, and developing a way for modelling the effects of galaxy bias.

If one is resorting to simulations then it may be possible to filter the data to remove some non-linearities before commencing the analysis of redshift-space distortions. An interesting procedure for doing this is to identify and collapse galaxy clusters. Since their high velocity dispersion is responsible for much of the suppression of P_2/P_0, their removal might lead to more robust estimates of β. Figure 6.9 illustrates the effect of collapsing clusters in our simulations. As expected, the anisotropy is much closer to the

linear theory prediction on large and intermediate scales. On small scales the quadrupole ratio converges on zero rather than becoming strongly negative. Cluster membership was established using a friends-of-friends algorithm, in which any pair of galaxies with separation less than 0.2 times the mean separation are classed as being in the same cluster. Each cluster member then has its velocity replaced with the mean velocity of the cluster itself, effectively eliminating the internal velocity dispersion of these virialized structures. The identification of galaxy clusters will be much more complex when dealing with real galaxy redshift surveys. Moore, Frenk, & White (1993) describe a way of applying this technique to the CfA survey using a redshift- and orientation-dependent linking length to define groups. Whatever algorithm one adopts can always be tested by running it on mock galaxy catalogues made from the *N*-body simulations.

Our assessment of the accuracy of these models is less positive than that of previous investigations (FN96, Taylor & Hamilton 1996; Peacock & Dodds 1994) because:

- **We do not "fix" the ZA.** Earlier authors (FN96 and Taylor & Hamilton 1996) have used the zero-crossing of the quadrupole-to-monopole ratio as an empirical parameter derived from the data in order to scale the ZA curve. We feel this approach completely denies the whole point of using the Zel'dovich approximation in the first place. Instead, we calculate the full ZA because of its greater predictive power.

- **We use a range of simulations.** Whereas previous work has generally used a single cosmology to compare with the ZA or the dispersion model, we check the applicability of the methods in a variety of cases, including a biased case, motivated by current observations of the large-scale structure in the universe. We will apply similar techniques to a much larger sample of cosmologies in Chapter 8.

- **We demand much greater accuracy than previous work.** Previous work has generally focussed on applying redshift distortion models to existing samples, where random errors are large. We, on the other hand, apply them to whole simulations with well determined $P(\mathbf{k})$. We feel this degree of rigour is justified, as future surveys will give us data of comparable quality, and systematic errors that have previously been deemed "small" will enter at a significant level.

Despite the failings of existing models pointed out in this work, redshift-space distortion analysis remains very interesting and promises to be of great use in extracting information from the next generation of galaxy surveys.

References

Ballinger W. E., Peacock J. A., Heavens A. F., 1996, MNRAS, 282, 877

Bean A. J., Ellis R. S., Shanks T., Efstathiou G., Peterson B. A., 1983, MNRAS, 205, 605

Bouchet F. R., Colombi S., Hivon E., Juszkiewicz R., 1995, A&A, 296, 575

Bromley B. C., Warren M. S., Zurek W. H., 1997, ApJ, 475, 414

Cole S., Fisher K. B., Weinberg D. H., 1994, MNRAS, 267, 785

Cole S., Fisher K. B., Weinberg D. H., 1995, MNRAS, 275, 515

Colless M., 1995, The 2df galaxy redshift survey, http://msowww.anu.edu.au/~heron/Colless/colless.html

da Costa L. N., Vogeley M. S., Geller M. J., Huchra J. P., Park C., 1994, ApJ Lett, 437, L1

Davis M., Peebles P. J. E., 1983, ApJ, 267, 465

Fisher K. B., 1995, ApJ, 448, 494

Fisher K. B., Davis M., Strauss M. A., Yahil A., Huchra J. P., 1994, MNRAS, 267, 927

Fisher K. B., Nusser A., 1996, MNRAS, 279, L1

Gregory S. A., Thompson L. A., 1978, ApJ, 222, 784

Gunn J. E., Weinberg D. H., 1995, in proceedings of the 35th Herstmonceux workshop. Cambridge University Press, Cambridge, astro-ph/9412080

Hamilton A. J. S., 1993, ApJ Letters, 406, 47

Hamilton A. J. S., 1997, astro-ph/9708102

Hamilton A. J. S., Kumar P., Lu E., Matthews A., 1991, ApJ Lett, 374, L1

Jackson J. C., 1972, MNRAS, 156, 1P

Jain B., Mo H. J., White S. D. M., 1995, MNRAS, 276, L25

Kaiser N., 1987, MNRAS, 227, 1

Loveday J., Efstathiou G., Maddox S. J., Peterson B. A., 1996, ApJ, 468, 1

Maddox S. J., Efstathiou G., Sutherland W. J., 1996, MNRAS, 283, 1227

Matsubara T., Suto Y., 1996, ApJ, 470, 1

Melott A. L., Pellman T. E., Shandarin S. F., 1994, MNRAS, 269, 626

Mo H. J., Jing Y. P., Borner G., 1997, MNRAS, 286, 979

Moore B., Frenk C. S., White S. D. M., 1993, MNRAS, 261, 827

Park C., Vogeley M. S., Geller M. J., Huchra J. P., 1994, ApJ, 431, 569

Peacock J. A., Dodds S. J., 1994, MNRAS, 267, 1020

Peebles P. J. E., 1993, Principles of Physical Cosmology. Princeton University Press, Princeton

Press W. H., Teukolsky S. A., Vetterling W. T., Flannery B. P., 1992, Numerical Recipes in FORTRAN, 2nd edition. Cambridge University Press, Cambridge

Ratcliffe A., Shanks T., Parker Q. A., Fong R., 1998b, MNRAS, 293, 197

Ratcliffe A., Shanks T., Parker Q. A., Fong R., 1998a, MNRAS, 296, 191

Sargent W. W., Turner E. L., 1977, ApJ, 212, L3

Shectman S. A., Landy S. D., Oemler A., Tucker D. L., Lin H., Kirshner R. P., Schechter P. L., 1996, ApJ, 470, 172

Strauss M. A., Willick J. A., 1996, Physics Reports, 261, 271

Tadros H., Efstathiou G., 1995, MNRAS, 276, 45

Taylor A. N., Hamilton A. J. S., 1996, MNRAS, 282, 767

Weinberg D. H., Cole S., 1992, MNRAS, 259, 652

White S. D. M., Efstathiou G., Frenk C. S., 1993, MNRAS, 262, 1023

Zel'dovich Y. B., 1970, A&A, 5, 84

Chapter 7

Statistical errors

THE ARGUMENT Future galaxy redshift surveys will enable us to measure the redshift-space power spectrum of the galaxy distribution to a high degree of accuracy. In placing constraints on parameters derived from these results, it is necessary to model the errors on the measured values of the power spectrum as a function of wavenumber. We review methods of calculating these errors, based on the assumption that the large-scale perturbations are well described by a Gaussian random field. We show how this method can also be applied to measurements of the quadrupole-to-monopole ratio used in determining the redshift-space distortions of the surveys. We also outline a technique for accurately modelling the effect of the survey geometry itself on the measured power spectrum, enabling us to remove the systematic biases thus introduced. Combining these techniques we estimate the accuracy with which various surveys (2dF, SDSS, PSCz) will be able to constrain the derived parameters σ_8, Γ, and β, representing respectively the normalization and shape of the power spectrum, and the linear redshift-space distortion factor.

7.1 Introduction

With any parameter estimation in science, one compares a model with the data that have been collected. In order to assess the statistical significance of a model fit, one must have an estimate of the uncertainty present in each datum. For laboratory-based science this can normally be achieved by making repeated measurements and assessing their spread, thus obtaining a measure of the width of the distribution from which they are taken. In astronomy this is rarely possible and we are left with two alternatives: Monte Carlo *simulation* of the repeated measurements, for which it is normally necessary to assume a certain combination of parameters for input into the simulations; or an analytic

calculation of the error, which again will rest on certain assumptions about the data themselves. This latter method has been employed by Feldman, Kaiser, & Peacock (1994, hereafter FKP), to estimate the variance in the measured power spectrum of density fluctuations from a galaxy redshift survey. The key assumption they make is that all the long-wavelength modes have independent, Gaussian-distributed Fourier components, in agreement with the available data on the Gaussianity of the large-scale density distribution.

In this chapter we concern ourselves with the accuracy with which we can measure derived parameters, such as the amplitude of the power spectrum, from a galaxy survey. We first outline a method for assessing the effect of the survey geometry itself on the power spectrum, which is crucial if we are to get the best use out of the data. We go on to summarize the results of FKP, who demonstrate how to derive an expression for the variance in the power spectrum, and then illustrate how this approach can be extended to measurements of the quadrupole-to-monopole ratio of $P(\mathbf{k})$.

We finish by combining our knowledge of the systematic bias caused by the survey window function with the random errors found by a Monte Carlo technique to estimate the confidence limits on the derived parameter β from a galaxy redshift survey. We apply this technique to the survey volumes of the PSCz, 2dF and SDSS catalogues to see how accurately they will respectively be able to measure β.

7.2 Modelling the effect of the window function

Determination of the galaxy density field from a redshift survey is affected by the finite window of the survey itself. This is a familiar phenomenon throughout physics, occurring, for example, in optics when a source is viewed through a slit which imposes its own diffraction pattern on the image, or indeed in branches of astronomy where measurements are made in the time domain, in which case the window function becomes the length of time that the signal is recorded for.

The estimate of the power spectrum is similarly convolved with the shape of the survey window function. It is desirable to remove the effect of this convolution before using the power spectrum to estimate physical parameters, or else the estimates themselves are prone to systematic biases. One way of correcting the problem would be simply to

perform a direct deconvolution with the window function, but this is prone to bias since the window function, particularly the radial selection function, has to be estimated from the survey itself, and is hence not known with complete accuracy. This problem can be overcome by using the iterative method of Lucy (1974). This is the approach used by Lin et al. (1996) for the Las Campanas redshift survey. This method is successful on small scales, but on wavelengths of size comparable to the survey size, the shape of the estimated power spectrum can be seriously affected by the convolution and the iterative correction process becomes unstable.

We describe below a technique for assessing this effect based on examining the results of a window function convolution on a model power spectrum that is close to that which we expect to observe from our current knowledge of large-scale structure. We thus obtain a correction factor that can be applied to a measured $P(\mathbf{k})$ to remove the effects of the convolution.

7.2.1 The model power spectrum

In order to assess the effect of the window function on the power spectrum estimation, we pick a model redshift-space power spectrum based on physically realistic values of Γ, σ_8, β and σ_v, the shape parameter, amplitude, linear redshift-space distortion parameter, and small-scale velocity dispersion respectively.

We assume that the power spectrum can be modelled with a Γ model transfer function as given by Bardeen et al. (1986), so the linear power is

$$P_L(k) \propto \frac{k^n \times [\ln(1+2.34q)/2.34q]^2}{[1+3.89q+(16.1q)^2+(5.46q)^3+(6.71q)^4]^{1/2}}. \tag{7.1}$$

Here $q = k/\Gamma$ and we set $n = 1$, $\Gamma = 0.25$, as suggested by observations of large-scale structure (Peacock & Dodds 1994). The normalization of $P_L(k)$ is determined by the requirement that σ_8, the variance in galaxy number density in spheres of radius $8h^{-1}\,\mathrm{Mpc}$, be equal to 0.96, the value determined for APM galaxies (Maddox, Efstathiou, & Sutherland 1996). The relation between σ_8 and the power spectrum is given by:

$$\sigma_8^2 = \frac{4\pi}{(2\pi)^3}\int W(k,8)^2 P(k) k^2 dk, \tag{7.2}$$

where

$$W(k,R) = 3\,\frac{\sin kR - kR\cos kR}{(kR)^3}, \tag{7.3}$$

is the Fourier transform of a spherical top hat function. We then take the line-of-sight vector and for each k-mode define μ to be the cosine of the angle between the line of sight and the wave-vector. In order for this definition to make sense, we must make the approximation that the entire galaxy sample being considered lies along a single line of sight. Surveys have a finite angular extent, and we take the line of sight to be the average direction of all the galaxies, ie. the direction of the centre of the redshift survey. We use the Kaiser formula (Kaiser 1987), derived in Appendix A,

$$K(\mu) = (1+\beta\mu^2)^2 \tag{7.4}$$

to model the effect of linear redshift-space distortions on the power spectrum. This formula is only strictly valid in the small-angle approximation, ie. when measuring galaxy pairs that are at small angular separation (Zaroubi & Hoffman 1996). We have thus assumed that the distant observer approximation is valid over the whole survey, and that the whole survey has a single line of sight. This is generally not true of real surveys, where, if they have a large opening angle, it is necessary to measure the redshift-space power spectrum by decomposition into spherical harmonics (Heavens & Taylor 1995). This method is more complex than the simple three-dimensional Fourier transforms that we employ, and we do not attempt to model it here. A volume of the Universe subtending a small opening angle has the same information content as the same volume placed locally, and the goal of the harmonic decomposition method is to remove the effect of a large opening angle on the clustering statistics in the local volume. We effectively do this by placing the observer infinitely distant from the survey.

We model the effect of non-linear velocity dispersions on the power spectrum by assuming the velocities are drawn from a pairwise exponential distribution, thus multiplying the power spectrum by a factor

$$E(k,\mu) = [1+(k\sigma_v\mu)^2/2]^{-1} \tag{7.5}$$

In the following chapter it is shown that this form represents the analytic distribution that is closest to that found in *N*-body simulations for the redshift-space distortions.

We obtain the redshift-space power spectrum by multiplying these three factors and adding a term to represent the shot-noise. In the volume limited case, the galaxy density is constant, and the shot-noise is simply equal to its reciprocal, $P_{\rm shot} = 1/\bar{n}$. We find the value of $\bar{n}$ by comparing with the selection function from one of the mock catalogues described in Chapter 4, depending on the cosmology and the particular survey selection function we are attempting to mimic. The density of the catalogue is then the number density at the redshift at which the catalogue is limited. For a magnitude limited sample, we calculate the shot-noise power using the FKP formula, equation 7.28, where we set $\alpha = 0$ to reflect the idealized case of having an infinitely dense random catalogue. The full power spectrum is then given by the combination of these four functions,

$$P^s(k,\mu) = P_L(k)K(\mu)E(k,\mu) + P_{\rm shot}. \tag{7.6}$$

7.2.2 The survey geometry

We model the window function of each survey by constructing a random (unclustered) catalogue of galaxies which satisfies the angular constraints of the real survey, out to a maximum redshift $z = 0.5$, where the number density has become negligible. Galaxies are subsequently weighted according to either a volume limited (keep only galaxies with $d < d_{\rm lim}$ and $d_{\rm max} > d_{\rm lim}$) or magnitude limited scheme. For a magnitude limited sample we employ the weighting scheme derived by FKP designed to result in the minimum variance estimate of the power spectrum, ie. each galaxy is weighted by

$$w(\mathbf{r}) = \frac{1}{1 + \bar{n}(\mathbf{r})P(k_{\rm R})}, \tag{7.7}$$

where $P(k_{\rm R})$ is the amplitude of the power spectrum at a representative scale, chosen such that it has roughly the same power as we expect to find on the scale we are interested in. This is an effective way of tabulating the combined angular and radial selection function on a grid in real space. A more elegant method would be to simply look at each of the 192^3 grid points and decide whether or not it was in the survey, and then give it a weight $\bar{n}(\mathbf{r})w(\mathbf{r})$ if it is. The result is identical, we simply choose to do it our way because it is convenient – we already have random catalogues with high density and the same angular selection functions as the real catalogues we are interested in, so

this crude method becomes attractive. Having constructed this window function, $W(\mathbf{r})$, on the grid, we Fourier transform it and normalize such that:

$$\sum_k |W(\mathbf{k})|^2 = 1. \tag{7.8}$$

This normalization ensures that, when we convolve with the power spectrum, the total power will be conserved. To assess the effect on the power spectrum we note that the estimator of the power spectrum, $\hat{P}(\mathbf{k})$, is given by

$$\hat{P}(\mathbf{k}) = |\hat{\delta}(\mathbf{k})|^2. \tag{7.9}$$

The effect of multiplying the density field, $\delta(\mathbf{r})$, by the window function, $W(\mathbf{r})$, is described in k-space by the convolution:

$$\hat{\delta}(\mathbf{k}) = \delta(\mathbf{k}) \otimes W(\mathbf{k}). \tag{7.10}$$

Hence

$$\hat{P}(\mathbf{k}) = |\delta(\mathbf{k}) \otimes W(\mathbf{k})|^2. \tag{7.11}$$

The convolution function states that the convolution of two functions is equal to the Fourier transform of the product of their Fourier transforms. Applying this law to the inner convolution in the last equation gives

$$\hat{P}(\mathbf{k}) = |FT[\delta(\mathbf{r})W(\mathbf{r})]|^2, \tag{7.12}$$

and applying it in reverse to the outer product

$$\hat{P}(\mathbf{k}) = FT\left[[\delta(\mathbf{r})W(\mathbf{r})] \otimes [\delta(\mathbf{r})W(\mathbf{r})]\right]. \tag{7.13}$$

The convolution can be written

$$[\delta(\mathbf{r})W(\mathbf{r})] \otimes [\delta(\mathbf{r})W(\mathbf{r})] \equiv \langle \delta(\mathbf{x})W(\mathbf{x})\delta(\mathbf{x}+\mathbf{r})W(\mathbf{x}+\mathbf{r})\rangle, \tag{7.14}$$

and, in the limit that the two fields $\delta(\mathbf{r})$ and $W(\mathbf{r})$ are uncorrelated, this implies

$$\hat{P}(\mathbf{k}) = FT\left[\langle \delta(\mathbf{x})\delta(\mathbf{x}+\mathbf{r})\rangle \langle W(\mathbf{x})W(\mathbf{x}+\mathbf{r})\rangle\right], \tag{7.15}$$

hence

$$\hat{P}(\mathbf{k}) = FT\left[\xi(\mathbf{r})\left[W(\mathbf{r}) \otimes W(\mathbf{r})\right]\right] \tag{7.16}$$

We square the k-space window function and inverse Fourier transform it back into real space, resulting in a function that is the auto-correlation $[W(\mathbf{r}) \otimes W(\mathbf{r})]$ of the survey geometry. We inverse-Fourier transform the power spectrum and multiply the resultant correlation function by the survey auto-correlation before Fourier transforming back to get the power spectrum estimator described by equation 7.16.

We thus obtain the convolved $P_0(k)$ and $P_2(k)$,

$$P_l(k) = \frac{2l+1}{2}\int_{-1}^{+1} \hat{P}(k,\mu)L_l(\mu)\mathrm{d}\mu, \tag{7.17}$$

where L_l is the Legendre polynomial of order l. The quadrupole statistic used for getting β from redshift surveys follows from this expression.

7.2.3 Results

Figures 7.1 and 7.2 show the effect of the survey window functions on both the monopole power, $P(k)$, and the quadrupole-to-monopole ratio $Q(k)$. As can be seen from these plots, the effect of the window function can be highly significant. A survey with a broad k-space window function causes significant smoothing of the power at large scales, resulting in a serious misjudgement of the overall shape of the power spectrum. This is particularly significant when we are considering CDM-like models of the power spectrum where Γ, the shape parameter, is a critical ingredient. The effect is again large for $Q(k)$, the convolution causing a serious damping of the quadrupole on large scales. Again, it is this regime which is crucial to our understanding of large-scale structure, since the information about the linear redshift-space distortion gives us a direct handle on the value of Ω_0.

We conclude, then, that it is crucial to account for the window function convolution in any measurement of the power spectrum or redshift-space distortion from galaxy redshift surveys.

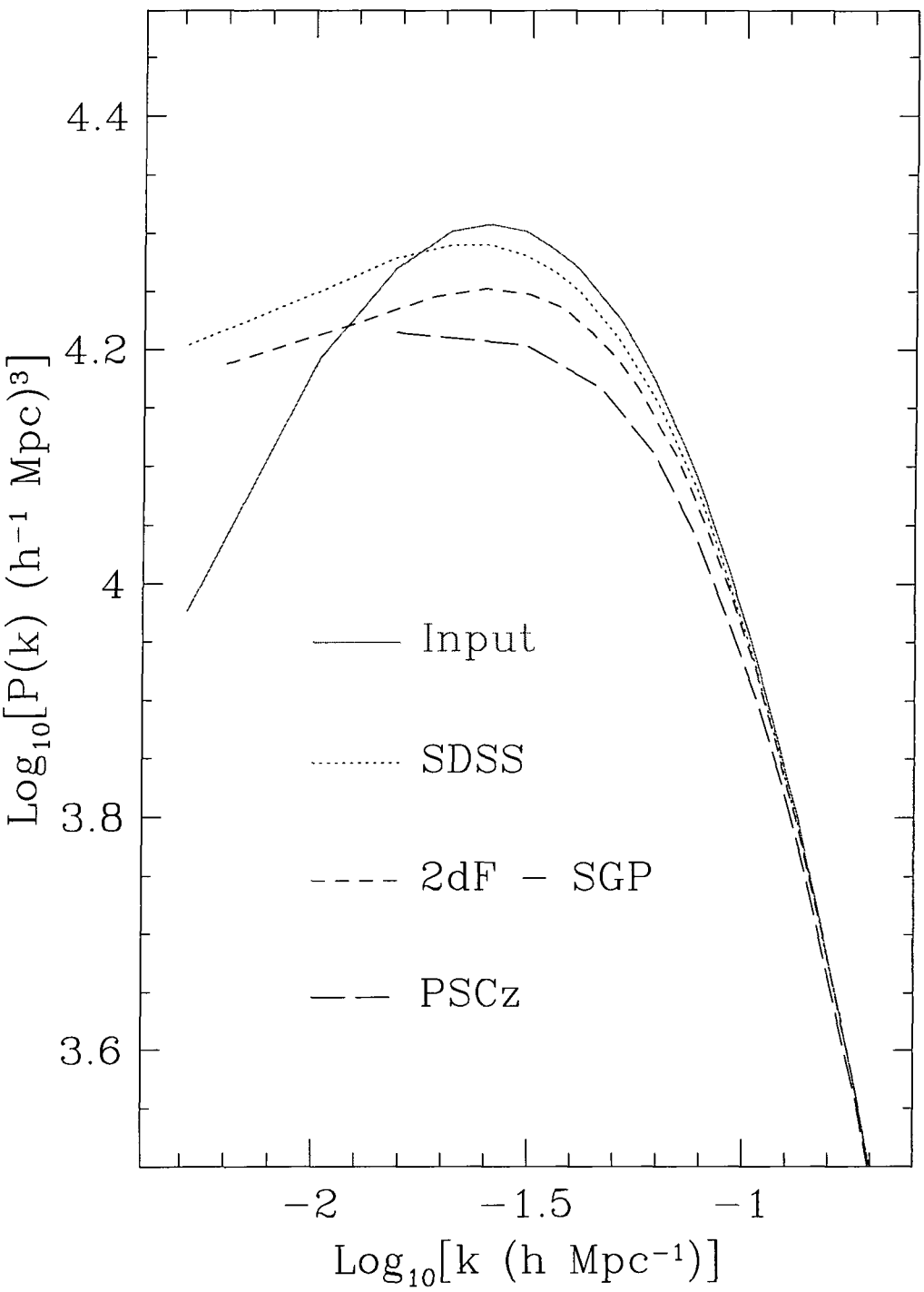

Figure 7.1: The effect of the window functions on the power spectrum for the three different surveys. We use the volume limited case for the selction function as described in section 7.4.3.

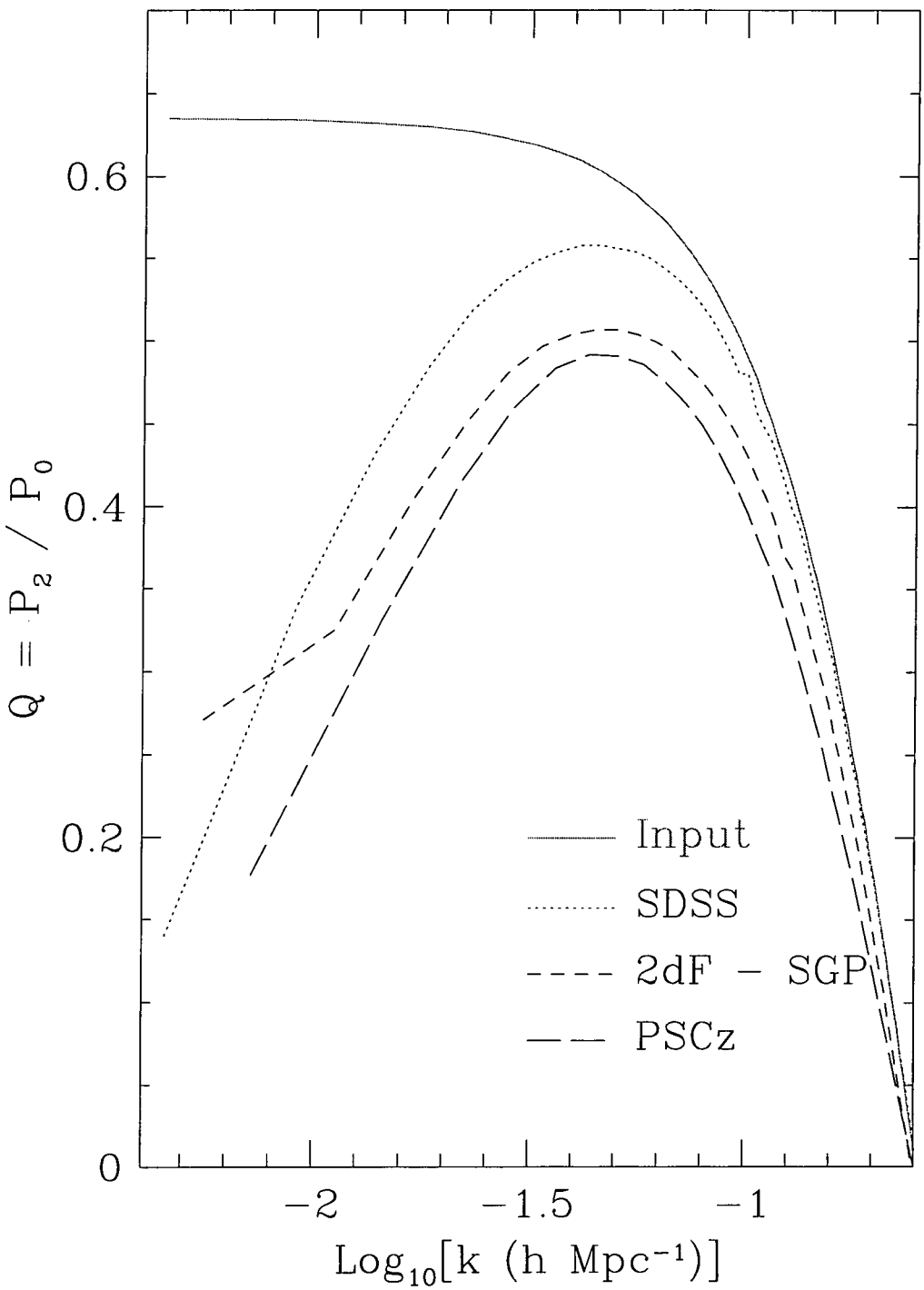

Figure 7.2: The effect of the window functions on the quadrupole-to-monopole ratio, Q, for the three different surveys. This time we use the magnitude limited case with FKP minimum-variance weighting as described in section 7.4.2.

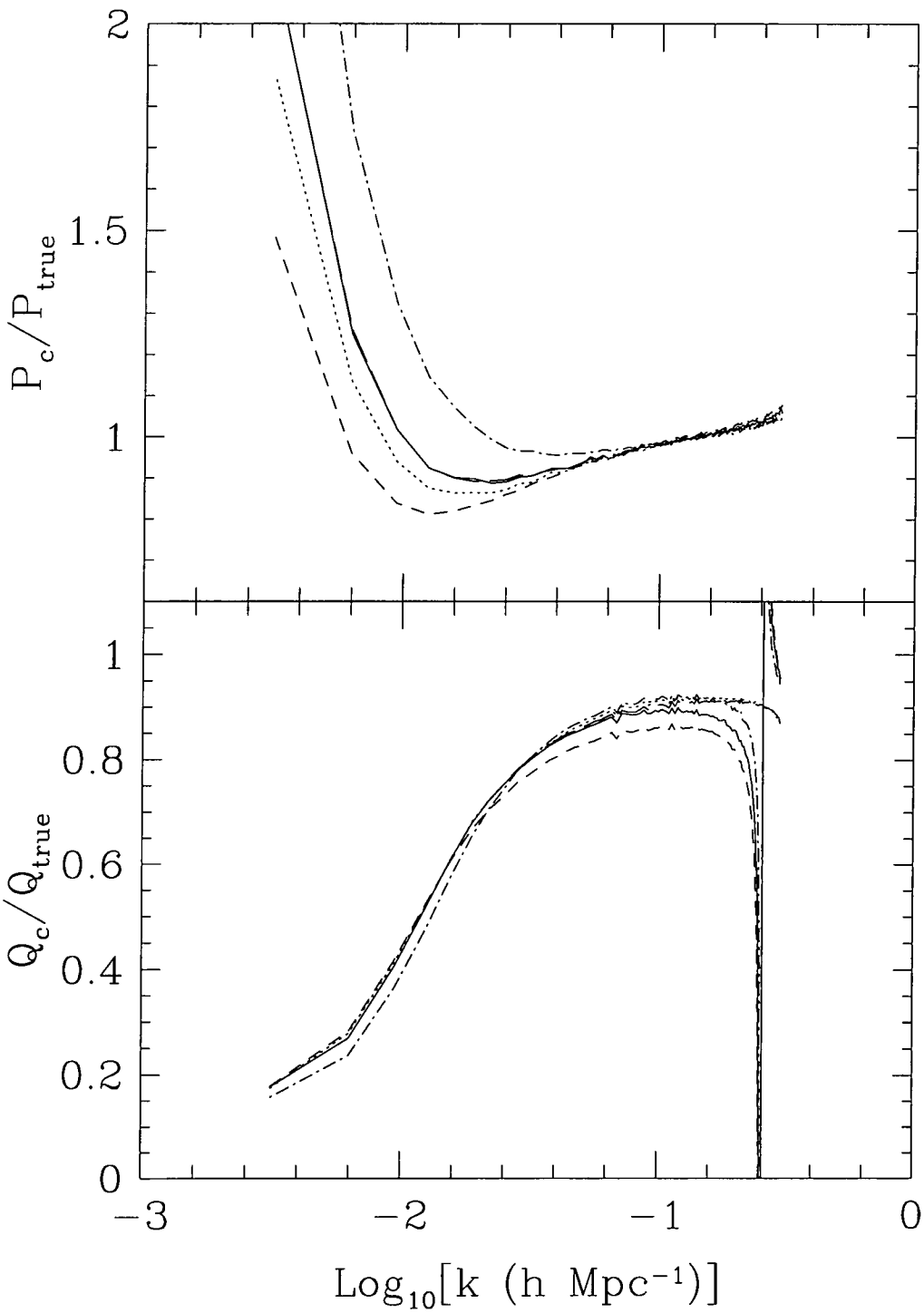

Figure 7.3: The model dependence of the convolution correction factor. The upper panel shows the correction to the monopole power, the lower one to the quadrupole-to-monopole ratio, for five models: a standard one with $(\Gamma, \beta, \sigma_v) = (0.25, 0.55, 650\mathrm{km\,s^{-1}})$ (solid line), and variants; $\beta = 1.0$ (dotted line), $\Gamma = 0.15$ (short dashed line), $\sigma_v = 400\mathrm{km\,s^{-1}}$ (long dashed line), and $\Gamma = 0.5$ (dot-dashed line).

7.2.4 Model dependency

Using this technique to correct for the effect of the survey convolution is model dependent, in that we have assumed parameters for the power spectrum used in making the correction. There are three parameters that are chosen, Γ, σ_v, and β. A model dependency introduces a possible loss of generality in the treatment, and a potential systematic bias in the estimation of these parameters from the data. In figure 7.3 we examine the extent of this model dependency in the monopole power spectrum, P_0, and the quadrupole-to-monopole ratio, Q. In each case we plot the ratio of the convolved statistic to its "true" value, ie. the analytic result coming from the correct choice of the power spectrum parameters.

For the monopole power in the upper panel, it can be seen that the different models can have a dramatic effect on the correction function at large scales. The chief cause of discrepancy is with the models with different Γ-values. The convolution effectively wipes out information on the large-scale shape of the power spectrum. The convolved power spectrum is insensitive to Γ, and hence the required correction changes substantially. Other considerations have little effect, with a slight change in the large-scale power for a substantial change in β. Unsurprisingly, changing σ_v has no effect at large scales on the power spectrum.

The variation of correction function with Γ is potentially problematic. To overcome it, we could correct the power spectrum with a variety of Γ values and find the one with the best goodness-of-fit, or find an analytic description for the variation of the correction factor with this parameters, and build it into the fitting procedure. Either way, the degeneracy increases the uncertainty on Γ. In section 7.4.4 we will assess the magnitude of the systematic bias and compare it with the random error on this quantity.

Note that values of σ_8 will probably be unaffected by the wrong choice of correction function. The amplitude of fluctuations in spheres of radius $8h^{-1}\,\mathrm{Mpc}$ is dominated by contributions from modes with wavelengths $\sim 30h^{-1}\,\mathrm{Mpc}$. Examining figure 7.3, it will be seen that the P_0 curves have all converged by $k \approx 10^{-1.2}h\,\mathrm{Mpc}^{-1}$, ie. wavelength $100h^{-1}\,\mathrm{Mpc}$. So the variation in σ_8 will be small.

The quadrupole-to-monopole ratio generally seems more robust than P_0. The different curves deviate near the zero crossing, but this is a numerical effect due to dividing by very

small numbers. However, there is a systematic tendency for the value of the convolved function to be smaller than its true value. This is easily explained. The convolution means that close bins are correlated. Thus, a measurement of Q at a particular wavenumber is really a weighted average over nearby modes. Since the gradient of Q increases with k, this average will generally be biased low compared to the real value at that scale. Thus Q will be lower than $Q_{\rm true}$, and go through zero earlier, which is why all the curves in the lower panel of figure 7.3 turn down to the singularity. This could also be the cause of the slight upturn in the upper panel of this figure; non-linear effects cause the slope of P_0 to become shallower with k, and hence the bias is in the opposite direction.

We will assess the magnitude of the systematic bias introduced in β in section 7.6.2. For now, we note that Q behaves approximately linearly to changes in β. The scatter between the different curves is, at most, of order 5%. Hence, adopting the wrong correction factor can only bias β by $\sim 5\%$. We shall later show that this is liable to be rather smaller than the random uncertainties.

7.3 The error on the power spectrum

The principle behind the analytic calculation of the variance is the assumption that each Fourier mode of the galaxy distribution is an independent Gaussian random variable drawn from a distribution with amplitude given by the power spectrum at this value of k. The assumption of Gaussianity is one that falls in with the theoretical prejudices of the Standard model. If the density perturbations we see today on large scales were seeded by quantum fluctuations in the early Universe, their distribution should indeed be Gaussian. On the other hand, if some non-standard physics is responsible for structure formation, such as the decay of textures, strings, or monopoles, the distribution is expected to have non-Gaussian qualities. Probing primordial Gaussianity is a difficult experimental task, as departures from it are generally expected to be small, and will only show up at long-wavelengths. On smaller scales, non-linear evolution is expected to produce a non-Gaussian signature regardless of the initial conditions. A variety of techniques have been used, including topological studies of the present-day galaxy distribution (Canavezes et al. 1998; FKP) and examination of the cosmic microwave background using *COBE* data (Kogut et al. 1996; Ferreira, Magueijo, & Gorski 1998). The genus statistic approach has generally found that Gaussianity cannot be ruled out with

the use of current data sets. FKP themselves describe a method of using their power spectrum analysis as a test for non-Gaussianity. If the power is Gaussian distributed, the cumulative distribution of power estimated for each mode is exponential (Stuart 1987). This relation is used to show that the power spectrum of the *IRAS* QDOT survey (Rowan-Robinson et al. 1990) obeys the Gaussian hypothesis to a very high degree. However, it has subsequently been shown (Fan & Bardeen 1994) that such one-point statistics do not truly probe the Gaussianity of the underlying field, since a non-Gaussian field can still have Gaussian distributed Fourier components. Ferreira, Magueijo, & Gorski (1998) claim to have found evidence in the four year *COBE* data that rules out the Gaussian hypothesis at the 95% confidence level, using a new statistic that is highly sensitive to non-Gaussian fluctuations.

There is, then, some controversy over the nature of primordial fluctuations, but we note for this work that departures from Gaussianity are small if they do indeed exist, and the following treatment is thus likely to be approximately valid.

We commence by calculating the scatter on the measurement of the amplitude of a single wavelength mode. We then describe different techniques for combining these errors to get a measure of the total uncertainty in the spherically averaged $P(k)$.

7.3.1 Variance from one mode

Considering the power in a field of real and imaginary components, δ_R and δ_I, the estimator of the power spectrum, $\hat{P}(k)$, is given by

$$\hat{P}(k) = \delta_R^2 + \delta_I^2 \tag{7.18}$$

The power spectrum itself is defined as

$$P(k) = \langle \hat{P}(k) \rangle = 2\langle \delta_R^2 \rangle = 2\langle \delta_I^2 \rangle = \langle \delta_R^2 + \delta_I^2 \rangle \tag{7.19}$$

Defining $\delta P(k)$ as $P(k) - \hat{P}(k)$, the variance in the estimate of the power in this mode is given by $\sigma^2 = \langle \delta P(k) \delta P(k) \rangle$. Expanding this we obtain

$$\begin{aligned}
\sigma^2 &= \left\langle \left(\delta_R^2 + \delta_I^2 - P(k)\right) \left(\delta_R^2 + \delta_I^2 - P(k)\right) \right\rangle \\
&= P(k)^2 - 2P(k) \left\langle \delta_R^2 + \delta_I^2 \right\rangle + \left\langle \left(\delta_R^2 + \delta_I^2\right) \left(\delta_R^2 + \delta_I^2\right) \right\rangle \\
&= \left\langle (\delta_R^2)^2 + 2(\delta_R^2 \delta_I^2) + (\delta_I^2)^2 \right\rangle - P(k)^2
\end{aligned} \tag{7.20}$$

We now apply the general relation for a bivariate Gaussian in x and y,

$$\langle x^2y^2\rangle = \langle x^2\rangle\langle y^2\rangle + 3\langle xy\rangle\sqrt{\langle x^2\rangle\langle y^2\rangle} - \langle xy\rangle^2 \tag{7.21}$$

Considering the two cases where x and y are either completely correlated (ie. identical) or completely uncorrelated,

$$\langle x^2y^2\rangle = \begin{cases} 3\langle x^2\rangle^2 & \text{for } x \text{ and } y \text{ equivalent} \\ \langle x^2\rangle\langle y^2\rangle & \text{for } x \text{ and } y \text{ completely uncorrelated} \end{cases}. \tag{7.22}$$

Thus,

$$\begin{aligned} \sigma^2 &= (3 + 2\times 1 + 3)\,\langle\delta_R^2\rangle^2 - P(k)^2 \\ &= P(k)^2. \end{aligned} \tag{7.23}$$

So, single measurements of the power in one k-mode will generally be distributed with a scatter equal to the mean power at this wavelength. The analytic derivation of the variance proceeds by assuming that, to get an estimate of the one-dimensional quantity $P(k)$, we spherically average the three-dimensional $P(\mathbf{k})$ into shells with $|\mathbf{k}| \approx k$.

7.3.2 FKP1: simple mode-counting errors

If we have N independent measurements of the power for modes within the spherical shell $|\mathbf{k}| \approx k$, the error on the mean goes down as $\sqrt{N}$. In the notation of FKP,

$$\hat{P}(k) = \frac{1}{V_k}\int \mathrm{d}^3k'\hat{P}(\mathbf{k}'), \tag{7.24}$$

where V_k is the volume (in k-space) of the shell being averaged over. The variance is given by

$$\sigma^2 = \langle[\hat{P}(k) - P(k)]^2\rangle = \frac{1}{V_k^2}\int \mathrm{d}^3k \int \mathrm{d}^3k'\langle\delta P(\mathbf{k})\delta P(\mathbf{k}')\rangle. \tag{7.25}$$

The key result of FKP is their equation 2.2.6,

$$\langle\delta P(\mathbf{k})\delta P(\mathbf{k}')\rangle = |P(\mathbf{k})W(\mathbf{k}-\mathbf{k}') + S(\mathbf{k}-\mathbf{k}')|^2, \tag{7.26}$$

where

$$W(\mathbf{k}) \equiv \frac{\int \mathrm{d}^3r\bar{n}^2(\mathbf{r})w^2(\mathbf{r})e^{i\mathbf{k}.\mathbf{r}}}{\int \mathrm{d}^3r\bar{n}^2(\mathbf{r})w^2(\mathbf{r})}, \tag{7.27}$$

and

$$S(\mathbf{k}) \equiv \frac{(1+\alpha)\int \mathrm{d}^3 r \bar{n}(\mathbf{r}) w^2(\mathbf{r}) e^{i\mathbf{k}.\mathbf{r}}}{\int \mathrm{d}^3 r \bar{n}^2(\mathbf{r}) w^2(\mathbf{r})}. \tag{7.28}$$

Here $\bar{n}$ is the average galaxy density as a function of position, α is the ratio of real to random galaxies used in the analysis, and $w(\mathbf{r})$ is a weighting function by which galaxies are assigned certain weights depending on their spatial position.

$W(\mathbf{k})$ thus represents a normalized window function, while $S(\mathbf{k})$ is a shot-noise term coming from the discreteness of the galaxies.

If we consider a volume limited subsample drawn from a real galaxy survey, $\bar{n}$ is a constant and $w(\mathbf{r}) = 1$. It can thus be seen that $W(\mathbf{k})$ and $S(\mathbf{k})$ are both just multiples of the Fourier transform of the survey volume itself, ie.

$$W(\mathbf{k}) \propto S(\mathbf{k}) \propto \int \mathrm{d}^3 r e^{i\mathbf{k}.\mathbf{r}}. \tag{7.29}$$

In the magnitude limited case, they are transforms of the window function weighted in slightly different ways.

Given this relationship, for a survey of characteristic scale D, both $W(\mathbf{k})$ and $S(\mathbf{k})$ are functions with width $\sim 1/D$. In this case, modes separated by $|\delta\mathbf{k}| \gg 1/D$ will in general be uncorrelated, whilst there will be correlations between wavenumbers of separation $\lesssim 1/D$. We can thus quantitatively define what is meant by averaging over N *independent* measurements - N is the number of coherence volumes in the shell, set by the survey geometry, rather than simply the number of modes our numerical resolution enables us to examine.

If the thickness of a shell in k-space is chosen to be large compared to the width of $W(\mathbf{k})$, $\mathbf{k} - \mathbf{k}'$ will be large for modes not in the same shell, so the integral over the shell of $W(\mathbf{k} - \mathbf{k}')$ is approximately equal to the integral over all space of $W(\mathbf{k}')$. Since $P(\mathbf{k})$ changes little over the shell, the integration over $\mathbf{k}$ just produces a factor of V_k, so the double integral in equation 7.25 reduces to

$$\sigma_0^2 = \frac{1}{V_k}\int \mathrm{d}^3 k' |P(\mathbf{k})W(\mathbf{k}') + S(\mathbf{k}')|^2. \tag{7.30}$$

Substituting for $W(\mathbf{k})$ and $S(\mathbf{k})$, and Fourier transforming, leads to an expression for the fractional variance in the power spectrum,

$$\frac{\sigma_0^2}{P^2} = \frac{(2\pi)^3}{V_k} \frac{\int \mathrm{d}^3 r \bar{n}^4 w^4 [1 + (1+\alpha)/\bar{n}P(k)]^2}{[\int \mathrm{d}^3 r \bar{n}^2 w^2]^2}. \tag{7.31}$$

So, for any given form of $\bar{n}(\mathbf{r})$ and $w(\mathbf{r})$ we can calculate a quadratic form for the dependence of the fractional error on wavenumber. Assuming an extremely dense random catalogue such that $\alpha \to 0$,

$$\frac{\sigma_0^2}{P^2} = \frac{(2\pi)^3}{V_k} \left[\eta_0 + \frac{\eta_1}{P(k)} + \frac{\eta_2}{P(k)^2}\right], \tag{7.32}$$

where

$$\eta_a = \frac{\int \mathrm{d}^3 r \bar{n}^{4-a} w^4}{[\int \mathrm{d}^3 r \bar{n}^2 w^2]^2}. \tag{7.33}$$

Again, we illustrate with the simpler expression for a volume limited subsample where we can take $\bar{n}$ and w out of the integrals,

$$\frac{\sigma_0^2}{P^2} = \frac{(2\pi)^3}{V_k} \frac{[1 + (1+\alpha)/\bar{n}P(k)]^2}{\int \mathrm{d}^3 r}. \tag{7.34}$$

As a consistency check, consider the power spectrum of a full, periodic simulation cube – in this case, $W(\mathbf{k})$ and $S(\mathbf{k})$, being discrete Fourier transforms of the whole volume, are only non-zero for the $k = 0$ mode, and so are proportional to Kronecker δ-functions, δ_K. Meanwhile,

$$\int \mathrm{d}^3 r = \text{ Volume of cube } = L_{\mathrm{BOX}}^3, \tag{7.35}$$

and the volume of a spherical shell in k-space is the number of modes in that shell times the volume of one k-mode,

$$V_k = N_k (\Delta k)^3 = N_k \left(\frac{2\pi}{L_{\mathrm{BOX}}}\right)^3. \tag{7.36}$$

Thus, under the assumption that we ignore discreteness effects (ie. no Poisson shot-noise term),

$$\frac{\sigma_0^2}{P^2} = \frac{(2\pi)^3}{V_k} \frac{1}{\int \mathrm{d}^3 r} = \frac{1}{N_k}, \tag{7.37}$$

so the error goes as $1/\sqrt{N_k}$, exactly as expected. Away from this idealized case, the method predicts that the fractional variance is the square root of the number of coherence volumes in a k-space shell.

7.3.3 FKP2: more complex method

FKP note that the above expression will blow up when the shell width is thin compared to the coherence length. They introduce the full expression for the uncertainty, which is better behaved and tends to a constant value as the shell size decreases:

$$\sigma_0^2 = \frac{2}{N_k^2} \sum_{\mathbf{k}'} \sum_{\mathbf{k}''} |P(\mathbf{k}) W(\mathbf{k}' - \mathbf{k}'') + S(\mathbf{k}' - \mathbf{k}'')|^2 \tag{7.38}$$

(FKP equation 2.4.6). Applying the same consistency check as used above, we ignore the shot-noise term and set $W(\mathbf{k}) = \delta_K(\mathbf{k})$. Performing the inner summation over $\mathbf{k}''$, we thus obtain

$$\sigma_0^2 = \frac{2}{N_k^2} \sum_{\mathbf{k}'} |P(\mathbf{k})|^2. \tag{7.39}$$

Now, there are by definition N_k modes in the shell we are averaging over; hence, performing the remaining summation leads to

$$\frac{\sigma_0^2}{P_0^2} = \frac{2}{N_k}. \tag{7.40}$$

This is twice the error that would be expected from equation 7.37. This apparent inconsistency is easily resolved. When calculating the power spectrum we have taken the complex Fourier transform of the density field, $\delta(\mathbf{r})$, which has no imaginary component. This implies that $\delta(\mathbf{k})$ is hermitian, and hence $P(\mathbf{k}) = P(-\mathbf{k})$. Thus, if we sum over *all* the modes in a spherical shell in k-space, we would count N_k modes, where N_k is actually twice the number of *independent* modes. This is the source of the discrepant factor of two between equations 7.40 and 7.37. In practice, then, we save computation time by only summing over the N_I independent modes in one hemisphere in k-space, leading to

$$\sigma^2 = \frac{1}{N_I^2} \sum_{\mathbf{k}'} \sum_{\mathbf{k}''} |P(\mathbf{k}) W(\mathbf{k}' - \mathbf{k}'') + S(\mathbf{k}' - \mathbf{k}'')|^2. \tag{7.41}$$

7.3.4 Monte Carlo method

The double summation method (FKP2) is very CPU intensive if one has to sum over every mode in the same shell, especially at high k where there are many modes in each shell. We must therefore look to alternative, faster methods for power spectrum estimation.

It was mentioned in section 7.3.3 that to obtain the full covariance matrix, we would need to run a large set of *N*-body simulations, each with a random set of initial density waves, but the same cosmological parameters. We would then extract mock catalogues from each simulation and measure their power spectra to compare the cross correlation between k-modes. This technique would accurately measure the variance on all scales, but would be enormously time consuming for large surveys like 2dF and SDSS since each simulation takes many CPU hours to run, and we need a large number of simulations to estimate the variance reasonably well. In Chapter 8 we will present the results of applying this method crudely, using the variance between ten realizations for a particular cosmological model.

In this section, we utilize the method of assessing the window function described in section 7.2. We assume that each individual k-mode of the density field is given by the square root of this power spectrum multiplied by a complex number containing a pair of Gaussian random variables as the real and imaginary parts, thus satisfying equations 7.18 and 7.19. We Fourier transform the resultant $\delta(k)$, and set the imaginary part to zero, giving an overdensity field, $\delta(\mathbf{r})$. We note that setting the imaginary part to zero effectively wipes out half the power, so we multiply the resultant field by a factor of $\sqrt{2}$ to compensate for this. Then, as in the real case, we multiply by the window function of the survey, thus introducing the necessary convolution. We then perform a power spectrum analysis on the resultant mock survey and estimate the variance on the power by repeating the procedure fifty times.

Figure 7.4 compares the three different methods outlined here. It can be seen that the Monte Carlo method is well approximated by the simple FKP1 error, which, at low-k, is close to the FKP2 curve. We do not model the shot-noise contribution from the FKP2, as this causes the computation to be even more time-consuming, but this comparison demonstrates that the methods are equivalent.

7.4 Error on derived parameters

We are now in possession of an accurate model for both the effect of the survey geometry on the power spectrum and the value of the uncertainty in the power spectrum as a

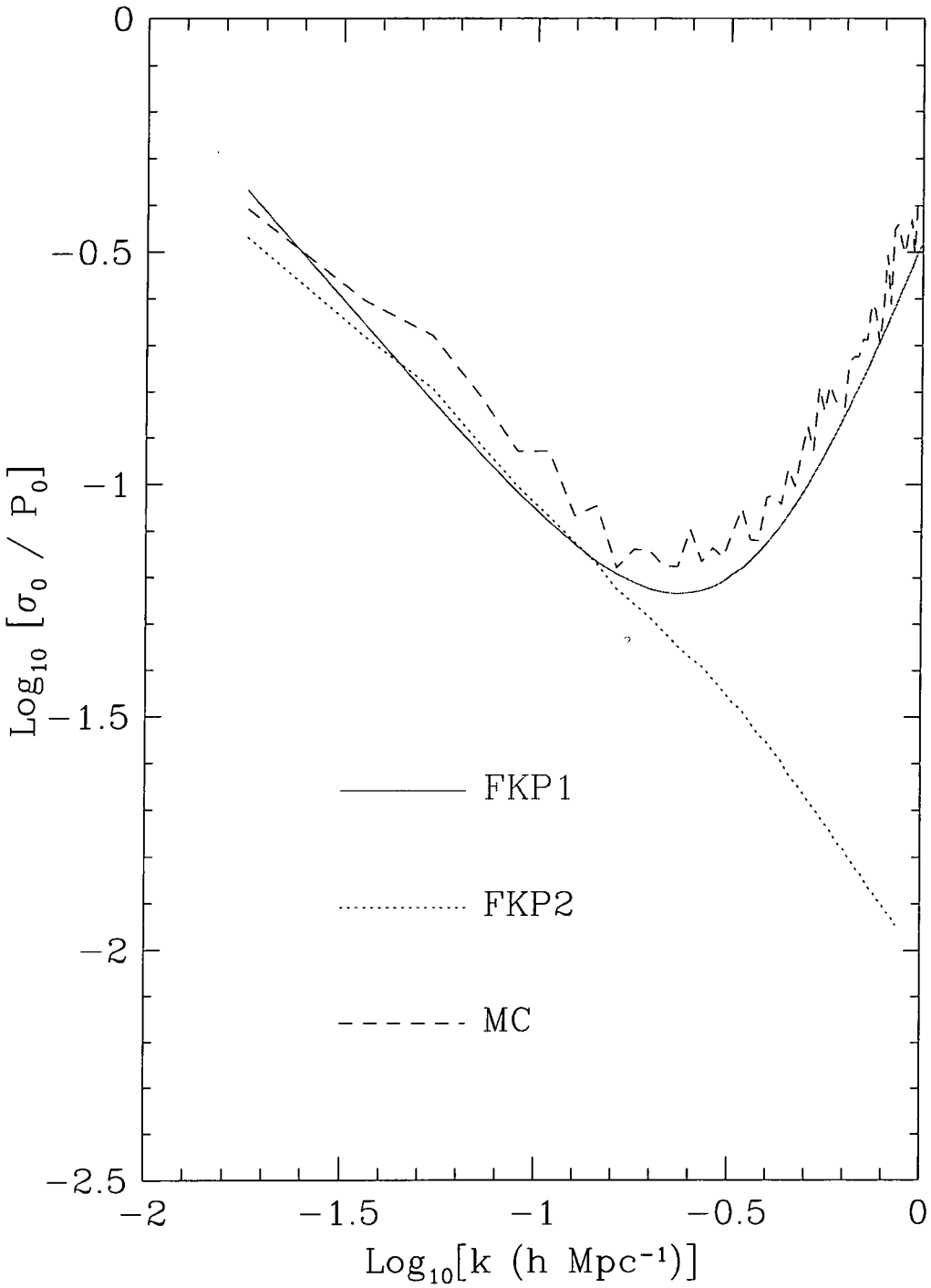

Figure 7.4: The fractional error on the monopole power spectrum, $P_0(k)$, under the three different estimation schemes. The solid line shows the simple FKP1 error, the dotted line the FKP2 (double summation method), and the dashed line is the error derived from Monte Carlo realizations of the overdensity field.

function of scale. In order to derive model parameters from the power spectrum, we will measure the χ^2 statistic for a model fit to the data,

$$\chi^2 = \sum_i \left(\frac{P_i - P_i^{\rm mod} C_i}{\sigma_i} \right)^2 \tag{7.42}$$

where C_i is the correction to the power spectrum caused by convolution with the window function, and $P^{\rm mod}$ is the model power spectrum.

The parameters estimated directly from the power spectrum are Γ and σ_8; we shall assume that we are in possession of the real-space power spectrum and hence that β and σ_v are irrelevant. Alternatively, we are measuring the shape and amplitude of the redshift-space power spectrum. Under this assumption we are able to rapidly find the values of the model parameters for which the fit has the minimum χ^2. From the values of χ^2 around this minimum, we can construct an error ellipse for the $1, 2$ and 3σ likelihood regions in parameter space, using table 7.1 to find the $\Delta\chi^2$ corresponding to the $68.3, 95.4$ and 99.73% confidence intervals for a fit with two degrees of freedom. We can also predict $1, 2$ and 3σ errors on Γ and σ_8 individually by taking the same confidence intervals for a fit with one degree of freedom, ie. $\Delta\chi^2 = 1, 4$ and 9, and finding the projection of these ellipses onto the Γ or σ_8 axes, as shown in figure 7.5.

Table 7.1. Values of $\Delta\chi^2$ for 1-,2- and 3-σ results for different numbers of degrees of freedom, ν.

Significance	Probability	$\Delta\chi^2$		
		$\nu = 1$	$\nu = 2$	$\nu = 3$
1σ	68.3%	1.00	2.30	3.53
2σ	95.4%	4.00	6.17	8.02
3σ	99.73%	9.00	11.8	14.2

We are left with the choice of what k-scale to extend our fit to. We note that our simple model for the power spectrum should not be expected to be accurate very far away from the linear regime. Hence we define a non-linear scale, $k_{\rm nl}$, equal to the wavenumber at which the quadrupole estimator crosses through zero. We restrict all our fits to $k < k_{\rm nl}$.

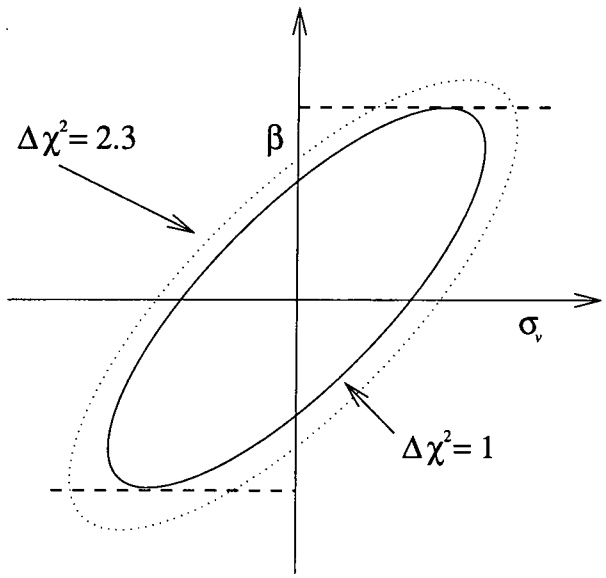

Figure 7.5: Error on β from our two parameter fit. The dashed contour, $\Delta\chi^2 = 2.30$ contains 68.3% of normally distributed data, but the 1σ error on β is obtained by projecting the extremities of the $\Delta\chi^2 = 1$ error ellipse on to the β axis.

We measure the power spectrum from one of the simulations presented in Chapter 4. The cosmology we select is $\Omega_0 = 1$ with power spectrum normalization chosen to match the observed abundance of rich clusters. For this simulation, we find a zero-crossing in the quadrupole at $k_{\rm nl} = 0.25h\,{\rm Mpc}^{-1}$. This prompts us to use a model power spectrum with $\sigma_v = 650{\rm km\,s}^{-1}$ to obtain the same zero-crossing.

We note that, for thin shells, the double sum method and the Monte Carlo method of error estimation tend to produce constant values of $\sigma_0(k)/P_0(k)$, independent of the shell thickness. Thus, if we double the size of the grid used in the FFT analysis of the power spectrum, each shell in k-space has the same variance as it did before, but we are now measuring the power at twice as many values of k. Thus, when applying a χ^2 statistic to the data, a certain change in model parameter values would now produce twice the value of $\Delta\chi^2$ as before. So, we would conclude that the error on the derived parameter has decreased – but it is obviously unreasonable that the accuracy should depend this much on the size of the grid used. The problem arises because we are effectively over-using the data; using thinner shells simply introduces correlations between the shells themselves, but the total information content of the data remains the same. This problem is resolved if the full covariance matrix is used in a maximum likelihood method, as FKP do for the

QDOT sample, rather than using the simple χ^2 technique which is equivalent to maximum likelihood in the regime where the data are uncorrelated.

This method is time consuming, and, though we will employ it in the rest of this chapter, we can get a good estimate of the error using the simple FKP1 method. We showed in section 7.3.2 that this method is equivalent to the more complex one when the volume of a k-mode used in the analysis is equal to the coherence volume of the survey: equivalently, when the volume of the grid is equal to the volume of the survey. At this point, the survey is entirely described by the Fourier modes present on the grid, and modes are uncorrelated. Moving to a larger grid size, we again increase the number of data points in the χ^2 analysis, but the volume of each spherical k-space shell, and hence the number of coherence volumes contained within it, has decreased, increasing the individual errors in such a way that the value of χ^2 is kept constant. Since it is desirable that the error on derived parameters should be independent of the grid size used for the analysis, the FKP1 method accurately predicts the error on quantities derived from the power spectrum.

7.4.1 The full covariance matrix

Under the assumptions of FKP1, the ability of a survey to measure derived parameters is entirely dictated by its volume. Whilst this is true to first order, in fact survey geometry can play an important role as well. A non-uniform survey can contain information about modes longer than those represented in a box of equivalent volume, since it has pairs of galaxies at larger separation than the box length. Such a survey is, therefore, not fully characterized by this collection of wavelengths. The equivalent volume assumption will thus lead to an over-prediction of the error; this is especially true if we are looking at parameters that are mostly determined by the linear end of the power spectrum, since a few extra modes at these scales can be worth many modes at smaller scales where they are of less consequence. In order to fully assess this effect, we employ the full covariance matrix of the data points, derived from the Monte Carlo method used to obtain the variances. The goodness of fit is now given by the full expression for χ^2,

$$\chi^2 = \mathbf{A}.\mathcal{M}.\mathbf{A}^T \tag{7.43}$$

where $\mathbf{A}$ is the vector of differences between model and data, and $\mathcal{M}$ is the inverse of the covariance matrix. In the case of no correlations, this reduces to the simple χ^2 formula (equation 7.42). In this case, it can be seen that $\mathcal{M}$ reduces to a diagonal matrix whose elements are given by $M_{ii} = 1/\sigma_i^2$. In the case of correlations between the data-points, much of the information contained in the matrix is redundant. We can thus restrict our analysis to the principal components, linear combinations of the data that contain nearly all the information. The matrix is fully describe by its n modes. However, we can choose to describe the matrix using a fewer ($m \leq n$) principal components by discarding those that contribute little to the overall variance. We obtain the principal components using singular value decomposition of the covariance matrix. Singular value decomposition of the matrix $\mathcal{S}$ returns the matrix $\mathcal{U}$, where

$$\mathcal{S} = \mathcal{U}.\mathcal{W}.\mathcal{U}^T. \tag{7.44}$$

$\mathcal{W}$ is the diagonal matrix containing the singular values. Where most of the n values of $\mathcal{W}$ are very small, the input matrix can be well approximated by the first few principal components. The inverse, $\mathcal{M} = \mathcal{S}^{-1}$, can be approximated by

$$\mathcal{S}^{-1} \approx \mathcal{U}_r.\mathcal{W}_r^{-1}.\mathcal{U}_r^T, \tag{7.45}$$

where the r denotes the reduced matrix, ie. that having only the first m columns. We choose to keep the first m modes such that they contribute to 99% of the total variance, ie.

$$\sum_1^m W_{ii} = 0.99 \times \sum_1^n W_{ii}. \tag{7.46}$$

The effect of applying this selection criterion to the principal components can be quite dramatic; for example, the analysis of the the 2dF SGP on a $2004h^{-1}\,\mathrm{Mpc}$ grid results in the selection of only $m = 39$ components out of a total $n = 81$, implying that only half the modes make a substantial contribution to the variance.

Wavenumbers that measure the power spectrum on scales where its amplitude is small will have correspondingly small absolute variances. In order to avoid discrimination against these modes we first normalize the covariance matrix by $\sigma_{ij} \to \sigma_{ij}/\sqrt{\sigma_{ii}\sigma_{jj}}$.

As an illustration of this method, we show in figure 7.6 a surface plot of an example covariance matrix. This matrix has been obtained using fifty random realizations of the

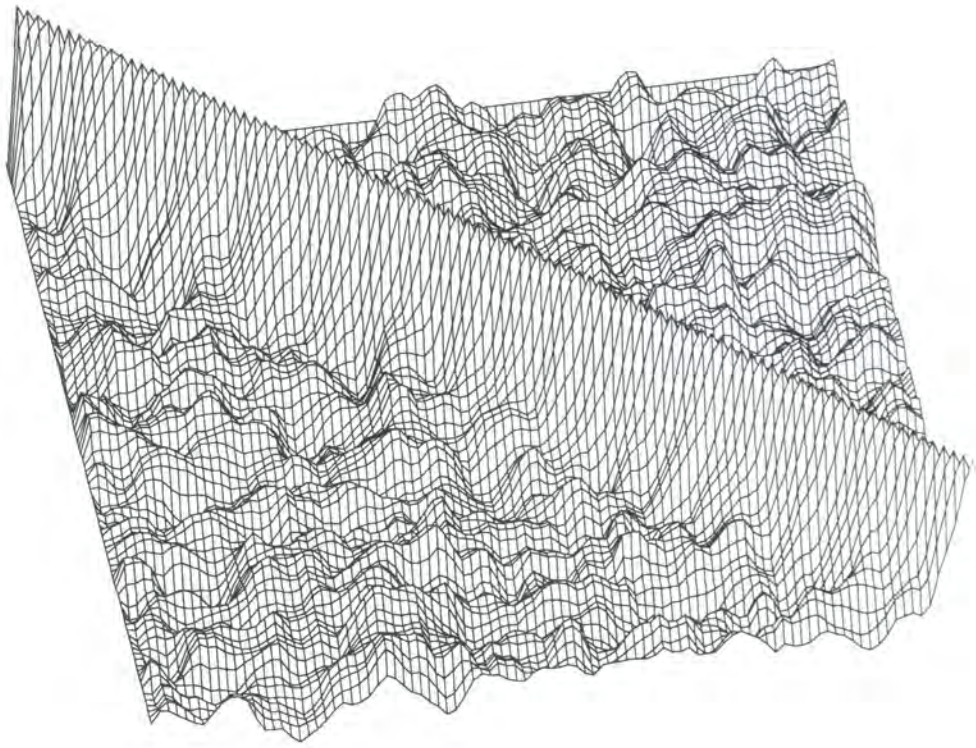

Figure 7.6: Surface plot of the covariance matrix. The matrix has been normalized so the on-diagonal elements have unit height. $k = k' = 0$ is in the upper left corner. It can clearly be seen that the convolution with the survey window function has the effect of smoothing the central peaks and introducing covariance between $k \neq k'$ modes, with width $|k - k'| \lesssim 1/D$, where D is the width if the survey window function in r-space.

overdensity and is normalized as described above. The matrix is close to diagonal, with the small fluctuations off to the sides being caused by the finite number of realizations, but it can clearly be seen that the window function causes a smoothing of the central peak into the nearest three or four off-diagonal modes. The smoothing scale is independent of the value of k, so adjacent modes are similarly correlated at all scales.

We now apply this technique to calculate the uncertainty on Γ and σ_8 when measured using the window functions used in creating the mock catalogues described in Chapter 4.

The technique is applied to the already completed PSCz survey of IRAS galaxies, the 2dF South Galactic strip, and the Sloan Digital Sky Survey. We do this for the full magnitude limited catalogues and for volume limited subsamples.

7.4.2 Magnitude limited case

The use of the full magnitude limited catalogue is obviously desirable since we keep the maximum amount of information. FKP derive a minimum variance weighting for the galaxies in a magnitude limited sample that provides the optimum measure of the power spectrum for a given value of $P(k)$. The weighting scheme effectively down-weights galaxies near the observer, where the expected number density is high and the error is dominated by the finite number of fluctuation volumes, and gives more weight to galaxies at large distances, where shot noise dominates the error.

Our only choice in this case is the value of $P(k_{\rm R})$ used in the weighting scheme. In general, we are most interested in the linear end of the power spectrum, and it would be useful to have error-bars as small as possible in this regime; hence we choose a value of $P(k_{\rm R}) = 5000h^{-3}\,{\rm Mpc}^3$. This is close to the value on large scales, and we note from FKP that the error analysis is relatively insensitive to small changes in $P(k_{\rm R})$.

	PSCz	2dF - SGP	SDSS
Γ	15.8%	4.7%	2.1%
σ_8	14.4%	5.9%	2.5%

Table 7.2. 1-σ percentage errors on Γ and σ_8. The results are for the magnitude limited case, using the full catalogue with FKP minimum variance weighting ($P(k_{\rm R}) = 5000h^{-3}\,{\rm Mpc}^3$), as described in section 7.4.2.

In table 7.2 we show the results of applying this method to the survey volumes of the PSCz, 2dF and SDSS catalogues. We find that, in general, the errors on the parameters derived from the power spectrum are rather low – current best estimates of the value of Γ happily range between 0.2 and 0.25, for instance, implying that our current $\gtrsim 10\%$ level of uncertainty will be radically improved upon in the next decade.

Several caveats, however, must be made in applying these results to the real surveys. Firstly, a galaxy redshift survey is performed in redshift, rather than real space, and the monopole power spectrum is distorted by the peculiar velocities of the galaxies we observe. Although we model a redshift-space power spectrum, our analysis of the errors on Γ and σ_8 assumes that the data can be perfectly corrected for the redshift-space distortions. In the rest of this chapter, we will demonstrate a technique for deriving the

error on β, the redshift-space distortion parameter, and we will find that it is generally much less well-determined than the errors given above. On linear scales, the redshift-space distortions provide a constant boost to the power spectrum, and since it is these scales that determine Γ, the value of the shape parameter will not be much affected by this effect. The amplitude, σ_8, is, however, severely degenerate with this boost, since the observed power spectrum depends on the product of the amplitude with the linear boost factor,

$$P(k) \propto \sigma_8^2 \left(1 + \frac{2\beta}{3} + \frac{\beta^2}{5}\right) \tag{7.47}$$

(Kaiser 1987). We can calculate the degeneracy of β and σ_8 by taking differentials at constant $P(k)$, leading to the expression that

$$\frac{\Delta\sigma_8}{\sigma_8} \Big/ \frac{\Delta\beta}{\beta} = \frac{\beta/3 + \beta^2/5}{1 + 2\beta/3 + \beta^2/5} \,. \tag{7.48}$$

This factor varies between 0.16 for $\beta = 0.5$ and 0.29 for $\beta = 1.0$, so the fractional error on σ_8 derived from the redshift-space power spectrum can never be less than roughly a sixth of the fractional error on β.

We also point out that the simple, two parameter power spectrum is a gross oversimplification of the true power measured from a redshift survey, even once the correction has been made accurately into real space. In reality, non-linear clustering occurs at quite moderate wavenumbers, and one is forced to either use a model with more parameters or to restrict the search for information about the linear power spectrum to higher wavelength modes. Given the behaviour of the errors with wavenumber, the fits are generally dominated by the low variance, quasi-linear part of the power spectrum. In the real Universe, this regime can be far less sensitive to Γ than in our simple model, thus it is important to check the goodness of the fit to see if it is a good one, and, if not, it may be appropriate to bias the procedure to favour the longer-wavelength modes, ie. by down-weighting data at the non-linear end of the power spectrum.

Despite these provisos, it should be noted that the shape and amplitude of the power spectrum measured in redshift space *will* be determined at the level suggested by the values in tables 7.2 and 7.5. For a survey like the 2dF, where the angular clustering of the parent catalogue has been extensively studied and used to provide accurate measurements of the real space power spectrum (Baugh & Efstathiou 1994), the combination of

these approaches will thus be a very powerful tool for examining the difference between real and redshift-space clustering over a very wide range of scales.

7.4.3 Volume limited case

The great advantage of surveys with such depth and sampling as 2dF and SDSS is the ability to construct volume limited samples of galaxies. We can thus look at the clustering properties of a particular class of galaxies, avoiding some of the effects of a bias that can depend on luminosity or morphology.

In a volume limited sample, we throw away all the galaxies beyond a certain redshift limit, and all galaxies with absolute luminosities such that they would not make it into the catalogue if they were located at that redshift limit. What criterion should be used to decide the depth of the volume limit? For a realistic result we should pick a distance that the real surveys will actually be able to give reliable data on, without errors due to shot noise dominating over the contribution to the error from cosmic variance.

Figure 4.7 in Chapter 4 shows some predicted 2dF and SDSS radial selection functions for an $\Omega_0 = 1$ cosmology. Both surveys have a median redshift of $\bar{z} \approx 0.1$, and a similar number density, although 2dF is somewhat deeper. The PSCz survey falls off at much closer distances, with $\bar{z} \approx 0.02$.

We require that the volume limit of the survey subsample be such that the signal from the power spectrum dominates over the shot noise contribution out to a certain fixed scale. As we extend the volume limit further, we throw away more galaxies, so the shot noise, which is the reciprocal of the number density, increases.

As mentioned previously, we fit out to a fixed wavenumber, $k_{\rm nl}$. We therefore pick this non-linear scale as the shot-noise limit for our analysis, and demand that $n(z_{\rm lim}) = 1/P(k_{\rm nl})$ for our sample volume limited at $z_{\rm lim}$. We employ the tabulated selection functions that were used to construct the galaxy catalogues outlined in Chapter 4 [1] to find this limiting redshift for the three surveys; the results are shown in table 7.3.

An alternative method for picking the redshift limit is to maximize the number of galaxies contained in the volume limited sample. We do this using the same selection functions, and in figure 7.7 plot the fraction of the total survey contained in a volume limited sample

[1] For an $\Omega_0 = 1$, structure normalized cosmology

	PSCz	2dF- SGP	SDSS
$z_{\rm LIM}$	0.035	0.29	0.23
$r_{\rm LIM}(h^{-1}\,{\rm Mpc})$	106	720	590

Table 7.3. Details of the redshift limits, and corresponding limits in comoving coordinates for the for the three different volume limited surveys, as described in 7.4.3.

as a function of the limiting redshift. This figure clearly shows the advantage that the future surveys will have over the PSCz in terms of the efficiency of creating volume limited samples, since nearly 30% of the galaxies in these catalogues can be used, a factor of two better than the smaller survey. We summarize these results in table 7.4. On the whole, the choice of this volume limit criterion produces smaller catalogues than the zero-crossing approach, and in what follows we stick to using the previous, less conservative method.

	PSCz	2dF- SGP	SDSS
$z_{\rm LIM}$	0.029	0.16	0.13
$r_{\rm LIM}(h^{-1}\,{\rm Mpc})$	88	440	359

Table 7.4. Equivalent to table 7.3, but this time the survey volume limits are picked so as to maximize the number of galaxies contained in the sample, as demonstrated in figure 7.7.

Including the FKP shot-noise error term leads to a curve that turns up at high k, being at a minimum when

$$\frac{d\ln P(k)}{d\ln k} + \bar{n}P(k) + 1 = 0. \tag{7.49}$$

Since $\frac{d\ln P(k)}{d\ln k} \approx -2$ at high k, the error starts to rise when $\bar{n}P(k) \approx 1$. It can thus be seen that our condition of demanding that the power spectrum should be equal to the shot noise at the zero-crossing is equivalent to demanding that the fractional variance in the power spectrum does not start increasing with increasing k in the regime where we are performing the fit.

Table 7.5 shows the results of fitting our two-parameter power spectrum to the power recovered from the volume limited surveys. The results are generally rather larger than those for the magnitude limited case, simply because we are using only a subset of

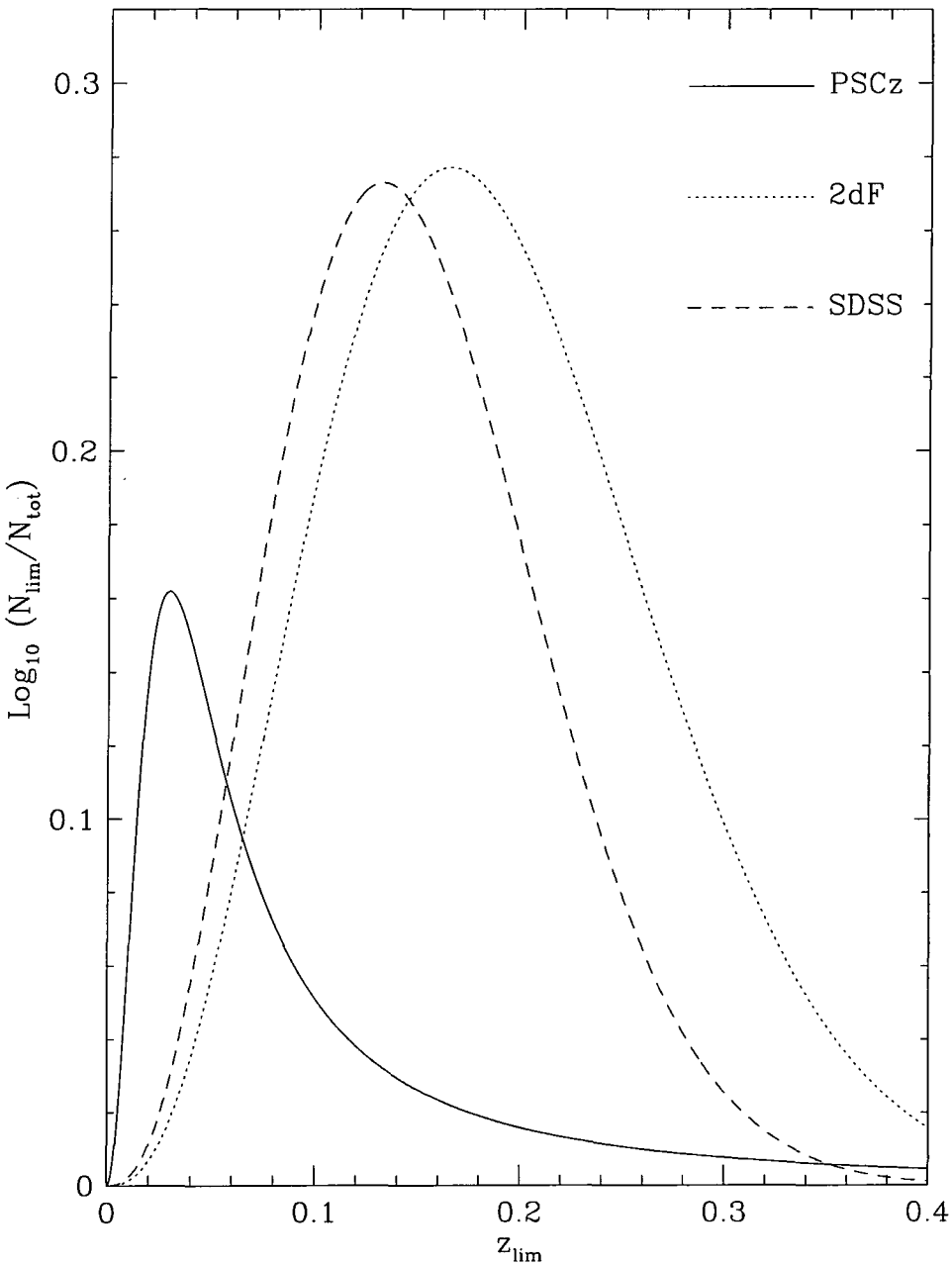

Figure 7.7: The behaviour of the number of galaxies in a volume limited sample, as a fraction of the total number of galaxies in the catalogue, versus the limiting redshift used to construct the sample.

	PSCz	2dF- SGP	SDSS
Γ	19.1%	5.7%	2.4%
σ_8	24.0%	7.2%	3.1%

Table 7.5. 1-σ errors on Γ and σ_8 from the three surveys. These results apply to the volume limited catalogues, as described in section 7.4.3 and table 7.3.

the data, probing a smaller volume of space with poorer sampling. The same caveats outlined in the previous section apply here also, regarding the simplicity of our models and the degeneracy of β and σ_8.

7.4.4 The wrong correction function

As was pointed out in section 7.2.4, the use of the wrong parameters in modelling the effect of the window function convolution on the power spectrum can lead to a bias in the derived parameters. We assess the likely extent of this bias in parameter estimation from the 2dF SGP, magnitude limited survey geometry. We consider the two variant models introduced in section 7.2.4 that produced the correction function for $P(k)$ most discrepant from the standard $[(\Gamma, \beta, \sigma_v) = (0.25, 0.55, 650\mathrm{km\,s^{-1}})]$ curve. These are the models with different Γ-values, 0.15 and 0.5. We correct the model power spectrum with the correction functions found when these values are assumed. In the low Γ case, we find this leads to a decrease in the estimated Γ of around 1%; in the high Γ case, a rise of around 3%. Thus an incorrect power spectrum can result in a bias in Γ that is comparable to the 1-σ bounds from this survey. This bias is not highly significant, but it seems prudent to include a systematic uncertainty if errors on Γ are quoted.

In a larger survey than this, the bounds on Γ are smaller, but the window function convolution will generally have a smaller effect on the power, and hence the different correction functions will be less disparate. Thus we expect the result that the systematic uncertainty be comparable to or less than the random error to be a general one.

As predicted in section 7.2.4, the choice of correction function has no appreciable effect on σ_8.

7.5 Extension to the quadrupole estimator

Just as we obtained the variance in the monopole power, $P(k)$, by spherically averaging over bins,

$$\hat{P}_0(k) = \frac{1}{V_k} \int \mathrm{d}^3k' \hat{P}(\mathbf{k}'), \tag{7.50}$$

implying an error of

$$\sigma_0^2 = \frac{1}{V_k^2} \int \mathrm{d}^3k \int \mathrm{d}^3k' \langle \delta P(\mathbf{k}) \delta P(\mathbf{k}') \rangle \tag{7.51}$$

by analogy we can do the same for the quadrupole estimator,

$$\hat{P}_2(k) = \frac{1}{V_k} \int \mathrm{d}^3k' \hat{P}(\mathbf{k}') \frac{5}{2} L_2(\mu), \tag{7.52}$$

where $L_2(\mu)$ is the second order Legendre polynomial in μ, the cosine of the angle between the vector $\mathbf{k}$ and the line of sight, $L_2(\mu) = \frac{1}{2}(3\mu^2 - 1)$. Now, $L_2(\mu)$ is a non-stochastic function, so it belongs outside any expression for "the expectation value of", enabling us to write

$$\sigma_2^2 = \frac{1}{V_k^2} \left(\frac{5}{2}\right)^2 \int \mathrm{d}^3k L_2(\mu) \int \mathrm{d}^3k' L_2(\mu') \langle \delta P(\mathbf{k}) \delta P(\mathbf{k}') \rangle. \tag{7.53}$$

For the case where bin size is large relative to the width of $W(\mathbf{k})$, the inner integral is effectively performed over only a small volume of k-space, and the value of μ' within that volume changes little from its average value, μ. Thus the expression for the error in this approximate regime is just like FKP's equation 2.3.1 but contains an extra factor of $L_2(\mu)^2$,

$$\sigma_2^2 = \frac{1}{V_k} \int \mathrm{d}^3\mathbf{k}' \left[\frac{5}{2} L_2(\mu)\right]^2 |P(\mathbf{k}) W(\mathbf{k}') + S(\mathbf{k}')|^2. \tag{7.54}$$

For a large galaxy survey, $W(\mathbf{k})$ and $S(\mathbf{k})$ are generally weak functions of the line-of-sight angle described by μ, so the integration over μ can be performed separately. Legendre polynomials are normalized by the relation:

$$\frac{2l+1}{2} \int_{-1}^{1} L_l(\mu)^2 d\mu = 1. \tag{7.55}$$

Therefore,

$$\frac{\sigma_2^2}{P_0^2} = \left(\frac{(2 \times 2) + 1}{(2 \times 0) + 1}\right) \frac{\sigma_0^2}{P_0^2} = 5 \frac{\sigma_0^2}{P_0^2}. \tag{7.56}$$

We will be using the redshift-space distortions to place constraints on the β-parameter that arises in linear theory. For a measurement of β, one is really interested in the quadrupole-to-monopole ratio, and we would therefore like to have an expression for the error on this quantity itself. The covariance between P_2 and P_0 is given by a similar expression to that for the variance used above,

$$\sigma_0\sigma_2 = \langle[\hat{P}_0(k) - P_0(k)][\hat{P}_2(k) - P_2(k)]\rangle = \frac{1}{V_k^2}\int \mathrm{d}^3k L_2(\mu)\int \mathrm{d}^3k'\langle\delta P(\mathbf{k})\delta P(\mathbf{k}')\rangle. \quad (7.57)$$

Under similar assumptions to those made for the variance, ie. the relative isotropy and compactness of $W(\mathbf{k})$ and $S(\mathbf{k})$,

$$\frac{\sigma_0\sigma_2}{P_0^2} = \frac{\sigma_0^2}{P_0^2}\frac{1}{2}\frac{5}{2}\int_{-1}^{+1}(3\mu^2 - 1)\,d\mu = 0. \quad (7.58)$$

Hence P_0 and P_2 are uncorrelated as a result of L_0 and L_2 being orthogonal functions. The error on their ratio is obtained by adding their fractional variances in quadrature:

$$\frac{\sigma_Q^2}{Q^2} = \frac{\sigma_2^2}{P_2^2} + \frac{\sigma_0^2}{P_0^2} = \frac{\sigma_0^2}{P_0^2}\left(1 + \frac{5}{Q^2}\right). \quad (7.59)$$

As described in Chapter 2, most measurements of β lie between 0.5 and 1.0. The linear value of the quadrupole-to-monopole ratio, $Q_{\rm lin}$, is given by the treatment of Kaiser (1987),

$$Q_{\rm lin} = \frac{4\beta/3 + 4\beta^2/7}{1 + 2\beta/3 + \beta^2/5}, \quad (7.60)$$

so the interesting range is $0.6 \lesssim Q_{\rm lin} \lesssim 1.0$. Non-linear effects always cause a suppression of the linear quadrupole, hence $Q \leq Q_{\rm lin}$. Thus the second term in the brackets of equation 7.59 will normally be much larger than the first, and the error will be dominated by the uncertainty in P_2 for all physically relevant situations. In this case, then, we are justified in making the assumption that

$$\sigma_Q \approx \sqrt{5}\frac{\sigma_0}{P_0}. \quad (7.61)$$

All these assumptions can be tested, as we tested the accuracy of the simplified FKP method in section 7.3.2. We compute the error on the quadrupole-to-monopole ratio using the Monte Carlo method and the FKP double-sum method (FKP2). In the Monte

Carlo method we calculate the variance in the measured quantity $Q(k)$ from fifty realizations, automatically taking in to account potential correlations between P_2 and P_0. For the double-sum method, we include the Legendre polynomials in the sum:

$$\sigma^2 = \frac{1}{N_I^2} \sum_{\mathbf{k}'} \sum_{\mathbf{k}''} L_2(\mu') L_2(\mu'') |P(\mathbf{k}) W(\mathbf{k}' - \mathbf{k}'') + S(\mathbf{k}' - \mathbf{k}'')|^2. \tag{7.62}$$

In figure 7.8 we compare these three different methods. The agreement of the curves confirms the accuracy of our treatment, but in order to fully take into account the covariance between the modes we will adopt the same Monte Carlo procedure as was used in the previous section to place constraints on the derived parameters.

7.6 Application to β

We now use the technique for estimating β outlined in the previous section and apply it to the window functions used in creating the mock catalogues described in Chapter 4. The technique is applied to the window functions of the already completed PSCz survey of IRAS galaxies, the 2dF South Galactic strip and the Sloan Digital Sky Survey. We use the method described in section 7.4 to estimate the errors on the two redshift-space parameters in our model power spectrum, β and σ_v.

Error	PSCz	2dF - SGP	SDSS
β	50.0%	14.3%	5.9%
σ_v	52.0%	9.5%	4.6%

Table 7.6. The 1-σ percentage errors on β and σ_v for the PSCz, the 2dF south galactic strip and the SDSS. Each estimate is using the full, magnitude limited survey.

Error	PSCz	2dF - SGP	SDSS
β	69.6%	20.1%	7.9%
σ_v	59.8%	15.8%	5.2%

Table 7.7. The 1-σ percentage errors on β and σ_v for the PSCz, the 2dF south galactic strip, and the SDSS – volume limited case.

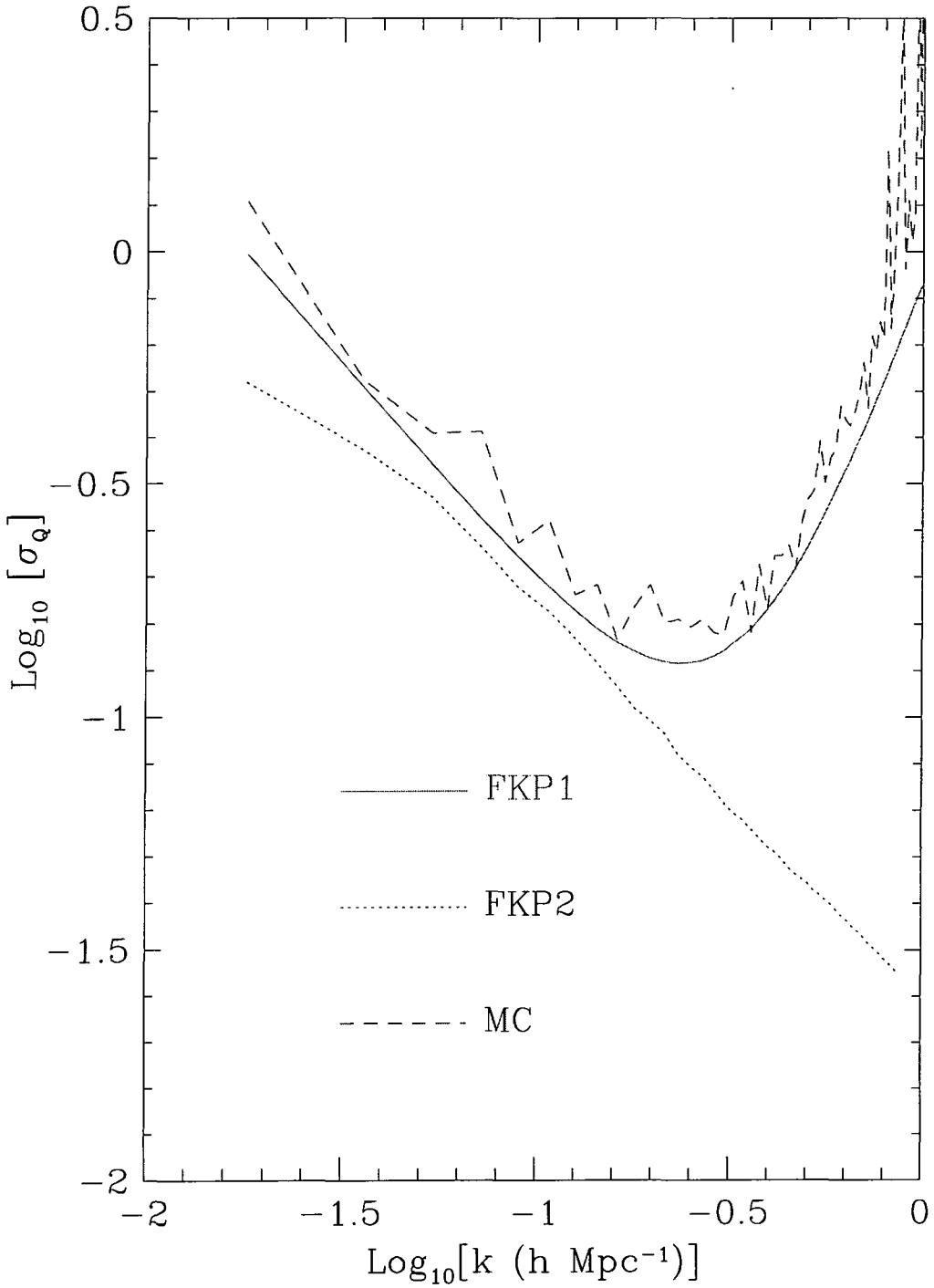

Figure 7.8: As for figure 7.4 but the error is now the fractional error on the quadrupole of the power spectrum, $P_2(k)$, for each of our three methods.

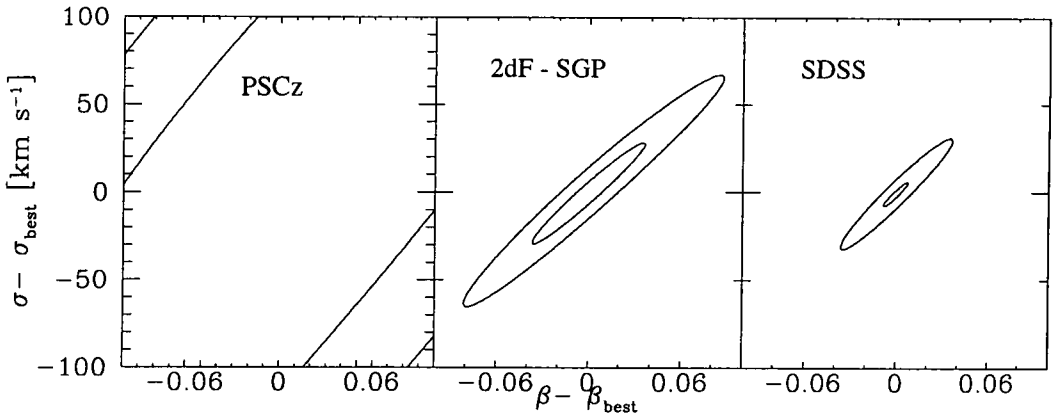

Figure 7.9: Error on β from our two parameter fit for the magnitude limited surveys as shown in table 7.6. The left panel is for the PSCz, the middle one for the 2dF South Galactic strip and the right one is for the SDSS. Contours show $\Delta\chi^2 = 1$ and 2 (39% and 63% joint confidence limits).

Tables 7.6 and 7.7 show the 1-σ percentage errors associated with measurement of these quantities in a magnitude and volume limited sample, respectively. The details of weighting and sampling are the same as those described in section 7.4. As with the real-space parameters, the errors are rather lower in the magnitude limited case which uses more of the sample. In figure 7.9 we show the $\Delta\chi^2 = 1$ and 2 confidence limits for the joint probability distribution of β and σ_v for the three surveys. The effect of using a larger survey in reducing the uncertainty on the parameters is visually very apparent.

A spherical harmonic decomposition analysis of distortions in the PSCz sample has already been performed (Tadros et al. 1998). The resultant constraint on β is 0.59 ± 0.26. This error (45% of the estimated value) is very close to the error we predict for the magnitude limited catalogue (50%). In fact, there are many differences between our treatment and the way the PSCz has been analysed, so the good agreement is something of a fluke, but it is encouraging that the results are of similar magnitude.

This time we note that we can be rather less wary of these results than those from the real-space power spectrum, since these come straight out of the model with no prior assumptions. The only real assumption is that redshift-space distortions can be modelled successfully two parameters. We shall show in the next chapter that this proves reasonable (at least up to the zero crossing of the quadrupole) for the class of *N*-body simulations we examine.

Why are the errors so large compared to those on the real space quantities? The answer for this is two-fold. Firstly, the value of $P_2(k)$ is simply less well-determined than that of $P_0(k)$, as shown in section 7.5. Secondly, the convolution with the survey geometry which causes the estimated $P(k)$ to flatten off at low k has the opposite effect on the quadrupole; this quantity is highly suppressed by the window function, and thus, when the correction is applied, the random errors on large scales are vastly increased.

7.6.1 A smaller velocity dispersion

The large velocity dispersion can also be blamed for providing a pessimistic estimate of the error on β. We have adopted the conservative view that our models for quasi-linear redshift-space distortion are only valid up to the zero-crossing of the quadrupole. Whilst this assumption seems reasonable for current models, we have used a value of σ_v such that the zero crossing in the model is close to that found for our structure normalized simulations. This requires $\sigma_v \approx 650\mathrm{km\,s^{-1}}$. Observations of redshift space distortions have generally led to rather smaller estimates of the dispersion: early studies of the CfA galaxy survey (Davis & Peebles 1983) produced a value for the pairwise velocity dispersion of $340\pm40\mathrm{km\,s^{-1}}$; more recently, Ratcliffe et al. (1998) find $\sigma_v = 416\pm36\mathrm{km\,s^{-1}}$ from the DUKST survey. With a smaller dispersion, the zero-crossing moves to higher k, giving a wider range to fit models over, thus reducing the errors. In the volume limited case this is partly cancelled out by the criterion we adopt for picking the sample size. We illustrate the effect of changing σ_v by using a more realistic value of $450\mathrm{km\,s^{-1}}$. The zero-crossing is now at $k_{\mathrm{nl}} = 0.35h\,\mathrm{Mpc}^{-1}$, and from examining the power spectrum we find $P(k_{\mathrm{nl}}) = 800h^{-3}\,\mathrm{Mpc}^3$. Examining the selection function, we find the redshift at which the density results in a shot-noise equal to this value of the power spectrum is $z(\bar{n} = 1/800) = 0.24$, so we volume limit the survey at this scale. This reduction in volume is not a problem in the magnitude limited case, which still uses the entire survey.

For 2dF, the 1-σ error on β from the whole SGP slice was 14%. Decreasing the velocity dispersion as described reduces this error to 10%. In the volume limited case, the error was previously 20%. The lower velocity dispersion model reduces this to 12%. Similar tightening of the confidence intervals will be seen in the results from the other surveys.

We noted in Chapter 6 that the velocity dispersion found in fitting a model to the quadrupole-to-monopole ratio was very sensitive to the method and amount of bias in

the galaxy sample. This implies that the dominant contribution to σ_v comes from galaxy clusters. If, as suggested in section 6.6, we are able to efficiently identify and remove clusters from the data, by collapsing the member galaxies to their mean redshift, then the effective σ_v will be much reduced. In this case, we will have a much wider range of scales over which a quasi-linear treatment is valid, and errors on β should go down accordingly.

7.6.2 The wrong correction function again

We again estimate the systematic bias that could result from an incorrect choice of correction function. We use the same discrepant Γ models as in section 7.4.4, $\Gamma = 0.15$ and 0.5. In the low Γ case, we find this leads to a rise in β of around 6%; in the high Γ case, a fall in of around 2%. Both these changes are well within the 1-σ bounds on β.

We again note that in a larger survey the bounds on β are smaller, but the different correction functions will be less disparate. Thus the correction is insensitive to the model chosen (within reasonable bounds), and the systematic bias in β which arises through correcting for the window function in this way is not significant.

7.6.3 Combining NGP and SGP

The 2dF survey contains an extra component: a region in the North Galactic polar area, with similar range of right ascension as the southern galactic strip, but with only two-thirds the declination range. Adding this extra volume to the survey enables us to measure the derived parameters more accurately, since the error on the power spectrum goes as the square root of the volume probed.

There are two ways of combining the data from the two strips:

- **Coherently**. The non-uniform geometry in the combined survey means that there are wavelengths probed by the survey as a whole that are twice the length of those probed by either survey individually. Thus we get much more information on large-scale power, where the behaviour of the quadrupole is most sensitive to the value of β. We simulate this effect by using the same Monte Carlo approach as outlined above, but using a survey window corresponding to the "whole" 2dF survey.

- **Incoherently**. In fact it is unlikely that the measurements can be combined coherently in this way. Wavelengths cannot easily be traced through the two sub-surveys because of uncertainty in the relative calibration of the photographic plates for the Northern and Southern strips. Neither can we simply add the errors in quadrature, as the two volumes are obviously correlated, so a measurement of β from one is not independent of a measure from the other. We account for this by adapting our Monte Carlo technique so that the power spectrum and quadrupole are averaged over the two volumes for each random realization. Thus we simulate the case in the real world, where we can only measure one realization of the density field. The covariance is then measured for this averaged quantity.

Error	SGP only	Coherent	Incoherent
β	20.1%	13.8%	16.9%

Table 7.8. The percentage errors on β from the 2dF survey using the SGP alone, combining coherently with the NGP, and combining incoherently. The incoherent measurement should reflect a realistic uncertainty on β from the 2dF.

Table 7.8 compares the errors on β for the volume limited 2dF using just the SGP with the error from the whole survey combined in these two ways. The coherent combination reduces the error substantially, showing that the use of those very long wavelengths enables much greater accuracy in determining β. The incoherent combination reduces the error close to the level expected if the two volumes were completely independent.

7.7 Discussion

We have shown in this Chapter that the uncertainty due to sampling only a finite volume of space with our surveys places a severe restriction on our ability to extract information on the parameters of the large-scale structure in the Universe.

We have examined the systematic biases introduced by the convolution with the window function of a galaxy survey, and developed a technique to correct for this. Using the results of FKP, we have assigned errors to the power spectrum and used these errors in order to determine the uncertainty in parameters derived from the power spectrum.

We have applied the FKP formalism to measurements of the quadrupole, and checked the results with our own independent technique. This method enables us to extend our parameter error estimation method to the redshift-space parameters, β and σ_v, in our simple model.

We have applied these techniques to the PSCz, 2dF south Galactic strip, and the SDSS, taking both volume limited and and FKP-minimum variance-weighted magnitude limited samples. The surveys generally show only a small improvement where the magnitude limited approach is taken, since the low weighting of distant regions means there is little overall gain in effective volume. The exception is the PSCz, which shows an enormous improvement when the whole survey is used. This is due to the shape of the survey's selection function: the peak is so nearby that creating a volume limited sample at cosmologically interesting scales is impractical, given the high shot noise so introduced. In order to probe these scales with such a survey we cannot afford to throw out galaxy pairs, and using the whole sample with FKP weighting is the best way forward.

We have quantified how the uncertainty due to sampling only a finite volume of space with our surveys places a limit on our ability to extract information on large-scale structure in the Universe. Several of the assumptions made in this treatment are violated in the case of a genuine redshift survey, generally making it a tough task for the analysis of the real data to get errors down to the level set by the finite volume of the survey. Some of these are:

- **The distant observer approximation**, which we are able to make in this idealized case, will not hold so well for the real surveys (Ballinger, Heavens, & Taylor 1995), and extracting information on the largest scales is thus a more complex process, possibly resulting in the loss of some information.

- **A perfect model**: the assumption of a perfect quasi-linear model for extracting β from the redshift-space distortions in a way that is robust to cosmology and biasing method is not something that has yet been achieved; this deficiency has been shown in Chapter 6 and will be further investigated in Chapter 8. More complex and physically realistic models of the real-space power spectrum exist (Peacock & Dodds 1994), but these involve a variety of parameters and are outside the scope of this work.

- **Mode coupling**: gravitational instability on small scales causes coupling between different modes of the density field, resulting in correlations between the phases of these modes. It is this phase correlation that produces the visible effect of large-scale structure that can be seen so clearly in real surveys. This coupling introduces a further covariance between modes that we have not attempted to model in our matrix approach, so we have over-estimated the amount of information contained in the modes towards the zero-crossing. Recent work (Meiksin & White 1999) has attempted to quantify this coupling.

Despite these concerns, there are reasons to suppose that the large data-sets being compiled at the moment may be able to measure the cosmological parameters rather better than we estimate. In our approach, we only fit the quadrupole out to its zero-crossing. On smaller scales than this, there is no reliable model for the distortions, and information about β is washed out by the small-scale velocities. Removing this non-linear effect should produce a signal that a stronger β dependence. This can be done by collapsing the galaxy clusters, as outlined in section 6.6. The effects of this process need to be studied in further detail using further numerical simulations if it is to be applied to real galaxy surveys. Heavens & Taylor (1997) find that distortion parameter can be measured much more accurately if the real-space power spectrum is measured independently, ie. deprojected from a parent (angular) catalogue.

In conclusion, then, it should be borne in mind that we apply this technique with reference to a very specific problem, and pay no attention to the difficulty of actually trying to get the real errors, whether statistical or systematic, down to the level of variance set by the finite volume of the survey. The solution of this problem is the goal of the next chapter.

References

Ballinger W. E., Heavens A. F., Taylor A. N., 1995, MNRAS, 276, L59

Bardeen J., Bond J., Kaiser N., Szalay A., 1986, ApJ, 304, 15

Baugh C. M., Efstathiou G., 1994, MNRAS, 267, 323

Canavezes A. et al., 1998, MNRAS, 297, 777

Davis M., Peebles P. J. E., 1983, ApJ, 267, 465

Fan Z. H., Bardeen J. M., 1994, American Astronomical Society Meeting, 184, 6206

Feldman H. A., Kaiser N., Peacock J. A., 1994, ApJ, 426, 23

Ferreira P. G., Magueijo J., Gorski K. M., 1998, ApJ Lett, 503, L1

Heavens A. F., Taylor A. N., 1995, MNRAS, 275, 483

Heavens A. F., Taylor A. N., 1997, MNRAS, 290, 456

Kaiser N., 1987, MNRAS, 227, 1

Kogut A., Banday A. J., Bennett C. L., Gorski K. M., Hinshaw G., Smoot G. F., Wright E. L., 1996, ApJ Lett, 464, L29

Lin H., Kirshner R. P., Shectman S. A., Landy S. D., Oemler A., Tucker D. L., Schechter P. L., 1996, ApJ, 471, 617

Lucy L. B., 1974, AJ, 79, 745

Maddox S. J., Efstathiou G., Sutherland W. J., 1996, MNRAS, 283, 1227

Meiksin A., White M., 1999, MNRAS, submitted, astro-ph/9812129

Peacock J. A., Dodds S. J., 1994, MNRAS, 267, 1020

Ratcliffe A., Shanks T., Parker Q. A., Fong R., 1998, MNRAS, 296, 191

Rowan-Robinson M. et al., 1990, MNRAS, 247, 1

Stuart A., 1987, Kendall's Advanced theory of statistics, 5th ed. Vol.1: Distribution theory. Charles Griffin, London

Tadros H. et al., 1998, in Large Scale Structure: Tracks and Traces. Proceedings of the 12th Potsdam Cosmology Workshop, September 1997. Eds. V. Mueller, S. Gottloeber, J.P. Muecket, J. Wambsganss. World Scientific., p. 221

Zaroubi S., Hoffman Y., 1996, ApJ, 462, 25

Chapter 8

A new model for the quadrupole

THE ARGUMENT Given the failure of existing models for redshift-space distortions to provide a really accurate measure of the β-parameter, and the ability of forthcoming surveys to obtain data with very low random errors, it becomes necessary to develop better models for the distortions. Here we review the failures of the dispersion models and present a new method for extracting β from the quadrupole statistic which has little systematic offset over a wide range of β and cosmologies. This empirical model is then applied to one of the mock catalogues described in Chapter 4, to illustrate the technique and see how accurately we can recover the true value of β.

8.1 Introduction

As shown in Chapter 7, the next generation of galaxy redshift surveys will theoretically be capable of constraining β to within a few per cent. It is therefore vital to have models for extracting β from the data that are accurate to similar levels. In this chapter we use *N*-body simulations, where the value of β is known *a priori*, to show that none of the velocity dispersion models described in Chapter 6 are capable of estimating β without substantial bias. These biases are found, in section 8.3, to be comparable to or greater than the random errors. In section 8.3.3 we present our new model, based on empirical results from the set of simulations described in Chapter 4, and show how it performs. In section 8.4 we apply this model to one of the mock catalogues, explain the limitations of applying the technique to a real data set, and estimate the variance in β using the technique described in Chapter 7. We obtain an external measure of the error on β using mock catalogues constructed from ten independent *N*-body simulations with the same cosmology and biasing method. We conclude in section 8.5.

8.2 Velocity dispersion models

In Chapter 6 we considered two extensions to the linear theory of redshift-space distortions, the Zel'dovich approximation, which was found to break down in the case of biased galaxy distributions, and the exponential model of velocity dispersions, which seemed to work well in that limit the velocity dispersions were high, ie. large $\sigma_8^{\rm gal}$. In fact, three models of velocity dispersion have generally been considered in the literature,

- **Gaussian**. Particle velocities are drawn from the distribution $\mathcal{P}(v) \propto \exp(-v^2/2\sigma_v^2)$. In this case the convolution in real space produces a multiplication of the $\delta(k)$ by the factor $\exp(-k^2\mu^2\sigma_v^2/2)$.

- **Exponential**. The particle velocities have $\mathcal{P}(v) \propto \exp(-\sqrt{2}|v|/\sigma_v)$. The $\delta(k)$ is then multiplied by $(1 + k^2\mu^2\sigma_v^2/2)^{-1}$.

- **Pairwise exponential**. In this case, the *pairwise* velocity dispersion of the particles is assumed to come from an exponential distribution like that of the exponential model. The boost factor is the square root of that in the previous case, and so the power spectrum itself is multiplied by $(1 + k^2\mu^2\sigma_v^2/2)^{-1}$.

The value of σ_v that appears in the pairwise formula is the pairwise velocity dispersion, equal to $\sqrt{2}$ times the pointwise dispersion. Thus, if we Taylor expand all three of the factors, we find that the first order term is the same in each case; the distributions have the same width, but different shapes.

As pointed out by Peacock & Dodds (1994), this effect cannot be considered in isolation; the linear Kaiser boost to the power spectrum also contains terms in μ, so the two factors must be multiplied together with the desired Legendre polynomial before averaging over the azimuthal angle. This can just about be performed by a human for the $l = 0$ case, but for $l = 2$ and $l = 4$ it is much more convenient to use a mathematical package such as MAPLE. In Appendix D we present a MAPLE worksheet used to calculate the velocity dispersion effect on the power spectrum with the linear Kaiser formula. We calculate the effect on the monopole, quadrupole and hexadecapole for all three of the above models.

8.3 Application to simulations

In order to test the reliability of the models, we use the same method outlined in Chapter 6 for obtaining the quadrupole-to-monopole ratio from the set of simulations described in Chapter 4. We use all the available cosmologies and all the bias models.

8.3.1 Errors

Since we are dealing with the full simulation cubes, with no window function introduced by looking at a catalogue, measurements of the power spectrum for each mode are completely uncorrelated, and we can avoid all the complexity used in Chapter 7 to deal with the correlations in a real galaxy survey. We use the same method outlined in Chapter 6, that of multiple random Zel'dovich approximation runs, to obtain the error on Q as a function of scale. We estimate β using a least-squares fitting procedure with β and σ_v as free parameters.

8.3.2 Results

In figure 8.1 we show the first of several scatter plots for the behaviour of $\beta_{\rm fit}$ with the known value of $\beta_8 = \Omega_0^{0.6}/b_8$ from the simulation, where the bias factor is defined as the ratio of rms fluctuations in spheres of radius $8h^{-1}\,{\rm Mpc}$ in the galaxy density to those in the mass density.

Each panel is labelled with the dispersion model used to make the fit, and the figure includes every biasing scheme of every cosmology outlined in Chapter 4. The black diagonal line represents an ideal, one-to-one correspondence between model and data. At the bottom of each panel we show the average difference between the fitted and true values, and the scatter in this result. It is immediately clear from this figure that the velocity dispersion models all produce a systematic offset between the fitted and true values of β. The pairwise exponential model comes closest to fitting the data, but this still results in a systematic underestimate of β by 0.1. We expect to find $\beta \approx 0.5$, so this represents a 20% bias in measuring β, certainly rather larger than the random errors we expect from Chapter 7. We are therefore motivated to develop a better β-estimator that does not suffer from such systematics.

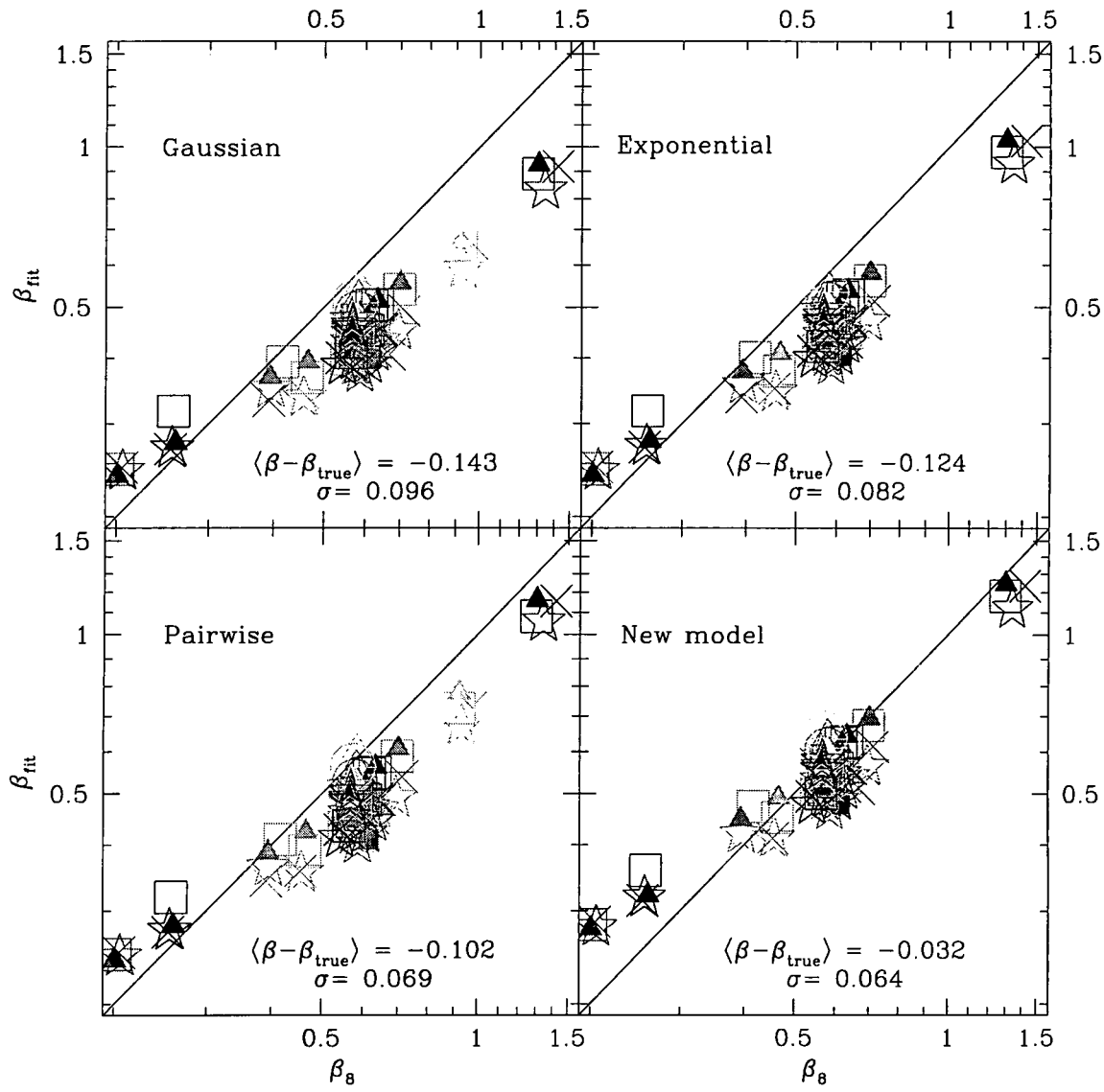

Figure 8.1: Scatter plots for $\beta_{\rm fit}$ for the entire sample of over one hundred simulations. Each panel shows the results of using a different redshift-space distortion model to extract the value of $\beta_{\rm fit}$, as specified by the name in the top left corner. We also quantify the systematic offset, $\langle \beta - \beta_{\rm true} \rangle$, and the scatter, σ, about the mean value. The point types reflect different bias types: model 1 (stars), 2 (crosses), 3 (circles), 4 (open squares), 5 (solid triangles), 6 (open triangles), and 7 (solid squares).

8.3.3 A new measure

The estimator we introduce here is empirically motivated. We have a large set of cosmological simulations spanning a wide range of parameter space, as described in Chapter 4. Under the assumption that the real Universe fits somewhere in this space, an estimator that can accurately and robustly measure β from the range of simulations should be able to do the same when applied to a real galaxy sample.

We expect the simple, linear formula for redshift-space distortions to be accurate at large scales. We thus require our model to asymptotically approach this form. When measuring the quadrupole, it is thus natural to use β, which fixes the large-scale amplitude of the quadrupole-to-monopole ratio, as a parameter. The other obvious choice is the scale at which the quadrupole passes through zero. Figure 8.2 shows the result of scaling the quadrupole-to-monopole ratios, Q, of all the simulations by their linear values, $Q_{\rm lin}$. Similarly, the wavenumber has been scaled by the factor $k_{\rm nl}$, the zero crossing in each case. At low k, there is substantial scatter between the curves, and a turn away from the linear value in the first two bins. This feature was explained in Chapter 4 as resulting from a random down-turn in power on these scales in the simulations we used: all the simulations are based on the same initial random phases, so this down-turn is repeated in all the simulations. Despite these facts, it can be seen that this scaling has resulted in a reasonably good empirical estimator for the quadrupole, which we plot as the thick, solid line in figure 8.2. This curve is given by:

$$\frac{Q(k)}{Q_{\rm lin}} = 1 - \left(\frac{k}{k_{\rm nl}}\right)^{1.22}. \tag{8.1}$$

This is rather similar to the approach used by Fisher & Nusser (1996) who fit an empirical curve to their analytic Zel'dovich approximations for the quadrupole using the same scalings. We stress that our approach is much more general since it is based on the "real", non-linear data output from simulations, and it covers a much broader range of cosmologies.

The bottom right panel of figure 8.1 shows the effect of employing this new estimator. The offset has been reduced by a factor of 3 or 4. In fact, it is interesting to restrict our study to the structure normalized set of models. All these models end up with $\beta \approx 0.6$. Figure 8.3 shows a similar scatter plot as figure 8.1, but zooming in on this subset of models. We make the point the form of the empirical fit was chosen to be robust over

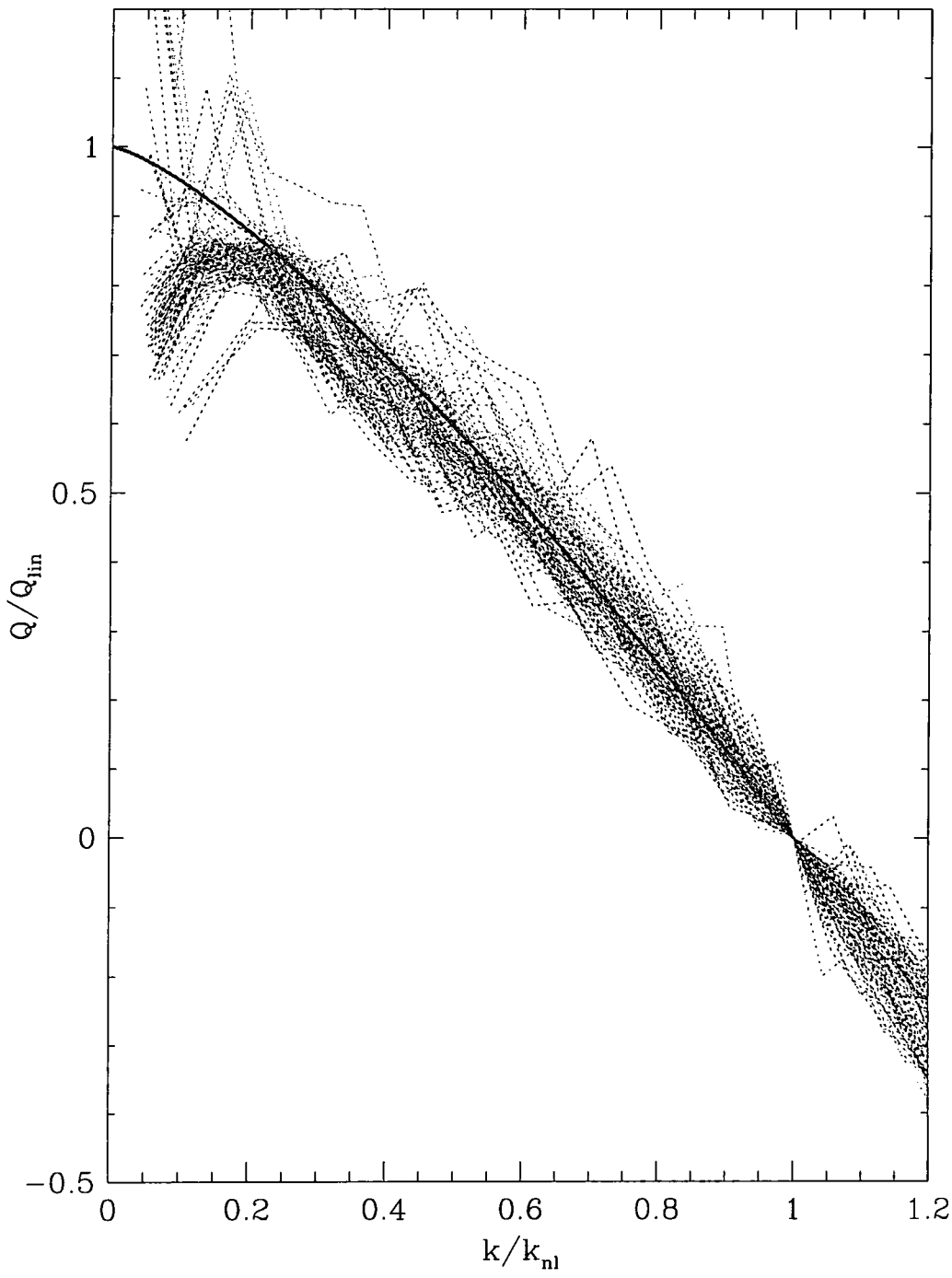

Figure 8.2: The scaled quadrupole-to-monopole ratio for all the simulations and bias models described in Chapter 4. The y-axis is scaled to the expected, linear theory value of Q, the x-axis is scaled to the zero-crossing scale of the quadrupole, $k_{\rm nl}$.

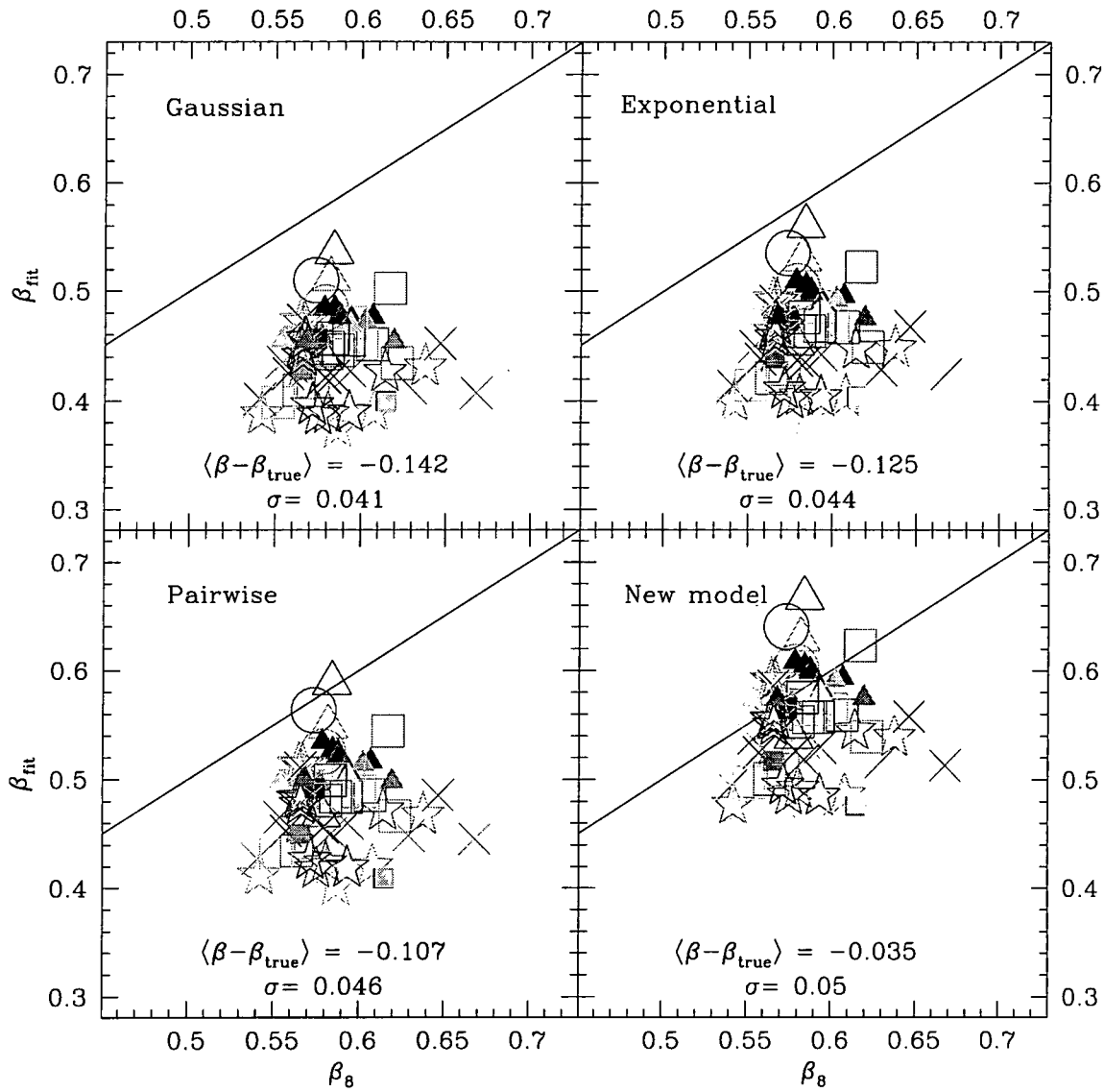

Figure 8.3: The same as figure 8.1, but including only the structure normalized simulations. These all have $\beta \approx 0.6$, enabling us to zoom in on this area of parameter-space. Bias prescriptions have the same point type as in figure 8.1, model 1 (stars), 2 (crosses), 3 (circles), 4 (open squares), 5 (solid triangles), 6 (open triangles), and 7 (solid squares).

a very wide range of cosmological parameters. If one requires a fit to only a particular sub-class of models, an even less biased estimator could be defined.

8.3.4 Scatter in the relationship

There are two sources of scatter in the curves we have looked at (figures 8.1 and 8.3):

- **Bias model.** Different prescriptions for biasing the galaxy catalogues result in systematically different best-fit values of β, even though they are constrained to have the same values of $\sigma_8^{\rm gal}$, and hence β_8. This is demonstrated in figures 8.4 and 8.5.
- **Random.** The simulations are of finite volume, and thus do not completely measure the power spectrum. This causes a random scatter. The process by which the simulations are biased involves the random (Poisson) sampling of the density field to create a galaxy field, and this stochastic effect also causes estimates of β to scatter around their mean value. This random scatter is shown in figure 8.6.

As well as reducing the systematic offset caused by using a poorly fitting model for the distortions, we would also like to use a statistic that minimizes the internal scatter from these sources.

The conventional method for describing the bias factor, b, is by the ratio of σ_8 in the galaxy and the mass fields. In the approximation that both power spectra have the same shape, or at least the same shape on scales that contribute to the fluctuations in $8h^{-1}\,{\rm Mpc}$ spheres, this is equivalent to a boost in the galaxy power spectrum normalization by a factor b^2 relative to the mass spectrum. Most physical prescriptions for galaxy formation, in contrast, result in a bias that is to some extent scale dependent (Mann, Peacock, & Heavens 1998). For example, the large scale galaxy distribution may have a constant bias, but this may be reduced in clusters where the number density is sufficiently high that a significant amount of merging has occurred.

In figures 8.4 and 8.5 we show the four simulations that have the widest range of biasing schemes. The E3S simulations have been biased using all seven schemes described in Chapter 4, and the L3S and O4S cosmologies have been biased using six out of the seven. The left hand panels show the scatter of $\beta_{\rm fit}$ with β_8. As can be seen, for any one simulation, most of the biasing prescriptions result in the same values of β_8: not

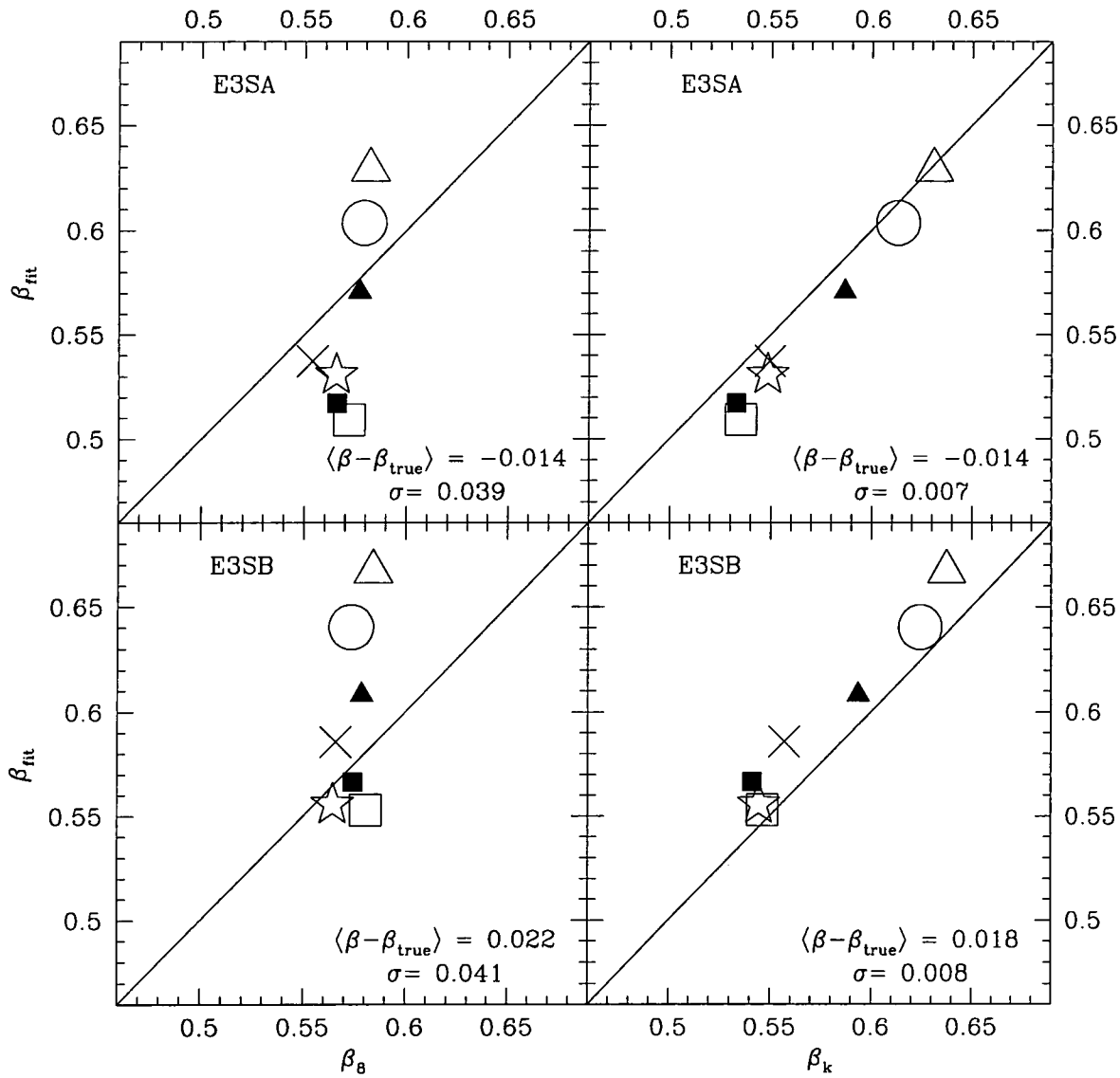

Figure 8.4: Scatter plots of $\beta_{\rm fit}$ from the E3S simulations ($\Omega_0 = 1.0, \Lambda_0 = 0.0$), realization A (top panels) and B (bottom panels). On the left we plot $\beta_{\rm fit}$ from our new model against β_8, the value of β obtained when the bias factor is defined through the ratio of rms fluctuations in $8h^{-1}$ Mpc spheres in the galaxy and mass distributions, and on the right we use $\beta_{\rm k}$, which is defined using a bias factor from the square root of the ratio of the large-scale power spectra of the two fields. The symbols represent: bias model 1 (stars), 2 (crosses), 3 (circles), 4 (open squares), 5 (solid triangles), 6 (open triangles), and 7 (solid squares).

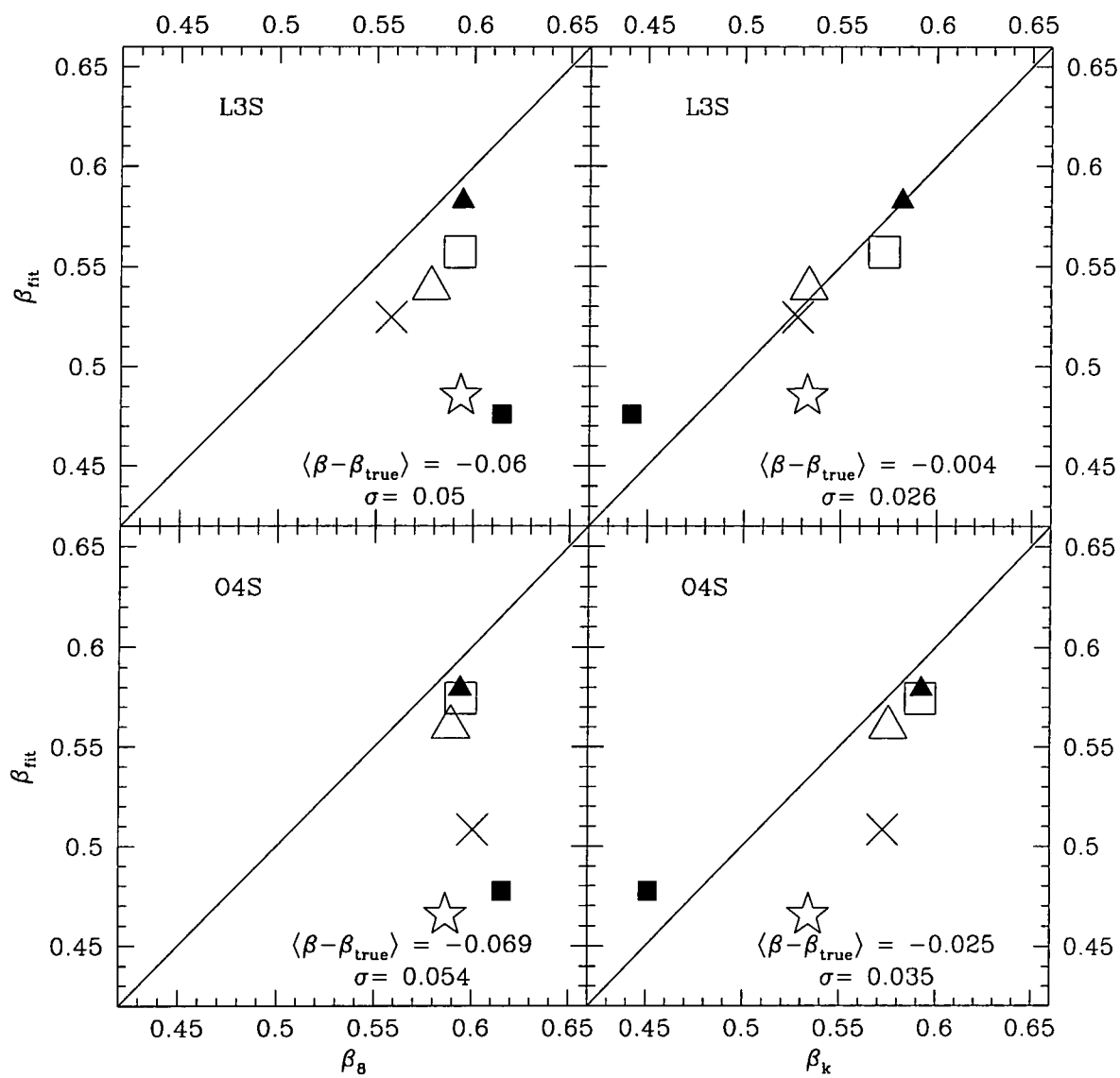

Figure 8.5: The same as figure 8.4, but for the L3S ($\Omega_0 = 0.3, \Lambda_0 = 0.7$) and O4S ($\Omega_0 = 0.4$, $\Lambda_0 = 0.0$) simulations.

really surprising since most of them were fixed to reproduce clustering on these scales. There is, however, a significant scatter in the values of $\beta_{\rm fit}$ for these different biases. In order to eliminate this scatter, on the right hand panel in each case we plot $\beta_{\rm fit}$ against $\beta_{\rm k}$, where $\beta_{\rm k}$ is obtained using the bias factor derived from the ratio $P_{\rm gal}(k)/P_{\rm mass}(k)$ at a fixed value of k. Ideally, we would like to use the smallest value of k possible, to reflect the asymptotic value of the bias. In practice, we find that the large uncertainty in the power spectrum at large scales, caused by the small number of modes to average over, produces its own scatter in the deduced bias. We find the value of k that minimizes the scatter is $k = 0.07272h\,{\rm Mpc}^{-1}$. Use of $\beta_{\rm k}$ rather than β_8 has a dramatic effect on the scatter of the different models, pulling them much closer to the $\beta = \beta_{\rm fit}$ line. The scatter is reduced by a factor of five in the E3S models and around two in the low-Ω models.

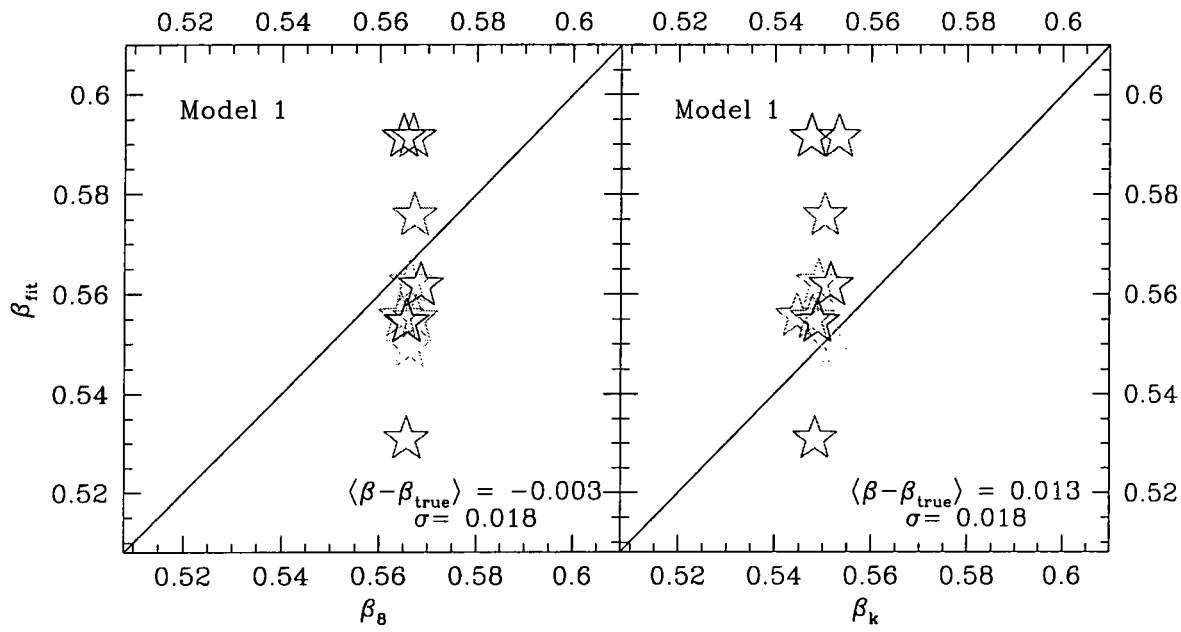

Figure 8.6: The scatter of $\beta_{\rm fit}$ for the ten independent E3S simulations with bias model 1. This scatter thus reflects the intrinsic random scatter between simulations with different initial phases and different Poisson sampling to obtain the galaxy distribution.

In figure 8.6 we look at true random scatter by comparing the values of β from the ten independent E3S simulations biased with model 1. This represents the intrinsic scatter. We see that changing the definition of $\beta_{\rm true}$ has no effect in this case. The resultant scatter of around 3% is thus the lowest uncertainty we could place on β by measuring it

from one of the simulations. In the next section, we will use these methods to analyse β from the mock catalogues. Since the mocks have been constructed from the simulations, they contain no extra information, and there is no way of determining β more accurately.

8.4 Application to mock catalogues

We now attempt to apply this model for the velocity dispersion directly to mock catalogues, as if they were real datasets. The problems of dealing with the survey window function in terms of its effect on the quadrupole itself and on the error on this quantity have been discussed in Chapter 7. Here, we will compare the estimated uncertainty on β derived previously with an estimate from measuring β in ten mock surveys drawn from independent *N*-body simulations. We choose to apply the technique to the 2dF South Galactic slice in an $\Omega_0 = 1$, structure normalized model.

8.4.1 A consistent approach

For the comparison to be worthwhile, we must take pains to ensure that the implementation of the two different methods is as similar as possible. There are several key considerations that must be dealt with.

- **The distant observer approximation**. As noted in Chapter 7, the linear theory formalism of Kaiser (1987) is applicable only when the redshift-space density field can be approximated as a sum of plane waves, so it will not work for surveys of large opening angle where this criterion is not met. Whilst there do exist methods of dealing with wide angle surveys in one go by expanding the density into spherical harmonics (Heavens & Taylor 1995), we do not concern ourselves with those here. Rather, we split the survey up into separate angular bins with relatively small opening angle, and treat each one with the plane parallel approximation. For the 2dF SGP geometry, the declination range is $15°$. It thus seems reasonable to pick a right ascension range for our angular bins of comparable extent. The azimuthal extent of the South Galactic strip is $\approx 90° \cos 30° = 78°$. We split the survey into three bins each spanning $26°$ in right ascension. Note that there are pairs of galaxies that span adjacent bins but still have opening angle less than the $26°$ bin width. To avoid throwing this data away, we also include the two overlapping bins. The effect of a finite opening angle

on the estimated value of β has been studied by Cole, Fisher, & Weinberg (1995). From their figure 8 it is clear that a $26°$ opening angle should only result in a one percent underestimate of the quadrupole-to-monopole ratio of the power spectrum. Since $Q_{\rm lin}(\beta)$ is approximately linear over a reasonable range of β, this introduces negligible systematic error. We thus perform our analysis for five bins of angular extent $\approx 26° \times 15°$ and average the resulting power spectrum estimates. The method of random realizations described in Chapter 7 is not affected by the distant observer approximation, but to make the treatment equivalent, we also split the survey into the same five angular bins. The bins sample a density field from the the same initial phases, and the results are combined incoherently, as described for the NGP and SGP in section 7.6.3.

- **Power at discrete k values**. Our mock 2dF catalogues have been drawn from *N*-body simulations that have been carried out on a finite, periodic grid. When the initial displacements are applied to the dark matter particles, power is given to the density field only at modes that are at discrete wavenumbers, integer multiples of the fundamental mode of the simulation cube. On small scales, non-linear evolution between the modes will result in the effective "leakage" of power from these modes. On large scales, this will not be the case, and to use a box for the Fourier analysis that is not equal to the the size of the original simulation cube will result in the sampling of modes that do not have a well defined amplitude. We thus restrict our analysis to a cube that has the length as the original simulation, $L_{\rm BOX} = 345.6h^{-1}\,{\rm Mpc}$ (see section 4.7).

- **Non-linear mode coupling**. In the simulations, as in reality, gravitational instability causes non-linear evolution of the density field such that it is no longer a good approximation to assume there is no "cross-talk" between nearby modes. Correlations are thus introduced between the modes on top of those caused by the convolution with the survey window function. On the largest scales, this result is expected to be negligible in comparison to the smoothing introduced by the window function, since the modes are still in the linear regime. As we extend to smaller scales, the effect of the window function in correlating nearby modes is constant: see figure 7.6. The non-linear behaviour gets stronger at smaller scales, so eventually the effects must become comparable, and on yet smaller scales the coupling effect will dominate.

Preliminary work on this topic (Meiksin & White 1999) suggests that it could be an issue on the scales (below the zero-crossing) that we consider, but the extent of the problem is highly dependent on the amplitude of the power spectrum used. The effect is likely to be even worse in redshift space than in a real-space *N*-body simulation, since virial velocities stretch out physically small non-linear structures (clusters), inevitably spreading information that may be localized in real-k-space over a range of scales in redshift-k-space. We make no attempt to introduce non-linear coupling into the random phase method of Chapter 7, which we have shown to be largely model-independent.

- **The zero-crossing scale**. The velocity dispersion in the simulations is such that $\mathbf{k}_{\rm nl} \approx 0.3h\,{\rm Mpc}^{-1}$. We model the same zero-crossing in the model power spectrum used to obtain the mode amplitudes by using a pairwise exponential model for the velocity distribution with dispersion $\sigma_v = 500{\rm km\,s}^{-1}$.

8.4.2 The true error

Having made the two methods as equivalent as possible, in advance of the analysis we now consider reasons why the errors derived on the clustering using these techniques, even if they agree with each other, may not accurately reflect the true error on β from a redshift survey.

- **Fundamental wavelength**. Related to the point about discrete wavenumbers made above, we note that by restricting the wavenumbers examined, we also limit the usefulness of the survey for studying large-scale modes, because there is no wavelength longer than $L_{\rm BOX}$. In order to again make the two treatments identical, we will also apply the random phase method to a box of the same size. Note that, especially in the case of a large survey with volume much greater than the size of this cube, this will not accurately reflect the real ability to measure the power spectrum on large scales, and will hence lead to an over-prediction of the uncertainty on parameters like β which rely on long-wavelength information to pin them down. In the next section we will assess the size of this effect by comparing the random phase method applied to a grid of $L_{\rm BOX} = 345.6h^{-1}\,{\rm Mpc}$ with results from a much larger cube.

- **The distant observer approximation**. As mentioned above, we combine our angular bins incoherently, ie. we do not measure power picked out by pairs of separation greater than $26°$. If the method of spherical harmonic decomposition, or indeed any other technique that does not rely on the plane-parallel expansion, can be applied to the data set in the same way, there is no need for this caution, and the value of β will be measured to rather greater accuracy. Assuming this is the case, we will quantify the size of this improvement by comparing the error from the random phase method applied to the five bins with the same technique applied exactly as in Chapter 7, ie. to the whole 2dF South Galactic strip in one go.

- **The zero-crossing scale**. As pointed out in Chapter 7, real galaxy catalogues have generally found rather smaller velocity dispersions than the ones measured from *N*-body simulations. This will again push the zero-crossing of the quadrupole out to higher k, giving a wider range of scales for which there is a reliable model of the effect of the non-linearity. Again, this increase in accuracy can be anticipated by using the random phase method with a more observationally realistic velocity dispersion.

- **Redshift to physical coordinates**. The conversion from redshift to true distance depends on the evolution of the expansion factor, which is a function of the geometry of space-time, ie. dependent on Ω_0 and Λ_0. Using the wrong values of these quantities in the coordinate transform will result in a bias in the anisotropy of the power spectrum. It is this bias that results in the so-called "cosmological" redshift-space distortions investigated by Nakamura, Matsubara, & Suto (1998). This is, in general, only a significant effect at redshifts comparable to unity; at low z, the translation is linear and not sensitive to the cosmology. The magnitude of the bias will have to be assessed when dealing with the real catalogues, since they do have appreciable depths. For this treatment we simply use the known value of $\Omega_0 = 1$ from the simulations to make the conversion, eliminating this bias.

8.4.3 The expected error

In this section we apply the formalism of the previous chapter to estimate how well we should be able to measure cosmological parameters from the 2dF South Galactic strip. As mentioned above, we use a model power spectrum with $\sigma_v = 500\mathrm{km\,s^{-1}}$ to accurately model the zero-crossing of the quadrupole. Our standard model has $\beta = 0.55$, which

is the value we expect to obtain from the simulations, as demonstrated in figure 8.6. When we perform our analysis on a grid of $L_{\rm BOX} = 345.6h^{-1}\,{\rm Mpc}$, the same size as the fundamental cube of the simulations, we find an expected, 1-σ error on β of 18%. As far as possible, we have made this analysis consistent with the analysis of the "real" mock catalogues presented below. If we perform the analysis using a larger cube[1] we find the error slightly reduced, to 15%. The reduction is minimal, as the window function for one angular division of the survey has a width comparable to the spacing of the modes on the fundamental grid. There is thus little to be gained in increasing the resolution.

This is for the survey split up as described above. Assuming the spherical harmonic method preserves all information, we can simulate this by running the model without splitting into angular bins. The resultant error on β will be lower because we can use more pairs at wide angular separation to probe the long-wavelength modes. We find an expected error of 11% for the case where we combine a larger box-size with use of the whole survey.

8.4.4 The measured PS

In figure 8.7 we plot the monopole power spectra and quadrupole-to-monopole ratios measured from the ten independent *N*-body mock catalogues. It can be seen that the mocks are generally in good agreement with each other, but that there is a considerable degree of scatter between the realizations, especially on large scales. As we predicted in section 7.5, $Q(k)$ is substantially less well-determined than the monopole power.

We use a two-parameter least squares fit to obtain values of β and $\mathbf{k}_{\rm nl}$ from each of the ten mock catalogues. This fit employs the covariance matrix found using the random realization method of Chapter 7. The model used in the fit is that described in section 8.3.3, which was found to be an unbiased estimator of β for the full simulation cubes from which the catalogues have been drawn. In the full simulation cubes, we used the method of multiple Zel'dovich runs to measure the expected error on $Q(k)$ as a function of scale. Effectively, then, we had a covariance matrix that had all off-diagonal elements set to zero. Here, we need to deal with correlations between modes due to the

[1] We use a $3\times$ fundamental cube, ie. $L_{\rm BOX} = 1036.8h^{-1}\,{\rm Mpc}$, larger than the limiting radial distance of the volume limited sample considered.

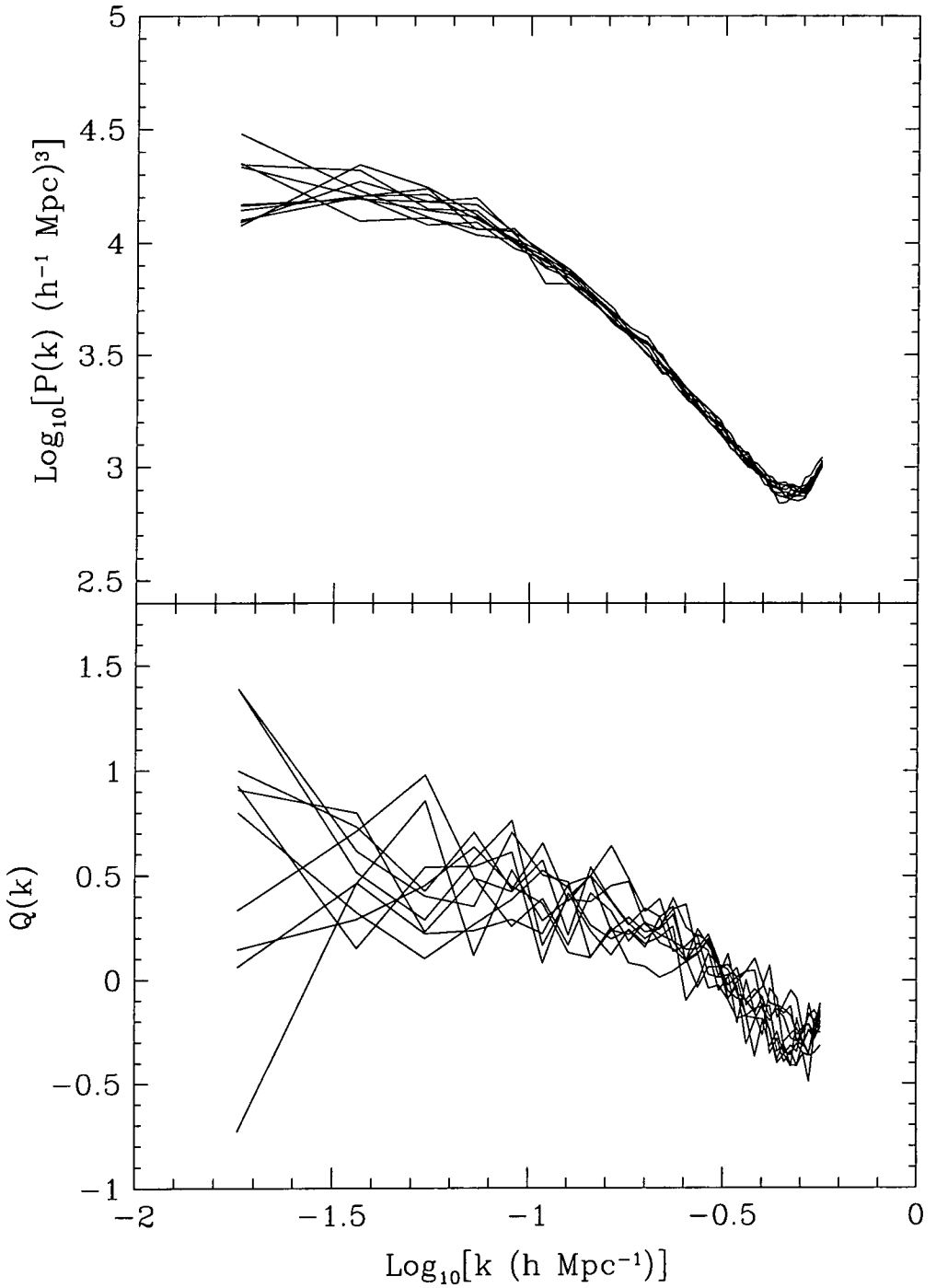

Figure 8.7: Power spectra, $P(k)$, and quadrupole-to-monopole ratios, $Q(k)$, for the ten independent mock 2dF catalogues, each constructed from simulations with the same cosmology and bias prescription.

survey window function, and to model this we use the non-diagonal covariance matrix obtained in the previous section with the method of multiple random realizations.

We measure the average value of β over the ten simulations, and the standard deviation between the estimates. We find $\beta_{\rm av} = 0.493 \pm 0.173$. Note that the standard error on the mean, since we have ten realizations, is $0.173/\sqrt{10} = 0.055$. The measured mean is approximately 1-σ discrepant from the true value ($\beta \approx 0.55$, from figure 8.6), and so our model is not significantly biased. The scatter on β, however, is around 35% of the mean; this is far in excess of the 18% error we expect from the previous section. We now address the question of the discrepancy between the two estimates.

Figure 8.8 shows the fractional error on $P(k)$ the absolute error on $Q(k)$ as a function of scale. We compare the variance we get from the ten independent realizations with the "expected" relationship from applying the random phase method to the same survey geometry. The correspondence between the two methods is clear; the random phase method has not under-predicted the degree of uncertainty on the distortion of each individual mode.

We conclude that the reason for underestimating the error must be that there exist serious correlations between the data points in addition to those due to the shape of the survey window function, which we have taken into account. If the correlations do not come from the convolution with the window function, and they are not modelled by the linear treatment of the random phase method, they must be caused by non-linear effects that invalidate our use of a Gaussian density field. It was pointed out in section 8.4.1 that non-linear evolution of the small-scale density modes introduces coupling between them, which we fail to take into account in using the random phase method, but which is implicit in the *N*-body method which has followed the evolution of these modes accurately. It will be seen from figure 3.2 that the dimensionless power spectrum from the $\Omega_0 = 1.0$, structure normalized simulation has an amplitude of around $10^{0.5}$ at the zero-crossing of the quadrupole, which occurs at around $k = 0.3$. Given that the bias factor on these scales is $b \approx 1.8$, the value of the mass power spectrum amplitude at the zero-crossing is $10^{0.5}/b^2$, approximately unity. Thus, the approximation that the modes are uncorrelated which, as shown in Appendix A, is true only when the amplitudes are much smaller than unity, is broken, and we should not be surprised that some mode-coupling has occurred.

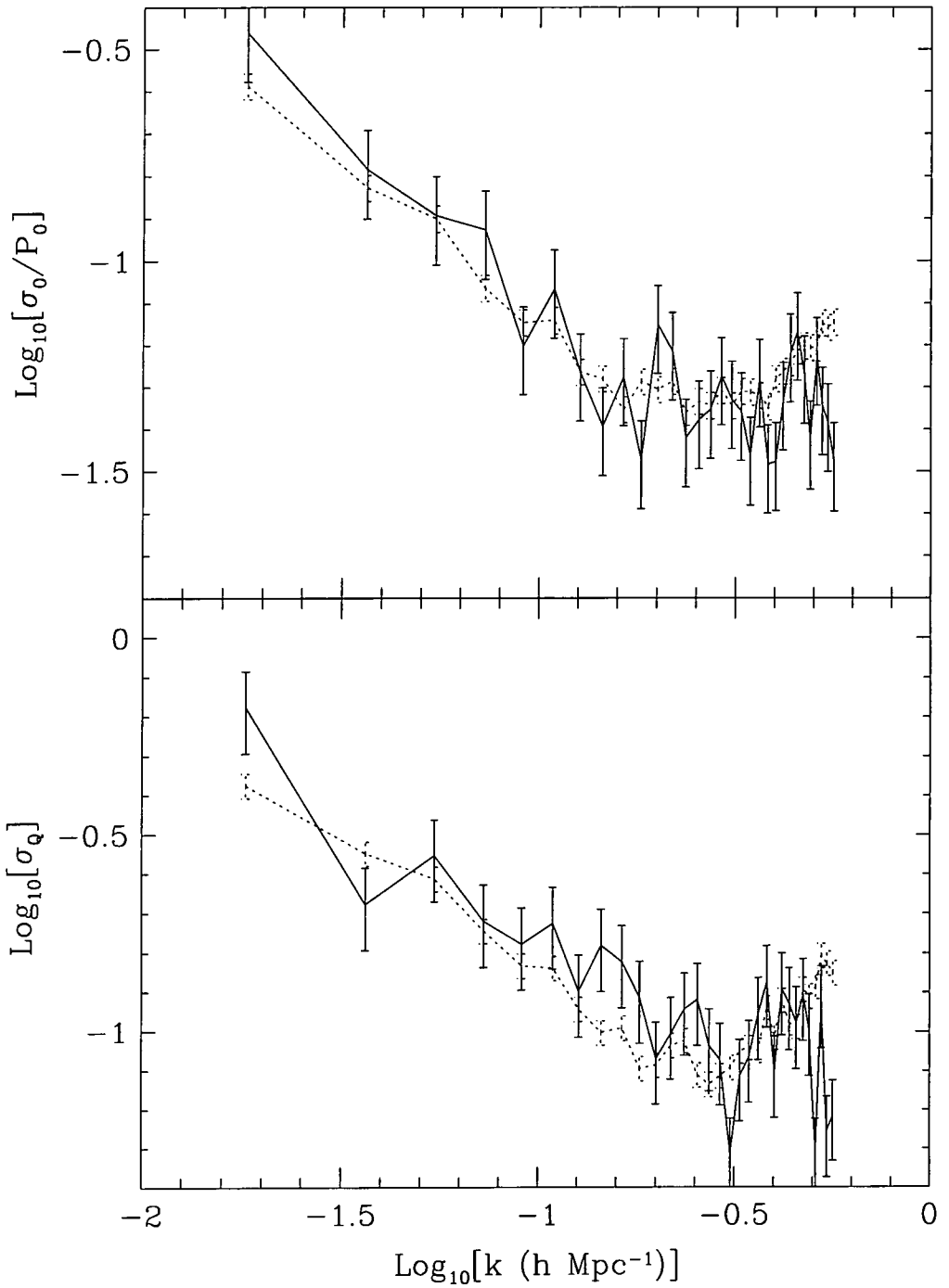

Figure 8.8: Fractional error on the power spectrum (upper panel) and absolute error on the quadrupole-to-monopole ratio (lower panel). The solid line is from the variance between then ten independent mock catalogue realizations of the survey, the dotted line is from applying the random phase technique of Chapter 7. To both curves we have Poisson errorbars to the points using the relation that the standard deviation of the scatter is given by $\sigma_{ss} = \sigma_s/\sqrt{2(N-1)}$, where σ_s is the measured scatter from N realizations (Barlow 1989).

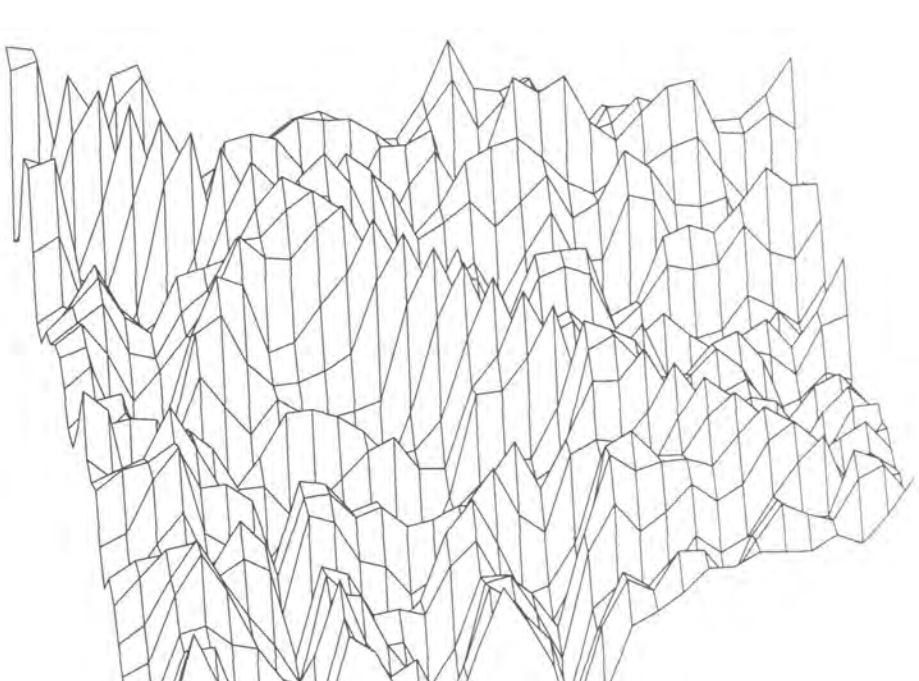

Figure 8.9: Covariance matrix from then ten indpendent mock catalogues. We have smoothed with a boxcar smoothing of width three cells. We have also normalized, as in figure 7.6, such that the $|k - k'| = 0$ modes have unit variance.

In figure 8.9 we show a similar covariance matrix to that in figure 7.6, only this one has been calculated from the ten independent mock catalogues. The use of only ten realizations, as opposed to the one hundred used in the random realization method, introduces noise in estimates of the covariance; we have removed some of this noise by smoothing the matrix in two dimensions, simply to make the effect of non-linearities more visually obvious. The decrease of the signal over the noise is quite clear as we progress to smaller scales (towards the bottom right-hand corner of the figure).

Quantifying the extent of this effect is a far harder task than showing it is significant. Just as we use one hundred random realizations to obtain the covariance matrix introduced by the survey window function, Meiksin & White (1999) use one hundred *N*-body simulations to examine the extent of correlations between the modes. This is an extremely time consuming job, and it is difficult to see how this could ever be practically used in

an iterative way to estimate the strength of the coupling. The amplitude of the power spectrum, which has generally been irrelevant to us since it drops out of the quadrupole-to-monopole ratio, is now an important additional factor in determining the strength of the effect. Meiksin & White also introduce a faster procedure of using repeated Zel'dovich approximation runs to achieve the same goal, but they find that this method underestimates the correlations since shell-crossing occurs, and key sources of non-linearity, ie. galaxy clusters, cannot be modelled accurately.

8.5 Conclusions

Are we left to conclude, then, that the 2dF survey will not be able to measure β much more accurately than 35%? If the coupling between modes is significant, developing a model that can follow the quadrupole-to-monopole ratio out to higher wavenumber is of little use. There are diminishing returns, since the modes are more and more correlated as we progress to smaller scales.

We have already seen that the width of the 2dF window function is such that using a longer box length is broadly irrelevant. We do, however, note that, if there is less to be gained in pushing to smaller scales, the shot-noise on these scales is less relevant. We could then choose to select a deeper volume limited sample that will determine longer wavelength modes rather better, with a narrower window function, at the expense of more noise on small scales. Alternatively, we could use the whole magnitude limited sample with an FKP minimum variance weighting scheme to optimize measurements of the power spectrum at extremely large scales.

8.5.1 Reducing non-linearities

In the random realizations method, we have assumed a convenient form for the net effect of non-linear velocity dispersion on the power spectrum. Whilst this is, on aggregate, a valid approach, in a real survey or an *N*-body simulation this is not how non-linearity comes about; the coupling between k-modes is a local effect in r-space, it takes place inside particular non-linear structures, ie. rich clusters. In these volumes, mode coupling is extremely strong. As pointed out in Chapter 6, if we can somehow excise these regions from our treatment, we could not only create a better behaved, more linear quadrupole-

to-monopole ratio, but have an even more dramatic effect in lessening the correlations between modes on these scales. This could be achieved by the identifying and removing the signal from clusters, as described in Chapter 6, or perhaps by performing the distortion analysis in r-space, by looking at the correlation function $\xi(\sigma, \pi)$. The spatially localized effect can be removed as it involves close transverse pairs.

8.5.2 Future surveys

It may prove difficult to deal with clusters accurately, since identifying them robustly in redshift space with a selection function is a complex issue (Moore, Frenk, & White 1993). If these difficulties cannot be overcome, then we may have to turn to larger surveys to accurately measure β. Large-scale modes are at a premium, because:

- The window function convolution is less significant if the volume is large.
- The redshift-space distortions are more close to their linear theory values.
- Non-linear mode-coupling will not be significant.

The finding of Heavens & Taylor (1997) that "width is better than depth" implies that a wider angle survey like the SDSS may be more efficient, even for a subsample that contained the same volume as 2dF. This strategy also lessens the potential contamination from evolutionary effects and cosmological redshift-space distortions (Ballinger, Peacock, & Heavens 1996; Matsubara & Suto 1996).

Finally, given the diminished relevance of the shot-noise if substantial correlations exist on small scales, a high number density of galaxies is not relevant. There is little to be lost, then, in a sparse sampling strategy. Heavens & Taylor (1997) find that the optimum sampling fraction, f, is given by $fP = 500h^{-3}\,\mathrm{Mpc}^3$, where P is the power at the wavelengths of greatest interest. In the standard model, outlined in Chapter 2, we expect to see the power spectrum turn over to the Harrison-Zel'dovich regime. Thus the power will decrease at the largest scales. To measure the very longest modes, sparse sampling is therefore not useful, but, referring to figure 2.5, it can be sen that the galaxy power spectrum is a long way from zero at the longest scales probed by the APM survey. To really constrain the power spectrum in three dimensions at the scale probed by *COBE*,

we should optimize our estimation for $P \approx 2000h^{-3}\,\mathrm{Mpc}^3$ The desirable characteristics of a survey specifically designed to measure β and *nothing else* might be:

- Large volume, to minimize convolution effects and non-linearity.
- Wide angular coverage, like PSCz, or 6dF, to measure large-scale power accurately and avoid contamination by evolutionary effects.
- Sparse sampling at a rate of roughly one-in-four, to measure long wavelength modes with maximum efficiency.
- Sharply peaked selection function, such that it is efficient for constructing a volume-limited sample.

References

Ballinger W. E., Peacock J. A., Heavens A. F., 1996, MNRAS, 282, 877

Barlow R. J., 1989, Statistics: a guide to the use of statistical methods in the physical sciences, Manchester physics series. Wiley

Cole S., Fisher K. B., Weinberg D. H., 1995, MNRAS, 275, 515

Fisher K. B., Nusser A., 1996, MNRAS, 279, L1

Heavens A. F., Taylor A. N., 1995, MNRAS, 275, 483

Heavens A. F., Taylor A. N., 1997, MNRAS, 290, 456

Kaiser N., 1987, MNRAS, 227, 1

Mann R. G., Peacock J. A., Heavens A. F., 1998, MNRAS, 293, 209

Matsubara T., Suto Y., 1996, ApJ, 470, 1

Meiksin A., White M., 1999, MNRAS, submitted, astro-ph/9812129

Moore B., Frenk C. S., White S. D. M., 1993, MNRAS, 261, 827

Nakamura T. T., Matsubara T., Suto Y., 1998, ApJ, 494, 13

Peacock J. A., Dodds S. J., 1994, MNRAS, 267, 1020

Chapter 9

Conclusions and further work

THE ARGUMENT We summarize the conclusions of the preceding chapter, and outline some directions for future work to take.

The focus of this thesis has been to develop techniques to estimate fundamental cosmological quantities from redshift surveys, especially from the ongoing Anglo-Australian 2dF, and the US Sloan Digital Sky Survey projects. These two surveys, the most ambitious ever in the area of large-scale structure, will open up a new era of high precision measurements in cosmology. In particular, the large volumes they probe will enable us, for the first time, to directly compare the clustering of *galaxies* with the amplitude of the *mass* fluctuations on the scales measured by *COBE*. The relationship between these two is fundamental to our understanding of galaxy formation.

In order to fully anticipate the arrival of such high quality data as the new surveys will provide, the use of mock catalogues that roughly mimic the selection functions and likely clustering of the real data is crucial. The suite of mocks we present in Chapter 4 is enormously useful for this, but is still restricted in many ways. A key future goal is to incorporate semi-analytic models (SAMs) for galaxy formation. SAMs are a powerful method for producing "realistic" galaxies with types, magnitudes, colours etc., without recourse to ultra-high resolution *N*-body simulation. They thus enable us to create big simulations that sample large-scale modes of the power spectrum, contain fair samples of clusters, and simultaneously contain a physically motivated bias between the galaxy and mass fluctuations. Ideally, we would like to increase the volumes beyond even those used in our catalogues, avoiding potential problems that arise due to periodicity and lack of k-space resolution that we discuss in Chapter 8. As discussed in Chapter 4, using large simulations like the Hubble volume as the source for our mocks allows us to incorporate

the effects of evolution very simply, since the simulation is output along the observer's light cone. This will be especially useful for modelling the deep surveys such as VIRMOS and DEEP, discussed in Chapter 1, that will be sensitive evolutionary probes.

The incorporation of non-cosmological effects in our catalogues has been illustrated in Chapter 5 where we examine the effect of Galactic dust on the clustering signal in the SDSS. It will be of great interest to extend this treatment to the APM catalogue, and hence the 2dF, and retrospectively the Stromlo-APM to see if this was at all biased.

Other planned or current uses for the mock catalogues include:

- Looking at cosmetic problems in the real catalogues, eg. errors due to the finite spacing of fibres.
- Studying the cosmological redshift-space distortions that arise when the wrong cosmology is used to convert the catalogue from redshift- to real-space.
- Calculating at what level the new catalogues will be able to discriminate against a fractal distribution of clustering, ie. large-scale departures from homogeneity.

One of the chief statistics we have employed has been the quadrupole-to-monopole ratio of the redshift-space power spectrum. This quantity is especially useful because, in the regimes considered, it is not directly sensitive to the amplitude or shape of the power spectrum. We have demonstrated in Chapter 6, by comparison with *N*-body results, that existing models for the redshift-space distortions, especially as measured via the quadrupole estimator, are inaccurate and can lead to substantial bias if applied to a large dataset. The exponential and Gaussian models for non-linear velocity dispersion do not generally replicate the shape of the curve on large scales, and the Zel'dovich approximation breaks down if there is a high velocity dispersion or a significant bias. In Chapter 8 we have extended this treatment to a much larger sample of different cosmologies and shown that, of the simple analytic forms for the correction to the power spectrum, the one that matches most closely is that of a pairwise exponential. We find from our simulations that this still provides a biased estimate of the β-parameter, and introduce our own, purely empirical relationship for the non-linear correction as a function of scale, which is shown to be unbiased, ie. the systematic differences are less than the intrinsic scatter.

The importance of accurate error estimation cannot be over-stressed. Scientific results are meaningless without it, since comparisons cannot be made between different

datasets without a reliable estimate of the relative accuracy of each. Our technique, of using repeated realizations of Gaussian random fields for the density, is outlined in Chapter 7. The comparison with our mock catalogues in Chapter 8 serves to confirm the validity of this treatment, demonstrating that it provides an accurate assessment of the error on derived parameters due to the finite volume contained within a given survey geometry. We consider that this technique will be a useful tool in optimizing the design of future galaxy redshift surveys.

On the whole, the immediate results of applying this treatment to the new generation of surveys are encouraging; but it transpires that a simple application to the data will not be able to constrain the power spectrum, especially on large scales, as accurately as we would wish, and errors on the key parameter β are significantly larger than anticipated. However, in Chapter 6 we applied one method in particular to our *N*-body simulations that was effective at removing much of the non-linear signal from the quadrupole estimator. This is the method of cluster collapse, which prevents these highly non-linear structures from contributing to the power spectrum and hence washing out the linear signal. We have high hopes for this method, but it remains to make a detailed study of its application to real surveys conducted in redshift-space. The ability to define cluster membership here is complicated by the smearing caused by the radial velocities within the clusters, and by errors in the selection function which is estimated from the dataset itself. Developing optimal methods for choosing the parameters of an anisotropic friends-of-friends search, and assessing the biases that may result from it, is another potential application of our mock catalogues.

A further possible refinement is to include non-linear effects in the covariance matrix used in fitting a model to the data. This introduces a further degree of complexity as these effects are sensitive to the amplitude of the underlying mass power spectrum, and currently they can only be measured by repeated *N*-body simulation. It is not unlikely, however, that further study will produce a simple empirical model for the degree of correlation between two modes as a function of scale and $\sigma_8^{\rm mass}$. This would be very easy to include in our treatment, by convolving the covariance matrix we obtain from the survey geometry effect with that which arises from non-linear coupling.

The final conclusion then is that, to really constrain cosmological parameters, we must probe long wavelengths accurately, or refine techniques for removing small-scale non-

linearities from the data. These methods must be further developed and tested before being applied to data from the new generation of redshift surveys currently in progress.

Appendix A

Linear theory

THE ARGUMENT We present the derivation of the linear theory for the growth of density perturbations which is the keystone of much of the work in this thesis.

A.1 Introduction

Throughout this work, we have used the power spectrum of density fluctuations as an important probe of the cosmological parameters. In this appendix we briefly outline the steps in deriving the linear growth of fluctuations with time.

A.2 Three equations

The whole of linear theory is based on three simple equations that are familiar from all branches of physics:

- First, the continuity equation, which simply states that the rate of change of density in a box is proportional to the rate of flow of matter out of it, in the absence of sources or sinks,

$$\frac{\partial \rho}{\partial t} + \nabla.(\rho \mathbf{v}) = 0 \tag{A.1}$$

- Next, the Euler equation relates the rate of change of momentum in a fluid to the potential gradient,

$$\frac{\partial \mathbf{v}}{\partial t} + (\mathbf{v}.\nabla)\mathbf{v} = -\nabla\phi \tag{A.2}$$

- Lastly, Poisson's equation relates the second derivative of the gravitational potential to the underlying density,

$$\nabla^2\phi = 4\pi G\rho \tag{A.3}$$

A.3 Comoving co-ordinates

We define a physical co-ordinate, $\mathbf{r}$, such that $\mathbf{r} = a(t)\mathbf{x}$, where $\mathbf{x}$ is the co-moving co-ordinate. The physical velocity, $\mathbf{v}$, is thus $\mathbf{v} = \dot{\mathbf{r}} = \dot{a}\mathbf{x} + a\dot{\mathbf{x}}$. This represents the Hubble expansion velocity with peculiar velocity superimposed. The co-moving peculiar velocity is $\mathbf{u} = \dot{\mathbf{x}}$. We begin this derivation by transforming the three equations above into co-moving co-ordinates. As $\mathbf{r} \to \mathbf{x}$,

$$\nabla_r = \frac{\nabla_x}{a(t)} \tag{A.4}$$

The chain rule for partial differentials states:

$$\left.\frac{\partial}{\partial t}\right|_r = \left.\frac{\partial}{\partial t}\right|_x + \left.\frac{\partial x}{\partial t}\right|_r \left.\frac{\partial}{\partial x}\right|_t \tag{A.5}$$

Now, from our definition of $\mathbf{x}$,

$$\left.\frac{\partial \mathbf{x}}{\partial t}\right|_r = -\mathbf{r}\frac{\dot{a}}{a^2} = -\mathbf{x}\frac{\dot{a}}{a}, \tag{A.6}$$

so

$$\left.\frac{\partial}{\partial t}\right|_r = \left.\frac{\partial}{\partial t}\right|_x - \frac{\dot{a}}{a}\mathbf{x}\nabla \tag{A.7}$$

We will also employ the vector calculus identity:

$$\nabla.(\phi\mathbf{v}) = \phi\nabla.\mathbf{v} + \mathbf{v}.\nabla\phi. \tag{A.8}$$

We define density fluctuations by

$$\rho(\mathbf{x},t) = \frac{\rho_0}{a^3}[1 + \delta(\mathbf{x},t)]. \tag{A.9}$$

These relations (equations A.4, A.7, A.8) are all we need to transform the continuity equation (A.1) into comoving co-ordinates:

$$\frac{\partial\delta}{\partial t} + \nabla.\mathbf{u} + \nabla.(\delta\mathbf{u}) = 0. \tag{A.10}$$

Similarly, for Euler's equation (A.2),

$$\frac{\partial \mathbf{u}}{\partial t} + 2\frac{\dot{a}}{a}\mathbf{u} + \mathbf{u}(\nabla.\mathbf{u}) = -\frac{\nabla\phi}{a^2} - \frac{\ddot{a}\mathbf{x}}{a}. \tag{A.11}$$

Under a Friedmann-Robertson-Walker metric with no cosmological constant, conservation of energy implies $\ddot{a} = -GM/a^2$. Using the Poisson equation, we can write

$$\nabla.\frac{\ddot{a}\mathbf{x}}{a} = 3\frac{\ddot{a}}{a} = 4\pi G\bar{\rho} = -\frac{\nabla^2\bar{\phi}}{a^2}. \tag{A.12}$$

Here we have rewritten the potential as the sum of an averaged and a perturbed component, $\phi = \bar{\phi} + \hat{\phi}$. Integrating both sides of the previous equation, we obtain

$$\frac{\ddot{a}\mathbf{x}}{a} = -\frac{\nabla\bar{\phi}}{a^2}. \tag{A.13}$$

Substituting this value into equation A.11 yields

$$\frac{\partial \mathbf{u}}{\partial t} + 2\frac{\dot{a}}{a}\mathbf{u} + \mathbf{u}(\nabla.\mathbf{u}) = -\frac{\nabla\hat{\phi}}{a^2}. \tag{A.14}$$

For the Poisson equation (A.3), we obtain

$$\frac{\nabla^2\hat{\phi}}{a^2} = 4\pi G\bar{\rho}\delta. \tag{A.15}$$

A.4 Fourier space

In order to deal with the evolution of individual Fourier modes of the overdensity field, we Fourier transform the three real space equations (A.10, A.14, A.15) into k-space. Any field, θ, in real space can be written in terms of its Fourier components,

$$\theta(\mathbf{x}) = \sum_{\mathbf{k}} \theta_{\mathbf{k}} \exp(-i\mathbf{k}.\mathbf{x}) \tag{A.16}$$

We use this relation to expand the cross-terms in equations A.10 and A.14,

$$\begin{aligned}
\nabla.(\mathbf{u}\delta) &= \nabla.\left(\sum_{\mathbf{k}_1}\delta_{\mathbf{k}_1}\exp(-i\mathbf{k}_1.\mathbf{x})\sum_{\mathbf{k}_2}\mathbf{u}_{\mathbf{k}_2}\exp(-i\mathbf{k}_2.\mathbf{x})\right) \\
&= \sum_{\mathbf{k}_1}\sum_{\mathbf{k}_2} -i(\mathbf{k}_1+\mathbf{k}_2)\delta_{\mathbf{k}_1}\mathbf{u}_{\mathbf{k}_2}\exp(-i(\mathbf{k}_1+\mathbf{k}_2).\mathbf{x}) \\
&= \sum_{\mathbf{k}}\sum_{\mathbf{k}'} -i\mathbf{k}\delta_{\mathbf{k}'}\mathbf{u}_{\mathbf{k}-\mathbf{k}'}\exp(-i\mathbf{k}.\mathbf{x})
\end{aligned} \tag{A.17}$$

Similarly,

$$\begin{aligned}\mathbf{u}(\nabla.\mathbf{u}) &= \sum_{\mathbf{k}_1} \mathbf{u}_{\mathbf{k}_1} \exp(-i\mathbf{k}_1.\mathbf{x}) \sum_{\mathbf{k}_2} i\mathbf{k}_2.\mathbf{u}_{\mathbf{k}_2} \exp(-i\mathbf{k}_2.\mathbf{x}) \\ &= \sum_{\mathbf{k}_1} \sum_{\mathbf{k}_2} i\mathbf{k}_2.\mathbf{u}_{\mathbf{k}_2} \mathbf{u}_{\mathbf{k}_1} \exp(-i(\mathbf{k}_1+\mathbf{k}_2).\mathbf{x}) \\ &= \sum_{\mathbf{k}} \sum_{\mathbf{k}'} i\mathbf{u}_{\mathbf{k}-\mathbf{k}'}.(\mathbf{k}-\mathbf{k}')\mathbf{u}_{\mathbf{k}'} \exp(-i\mathbf{k}.\mathbf{x}). \end{aligned} \tag{A.18}$$

If we Fourier transform equations A.10, A.14, and A.15, and substitute these results, we obtain:

- from the continuity equation

$$\frac{\partial \delta_k}{\partial t} - i\mathbf{k}.\mathbf{u}_k - \sum_{k'} i\delta_{k'}\mathbf{k}.\mathbf{u}_{k-k'} = 0, \tag{A.19}$$

- from the Euler equation

$$\frac{\partial \mathbf{u}_k}{\partial t} + 2\frac{\dot{a}}{a}\mathbf{u}_k - \sum_{k'} i\mathbf{u}_{k'}.(\mathbf{k}-\mathbf{k}')\mathbf{u}_{k-k'} = \frac{i\mathbf{k}\hat{\phi}_k}{a^2}, \tag{A.20}$$

- and from the Poisson equation,

$$\frac{\hat{\phi}_k}{a^2} = -4\pi G\bar{\rho}\frac{\delta_k}{k^2}. \tag{A.21}$$

These formulae are the Fourier-space analogues of the three equations we started with. If we restrict ourselves to the linear regime where the fields have values much less than unity, we can discard the summation terms in the above equations since they contain products of two fields. Since the cross-terms have been thrown out, we have effectively removed the coupling between modes with different wavenumber, and the modes will evolve independently of each other.

A.5 Solutions

Keeping just the linear theory terms, we differentiate equation A.19 with respect to time to get

$$\ddot{\delta}_k - i\mathbf{k}.\dot{\mathbf{u}}_k = 0. \tag{A.22}$$

Now, combining the other two equations, A.20 and A.21, to eliminate $\hat{\phi}$,

$$\dot{\mathbf{u}}_k + 2\left(\frac{\dot{a}}{a}\right)\mathbf{u}_k = -4\pi i G\rho\frac{\delta_k}{k} = -3i\left(\frac{\ddot{a}}{a}\right)\frac{\delta_k}{k} \tag{A.23}$$

Multiply this equation by $-i\mathbf{k}$,

$$-i\mathbf{k}.\dot{\mathbf{u}}_k = 2i\left(\frac{\dot{a}}{a}\right)\mathbf{k}.\mathbf{u}_k - 3\left(\frac{\ddot{a}}{a}\right)\delta_k. \tag{A.24}$$

Substitute this result into equation A.22

$$\ddot{\delta}_k + 2i\left(\frac{\dot{a}}{a}\right)\mathbf{k}.\mathbf{u}_k - 3\left(\frac{\ddot{a}}{a}\right)\delta_k = 0. \tag{A.25}$$

Finally, from equation A.19, substitute $i\mathbf{k}.\mathbf{u}_k = \dot{\delta}_k$

$$\ddot{\delta}_k + 2\left(\frac{\dot{a}}{a}\right)\dot{\delta}_k - 3\left(\frac{\ddot{a}}{a}\right)\delta_k = 0. \tag{A.26}$$

This is the general second-order differential equation for the linear evolution of the over-density field, δ_k.

In the special case of an Einstein-de Sitter Universe, $a \propto t^{2/3}$, so

$$\frac{\dot{a}}{a} = \frac{2}{3}t^{-1} \quad \text{and} \quad \frac{\ddot{a}}{a} = -\frac{2}{9}t^{-2} \tag{A.27}$$

Looking for power-law solutions, $\delta \propto t^n$, we obtain

$$\delta_k = A_k t^{2/3} + B_k t^{-1}. \tag{A.28}$$

It can thus be seen that perturbations in the density field are superpositions of growing and decaying states.

A.6 The peculiar velocity field

For the general case where the growing mode of the density field dominates, $\delta_k = A_k D(t)$, we use the continuity equation (A.19) to first order,

$$i\mathbf{k}.\mathbf{u}_k = \frac{\partial \delta_k}{\partial t} = \delta_k \frac{\dot{D}}{D} = \delta_k H f, \tag{A.29}$$

where we define $f = \dot{D}/DH$. Dividing by $i\mathbf{k}$ gives:

$$\mathbf{u}_k = -\frac{i\mathbf{k}}{k^2}\delta_k H f. \tag{A.30}$$

Taking the inverse Fourier transform of this result gives us a relation between the peculiar velocity of a particle and its initial position, $\mathbf{q}$:

$$\mathbf{u}(\mathbf{q}) = -Hf\frac{1}{(2\pi)^3}\sum_k \frac{i\mathbf{k}}{k^2}\delta_k \exp(-i\mathbf{k}.\mathbf{q}) \tag{A.31}$$

This equation can then be integrated to calculate the displacement of particles from their initial positions.

$$\begin{aligned} \mathrm{d}(\mathbf{q},t) &= \int_0^t \mathbf{u}(\mathbf{q})dt \\ &= \frac{D(t)}{(2\pi)^3}\sum_k \frac{i\mathbf{k}}{k^2}A_k \exp(-i\mathbf{k}.\mathbf{q}). \end{aligned} \tag{A.32}$$

These final two equations describe the Zel'dovich approximation used in our simulations to give particles initial displacements and velocities from a set of Fourier amplitudes A_k.

A.7 Redshift-space distortions

Under linear theory it is possible to derive a simple equation for the effect of the peculiar velocity field on the observed clustering as measured by the power spectrum in redshift-space (Kaiser 1987; Cole, Fisher, & Weinberg 1994).

$$\rho^s(\mathbf{s}) = \rho^r(\mathbf{r})\left[1+\frac{U(\mathbf{r})-U(\mathbf{0})}{Hr}\right]^{-2}\left[1+\frac{dU(\mathbf{r})}{Hdr}\right]^{-1} \tag{A.33}$$

The first factor comes from the effect of the peculiar velocity on the cross-sectional area of the volume in question, the second from the expansion or compression in the radial direction. Making the assumption of a distant observer sets the first term to unity, and in the limit that $|dU/dr| \ll H$, the radial term is well approximated by a first-order expansion, and

$$\rho^s(\mathbf{s}) = \rho^r(\mathbf{r})\left(1-\frac{1}{H}\frac{dU}{dr}\right). \tag{A.34}$$

now, $\rho/\bar{\rho} \equiv (1+\delta)$, so

$$1+\delta^s(\mathbf{s}) = [1+\delta^r(\mathbf{r})]\left(1-\frac{1}{H}\frac{dU}{dr}\right) \tag{A.35}$$

Making the further assumption that $|\delta^r| \ll 1$, this leads to

$$\delta^s(\mathbf{s}) = \delta^r(\mathbf{r}) - \frac{1}{H}\frac{dU}{dr}. \tag{A.36}$$

Now, the peculiar velocity field is given by equation A.31 above. This holds when A_k is a perturbation in the mass density field. For a perturbation in the galaxy density field, under the assumption of linear bias ($\delta^{\rm gal} = b\delta^{\rm mass}$), $f(\Omega_0)$ is replaced by $\beta = f(\Omega_0)/b$. The radial component of the velocity field is:

$$U(\mathbf{r}) = \mathbf{u}(\mathbf{r}).\hat{\mathbf{r}} = -H\beta\frac{1}{(2\pi)^3}\sum_k \frac{i\mu}{k}\delta_k \exp(-i\mathbf{k}.\mathbf{r}), \tag{A.37}$$

where μ is the angle between the wave-vector and the line of sight. Thus

$$\begin{aligned}\frac{dU}{dr} &= -H\beta\frac{1}{(2\pi)^3}\sum_k \mu^2\delta_k \exp(-i\mathbf{k}.\mathbf{r}) \\ &= -H\beta\mu^2\delta^r. \end{aligned} \tag{A.38}$$

Inserting this result into equation A.36 leads to

$$\delta^s(\mathbf{s}) = \delta^r(\mathbf{r})(1+\beta\mu^2) \tag{A.39}$$

This is the linear theory result for the effect of redshift-space distortions used extensively in this thesis.

References

Cole S., Fisher K. B., Weinberg D. H., 1994, MNRAS, 267, 785

Kaiser N., 1987, MNRAS, 227, 1

Appendix B

Analytic Zel'dovich approximation

THE ARGUMENT. We present the analytic derivation for the redshift-space distortion to the power spectrum under the assumption of the Zel'dovich approximation for particle displacements. We show that a first-order expansion of the resulting expression produces the linear theory formula. We also give some insight into numerical methods for computing the full integral.

B.1 Introduction

The Zel'dovich approximation has been used to calculate quasi-linear redshift-space distortions by (Fisher & Nusser 1996; Taylor & Hamilton 1996). Fisher & Nusser present the initial steps in such a calculation. Here we present the full calculation up to the point where numerical methods must be used. We also confirm that the linear theory expression for the distortion can be obtained by making a first order expansion of the ZA equation.

B.2 The calculation

The transformation between real-space coordinates ($\mathbf{x}$) and redshift-space coordinates ($\mathbf{s}$) is described by the mapping

$$\mathbf{s} = \mathbf{x} + (\mathbf{v}.\mathbf{l})\mathbf{l}, \tag{B.1}$$

where $\mathbf{v}$ is the particle velocity and $\mathbf{l}$ the line of sight vector. The Zel'dovich approximation maps particles at initial positions $\mathbf{q}$ to new positions $\mathbf{x}$ such that $\mathbf{x} = \mathbf{q}+\mathbf{t}$, where $\mathbf{t} = f^{-1}\mathbf{v}$. So, we can combine the two mappings with

$$\mathbf{s} = \mathbf{q} + \mathbf{t} + f(\mathbf{t}.\mathbf{l})\mathbf{l} = \mathbf{q} + \mathcal{M}\mathbf{t}. \tag{B.2}$$

The original density field is assumed to be uniform, $\rho(\mathbf{q}) = \bar{\rho}_0$, so density fluctuations come about purely from this mapping. Thus,

$$\delta^s = \int d^3\mathbf{q}\delta_D[\mathbf{s} - (\mathbf{q} + \mathcal{M}\mathbf{t})] - 1, \tag{B.3}$$

where δ_D is the Dirac delta function. Fourier transforming equation B.3 leads to

$$\begin{aligned}
\delta^s_{\mathbf{k}} &= \int d^3\mathbf{s}\delta^s(\mathbf{s})\exp(i\mathbf{k}.\mathbf{s}) \\
&= \left(\int d^3\mathbf{s}\exp(i\mathbf{k}.\mathbf{s})\int d^3\mathbf{q}\delta_D[\mathbf{s} - (\mathbf{q} + \mathcal{M}\mathbf{t})]\right) - \int d^3\mathbf{s}\exp(i\mathbf{k}.\mathbf{s}) \\
&= \int d^3\mathbf{q}\exp[i\mathbf{k}.(\mathbf{q} + \mathcal{M}\mathbf{t})] - \int d^3\mathbf{q}\exp(i\mathbf{k}.\mathbf{q}) \\
&= \int d^3\mathbf{q}\exp(i\mathbf{k}.\mathbf{q})[\exp(i\mathbf{k}.\mathcal{M}\mathbf{t}) - 1].
\end{aligned} \tag{B.4}$$

For $k \neq 0$ we can ignore the the -1, so from now on we only consider non-zero k.

The expectation value of the product of the amplitudes of two Fourier modes is given by:

$$\langle\delta_{\mathbf{k}}\delta^*_{\mathbf{k}'}\rangle = \int d^3\mathbf{q}d^3\mathbf{q}'\exp[i(\mathbf{k}.\mathbf{q} - \mathbf{k}'.\mathbf{q}')]\langle\exp[i(\mathbf{k}.\mathcal{M}\mathbf{t} - \mathbf{k}'.\mathcal{M}\mathbf{t}')]\rangle \tag{B.5}$$

we substitute for $\mathbf{q}'$ with $\mathbf{r} = \mathbf{q}' - \mathbf{q}$,

$$\begin{aligned}
\langle\delta_{\mathbf{k}}\delta^*_{\mathbf{k}'}\rangle &= \int d^3\mathbf{q}d^3\mathbf{r}\exp[i(\mathbf{k}.\mathbf{q} - \mathbf{k}'.\mathbf{q} - \mathbf{k}'.\mathbf{r})]\langle\exp[i(\mathbf{k}.\mathcal{M}\mathbf{t} - \mathbf{k}'.\mathcal{M}\mathbf{t}')]\rangle \\
&= \int d^3\mathbf{q}\exp[i(\mathbf{k} - \mathbf{k}').\mathbf{q}]\int d^3\mathbf{r}\exp(-i\mathbf{k}'.\mathbf{r})\langle\exp[i(\mathbf{k}.\mathcal{M}\mathbf{t} - \mathbf{k}'.\mathcal{M}\mathbf{t}')]\rangle \\
&= \delta_D(\mathbf{k} - \mathbf{k}')\int d^3\mathbf{r}\exp(-i\mathbf{k}'.\mathbf{r})\langle\exp[i(\mathbf{k}.\mathcal{M}\mathbf{t} - \mathbf{k}'.\mathcal{M}\mathbf{t}')]\rangle
\end{aligned} \tag{B.6}$$

The integration over $\mathbf{q}$ is possible only if the expectation value in the integrand is independent of $\mathbf{q}$. This result will be shown in equation B.15. Now, the power spectrum is defined by

$$\langle\delta_{\mathbf{k}}\delta^*_{\mathbf{k}'}\rangle = (2\pi)^3\delta_D(\mathbf{k} - \mathbf{k}')P^s(\mathbf{k}) \tag{B.7}$$

So

$$P^s(\mathbf{k}) = \int \langle \exp[i(\mathbf{k}.\mathcal{M}\mathbf{t} - \mathbf{k}.\mathcal{M}\mathbf{t}')] \rangle \exp(-i\mathbf{k}.\mathbf{r}) d^3\mathbf{r} \tag{B.8}$$

B.3 Evaluating the expectation value

Define a vector $\mathcal{T} = (t_1, t_2, t_3, t_1', t_2', t_3')$ or, in more compact notation, $(\mathbf{t}, \mathbf{t}')$. Then

$$\Pr(\mathcal{T}) = \exp\left(-\frac{\mathcal{T}\mathcal{G}^{-2}\mathcal{T}}{2}\right) \times \frac{1}{(2\pi)^3|\mathcal{G}|} \tag{B.9}$$

where $\mathcal{G}^2$ is a matrix describing the covariance of the components of the displacement vectors $\mathbf{t}$ and $\mathbf{t}'$, ie.

$$\mathcal{G}^2 = \begin{pmatrix} \langle t_1 t_1 \rangle & \langle t_1 t_2 \rangle & \dots & \langle t_1 t_1' \rangle & \dots & \langle t_1 t_3' \rangle \\ \langle t_2 t_1 \rangle & & & & & \vdots \\ \vdots & & & & & \vdots \\ \langle t_3' t_1 \rangle & \dots & \dots & \dots & \dots & \langle t_3' t_3' \rangle \end{pmatrix}$$

$$= \begin{pmatrix} \mathcal{C}_0 & \mathcal{C} \\ \mathcal{C} & \mathcal{C}_0 \end{pmatrix}, \quad \mathcal{C} = \begin{pmatrix} \langle t_1' t_1 \rangle & \langle t_1' t_2 \rangle & \langle t_1' t_3 \rangle \\ \langle t_2' t_1 \rangle & \langle t_2' t_2 \rangle & \langle t_2' t_3 \rangle \\ \langle t_3' t_1 \rangle & \langle t_3' t_2 \rangle & \langle t_3' t_3 \rangle \end{pmatrix}. \tag{B.10}$$

Now define another 6-vector, $\mathcal{K} = (\mathbf{k}\mathcal{M}, -\mathbf{k}'\mathcal{M})$, so that

$$\mathcal{K}.\mathcal{T} = \mathbf{k}.\mathcal{M}\mathbf{t} - \mathbf{k}'.\mathcal{M}\mathbf{t}'. \tag{B.11}$$

Then

$$\langle \exp(i\mathcal{K}.\mathcal{T}) \rangle = \int \Pr(\mathcal{T}) \exp(i\mathcal{K}.\mathcal{T}) d^6\mathcal{T} \tag{B.12}$$

For a multivariate Gaussian, we can find the expectation value by completing the square in the same way as in the one-dimensional case:

$$\begin{aligned} \langle \exp(i\mathcal{K}.\mathcal{T}) \rangle &= \int \exp\left[-\frac{1}{2}(\mathcal{T}\mathcal{G}^{-1} - i\mathcal{K}\mathcal{G})(\mathcal{G}^{-1}\mathcal{T} - i\mathcal{G}\mathcal{K})\right] \times \exp\left(-\frac{\mathcal{K}\mathcal{G}^2\mathcal{K}}{2}\right) d^6\mathcal{T} \\ &= \exp\left(-\frac{\mathcal{K}\mathcal{G}^2\mathcal{K}}{2}\right) \end{aligned} \tag{B.13}$$

Now,

$$\mathcal{K}\mathcal{G}^2\mathcal{K} = \begin{pmatrix} \mathbf{k}\mathcal{M} & -\mathbf{k}'\mathcal{M} \end{pmatrix} \times \begin{pmatrix} \mathcal{C}_0 & \mathcal{C} \\ \mathcal{C} & \mathcal{C}_0 \end{pmatrix} \times \begin{pmatrix} \mathcal{M}\mathbf{k} \\ -\mathcal{M}\mathbf{k}' \end{pmatrix}$$

$$= \begin{pmatrix} \mathbf{k}\mathcal{M} & -\mathbf{k}'\mathcal{M} \end{pmatrix} \times \begin{pmatrix} \mathcal{C}_0\mathcal{M}\mathbf{k} - \mathcal{C}\mathcal{M}\mathbf{k}' \\ \mathcal{C}\mathcal{M}\mathbf{k} - \mathcal{C}_0\mathcal{M}\mathbf{k}' \end{pmatrix}$$

$$= \mathbf{k}\mathcal{M}\mathcal{C}_0\mathcal{M}\mathbf{k} - \mathbf{k}\mathcal{M}\mathcal{C}\mathcal{M}\mathbf{k}' - \mathbf{k}'\mathcal{M}\mathcal{C}\mathcal{M}\mathbf{k} + \mathbf{k}'\mathcal{M}\mathcal{C}_0\mathcal{M}\mathbf{k}'. \tag{B.14}$$

We are considering $\mathbf{k} = \mathbf{k}'$, so

$$\langle \exp(i\mathcal{K}.\mathcal{T}) \rangle = \exp[\mathbf{k}\mathcal{M}(\mathcal{C} - \mathcal{C}_0)\mathcal{M}\mathbf{k}] \tag{B.15}$$

and

$$P^s(\mathbf{k}) = \int \exp[\mathbf{k}\mathcal{M}(\mathcal{C} - \mathcal{C}_0)\mathcal{M}\mathbf{k}] \exp(-i\mathbf{k}.\mathbf{r}) d^3\mathbf{r}. \tag{B.16}$$

Equation B.16 is the key result of this appendix. The rest of this work is concerned with putting this expression into a form that can be dealt with numerically.

Choosing the z-axis as the line of sight, the matrix $\mathcal{M}$ is given by:

$$\mathcal{M} = \begin{pmatrix} 1 & 0 & 0 \\ 0 & 1 & 0 \\ 0 & 0 & 1+\beta \end{pmatrix} \tag{B.17}$$

It has been shown by Gorski (1998) that the displacement field correlation matrix, $\mathcal{C}$, can be expressed as:

$$\mathcal{C}_{ij} = \delta_{ij} C_\perp(r,t) + \hat{r}_i \hat{r}_j [C_{//}(r,t) - C_\perp(r,t)] \tag{B.18}$$

where

$$C_\perp = \frac{2}{(2\pi)^2} \int P(k') \frac{j_1(k'r}{k'r} dk'$$

$$C_{//} = \frac{2}{(2\pi)^2} \int P(k') \left[j_0(k'r) - \frac{j_1(k'r)}{k'r} \right] dk'. \tag{B.19}$$

Also note that $C_{//}(0,t) = C_\perp(0,t)$, implying that $\mathcal{C}_{ij}(0) = \delta_{ij} C_\perp(0,t)$. If we define new functions,

$$G_+ = C_\perp - C_\perp(0)$$

$$G_- = C_{//} - C_\perp, \tag{B.20}$$

then,

$$\mathcal{C}-\mathcal{C}_0 = \begin{pmatrix} G_+ + \hat{x}\hat{x}G_- & \hat{x}\hat{y}G_- & \hat{x}\hat{z}G_- \\ \hat{y}\hat{x}G_- & G_+ + \hat{y}\hat{y}G_- & \hat{y}\hat{z}G_- \\ \hat{z}\hat{x}G_- & \hat{z}\hat{y}G_- & G_+ + \hat{z}\hat{z}G_- \end{pmatrix} \tag{B.21}$$

where, in spherical co-ordinates,

$$\begin{aligned} \hat{x} &= \sin(\theta)\cos(\phi) \\ \hat{y} &= \sin(\theta)\sin(\phi) \\ \hat{z} &= \cos(\theta). \end{aligned} \tag{B.22}$$

Given the vector $\mathbf{k} = (k_x, k_y, k_z)$, $\mathcal{M}\mathbf{k} = (k_x, k_y, (1+\beta)k_z)$, we can reduce the dimensionality of the problem by considering the symmetry between directions perpendicular to the line of sight, in other words we are free to set k_y to zero. Thus

$$\begin{aligned} \mathbf{k}\mathcal{M}(\mathcal{C}-\mathcal{C}_0)\mathcal{M}\mathbf{k} &= \begin{pmatrix} k_x & (1+\beta)k_z \end{pmatrix} \begin{pmatrix} G_+ + \hat{x}\hat{x}G_- & \hat{x}\hat{z}G_- \\ \hat{z}\hat{x}G_- & G_+ + \hat{z}\hat{z}G_- \end{pmatrix} \begin{pmatrix} k_x \\ (1+\beta)k_z \end{pmatrix} \\ &= k_x^2[G_+ + \hat{x}\hat{x}G_-] + 2k_xk_z(1+\beta)\hat{x}\hat{z}G_- + k_z^2(1+\beta)^2[G_+ + \hat{z}\hat{z}G_-] \end{aligned} \tag{B.23}$$

B.4 Doing it numerically

To evaluate the power spectrum, equation B.16 shows that we will need to Fourier transform the exponential of equation B.23. The function is obviously real, and, by considering the effect of a rotation in the θ direction, it will be seen that it is also even.

$$\begin{aligned} \text{Under} \quad \theta &\longrightarrow \theta + \pi, \\ \cos(\theta) &\longrightarrow -\cos(\theta) \\ \sin(\theta) &\longrightarrow -\sin(\theta) \\ \text{So,} \quad \hat{x}\hat{x} &\longrightarrow \hat{x}\hat{x} \\ \hat{z}\hat{z} &\longrightarrow \hat{z}\hat{z} \\ \hat{x}\hat{z} &\longrightarrow \hat{x}\hat{z} \end{aligned} \tag{B.24}$$

This means that the Fourier transform is also real, so we only need to use the real part of the complex exponential when transforming.

$$\exp(i\mathbf{k}.\mathbf{r}) \longrightarrow \cos(\mathbf{k}.\mathbf{r}) = \cos[r(k_x\hat{x} + k_z\hat{z})] \tag{B.25}$$

So, we are left needing to perform the integration

$$P^s(k) = \int_0^{2\pi}\int_{-1}^{+1}\int_0^{\infty} \cos[r(k_x\hat{x}+k_z\hat{z})]\exp\left(k_x^2[G_+ + \hat{x}\hat{x}G_-] + 2k_xk_z(1+\beta)\hat{x}\hat{z}G_- + k_z^2(1+\beta)^2[G_+ + \hat{z}\hat{z}G_-]\right) r^2 dr\, d\cos\theta\, d\phi \quad \text{(B.26)}$$

As a preliminary measure, we tabulate the G_+ and G_- terms on a logarithmic scale in r, since they are well-behaved functions and it is much quicker to use a look-up table than to calculate them every time. We proceed with the integration using the Numerical Recipes (Press et al. 1992) QROMB routine to implement a Romberg integration of the inner integral over ϕ for given k, r, μ. We then turn to the integral over μ. The cosine term oscillates in μ with frequency kr. We thus break the integral up into $2\pi/kr$ sections, use QROMB to evaluate each one separately, and sum up. For the outer integral, we use QROMB to integrate this function over one oscillation of the cosine term in r. We pass the output value to the EULSUM routine which uses Euler's method to find the sum of an alternating divergent series. We repeat with subsequent oscillations until the sum converges.

All that remains is to integrate this function over the angle between wave-vector and line of sight for every value of k we are interested in, to obtain the quadrupole-to-monopole ratio.

B.5 A check: linear theory from the ZA

In order to show that we have obtained the correct expression for the integral, we show how the linear theory of redshift-space distortions can be obtained directly from equation B.16. Assuming that the exponent in this equation is small, we can make the expansion $\exp(x) = 1 + x$.

For clarity, we now split the integral up into three parts and treat each separately.

B.5.1 the $\beta = 0$ term

First, we collect the terms of zeroth order in β.

$$k_x^2[G_+ + \hat{x}\hat{x}G_-] + 2k_xk_z\hat{x}\hat{z}G_- + k_z^2[G_+ + \hat{z}\hat{z}G_-] = k^2\mu^2G_+ + k^2G_- \quad \text{(B.27)}$$

Integrating this function over ϕ, we obtain

$$P_0^s(k) = 2\pi k^2 \int \exp(-ikr\mu)(G_- + \mu^2 G_+) r^2 dr d\mu. \tag{B.28}$$

We now use the identities

$$\int \exp(-ikr\mu)d\mu = 2j_0(kr) \text{ and } \int \exp(-ikr\mu)\mu^2 d\mu = 2\left[j_0(kr) - \frac{2j_1(kr)}{kr}\right] \tag{B.29}$$

to show that

$$P_0^s(k) = 4\pi k^2 \int r^2 dr \left[G_- j_0(kr) + G_+ j_0(kr) - \frac{2G_+ j_1(kr)}{kr}\right] \tag{B.30}$$

From the definitions of the C's in equation B.20, we can write

$$G_- + G_+ = C_{//} - C_\perp(0) \tag{B.31}$$

From equation B.19 we also have a convenient definition for $C_\perp(0)$,

$$C_\perp(0) = \frac{2}{(2\pi)^2} \int P(k') \frac{j_1(cr)}{cr} dk' \text{ with } c = 0 \tag{B.32}$$

Substituting into equation B.30, we obtain:

$$\begin{aligned} P_0^s(k) = \frac{8\pi k^2}{(2\pi)^2} \int r^2 dr \int dk' P(k') \Bigg[& -\frac{2j_1(k'r)j_0(kr)}{k'r} - \frac{j_0(kr)j_1(cr)}{cr} \\ & + j_0(k'r)j_0(kr) - \frac{2j_0(k'r)j_1(kr)}{kr} + \frac{6j_1(k'r)j_1(kr)}{k'r\ kr}\Bigg] \end{aligned} \tag{B.33}$$

We now employ the Bessel function identities that will be stated section B.6 to show that, for the five terms in the square bracket in the previous equation,

- if $k > k'$, the fourth and fifth terms cancel, and the first term is equal to zero;
- if $k < k'$, the first and fifth terms cancel, and the fourth term is equal to zero;
- the second term is zero if $k > c$, which it always is since $c = 0$ and we do not consider the $k = 0$ mode;
- the value of the third term is $\frac{\pi}{2}\frac{\delta(k-k')}{k^2}$.

Only the third term, therefore, contributes to the integral, and we have:

$$\begin{aligned} P_0^s(k) &= \frac{8\pi k^2}{(2\pi)^2}\frac{\pi}{2} \int P(k')\delta(k-k')dk' \\ &= P^r(k) \end{aligned} \tag{B.34}$$

B.5.2 Co-ordinate transform

Having got this part, we now turn to the first and second order terms in β. The β^2 term gives

$$P_2^s(k) = \int \exp(-ikr\mu)(k_z^2 G_- + k_z^2 \hat{z}\hat{z} G_+) r^2 dr\, d\cos\theta\, d\phi. \tag{B.35}$$

This time the azimuthal integral is not trivial. The integration is over the angle between the vector $\mathbf{k}$ and the co-ordinate system, θ_{kr}. the unit vectors $\hat{x}, \hat{z}$ are defined in terms of the angle between $\mathbf{k}$ a nd the line of sight. We must therefore employ a co-ordinate transform,

$$\hat{k}^1 = \frac{k_x \hat{i} + k_z \hat{k}}{k}, \hat{k}^2 = \frac{k_z \hat{i} - k_x \hat{k}}{k}, \text{ and } \hat{k}^3 = \hat{j} \tag{B.36}$$

Thus, $\hat{r} = \mu_{kr}\hat{k}^1 + \sin\theta_{kr}\cos\phi_{kr}\hat{k}^2 + \sin\theta_{kr}\sin\phi_{kr}\hat{k}^3$, and

$$\begin{aligned} \hat{r}.\hat{k} &= \frac{\mu_{kr}k_z}{k} - \frac{k_x \sin\theta_{kr}\cos\phi_{kr}}{k} = \hat{z} \\ \hat{r}.\hat{i} &= \frac{\mu_{kr}k_x}{k} + \frac{k_z \sin\theta_{kr}\sin\phi_{kr}}{k} = \hat{x} \end{aligned} \tag{B.37}$$

This transformation then implies

$$\begin{aligned} \int_0^{2\pi} \hat{z}\hat{z} d\phi_{kr} &= 2\pi \left[\left(\mu_{kr}\frac{k_z}{k}\right)^2 + \frac{1}{2}\left(\sin\theta_{kr}\frac{k_x}{k}\right)^2 \right] \\ \int_0^{2\pi} \hat{x}\hat{z} d\phi_{kr} &= 2\pi \left[\mu_{kr}^2 \frac{k_z k_x}{k^2} - \frac{1}{2}\sin^2\theta_{kr}\frac{k_x k_z}{k^2} \right] \end{aligned} \tag{B.38}$$

We can thus expand equation B.35 to obtain

$$P_2^s(k) = 2\pi \int \exp(-ikr\mu) \left[k_z^2 G_- + \frac{k_z^2 G_+}{k^2}\left(\mu^2 k_z^2 + \frac{1}{2}k_x^2(1-\mu^2)\right)\right] r^2 dr\, d\mu \tag{B.39}$$

Making the same substitutions and expansions as in the previous section, we find that, again, all the terms except one cancel, and we are left with

$$P_2^s(k) = P^r(k)\frac{k_z^4}{k^4} = P^r(k)\mu^4. \tag{B.40}$$

We are left with the first order term in β. This is twice the second order term, plus a component such that

$$P_1^s(k) = 2\mu^4 P^r(k) + 2\int \exp(ikr\mu) k_x k_z \hat{x}\hat{z} G_- r^2 dr\, d\mu\, d\phi. \tag{B.41}$$

When this is expanded as above, there is again only one term that does not cancel, resulting in:

$$P_1^s(k) = P^r(k)[2\mu^4 + 2\mu^2(1-\mu^2)] = P^r(k)2\mu^2 \tag{B.42}$$

We thus see that

$$P^s(k) = P^r(k)(1 + 2\beta\mu^2 + \beta^2\mu^4) = P^r(k)(1+\beta\mu^2)^2 \tag{B.43}$$

This is the result of linear theory as described in Appendix A. It is clear that our expression thus reduces to the linear theory result in a first order approximation.

B.6 Bessel functions

To perform the linear theory calculations in section B.5, we must use some identities for spherical Bessel functions.

B.6.1 Regular Bessel functions

Bessel functions are defined by the equation

$$J_n(x) = \sum_{p=0}^{\infty} \frac{(-1)^p}{\Gamma(p+1)\Gamma(p+n+1)} \left(\frac{x}{2}\right)^{2p+n} \tag{B.44}$$

We quote without proof the following expressions for integrals over combinations of Bessel functions from Watson 1922.

$$\int_0^\infty J_n(at)J_n(bt)\frac{dt}{t} = \frac{1}{2n} \times \begin{cases} b^n a^{-n} & \text{for } a > b \\ 1 & a = b \\ a^n b^{-n} & a < b \end{cases} \tag{B.45}$$

$$\int_0^\infty J_n(at)J_{n-1}(bt)dt = 1 \times \begin{cases} b^{n-1}a^{-n} & \text{for } a > b \\ b^{-1}/2 & a = b \\ 0 & a < b \end{cases} \tag{B.46}$$

$$\int_0^\infty J_n(at)J_n(bt)tdt = \frac{\delta(a-b)}{a} \tag{B.47}$$

B.6.2 Spherical Bessel functions

Spherical Bessel functions are related to their cylindrical counterparts by

$$j_n(x) = \sqrt{\frac{\pi}{2x}} J_{n+1/2}(x). \tag{B.48}$$

The above identities therefore become:

$$\int_0^\infty j_n(at) j_n(bt) dt = \frac{\pi}{2} \frac{1}{2n+1} \times \begin{cases} b^n a^{-n-1} & \text{for } a > b \\ b^{-1} & a = b \\ a^n b^{-n-1} & a < b \end{cases} \tag{B.49}$$

$$\int_0^\infty j_n(at) j_{n-1}(bt) t dt = \frac{\pi}{2} \times \begin{cases} b^{n-1} a^{-n-1} & \text{for } a > b \\ b^{-2}/2 & a = b \\ 0 & a < b \end{cases} \tag{B.50}$$

$$\int_0^\infty j_n(at) j_n(bt) t^2 dt = \frac{\pi}{2} \frac{\delta(a-b)}{a^2} \tag{B.51}$$

References

Fisher K. B., Nusser A., 1996, MNRAS, 279, L1

Gorski K., 1988, ApJ, 332, L7

Press W. H., Teukolsky S. A., Vetterling W. T., Flannery B. P., 1992, Numerical Recipes in FORTRAN, 2nd edition. Cambridge University Press, Cambridge

Taylor A. N., Hamilton A. J. S., 1996, MNRAS, 282, 767

Watson G. N., 1922, A treatise on the theory of Bessel functions. Cambridge University Press

Appendix C

The dispersion model: multipole formulae

THE ARGUMENT We present the results of the correction to the linear theory power spectrum moments due to peculiar velocities using Gaussian, exponential and pairwise exponential forms for the distribution of velocities. These formulae are presented as the output from the MAPLE computer program.

C.1 Introduction

In Chapters 6, 7, and 8, we use models of non-linear velocity dispersion to extend the linear theory of redshift-space distortions into the quasi-linear regime. In this Appendix we present the formulae used in this analysis to obtain the redshift-space correction factors, P_l^s/P_0^r, for the multipoles of order $l = 0,2,4$. Results are given for all three of the commonly assumed peculiar velocity distributions, ie. Gaussian, exponential and pairwise exponential. Beyond the monopole term, the results are tedious to calculate by hand, and we resort to the MAPLE computer program to aid in book-keeping. For convenience, we present the results as the output from the MAPLE worksheet used in the calculations, with some notes added for clarity.

C.2 Definitions

First, we define the linear theory result from Kasier,

```
> L:=(mu)->(1+beta*mu^2)^2;
```

$$L := \mu \to (1 + \beta\,\mu^2)^2 \tag{C.1}$$

Now, the exponential, Gaussian and pairwise exponential distributions,

```
> E:=(k,mu)->(1 + (k*mu*sigma)^2/2)^(-2);
```

$$E := (k,\ \mu) \to \frac{1}{(1 + \frac{1}{2}\,k^2\,\mu^2\,\sigma^2)^2} \tag{C.2}$$

```
> P:=(k,mu)->(1 + (k*mu*sigma)^2/2)^(-1);
```

$$P := (k,\ \mu) \to \frac{1}{1 + \frac{1}{2}\,k^2\,\mu^2\,\sigma^2} \tag{C.3}$$

Note that under this definition, the dispersion that goes into the formula is the pairwise velocity, $\sigma_{\rm pair} = \sigma_{\rm gal}\sqrt{2}$. With this definition, a binomial expansion of these formulae swiftly shows that, to first order, the distributions all have the same width.

```
> G:=(k,mu)->exp(-(k*mu*sigma)^2);
```

$$G := (k,\ \mu) \to e^{(-k^2\,\mu^2\,\sigma^2)} \tag{C.4}$$

Finally, the Legendre polynomials in μ of order $0, 2, 4$.

```
> p0:=(mu)->1;
```

$$p0 := 1 \tag{C.5}$$

```
> p2:=(mu)->(3*mu^2 - 1)/2;
```

$$p2 := \mu \to \frac{3}{2}\,\mu^2 - \frac{1}{2} \tag{C.6}$$

```
> p4:=(mu)->(35*mu^4 -30*mu^2 +3)/8;
```

$$p4 := \mu \to \frac{35}{8}\,\mu^4 - \frac{15}{4}\,\mu^2 + \frac{3}{8} \tag{C.7}$$

For each distribution we will calculate the moments

$$\frac{2l+1}{2}\int_{-1}^{1} L(\mu)X(k,\mu)P_l(\mu)d\mu \tag{C.8}$$

for multipoles $l = 0,2,4$, with $X = E,P$, and G.

C.3 Exponential

```
> (1/2)*Int(L(mu)*E(k,mu),mu=-1..1);
```

$$\frac{1}{2}\int_{-1}^{1} \frac{(1 + \beta\,\mu^2)^2}{(1 + \frac{1}{2}\,k^2\,\mu^2\,\sigma^2)^2}\,d\mu \tag{C.9}$$

```
> (1/2)*int(L(mu)*E(k,mu),mu=-1..1);
```

$$(24\beta^2 k\sigma + 8\beta^2 k^3\sigma^3 + 2k^5\sigma^5 + 2\sqrt{2}\,\%1\,k^4\sigma^4 + \sqrt{2}\,\%1\,k^6\sigma^6 - 24\beta^2\sqrt{2}\,\%1 - 12\beta^2\sqrt{2}\,\%1\,k^2\sigma^2 - 8\beta k^3\sigma^3 + 8\beta\sqrt{2}\,\%1\,k^2\sigma^2 + 4\beta\sqrt{2}\,\%1\,k^4\sigma^4)\Big/(2k^5\sigma^5 (2+k^2\sigma^2))$$

$$\%1 := \arctan(\frac{1}{2}k\sigma\sqrt{2})$$

```
> (5/2)*Int(L(mu)*E(k,mu)*p2(mu),mu=-1..1);
```

$$\frac{5}{2}\int_{-1}^{1}\frac{(1+\beta\mu^2)^2(\frac{3}{2}\mu^2-\frac{1}{2})}{(1+\frac{1}{2}k^2\mu^2\sigma^2)^2}\,d\mu \tag{C.10}$$

```
> (5/2)*int(L(mu)*E(k,mu)*p2(mu),mu=-1..1);
```

$$\frac{5}{4}(-144\beta\sqrt{2}\,\%1\,k^2\sigma^2 - 80\beta\sqrt{2}\,\%1\,k^4\sigma^4 + 144\beta k^3\sigma^3 + 56\beta k^5\sigma^5 - 104\beta^2 k^3\sigma^3 + 144\beta^2\sqrt{2}\,\%1\,k^2\sigma^2 + 12\beta^2\sqrt{2}\,\%1\,k^4\sigma^4 - 240\beta^2 k\sigma - 2k^7\sigma^7 + 240\beta^2\sqrt{2}\,\%1 + 4\sqrt{2}\,\%1\,k^6\sigma^6 - \sqrt{2}\,\%1\,k^8\sigma^8 - 12k^5\sigma^5 + 12\sqrt{2}\,\%1\,k^4\sigma^4 - 4\beta\sqrt{2}\,\%1\,k^6\sigma^6)\Big/(k^7\sigma^7 (2+k^2\sigma^2))$$

$$\%1 := \arctan(\frac{1}{2}k\sigma\sqrt{2})$$

```
> (9/2)*Int(L(mu)*E(k,mu)*p4(mu),mu=-1..1);
```

$$\frac{9}{2}\int_{-1}^{1}\frac{(1+\beta\mu^2)^2(\frac{35}{8}\mu^4-\frac{15}{4}\mu^2+\frac{3}{8})}{(1+\frac{1}{2}k^2\mu^2\sigma^2)^2}\,d\mu \tag{C.11}$$

```
> (9/2)*int(L(mu)*E(k,mu)*p4(mu),mu=-1..1);
```

$$-\frac{3}{16}(-1832\beta^2 k^5\sigma^5 + 952\beta k^7\sigma^7 + 1620\sqrt{2}\,\%1\,k^6\sigma^6 + 2520\sqrt{2}\,\%1\,k^4\sigma^4 - 16800\beta\sqrt{2}\,\%1\,k^2\sigma^2 - 2232\beta\sqrt{2}\,\%1\,k^6\sigma^6 - 36\beta\sqrt{2}\,\%1\,k^8\sigma^8 - 9\sqrt{2}\,\%1\,k^{10}\sigma^{10} + 18960\beta^2\sqrt{2}\,\%1\,k^2\sigma^2 - 12720\beta\sqrt{2}\,\%1\,k^4\sigma^4 + 108\beta^2\sqrt{2}\,\%1\,k^6\sigma^6 + 162\sqrt{2}\,\%1\,k^8\sigma^8 + 3816\beta^2\sqrt{2}\,\%1\,k^4\sigma^4 - 15040\beta^2 k^3\sigma^3 - 2520k^5\sigma^5 - 23520\beta^2 k\sigma + 16800\beta k^3\sigma^3 - 18k^9\sigma^9 - 1200k^7\sigma^7 + 9920\beta k^5\sigma^5 + 23520\beta^2\sqrt{2}\,\%1)\Big/(k^9\sigma^9 (2+k^2\sigma^2))$$

$$\%1 := \arctan(\frac{1}{2}k\sigma\sqrt{2})$$

C.4 Gaussian

```
> (1/2)*Int(L(mu)*G(k,mu)*p0(mu),mu=-1..1);
```

$$\frac{1}{2}\int_{-1}^{1}(1+\beta\mu^2)^2\,e^{(-k^2\mu^2\sigma^2)}\,d\mu \tag{C.12}$$

```
> (1/2)*int(L(mu)*G(k,mu)*p0(mu),mu=-1..1);
```

$$(\frac{1}{2}\sqrt{\pi}\,\mathrm{erf}(k\sigma)\,k^4\sigma^4\,e^{(k^2\sigma^2)}-\beta k^3\sigma^3+\frac{1}{2}k^2\sigma^2\beta\sqrt{\pi}\,\mathrm{erf}(k\sigma)\,e^{(k^2\sigma^2)}-\frac{1}{2}\beta^2k^3\sigma^3$$
$$-\frac{3}{4}\beta^2k\sigma+\frac{3}{8}\beta^2\sqrt{\pi}\,\mathrm{erf}(k\sigma)\,e^{(k^2\sigma^2)})e^{(-k^2\sigma^2)}\Big/(k^5\sigma^5)$$

```
> (5/2)*Int(L(mu)*G(k,mu)*p2(mu),mu=-1..1);
```

$$\frac{5}{2}\int_{-1}^{1}(1+\beta\mu^2)^2\,e^{(-k^2\mu^2\sigma^2)}\,(\frac{3}{2}\mu^2-\frac{1}{2})\,d\mu \tag{C.13}$$

```
> (5/2)*int(L(mu)*G(k,mu)*p2(mu),mu=-1..1);
```

$$5(-\frac{3}{4}k^5\sigma^5+\frac{3}{8}\sqrt{\pi}\,\mathrm{erf}(k\sigma)\,k^4\sigma^4\,e^{(k^2\sigma^2)}-\frac{1}{4}\sqrt{\pi}\,\mathrm{erf}(k\sigma)\,k^6\sigma^6\,e^{(k^2\sigma^2)}-\beta k^5\sigma^5-\frac{9}{4}\beta k^3\sigma^3$$
$$+\frac{9}{8}k^2\sigma^2\beta\sqrt{\pi}\,\mathrm{erf}(k\sigma)\,e^{(k^2\sigma^2)}-\frac{1}{4}k^4\sigma^4\beta\sqrt{\pi}\,\mathrm{erf}(k\sigma)\,e^{(k^2\sigma^2)}-\frac{1}{2}\beta^2k^5\sigma^5-\frac{3}{2}\beta^2k^3\sigma^3$$
$$-\frac{45}{16}\beta^2k\sigma+\frac{45}{32}\beta^2\sqrt{\pi}\,\mathrm{erf}(k\sigma)\,e^{(k^2\sigma^2)}-\frac{3}{16}\beta^2k^2\sigma^2\sqrt{\pi}\,\mathrm{erf}(k\sigma)\,e^{(k^2\sigma^2)})e^{(-k^2\sigma^2)}\Big/(k^7\sigma^7)$$

```
> (9/2)*Int(L(mu)*G(k,mu)*p4(mu),mu=-1..1);
```

$$\frac{9}{2}\int_{-1}^{1}(1+\beta\mu^2)^2\,e^{(-k^2\mu^2\sigma^2)}\,(\frac{315}{8}\mu^4-\frac{135}{4}\mu^2+\frac{27}{8})\,d\mu \tag{C.14}$$

```
> (9/2)*int(L(mu)*G(k,mu)*p4(mu),mu=-1..1);
```

$$(-\frac{405}{16}k^4\sigma^4\beta\sqrt{\pi}\,\mathrm{erf}(k\sigma)\,e^{(k^2\sigma^2)}+\frac{4725}{64}k^2\sigma^2\beta\sqrt{\pi}\,\mathrm{erf}(k\sigma)\,e^{(k^2\sigma^2)}$$
$$-\frac{135}{16}\sqrt{\pi}\,\mathrm{erf}(k\sigma)\,k^6\sigma^6\,e^{(k^2\sigma^2)}+\frac{27}{16}\sqrt{\pi}\,\mathrm{erf}(k\sigma)\,k^8\sigma^8\,e^{(k^2\sigma^2)}-9\beta k^7\sigma^7$$
$$+\frac{27}{16}k^6\sigma^6\beta\sqrt{\pi}\,\mathrm{erf}(k\sigma)\,e^{(k^2\sigma^2)}+\frac{945}{64}\sqrt{\pi}\,\mathrm{erf}(k\sigma)\,k^4\sigma^4\,e^{(k^2\sigma^2)}-\frac{9}{2}\beta^2k^7\sigma^7-\frac{117}{4}\beta^2k^5\sigma^5$$
$$-\frac{6975}{64}\beta^2k^3\sigma^3-\frac{33075}{128}\beta^2k\sigma-\frac{2025}{64}\beta^2k^2\sigma^2\sqrt{\pi}\,\mathrm{erf}(k\sigma)\,e^{(k^2\sigma^2)}$$
$$+\frac{81}{64}k^4\sigma^4\beta^2\sqrt{\pi}\,\mathrm{erf}(k\sigma)\,e^{(k^2\sigma^2)}-\frac{765}{16}\beta k^5\sigma^5-\frac{4725}{32}\beta k^3\sigma^3$$
$$+\frac{33075}{256}\beta^2\sqrt{\pi}\,\mathrm{erf}(k\sigma)\,e^{(k^2\sigma^2)}-\frac{45}{16}k^7\sigma^7-\frac{945}{32}k^5\sigma^5)e^{(-k^2\sigma^2)}\Big/(k^9\sigma^9)$$

C.5 Pairwise exponential

```
> (1/2)*Int(L(mu)*P(k,mu)*p0(mu),mu=-1..1);
```

$$\frac{1}{2}\int_{-1}^{1}\frac{(1+\beta\mu^2)^2}{1+\frac{1}{2}k^2\mu^2\sigma^2}\,d\mu \tag{C.15}$$

```
> (1/2)*int(L(mu)*P(k,mu)*p0(mu),mu=-1..1);
```

$$\frac{1}{3}(2\beta^2 k^3\sigma^3 + 12\beta k^3\sigma^3 - 12\beta^2 k\sigma + 3\sqrt{2}\arctan(\frac{1}{2}k\sigma\sqrt{2})k^4\sigma^4 - 12\beta\sqrt{2}\arctan(\frac{1}{2}k\sigma\sqrt{2})k^2\sigma^2 + 12\beta^2\sqrt{2}\arctan(\frac{1}{2}k\sigma\sqrt{2}))\Big/(k^5\sigma^5)$$

```
> (5/2)*Int(L(mu)*P(k,mu)*p2(mu),mu=-1..1);
```

$$\frac{5}{2}\int_{-1}^{1}\frac{(1+\beta\mu^2)^2(\frac{3}{2}\mu^2-\frac{1}{2})}{1+\frac{1}{2}k^2\mu^2\sigma^2}\,d\mu \tag{C.16}$$

```
> (5/2)*int(L(mu)*P(k,mu)*p2(mu),mu=-1..1);
```

$$\frac{1}{6}(8\beta^2 k^5\sigma^5 + 360\beta^2 k\sigma - 15\sqrt{2}\%1\,k^6\sigma^6 + 90k^5\sigma^5 - 90\sqrt{2}\%1\,k^4\sigma^4 + 60\beta\sqrt{2}\%1\,k^4\sigma^4 + 360\beta\sqrt{2}\%1\,k^2\sigma^2 - 360\beta k^3\sigma^3 - 60\beta^2\sqrt{2}\%1\,k^2\sigma^2 - 360\beta^2\sqrt{2}\%1)\Big/(k^7\sigma^7)$$

$$\%1 := \arctan(\frac{1}{2}k\sigma\sqrt{2})$$

```
> (9/2)*Int(L(mu)*P(k,mu)*p4(mu),mu=-1..1);
```

$$\frac{9}{2}\int_{-1}^{1}\frac{(1+\beta\mu^2)^2(\frac{315}{8}\mu^4-\frac{135}{4}\mu^2+\frac{27}{8})}{1+\frac{1}{2}k^2\mu^2\sigma^2}\,d\mu \tag{C.17}$$

```
> (9/2)*int(L(mu)*P(k,mu)*p4(mu),mu=-1..1);
```

$$\frac{3}{8}(-420k^5\sigma^5 + 1680\beta k^3\sigma^3 - 110k^7\sigma^7 + 440\beta k^5\sigma^5 - 36\beta\sqrt{2}\%1\,k^6\sigma^6 + 36\beta^2\sqrt{2}\%1\,k^4\sigma^4 + 9\sqrt{2}\%1\,k^8\sigma^8 - 1680\beta^2 k\sigma + 1680\beta^2\sqrt{2}\%1 - 1680\beta\sqrt{2}\%1\,k^2\sigma^2 + 420\sqrt{2}\%1\,k^4\sigma^4 - 440\beta^2 k^3\sigma^3 + 720\beta^2\sqrt{2}\%1\,k^2\sigma^2 + 180\sqrt{2}\%1\,k^6\sigma^6 - 720\beta\sqrt{2}\%1\,k^4\sigma^4)\Big/(k^9\sigma^9)$$

$$\%1 := \arctan(\frac{1}{2}k\sigma\sqrt{2})$$

References

Abbreviations

MNRAS; Monthly Notices of the Royal Astronomical Society

ApJ; The Astrophysical Journal

ApJ Lett; The Astrophysical Journal Letters

ApJ Supp; The Astrophysical Journal Supplement

AJ; The Astronomical Journal

A&A; Astronomy & Astrophysics

A&A Supp; Astronomy & Astrophysics Supplement

ARA&A; Annual Review of Astronomy & Astrophysics

Ap&SS; Astrophysics and Space Science

References

Arp H., 1999, A&A, 341, L5

Bagla J. S., 1998, MNRAS, 299, 417

Ballinger W. E., Heavens A. F., Taylor A. N., 1995, MNRAS, 276, L59

Ballinger W. E., Peacock J. A., Heavens A. F., 1996, MNRAS, 282, 877

Bardeen J., Bond J., Kaiser N., Szalay A., 1986, ApJ, 304, 15

Barlow R. J., 1989, Statistics: a guide to the use of statistical methods in the physical sciences, Manchester physics series. Wiley

Barrow J. D., Magueijo J., 1999, Physics Letters B, in press, astro-ph/9811072

Baugh C. M., 1996, MNRAS, 280, 267

Baugh C. M., Efstathiou G., 1993, MNRAS, 265, 145

Baugh C. M., Efstathiou G., 1994, MNRAS, 267, 323

Baugh C. M., Gaztañaga E., Efstathiou G., 1995, MNRAS, 275, 1049

Bean A. J., Ellis R. S., Shanks T., Efstathiou G., Peterson B. A., 1983, MNRAS, 205, 605

Benson A. J., Cole S., Baugh C. M., Frenk C. S., Lacey C. G., 1999, MNRAS

Bertin E., Dennefeld M., 1997, A&A, 317, 43

Bond J., Efstathiou G., 1991, Phys. Lett. B, 265, 245

Bond J. R., Kaiser N., Cole S., Efstathiou G., 1991, ApJ, 379, 440

Bouchet F. R., Colombi S., Hivon E., Juszkiewicz R., 1995, A&A, 296, 575

Boulanger F., Perault M., 1988, ApJ, 330, 964

Bower R. G., Coles P., Frenk C. S., White S. D. M., 1993, ApJ, 405, 403

Bromley B. C., Warren M. S., Zurek W. H., 1997, ApJ, 475, 414

Burstein D., Heiles C., 1978, ApJ, 225, 40

Burstein D., Heiles C., 1982, AJ, 87, 1165

Burstein D., McDonald L. H., 1975, AJ, 80, 17

Canavezes A. et al., 1998, MNRAS, 297, 777

Carlberg R. G., Couchman H. M. P., Thomas P. A., 1990, ApJ Lett, 352, L29

Carlberg R. G., Yee H. K. C., Ellingson E., 1997, ApJ, 478, 462

Carlberg R. G. et al., 1998, in Large Scale Structure in the Universe, Royal Society Discussion Meeting, March 1998

Cen R., Ostriker J. P., 1992, ApJ, 399, 331

Cen R., Ostriker J. P., 1993, ApJ, 417, 415

Chaboyer B., Demarque P., Kernan P. J., Krauss L. M., 1996, Science, 271, 957

Cheng E. S. et al., 1997, ApJ Lett, 488, L59

Cole S., 1997, MNRAS, 286, 38

Cole S., Fisher K. B., Weinberg D. H., 1994, MNRAS, 267, 785

Cole S., Fisher K. B., Weinberg D. H., 1995, MNRAS, 275, 515

Cole S., Weinberg D. H., Frenk C. S., Ratra B., 1997, MNRAS, 289, 37

Colless M., 1995, The 2df galaxy redshift survey, http://msowww.anu.edu.au/~heron/Colless/colless.html

Colless M., Ellis R. S., Taylor K., Hook R. N., 1990, MNRAS, 244, 408

Couchman H. M. P., 1991, ApJ, 368, 23

da Costa L. N. et al., 1994, ApJ, 424, 1

da Costa L. N. et al., 1988, ApJ, 327, 544

da Costa L. N., Vogeley M. S., Geller M. J., Huchra J. P., Park C., 1994, ApJ Lett, 437, L1

Davis M., Efstathiou G., Frenk C. S., White S. D. M., 1985, ApJ, 292, 371

Davis M., Faber S. M., 1998, astro-ph/9810489, Preprint

Davis M., Peebles P. J. E., 1983, ApJ, 267, 465

Dekel A., 1998, in Wide Field Surveys in Cosmology, 14th IAP meeting held May 1998, Paris. Editions Frontieres., p. 47

Efstathiou G., Bond J. R., White S. D. M., 1992, MNRAS, 258, 1

Efstathiou G., Davis M., White S. D. M., Frenk C. S., 1985, ApJS, 57, 241

Efstathiou G., Sutherland W. J., Maddox S. J., 1990, Nature, 348, 705

Eisenstein D. J., Hu W., 1998, ApJ, 496, 605

Eke V. R., Cole S., Frenk C. S., 1996, MNRAS, 282, 263

Eke V. R., Cole S., Frenk C. S., Henry J. P., 1998, MNRAS, 298, 1145

Epchtein N. et al., 1994, Ap&SS, 217, 3

Faber S. M., 1973, ApJ, 179, 731

Fan Z. H., Bardeen J. M., 1994, American Astronomical Society Meeting, 184, 6206

Feldman H. A., Kaiser N., Peacock J. A., 1994, ApJ, 426, 23

Ferreira P. G., Magueijo J., Gorski K. M., 1998, ApJ Lett, 503, L1

Fisher K. B., 1992, Ph.D. thesis, AA (California Univ.)

Fisher K. B., 1995, ApJ, 448, 494

Fisher K. B., Davis M., Strauss M. A., Yahil A., Huchra J. P., 1994, MNRAS, 267, 927

Fisher K. B., Nusser A., 1996, MNRAS, 279, L1

Frenk C. S., Evrard A. E., White S. D. M., Summers F. J., 1996, ApJ, 472, 460

Gardner J. P., Sharples R. M., Frenk C. S., Carrasco B. E., 1997, ApJ Lett, 480, L99

Geller M. J., De Lapparent V., Kurtz M. J., 1984, ApJ Lett, 287, L55

Geller M. J., Huchra J. P., 1989, Science, 246, 897

Giovanelli R., Haynes M. P., 1991, ARA&A, 29, 499

Gorski K., 1988, ApJ, 332, L7

Governato F., Baugh C. M., Frenk C. S., Cole S., Lacey C. G., Quinn T., Stadel J., 1998, Nature, 392, 359

Gregory S. A., Thompson L. A., 1978, ApJ, 222, 784

Groth E. J., Peebles P. J. E., 1977, ApJ, 217, 385

Gunn J. E., Weinberg D. H., 1995, in proceedings of the 35th Herstmonceux workshop. Cambridge University Press, Cambridge, astro-ph/9412080

Hamilton A. J. S., 1993, ApJ Letters, 406, 47

Hamilton A. J. S., 1997, astro-ph/9708102

Hamilton A. J. S., Kumar P., Lu E., Matthews A., 1991, ApJ Lett, 374, L1

Hancock S., Gutierrez C. M., Davies R. D., Lasenby A. N., Rocha G., Rebolo R., Watson R. A., Tegmark M., 1997, MNRAS, 289, 505

Heavens A. F., Taylor A. N., 1995, MNRAS, 275, 483

Heavens A. F., Taylor A. N., 1997, MNRAS, 290, 456

Heiles C., 1975, A&A Supp, 20, 37

Heiles C., 1976, ApJ, 204, 379

Henry J. P., Arnaud K. A., 1991, ApJ, 372, 410

Heydon-Dumbleton N. H., Collins C. A., Macgillivray H. T., 1989, MNRAS, 238, 379

Hilditch R. W., Hill G., Barnes J. V., 1976, MNRAS, 176, 175

Hubble E., 1929, Proc N.A.S., 15, 168

Huchra J. E. et al., 1992, in Center for Astrophysic Redshift catalog, 1992 version.

Huchra J. E., Davis M., Latham D., Tonry J., 1983, ApJS, 52, 89

Humason M. L., 1931, ApJ, 74, 35

Humason M. L., Mayall N. U., Sandage A. R., 1956, AJ, 61, 97

Jackson J. C., 1972, MNRAS, 156, 1P

Jain B., Mo H. J., White S. D. M., 1995, MNRAS, 276, L25

Jenkins A. et al., 1998, ApJ, 499, 20

Jimenez R., Padoan P., 1998, ApJ, 498, 704

Jones L. R., Fong R., Shanks T., Ellis R. S., Peterson B. A., 1991, MNRAS, 249, 481

Kaiser N., 1987, MNRAS, 227, 1

Kantor F. W., 1977, Information Mechanics. Wiley, New York

Kantor F. W., 1999, International Journal of Theoretical Physics, accepted, astro-ph/9812444

Katz N., Hernquist L., Weinberg D. H., 1992, ApJ Lett, 399, L109

Kauffmann G., Nusser A., Steinmetz M., 1997, MNRAS, 286, 795

Kauffmann G., White S., Guiderdoni B., 1993, MNRAS, 264, 201

Kay S. T., Bower R. G., 1998, MNRAS, in press, astro-ph/9807240

Kirshner R. P., Oemler J., A., Schechter P. L., 1978, AJ, 83, 1549

Kirshner R. P., Oemler J., A., Schechter P. L., Shectman S. A., 1981, ApJ Lett, 248, L57

Kogut A., Banday A. J., Bennett C. L., Gorski K. M., Hinshaw G., Smoot G. F., Wright E. L., 1996, ApJ Lett, 464, L29

Kolb E. W., Turner M. S., 1990, The early universe. Addison-Wesley

Kristian J., Minkowski R., 1972, in Sandage A., Sandage M., Kristian J., ed, Galaxies in the Universe. University of Chicago press

Lawrence C. R., Lange A. E., 1997, American Astronomical Society Meeting, 191, 4120

Lin H., Kirshner R. P., Shectman S. A., Landy S. D., Oemler A., Tucker D. L., Schechter P. L., 1996, ApJ, 471, 617

Loveday J., Efstathiou G., Maddox S. J., Peterson B. A., 1996, ApJ, 468, 1

Loveday J., Efstathiou G., Peterson B. A., Maddox S. J., 1992a, ApJ Lett, 400, L43

Loveday J., Peterson B. A., Efstathiou G., Maddox S. J., 1992b, ApJ, 390, 338

Lucy L. B., 1974, AJ, 79, 745

Maddox S. J., Efstathiou G., Sutherland W. J., 1996, MNRAS, 283, 1227

Maddox S. J., Efstathiou G., Sutherland W. J., Loveday J., 1990a, MNRAS, 243, 692

Maddox S. J., Efstathiou G., Sutherland W. J., Loveday J., 1990b, MNRAS, 242, 43P

Mann R. G., Peacock J. A., Heavens A. F., 1998, MNRAS, 293, 209

Matsubara T., Suto Y., 1996, ApJ, 470, 1

Meiksin A., White M., 1999, MNRAS, submitted, astro-ph/9812129

Melott A. L., Pellman T. E., Shandarin S. F., 1994, MNRAS, 269, 626

Metcalfe N., Shanks T., Fong R., Jones L. R., 1991, MNRAS, 249, 498

Mo H. J., Jing Y. P., Borner G., 1997, MNRAS, 286, 979

Moore B., Frenk C. S., White S. D. M., 1993, MNRAS, 261, 827

Nakamura T. T., Matsubara T., Suto Y., 1998, ApJ, 494, 13

Netterfield C. B., Devlin M. J., Jarolik N., Page L., Wollack E. J., 1997, ApJ, 474, 47

Nichol R. C., Collins C. A., 1993, MNRAS, 265, 867

Pahre M. A., Djorgovski S. G., De Carvalho R. R., 1996, ApJ Lett, 456, L79

Park C., Vogeley M. S., Geller M. J., Huchra J. P., 1994, ApJ, 431, 569

Peacock J. A., Dodds S. J., 1994, MNRAS, 267, 1020

Peacock J. A., Dodds S. J., 1996, MNRAS, 280, L19

Peebles P. J. E., 1980, The large-scale structure of the universe. Princeton University Press, Princeton, N.J.

Peebles P. J. E., 1981, ApJ, 248, 885

Peebles P. J. E., 1993, Principles of Physical Cosmology. Princeton University Press, Princeton

Perlmutter S. et al., 1999, ApJ, in press, astro-ph/9812133

Philips L. A., Turner E. L., 1998, ApJ, submitted, astro-ph/9802352

Pound R. V., Rebka G. A., 1959, Phys. Rev. Lett., 3, 439

Press W. H., Schechter P., 1974, ApJ, 187, 425

Press W. H., Teukolsky S. A., Vetterling W. T., Flannery B. P., 1992, Numerical Recipes in FORTRAN, 2nd edition. Cambridge University Press, Cambridge

Ratcliffe A., Shanks T., Broadbent A., Parker Q. A., Watson F. G., Oates A. P., Fong R., Collins C. A., 1996, MNRAS, 281, L47

Ratcliffe A., Shanks T., Parker Q. A., Fong R., 1998b, MNRAS, 293, 197

Ratcliffe A., Shanks T., Parker Q. A., Fong R., 1998a, MNRAS, 296, 191

Renzini A. et al., 1996, ApJ Lett, 465, L23

Rowan-Robinson M. et al., 1990, MNRAS, 247, 1

Rugers M., Hogan C. J., 1996, ApJ Lett, 459, L1

Salaris M., Degl'Innocenti S., Weiss A., 1997, ApJ, 484, 986

Sandage A., Tammann G., 1987, in Carnegie Institution of Washington Publication, Washington: Carnegie Institution, 1987, 2nd ed.

Santiago B. X., Strauss M. A., Lahav O., Davis M., Dressler A., Huchra J. P., 1995, ApJ, 446, 457

Sargent W. W., Turner E. L., 1977, ApJ, 212, L3

Saunders W. et al., 1994, in Proceedings of the 35th Herstmonceux workshop. Cambridge University Press, Cambridge

Schechter P., 1976, ApJ, 203, 297

Scherrer R. J., Weinberg D. H., 1998, ApJ, 504, 607

Schlegel D. J., Finkbeiner D. P., Davis M., 1998, in Wide Field Surveys in Cosmology, eds. S. Colombi and Y. Mellier

Schlegel D. J., Finkbeiner D. P., Davis M., 1998, ApJ, 500, 525

Schmidt B. P. et al., 1998, ApJ, 507, 46

Seljak U., Zaldarriaga M., 1996, ApJ, 469, 437

Shane C. D., Wirtanen C. A., 1967, Pub. Lick Obs., 22, 1

Shectman S. A., Landy S. D., Oemler A., Tucker D. L., Lin H., Kirshner R. P., Schechter P. L., 1996, ApJ, 470, 172

Smoot G. F. et al., 1992, ApJ Lett, 396, L1

Smoot G. F., Gorenstein M. V., Muller R. A., 1977, Physical Review Letters, 39, 898

Soifer B. T., Sanders D. B., Madore B. F., Neugebauer G., Danielson G. E., Elias J. H., Lonsdale C. J., Rice W. L., 1987, ApJ, 320, 238

Stark A. A., Gammie C. F., Wilson R. W., Bally J., Linke R. A., Heiles C., Hurwitz M., 1992, ApJ Supp, 79, 77

Steigman G., 1976, ARA&A, 14, 339

Strauss M. A., Davis M., Yahil A., Huchra J. P., 1990, ApJ, 361, 49

Strauss M. A., Huchra J. P., Davis M., Yahil A., Fisher K. B., Tonry J., 1992, ApJ Supp, 83, 29

Strauss M. A., Willick J. A., 1996, Physics Reports, 261, 271

Stuart A., 1987, Kendall's Advanced theory of statistics, 5th ed. Vol.1: Distribution theory. Charles Griffin, London

Sugiyama N., 1995, ApJ Supp, 100, 281

Summers F. J., Davis M., Evrard A. E., 1995, ApJ, 454, 1

Sunyaev R. A., Zel'dovich Y. B., 1972, Comm. Astrophys. Space Phys., 4, 173

Sylos Labini F., Montuori M., 1998, A&A, 331, 809

Tadros H. et al., 1998, in Large Scale Structure: Tracks and Traces. Proceedings of the 12th Potsdam Cosmology Workshop, September 1997. Eds. V. Mueller, S. Gottloeber, J.P. Muecket, J. Wambsganss. World Scientific., p. 221

Tadros H., Efstathiou G., 1995, MNRAS, 276, 45

Tanvir N., Shanks T., Ferguson H., Robinson D., 1995, Nature, 377, 27

Taylor A. N., Hamilton A. J. S., 1996, MNRAS, 282, 767

Tegmark M., 1996, in Dark matter in the universe: Proc. Enrico Fermi, Course CXXXII, astro-ph/9511148

Tormen G., Bertschinger E., 1996, ApJ, 472, 14

Trumpler R. J., 1930, Lick Observatory Bulletin, 420, 154

Tully R. B., Fisher J. R., 1987, in Cambridge: University Press, 1987

Tytler D., Fan X.-M., Burles S., 1996, Nature, 381, 207

Walker T. P., Steigman G., Kang H.-S., Schramm D. M., Olive K. A., 1991, ApJ, 376, 51

Wasserburg G. J., Papanastassiou D. A., Tera F., Huneke J. C., 1977, Royal Society of London Philosophical Transactions Series, 285, 7

Watson G. N., 1922, A treatise on the theory of Bessel functions. Cambridge University Press

Weinberg D. H., Cole S., 1992, MNRAS, 259, 652

Wheelock S. L. et al., 1994, IRAS sky survey atlas: Explanatory supplement. JPL publication 94-11

White M., Bunn E., 1996, ApJ, 460, 1071

White M., Bunn E. F., 1995, ApJ, 450, 477

White S. D. M., 1996, in Schaeffer R., ed, Cosmology and large scale structure : Les Houches, session LX, 1-28 August 1993. Elsevier Science, Amsterdam, astro-ph/9410043

White S. D. M., Efstathiou G., Frenk C. S., 1993, MNRAS, 262, 1023

White S. D. M., Frenk C. S., Davis M., Efstathiou G., 1987, ApJ, 313, 505

Yee H. K. C., Ellingson E., Carlberg R. G., 1996, ApJS, 102, 269

Zaroubi S., Hoffman Y., 1996, ApJ, 462, 25

Zel'dovich Y. B., 1970, A&A, 5, 84

Zel'dovich Y. B., 1972, MNRAS, 160, 1P

Zucca E. et al., 1996, Astrophysics Letters and Communications, 33, 99

Zucca E. et al., 1997, A&A, 326, 477